UNIVERSITAT POLITÈCNICA DE VALÈNCIA

DEPARTAMENTO DE MÁQUINAS Y MOTORES TÉRMICOS

DOCTORAL THESIS

ON THE INFLUENCE OF INLET GEOMETRY ON TURBOCHARGER COMPRESSOR NOISE

PRESENTED BY
D. Ferran Roig Villanueva

SUPERVISED BY
Dr. D. Alberto Broatch Jacobi

FOR THE DEGREE OF
Doctor of Philosophy

January 2023

DOCTORAL THESIS

"On the influence of inlet geometry on turbocharger compressor noise"

Presented by: D. Ferran Roig Villanueva
Supervised by: Dr. D. Alberto Broatch Jacobi

THESIS EXAMINERS

Dr. D. Gianluca Montenegro
Dr. D. Jorge Luis Parrondo Gayo
Dr. D. Hans Rämmal

DEFENSE COMITTEE

Chairman: Dr. D. José Galindo Lucas
Secretary: Dr. D. Francisco Javier Martos Ramos
Member: Dr. D. Gianluca Montenegro

Valencia, January 2023

Abstract

In today's society, there is a growing awareness of the importance of global warming. This concern is reflected by the legislative powers of Western nations in increasingly restrictive emissions regulations. In this context, the automotive industry has been strongly encouraged to develop more efficient thermal engines and even to explore new propulsion solutions, such as the electric motor.

The trend adopted to improve the energy efficiency of reciprocating internal combustion engines is the reduction of engine size. This has forced compressors to work in more extreme conditions, where their acoustic emission becomes troublesome. The problem of acoustic response takes on greater relevance in the context of competition against the electric car, which is inherently quieter. Even hybrid vehicles that incorporate downsized thermal engines to power the electric motor batteries have the aforementioned compressor noise problems, which remain a disadvantage compared to fully-electric vehicles. The emergence of new technologies such as drones, whose presence is rapidly increasing in urban and industrial environments, reinforces the interest in methodologies for analyzing the acoustic emissions of turbomachines.

The literature review carried out in this thesis shows that in the last two decades, there has been a great boom of research in the acoustics of radial turbocharger compressors. Despite the progress made, there is still no consensus about the cause of specific spectrum components, such as the broadband noises known as *whoosh* and Tip Clearance Noise (TCN). The influence of compressor inlet duct geometry on noise is also scarcely explored. This thesis presents a computational methodology of flow field analysis that allows the identification of the flow structures responsible for the most relevant spectral components and the analysis of the influence of operating conditions and inlet geometries on them.

The pressure field inside the compressor is analyzed through modal decomposition techniques. These allow identifying spatial patterns and associating them to the frequencies of the measured spectrum in an objective manner. Subsequently, the flow structures corresponding to these patterns are identified, and their evolution with the operating conditions and the inlet geometry is analyzed. Through the application of the described methodology, the different mechanisms of generation of the tonal noises in the inducer and the impeller trailing edge are identified. While the former is related to the

sonic conditions at the leading edge, the latter is excited by the asymmetric pressure field in the diffuser. As for the aforementioned broadband noises, the vortices encountered upstream of the inducer generate oscillations in the *whoosh* frequency band and favor rotating stall, contributing to such noise in the diffuser and volute. Unsteady blade surface loading is identified as an important contributor to TCN noise.

The influence of operating conditions on noise generation manifests through the intensity of the backflow in the inducer. The occurrence of backflow is characteristic of low mass flow points, although it is also found, with less intensity, at some higher mass flow points. The backflow inhibits the sonic conditions at the leading edge, weakening the tonal noise at the blade passing frequency. As for broadband noise, reverse flow is the cause of vortices in the inducer that produce *whoosh* noise and rotating stall. It also promotes the unsteady blade loading associated with TCN.

The role of the inlet duct geometry in the noise depends on its degree of interaction with the inducer vortices. In geometries that limit the upstream extent of these vortices, such as low curvature radii elbows, intense interaction of the vortices with the duct walls and other vortices occurs. This is correlated with an increase in *whoosh* noise. Inlet ducts that are sufficiently separated from the vortices only affect noise through their transmission properties regarding acoustic oscillations generated in the impeller and diffuser.

At the end of the thesis, reflections are offered on the contributions of the results to the current knowledge on compressor noise. In addition, new lines of research are proposed to extend the methodology presented and to complete the set of operating conditions and inlet geometries analyzed in this work.

Resumen

En la sociedad actual hay cada vez una mayor conciencia de la importancia del calentamiento global. Esta preocupación se ve reflejada por los poderes legislativos de las naciones occidentales en normativas de emisiones cada vez más restrictivas. En este contexto, la industria automovilísitca se ha visto fuertemente incentivada a desarrollar motores térmicos más eficientes e incluso a explorar nuevas soluciones propulsivas, como el motor eléctrico.

La tendencia adoptada para mejorar la eficiencia energética de los motores de combustión interna alternativos es la reducción del tamaño de los motores. Esto ha obligado a los compresores a trabajar en condiciones más extremas, en las que su emisión acústica llega a ser problemática. El problema de la respuesta acústica adquiere una mayor relevancia en el contexto de la competencia frente al coche eléctrico que es intrínsecamente más silencioso. Incluso los vehículos híbridos que incorporan motores térmicos para alimentar las baterías del motor eléctrico, presentan estos problemas de ruido del compresor, que siguen suponiendo una desventaja frente a los vehículos enteramente eléctricos. La emergencia de nuevas tecnologías como los drones, cuya presencia se incrementa rápidamente en los ámbitos urbano e industrial, refuerza el interés en las metodologías de análisis de las emisiones acústicas de las turbomáquinas.

La revisión bibliográfica llevada a cabo en esta tesis muestra que en las últimas dos décadas ha habido un gran auge de la investigación en acústica de compresores radiales de sobrealimentación. A pesar de los avances conseguidos, sigue sin haber consenso acerca de la causa de ciertas componentes del espectro, como los ruidos de banda ancha conocidos cono *whoosh* y *Tip Clearance Noise* (TCN). La influencia en el ruido de la geometría de los conductos de entrada al compresor está asimismo poco explorada. Esta tesis presenta una metodología computacional de análisis del campo de flujo que permite la identificación de las estructuras de flujo responsables de las componentes espectrales más relevantes, así como el análisis de la influencia en éstas de las condiciones de operación y las geometrías de entrada.

El campo de presión en el interior del compresor se analiza mediante técnicas de descomposición modal. Éstas permiten identificar patrones espaciales y asociarlos a las frecuencias del espectro medido de forma objetiva. Posteriormente se identifica las estructuras de flujo correspondientes a dichos patrones, y su evolución con las condiciones de operación y la geometría de

entrada. Mediante la aplicación de la metodología descrita se describe los diferentes mecanismos de generación de los ruidos tonales en el inductor y el borde de fuga del rotor. Mientras que el primero está relacionado con las condiciones sónicas en el borde de ataque, el segundo está excitado por el campo de presiones asimétrico en el difusor. En cuanto a los ruidos de banda ancha mencionados, los vórtices encontrados aguas arriba del inductor generan oscilaciones en la banda de frecuencias del *whoosh*, y favorecen el desprendimiento rotativo, que contribuye a dicho ruido en el difusor y la voluta. La carga no estacionaria sobre la superficie de los álabes es identificada como un importante contribuidor al ruido TCN.

La influencia de las condiciones de operación en la generación de ruido se manifiesta a través de la intensidad del flujo inverso en el inductor. La aparición de este flujo inverso es característica de los puntos de bajo gasto másico, aunque se sigue apreciando, con menor intensidad, en algunos puntos de alto gasto. El flujo inverso inhibe las condiciones sónicas en el borde de ataque, debilitando el ruido tonal a la frecuencia de paso de álabe. En cuanto a los ruidos de banda ancha, el flujo inverso es la causa de los vórtices en el inductor que producen el ruido *whoosh* y el despegue rotativo, y además promueve la carga no estacionaria de los álabes, asociada con el TCN.

El papel de la geometría del conducto de entrada en el ruido depende de su grado de interacción con los vórtices del inductor. En aquellas geometrías que limitan la extensión aguas arriba de los vórtices del inductor, como los codos con radio de curvatura reducido, tiene lugar una interacción intensa de los vórtices con las paredes del conducto y con otros vórtices. Ello está correlacionado con un aumento del ruido *whoosh*. Los conductos de entrada que están suficientemente separados de los vórtices, intervienen en el ruido solamente a través de sus propiedades de transmisión de las oscilaciones acústicas generadas en el rotor y el difusor.

Al final de la tesis se reflexiona sobre las contribuciones de los resultados expuestos al estado del arte de la investigación en el ruido de compresores. Además, se propone nuevas líneas de investigación para extender la metodología presentada, y completar el conjunto de condiciones de funcionamiento y geometrías de entrada analizadas en este trabajo.

Resum

En la societat actual hi ha cada vegada una major consciència de la importància del calfament global. Aquesta preocupació es veu reflectida pels poders legislatius de les nacions occidentals en normatives d'emissions cada vegada més restrictives. En aquest context, la indústria de l'automòbil s'ha vist fortament incentivada a desenvolupar motors tèrmics més eficients i fins i tot a explorar noves solucions propulsives, com el motor elèctric.

La tendència adoptada per a millorar l'eficiència energètica dels motors de combustió interna alternatius és la reducció de la grandària dels motors. Això ha obligat els compressors a treballar en condicions més extremes, en les quals la seua emissió acústica arriba a ser problemàtica. El problema de la resposta acústica adquireix una major rellevància en el context de la competència amb del cotxe elèctric que és intrínsecament més silenciós. Fins i tot els vehicles híbrids que incorporen motors tèrmics per a alimentar les bateries del motor elèctric, presenten aquests problemes de soroll del compressor, que continuen suposant un desavantatge enfront dels vehicles completament elèctrics. L'emergència de noves tecnologies com els drons, la presència dels quals s'incrementa ràpidament en els àmbits urbà i industrial, reforça l'interés en les metodologies d'anàlisis de les emissions acústiques de les turbomàquines.

La revisió bibliogràfica duta a terme en aquesta tesi mostra que en les últimes dues dècades hi ha hagut un gran auge de la investigació en acústica de compressors radials de sobrealimentació. Malgrat els avanços aconseguits, segueix sense haver-hi consens sobre la causa d'unes certes components de l'espectre, com els sorolls de banda ampla coneguts con *whoosh* i *Tip Clearance Noise* (TCN). La influència en el soroll de la geometria dels conductes d'entrada al compressor està així mateix poc explorada. Aquesta tesi presenta una metodologia computacional d'anàlisi del camp de flux que permet la identificació de les estructures de flux responsables de les components espectrals més rellevants, així com l'anàlisi de la influència en aquestes de les condicions d'operació i les geometries d'entrada.

El camp de pressió a l'interior del compressor s'analitza mitjançant tècniques de descomposició modal. Aquestes permeten identificar patrons espacials i associar-los a les freqüències de l'espectre mesurat de manera objectiva. Posteriorment s'identifica les estructures de flux corresponents a aquests patrons, i la seua evolució amb les condicions d'operació i la geometria d'entrada. Mitjançant l'aplicació de la metodologia descrita es descriu els diferents mecan-

ismes de generació dels sorolls tonals en l'inductor i la vora de fugida del rotor. Mentre que el primer està relacionat amb les condicions sòniques en la vora d'atac, el segon està excitat pel camp de pressions asimètric en el difusor. Quant als sorolls de banda ampla esmentats, els vòrtexs trobats aigües amunt de l'inductor generen oscil · lacions en la banda de freqüències del *whoosh*, i afavoreixen el despreniment rotatiu, que contribueix a aquest soroll en el difusor i la voluta. La càrrega no estacionària sobre la superfície dels àleps és identificada com un important contribuïdor al soroll TCN.

La influència de les condicions d'operació en la generació de soroll es manifesta a través de la intensitat del flux invers en l'inductor. L'aparició d'aquest flux invers és característica dels punts de baixa despesa màssica, encara que es continua apreciant, amb menor intensitat, en alguns punts d'alta despesa. El flux invers inhibeix les condicions sòniques en la vora d'atac, afeblint el soroll tonal a la freqüència de pas d'àlep. Quant als sorolls de banda ampla, el flux invers és la causa dels vòrtexs en l'inductor que produeixen el soroll *whoosh* i el despreniment rotatiu, i a més promou la càrrega no estacionària dels àleps, associada amb el TCN.

El paper de la geometria del conducte d'entrada en el soroll depén del seu grau d'interacció amb els vòrtexs de l'inductor. En aquelles geometries que limiten l'extensió aigües amunt dels vòrtexs de l'inductor, com els colzes amb radi de curvatura reduït, té lloc una interacció intensa dels vòrtexs amb les parets del conducte i amb altres vòrtexs. Això està correlacionat amb un augment del soroll *whoosh*. Els conductes d'entrada que estan prou separats dels vòrtexs, intervenen en el soroll solament a través de les seues propietats de transmissió de les oscil · lacions acústiques generades en el rotor i el difusor.

Al final de la tesi es reflexiona sobre les contribucions dels resultats exposats a l'estat de l'art de la investigació en el soroll de compressors. A més, es proposa noves línies d'investigació per a estendre la metodologia presentada, i completar el conjunt de condicions de funcionament i geometries d'entrada analitzades en aquest treball.

List of Publications

The following articles were published in the framework of the research carried out in the present thesis.

1. Alberto Broatch, Jorge García-Tíscar, Ferran Roig, and Sidharath Sharma. "Dynamic mode decomposition of the acoustic field in radial compressor". *Aerospace Science and Technology*, 2019.

2. Alberto Broatch, Xandra margot, Jorge García-Tíscar, and Ferran Roig. "Impact of simple surge-enhancing inlet geometries on the acoustic behavior of a turbocharger compressor". *International Journal of Engine Research*, 2018.

3. Alberto Broatch, Santiago Ruiz, Jorge García-Tíscar, and Ferran Roig. "On the influence of inlet elbow radius on recirculating backflow, whoosh noise and efficiency in turbocharger compressors". *Experimental Thermal and Fluid Science*, 2018.

Division of work between authors

The research work presented in this thesis was carried out in collaboration with other researchers. The respondent is the co-author of all the articles on which this thesis is based. The authors' signatures on these articles are in order of seniority. The respondent has elaborated the numerical models of the studied compressors, implemented the methodology of analysis of the noise-generating flow structures, processed the results, and elaborated the conclusions. Discussions were performed with the collaboration of the supervisor Prof. Broatch and the other co-authors. The experimental measurements were not carried out by the respondent and are thus gratefully acknowledged.

Funding acknowledgements

The respondent wishes to acknowledge the financial support received through contract FPI-Subp1 of the Programa de Apoyo para la Investigación y Desarrollo (PAID-01-17) of Universitat Politècnica de València.

Acknowledgements

Plato described as "*rough and steep*" the road that must be traveled to leave the cavern of ignorance "*until finding the clarity of the sun*" that represents scientific knowledge. It is certainly not an easy road, although fortunately, I have not had to travel it alone. In the first place, I owe special thanks to my supervisor, Prof. Broatch, for his support and guidance during the development of this work.

Thanks to all my colleagues at the Noise and Thermal Management line, among whom I would like to express my admiration and gratitude to Dr. Jorge García-Tíscar for his always generous collaboration. I would also like to acknowledge all the colleagues at CMT - Motores Térmicos, starting with Professors Payri and Desantes. Antonio Gil and Pau Raga for their support with the computational resources, Dr. Roberto Navarro for the numerical models and much-appreciated feedback, and of course, all the administrative staff, especially Amparo Cutillas, for her invaluable help with all the paperwork over the years.

I also have a fond memory of my internship at KTH - Royal Institute of Technology, which unfortunately had to be virtual due to the COVID-19 pandemic. I would like to thank Prof. Mihăescu and his collaborators for their warm welcome in their research group at CCGEx.

I also had the pleasure of meeting wonderful people among my fellow Ph.D. students: Pablo, Edu, Sid, Bárbara, Johan, Andrés, and all the other members of the Doctoral Day Organization, to name only a few. Thank you for your friendship and for all the good memories.

Last but not least, I would like to thank my family, Salva, Ángeles, Andreu, and Diana, for their unconditional love and support. Also, to my friends, whose encouragement has been essential to me. And finally, thank you, Melani, for making the sun shine in my life, even on rainy days.

Valencia, January 2023

"He who does not know what the world is, does not know where he is. He who does not know what he was born for, does not know who he is. He who neglects even one of these questions can neither say what the world is nor what he was born for. What to think of those who chase after the noise of those who applaud, who do not know where they are or who they are?"

Marcus Aurelius, Meditations.

Contents

List of Figures

List of Tables

List of Symbols

Latin

c_v	Specific heat capacity at constant volume	J kg^{-1} K^{-1}
D	Diameter	m
E	Energy	J
E_i	Modal relevance metric	-
e	Specific energy	J kg^{-1}
f	Frequency	Hz
k	Thermal conductivity	W m^{-1} K^{-1}
Ma	Mach Number	-
p	Pressure	Pa
$\mathbf{Q}$	Heat flux per unit area	W m^{-2}
R	Specific gas constant	J kg^{-1} K^{-1}
r	Radial coordinate	m
rev	Revolution	-
T	Period	s
T	Temperature	K
t	Time	s
u	Velocity component	m s^{-1}
u_τ	Friction velocity	m s^{-1}
v	Velocity component	m s^{-1}
$\mathbf{v}$	Velocity vector	m s^{-1}
w	Velocity component	m s^{-1}
y^+	Dimensionless wall distance	-

Greek

α_i	Modal amplitude	Pa
γ	Ratio of specific heats	-
δ_{ij}	Kronecker Delta	-
η_s	Isentropic efficiency	-
θ	Azimuthal angle	rad
ε_R	Relative error	%
κ	Wavenumber	m
λ_i	Egenvalue of DMD mode i	-
μ	Dynamic viscosity coefficient	Pa s
ν	Kinematic viscosity	$\mathrm{m^2\ s^{-1}}$
Π_{tt}	Total-to-total pressure ratio	-
ρ	Density	$\mathrm{kg\ m^{-3}}$
σ_{ij}	Viscous stress tensor	Pa
τ_w	Wall shear stress	Pa
Φ_i	DMD mode i	-
Ω	Angular velocity	$\mathrm{rad\ s^{-1}}$
ω	Angular frequency	$\mathrm{rad\ s^{-1}}$

Sub- and superscripts

abs	Absolute velocity
co	cut-on / cut-off
frame	Velocity of the moving reference frame
in	Inlet duct
out	Outlet duct
PW	Plane wave
rel	Relative velocity
s	Isentropic
T	Total (pressure or temperature)
tt	Total-to-total

Acronyms

bep	Best Efficiency Point
BPF	Blade Passing Frequency
CFD	Computational Fluid Dynamics
CFL	Courant-Friedrich-Levy (number)
DES	Detached Eddy Simulation
DFT	Discrete Fourier Transform
DMD	Dynamic Mode Decomposition
e0D75	Compressor c2 elbow inlet with curvature radius 0.75 D
e1D	Compressor c2 elbow inlet with curvature radius 1 D
e1D5	Compressor c2 elbow inlet with curvature radius of 1.5 D
EEA	European Economic Area
elb	Compressor c1 elbow inlet duct
FFT	Fast Fourier Transform
FW-H	FfowcsWilliams and Hawkings acoustic analogy
hpr	Highest Pressure Ratio
ICSU	International Council for Science
IDDES	Improved Delayed Detached Eddy Simulation
IGV	Inlet Guide Vanes
LE	Leading Edge
LES	Large Eddy Simulation
LIC	Line Integral Convolution
nsg	Near Surge
PIV	Particle Image Velocimetry
POD	Proper Orthogonal Decomposition
PS	Pressure Side
PSD	Power Spectral Density
RANS	Reynolds-Averaged Navier Stokes
RO	Rotating Order
rpm	Revolutions Per Minute
rsd	Reference Straight Ducts
rsv	Compressor c1 reservoir inlet duct
SBES	Stress-Blended Eddy Simulation

SGS	Sub-Grid Scale
SPL	Sound Pressure Level
SS	Suction Side
SST	Shear Stress Transport
str	Compressor c1 straight inlet duct
tap	Compressor c1 tapered inlet duct
TC	Tip Clearance
TCN	Tip Clearance Noise
TE	Trailing Edge
TS	Time Step
UNEP	United Nations Environment Programme
URANS	Unsteady RANS
VT	Volute Tongue
WMO	World Meteorological Organization
WWII	World War Two

1

Introduction

Contents

> *"What is essential for [solving] this problem is a global consciousness, a view that transcends our exclusive identifications with the generational and political groupings into which, by accident, we have been born. The solution to these problems requires a perspective that embraces the planet and the future because we are all in this greenhouse together."*
>
> Carl Sagan, before the U.S. Congress, 1985

1.1 Introduction

Dr. Sagan spoke before the U.S. Congress as a scientific witness in December 1985 [1]. His task was to explain the greenhouse effect and its potential consequences. That intervention took place in the context of a growing social concern for the environment and the influence of human beings on it. Previously that year, the "International Assessment Conference on CO_2 and other Greenhouse gases" was held in Austria. It was a joint UNEP/WMO/ICSU conference in which scientists from twenty-nine countries assessed the effect of the increase of CO_2 and other greenhouse gases in the atmosphere. They concluded that greenhouse gases were causing climate change by increasing the global temperature, which would have catastrophic consequences on ecosystems and the planet's habitability [2].

The greenhouse effect was first proposed in 1824 by Joseph Fourier [3]. Human influence on this phenomenon has been known since the beginning of the last century. As an example, it is worth mentioning an article in the March 1912 issue of Popular Mechanics Magazine [4], which warns about the consequences of CO_2 emissions resulting from the burning of fossil fuels: "*This tends to make the air a more effective blanket for the Earth and to raise its temperature. The effect may be considerable in a few centuries*". Since that warning, more than a century has passed, during which the emissions rate has increased enormously.

The greenhouse effect works as follows: solar radiation in the visible spectrum reaches the Earth through the atmosphere. At these wavelengths, atmospheric gases are transparent, allowing solar energy to reach the surface. However, the Earth radiates that energy back into space in the infrared spectrum. Greenhouse gases present in the atmosphere, such as CO_2, water vapor, methane, and nitrous oxide, are opaque in the infrared wavelengths, preventing this energy from leaving the Earth. This mechanism increases planetary temperature, which can trigger climate redistribution, extreme weather events, and sea level rise due to the melting of the polar ice caps.

In recent decades, governments in western countries have passed laws to reduce greenhouse gases emissions. In the automotive field, in which this doctoral thesis is framed, the Euro VI standard applies to new road vehicles sold in the European Union, EEA member states and the UK, and ships in EU waters [5]. In the United States, the Corporate Average Fuel Economy (CAFE) Standards were set with the same intent. They are aimed at reducing

energy consumption by increasing the fuel economy of cars and light trucks [6].

During the three decades that Euro standards have been in force, the automotive industry has been designing increasingly energy-efficient engines and developing after-treatment systems to effectively reduce emissions. Downsizing has been one of the strategies used to obtain more efficient engines [7]. This technique consists of reducing engine displacement since thermal and frictional losses increase with the displaced volume. However, the rated power is also proportional to the displacement; therefore, to maintain performance, it has been necessary to increase the supercharging of the engines.

The supercharging of thermal engines consists of increasing the intake air's density using a compressor. The residual energy in the exhaust gases is used to drive a turbine that shares the shaft with a centrifugal compressor in the intake line. More details can be found, for example, in the book by Payri and Desantes [8].

Downsized and highly supercharged engines need compressors that provide a high pressure ratio even at the lowest mass flow operating points. Thus, the compressor operates closer to its surge limit, increasing the acoustic emissions [9], [10].

The problem of turbocharger noise is exacerbated by the increasingly quiet combustion of today's engines [11]. Compressor noise has a signature that causes discomfort to users, as it is different from the noise associated with a normal vehicle operation. It can even be perceived as caused by a malfunction of the engine [12], [13].

A parallel line of innovation to the improvement in the efficiency of thermal engines is the introduction of the electric car. The main environmental advantage of the electric car is that the production of emissions associated with power generation occurs far from cities. This reduces the emission of pollutants such as NOx, CO, particulate matter (PM), or soot in populated areas, improving air quality. In addition, there is the possibility of generating electricity from renewable sources (solar, wind, hydro) that do not contribute to the greenhouse effect. However, electricity from renewable sources in the EU still accounts for only 33% of the total [14]. Fossil-fuel-fired power plants generate some 35.6% of the electric energy. Although these plants are more efficient than the internal combustion engines used in the automotive industry, the transport and storage of electric energy to vehicle batteries reduces the efficiency improvements.

However, the widespread deployment of the electric car will require significant infrastructure. First, the power installed in the different countries will have to support the demand of vehicles, which currently account for 28.4% of the total energy consumed in the EU [15]. Furthermore, an extensive network of recharging points for these vehicles is needed, which certainly does not exist today.

On June 2022, the European Council agreed to introduce a 100% CO_2 emissions reduction target by 2035 for new cars and vans [16]. There is controversy as to whether it is feasible to replace the current fleet of thermal

engine vehicles by that date. What is certain is that, for at least the next 13 years, there will be an automotive industry with thermal engines.

Hybrid vehicles are the middle way between the thermal engine and the electric motor. These vehicles operate with an electric motor powered by a generator coupled to a thermal engine. The internal combustion engine can operate under maximum efficiency conditions. In populated areas, the electric motor can be used with the energy stored in the battery to avoid polluting emissions. These vehicles currently have a greater range than purely electric ones and can be refueled at the currently available service stations.

The combustion engines used in hybrid vehicles are also downsized [17], [18] and are, therefore, subject to the compressor noise problems mentioned previously. It follows from the above that in the next decade, internal combustion engine vehicles will compete in a market with an increasing presence of quieter electric vehicles. Therefore, turbocharger noise will be an essential factor in the industry for the foreseeable future.

Besides the automotive industry, turbomachinery noise problems have been known for decades in the aircraft industry. Since the 1950s, jet engine noise from aircraft flying over residential areas was a problem that motivated research in aeroacoustics [19]. In addition to the aeronautical industry, turbomachinery is present in many applications, such as vacuum cleaners, dryers, or domestic fans, whose annoying acoustic signature is well known worldwide. Recently, drone technology has posed new noise problems of aeroacoustic nature in cities [20]. It is clear, then, that the investigation methods on aeroacoustic sources in turbomachinery, to which this thesis contributes, are of great interest to industry and society today.

1.2 State of the art

In the last decade, research in centrifugal compressor acoustics has experienced a considerable rise. From the experimental standpoint, thorough characterizations of compressor noise along the operating map have been carried out. The main flow characteristics at various spots in the compressor have been identified through optical techniques and pressure probes. The experimental data have been complemented with precise numerical models of the flow field inside the compressor. These models have allowed accurate calculations of performance and the flow's main characteristics. In addition, the acoustic response has been predicted for many operating conditions. However, there is still no consensus on the cause of specific components of the acoustic spectrum, especially certain broadbands, including the so-called *whoosh* noise.

The influence of inlet duct geometry on compressor acoustics is one of the least studied topics in this area. Most measurements and numerical calculations have been carried out with large straight ducts at the inlet or with bell mouths taking in quiescent air. However, these conditions rarely occur in vehicles employing compressors, where elbows and section changes are frequently found upstream of the compressor for space reasons.

Furthermore, to date, there is no standard methodology for identifying the flow structures responsible for the different spectral components. Frequently, the estimation of the frequencies excited by a given flow structure comes from snapshots of intrinsically unstable and time-irregular phenomena.

This thesis proposes a flow field analysis methodology to objectively relate the frequencies of the spectrum to the flow structures that cause them. In addition, the effect of operating conditions and inlet duct geometry on the noise-generating flow structures is analyzed.

1.3 Objectives

The main objective of this thesis is to improve the understanding of the flow structures responsible for the most relevant aeroacoustic noise components in radial compressors. In order to achieve this objective, a series of partial objectives are proposed:

- To develop and apply a systematic methodology for analyzing the compressor flow field to identify flow patterns associated with spectral components.
- To evaluate the impact of different inlet geometries commonly found in the automotive industry on compressor acoustic emissions.
- To understand the evolution of the main noise-generating flow structures with the operating conditions.

1.4 Methodology

The constructive characteristics of radial compressors in the automotive industry make experimental access to the internal flow field difficult. For this reason, a numerical model will be used for the aeroacoustic analysis of the flow field.

The dynamic mode decomposition (DMD) tool allows expressing the flow field as a sum of spatial modes with harmonic time evolution. In this way, an objective relationship can be established between specific regions of the numerical domain, their spatial distribution, and the frequencies of the acoustic spectrum.

Proper Orthogonal Decomposition (POD) is another modal decomposition technique that decomposes the flow field into orthogonal modes whose time evolution is not necessarily harmonic. A POD mode can have spectral content at different frequencies, including broad bands. For that reason, it could be an interesting tool to study broadband phenomena such as *whoosh* noise. However, the POD method does not provide phase information [21], making it difficult to interpret the spatial evolution of the modes. An example of this analysis on radial compressors is shown in the work of Sharma et al. [22]. The heterogeneous frequency content and the difficulty of analyzing the time

evolution of the POD modes make DMD preferred for the analysis carried out in this thesis. This method allows a clear association of frequencies with a single spatial pattern whose temporal evolution is easy to interpret.

The study of the pressure field utilizing DMD will be complemented by the study of the conventional flow field. In this way, the DMD modes will be identified with flow patterns in terms of the fluid dynamic variables. Therefore, the flow patterns identified with each mode are responsible for the oscillations at the corresponding frequency.

Finally, the impact of inlet geometry and operating conditions on the previously identified noise-generating flow structures will be evaluated. The outlined methodology complements the information obtained experimentally, where each geometry and operating point is associated with a pressure spectrum. Through the analysis carried out, information on the noise-generating flow structures is provided. Figure 1.1 shows the block diagram of the methodology used in the thesis, that has been described above.

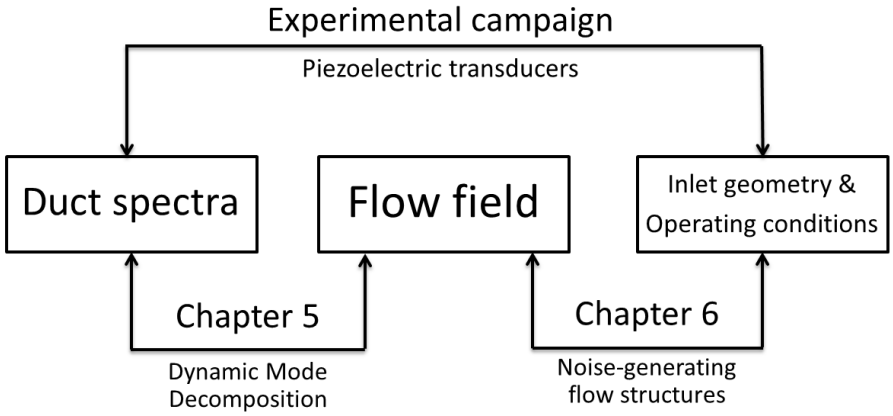

Figure 1.1: *Block diagram of the methodology followed in this thesis for analyzing the noise-generating flow structures and their relationship with the inlet geometry and operating conditions.*

In the theses addressing numerically the aeroacoustics related to radial compressors, the preliminary discussion of the aeroacoustic calculation method has become commonplace [23] [24] [25].

The direct method consists of calculating the flow field with a spatial and temporal discretization (acoustic CFL number) with sufficient resolution to reproduce the acoustic oscillations accurately. The propagation of such oscillations along the computational domain requires maintaining the high spatio-temporal resolution in a large volume, with the resulting high computational cost.

The method based on the acoustic analogy of Ffowcs Williams and Hawkings (FW-H) is based on the detailed calculation of the flow field in the region where the aeroacoustic sources are present. Subsequently, the acoustic oscillations are propagated analytically to the far field. This method, motivated

by the noise problems of the aeronautical industry, is suitable when there is interest in the propagation of the noise at large distances from the source in an unobstructed domain. However, the presence of the compressor housing and the inlet and outlet ducts, together with the lack of interest in propagating this noise to an actual far field, makes this method not the preferred one in the study of radial compressor acoustics. However, this method does allow the location of acoustic sources and calculating their intensity. Furthermore, close to the inducer, where duct walls do not hinder acoustic propagation, or in compressors with inlet bell mouth, the method provides realistic and valuable results of acoustic oscillations.

The computational cost is an additional consideration for the selection of the calculation method. In this thesis 17 combinations of two compressors, three operating points, and various inlet geometries are analyzed. Thus, it is necessary to consider the available computational resources. Moreover, the less computationally expensive the application of the methodology is, the more interesting it will be for industries that do not have access to high-performance computing (HPC).

In this thesis, the direct method is used to calculate the aeroacoustics inside the compressor. However, the spatial resolution is progressively reduced in the ducts to reduce computational costs. The direct acoustic calculation is complemented with the FW-H analogy by placing probes in the inlet duct in the vicinity of the inducer. In addition, the dipole term of the acoustic sources is calculated on the impeller surface to facilitate the identification of specific noise-generation flow structures.

1.5 Thesis outline

The following is a preview of the content of the thesis divided by chapters:

Chapter 2 presents the literature review. The most important articles describing noise phenomena in radial compressors are analyzed. Existing numerical models and quantification techniques of acoustic sources are also reviewed. Finally, studies previously carried out on the influence of inlet ducts are discussed.

Chapter 3 describes the numerical model utilized in this thesis. First, the two compressors analyzed are presented, and the selection of inlet duct geometries and operating conditions is justified. Finally, the numerical models used are described, emphasizing the treatment of turbulence.

The experimental validation of the computational approach is presented in chapter 4. The numerical predictions of the compressor operating variables are compared with the measured values. The numerical pressure spectra are then compared with the measured ones to validate the noise prediction. Available measurements of the local flow field are also compared with the numerical calculations.

Chapter 5 is devoted to the study of the pressure field using the DMD. The frequencies of the most relevant modes are compared with the measured

spectra, thus identifying the main noise components captured by the numerical model. The spatial and temporal distributions of the most relevant modes are then analyzed. Finally, the modes in the rotating impeller region are addressed, together with the dipole acoustic sources.

Chapter 6 analyzes the compressor flow field under different operating conditions and inlet geometries. The main flow structures coherent with the spatial and temporal patterns highlighted by the DMD modes in the previous chapter are identified. Finally, conclusions are drawn on the influence of operating conditions and inlet geometry on the noise-generating flow structures.

Finally, Chapter 7 summarizes the results obtained in the thesis. The original contributions to the study of noise in radial compressors are highlighted. The achievement of the objectives set out in this section is commented, and to conclude, suggestions for further studies on the phenomena discussed in this thesis are offered.

2

Literature review

Contents

2.1 Introduction

Research on radial compressor noise started at the beginning of this century. The downsizing trend in internal combustion engines during the last decades, together with quieter combustion, motivated the inquiry about the sources of compressor noise, as they began to pose a problem for the automotive industry. Since the groundbreaking work of Raitor and Neise [26], much has been investigated both experimentally and numerically. Thanks to these efforts, the current work has a good number of references, among which it is worth highlighting the doctoral theses of Navarro [24], García-Tíscar [27] , Sundström [28] and Sharma [25].

After almost two decades of research, the experimental methodologies are well established. The characteristics of noise have been measured through pressure transducers in the inlet and outlet ducts, microphones near the air intake for ingestion noise, and in the far field. In addition, techniques such as PIV and the installation of thermocouples and pressure probes have made it possible to identify local flow field patterns related to noise generation, among which surge and rotating stall stand out.

Meanwhile, the numerical methods have also been refined, from the first RANS models of turbulence to the current LES, to achieve good predictive capabilities of noise and its sources. However, to this day, there is still a lack of consensus on the phenomena responsible for all the components observed in the pressure spectra emitted by the compressors. This demonstrates the complexity of the phenomena treated, and the difficulty of configuring tools capable of unambiguously detecting them.

This doctoral thesis aims to study the impact of the inlet duct geometry on centrifugal compressor acoustics. Thus the aforementioned methodologies are reviewed, as they are going to be used for improving the understanding of the compressor noise and its sources. In the sections below, a survey of the most notable works, their contributions and limitations is made, and finally conclusions are drawn about the state of the art on this research topic.

2.2 Measurements of radial compressor noise signature

The first articles to be published concerning the acoustics of centrifugal compressors were carried out by automotive manufacturers. In them, the compressor was regarded as a sub-system of the engine that presented a problematic acoustic performance. In fact, a distinctive feature of these papers is the representation of noise spectrograms as a function of engine speed instead of proper compressor map variables. In these articles, the compressor noise was measured and the damping capabilities of different devices were tested. Although the noise generating mechanisms were sometimes hypothesized, the responsible aeroacoustic phenomena were not identified. The focus was set on the removal rather than on the generation of noise.

2.2. Measurements of radial compressor noise signature

In 2001 Trochon [29] tested the effectiveness of a broadband silencer for pulsating noise and "blow noise", whose proposed sources were related to the rotor geometry imbalance and aerodynamic turbulence respectively.

Soh et al. [30] describe the modification of the ducts and compressor hardware to reduce synchronous, subsynchronous, and BPF (blade passing frequency) noise. The effects of rotor shaft unbalance correction, optimization of bearing clearance, rigidity reinforcement of exhaust system and modification of the turbocharger housing were assessed.

Evans et al. [31] measured a broadband noise called "whoosh", below 3 kHz. The engine and compressor conditions where the noise is generated were studied, identifying the proximity to the point of marginal surge (horizontal slope of the iso-velocity line) as the main factor. "Turbulence in the compressor" was proposed as the source of broadband noise. Duct thickness increase and a broadband resonator at the outlet were tested to reduce such noise. The use of a larger compressor was proposed to operate further away from marginal surge. The influence of the inlet ducting was suggested, as noise generation was favored by "turbulence at the compressor generated by flow separation in the inlet system".

In their work [32] Gaudé et al. carried out measurements of sound intensity in ducts and vibration in mechanical elements. They listed the origin of the different noise components observed in both mechanical vibrations and aeroacoustic sources, without providing evidence on the specific flow mechanism for the latter. Broadband content termed "hiss" noise was identified in the 0 to 20 kHz range.

Teng et al. [33] measured a broadband noise between 5 and 7 kHz, whose origin is related to "compressor surge or marginal surge". The correlation of this phenomenon with an increase in temperature and pressure pulsations in the inlet duct was verified. To reduce noise, compressors with different trims were tested. The use of inlet guide vanes for negative pre-whirl, which presented the downside of a notable pressure drop, and resonators in the inlet duct that were effective but impossible to implement due to space limitations, were assessed as well.

Pai et al. [34] measured the noise of a radial compressor operating in non-stationary conditions (throttle tip-in and tip-out maneuvers). They found that the surge noise frequencies match the resonance frequencies of the inlet and outlet ducts, and proposed using a structure inside the duct to inhibit the oscillation modes associated with those frequencies.

With the work of Raitor and Neise [26] the approach to centrifugal compressor noise research was changed. These researchers pointed out the importance of understanding noise sources in order to eliminate them as the best strategy to achieve quieter machines. In addition, they brought classic tools from aeroacoustic research on axial compressors, such as the study of oscillation modes in ducts, and some of the known noise sources, e.g. tip clearance noise (TCN), and the interaction of the impeller with rotating instabilities.

In their paper, Raitor and Neise carried out the first systematic investigation of noise generation mechanisms in radial compressors. They identified

three components in the pressure spectrum in the ducts. At high speeds, with sonic conditions at the blades, the spectrum is dominated by the harmonics of the rotating order (RO) called buzz saw noise, and those of the BPF. At lower speeds, with transonic conditions at the tip of the blade, noise is dominated by the BPF, and at lower speeds, a narrow band at around half the BPF was observed. This noise was called TCN due to its similarity to the tip clearance noise in axial compressors, and it was shown to be consistent with the interaction between the passage of blades with a rotating instability, although no experimental evidence of this flow mechanism was presented. The measurement of the azimuthal modes in the inlet duct was used to relate the observed components to the proposed sources.

Rämmal et al. [35] related the different noise components found by Raitor and Neise [26] to the aeroacoutic sources described in Lighthill's acoustic analogy [36], [37]. They assign the buzz-saw noise to monopole sources due to shock waves, BPF tones and TCN broadband noise to dipole sources due to fluctuating pressure on the rotor surface, interacting with stationary and non-stationary pressure disturbances respectively. The importance of quadrupole sources due to turbulence is disregarded for radial compressors.

Tiikoja et al. [38] measured the noise emitted by various compressors, also identifying broadband noise "TCN" and the tones corresponding to the BPF and its harmonics. The transmission properties of the compressor and the ducts were considered through the acoustic two-port approach.

Figurella et al. [39] identified broadband noise between 4 and 12 kHz near the line of marginal surge. When the operating conditions approached the surge line, and therefore the angle of incidence increased, reverse flow was detected by temperature rise at the inlet duct, and the broadband component of noise in the aforementioned frequency range was reduced.

Guillou et al. [40] characterized the noise of a compressor with a ported shroud at three characteristic operating points: high mass flow, marginal surge and deep surge. The noise in stable working conditions is dominated by the BPF, but in marginal surge, low frequency oscillations show up, which are more noticeable in deep surge. The use of PIV at the compressor inlet grants access the characteristics of the inlet flow at the different operating points. The flow pattern known as stall, found in marginal surge conditions, and the filling and emptying pattern typical of surge were identified.

Torregrosa et al. [9] established a methodology for the characterization of compressor noise measuring in-duct sound intensity. They clearly identified surge noise and the broadband whoosh as distinct components in their characteristic frequency bands.

The effect of local flow features was studied by Torregrosa et al. [41] by measuring noise inside the ducts, and at the inducer and diffuser using miniaturized pressure probes. The presence of backflow at the inlet was detected by an array of thermocouples. In all operating conditions the BPF and its harmonics were detected as well as a narrow band noise around 2 kHz identified as whoosh. On the other hand, a broadband noise was observed consistent with TCN reports in other papers [39] (4-12 kHz), [33] (5-7 kHz). In this work

an important difference between these two noises is established. By calculating the cut-off frequency in the ducts for the first asymmetric mode [42], it is observed that whoosh always takes place in the plane wave range at a fixed frequency band, while the TCN varies its frequency depending on the point where it is measured. Furthermore, the TCN band cuts abruptly at the plane wave threshold, suggesting that it cannot propagate below this frequency. Therefore they might be two different phenomena, which usually have not been described separately in the literature. Another interesting observation is reported regarding the whoosh generation mechanism. Although this narrow band presents maximum intensity at mild surge points where reversed flow appears at the inlet, the noise is detected in all operating conditions. This suggests that while whoosh propagation is favored by the convective effects of backflow, the generating mechanism is not exclusive of the unstable flow at mild surge, nor is it directly related with the backflow itself.

In the thesis by García-Tíscar [27], an insightful synthesis of the different noise components measured in recent decades was made, as depicted in figure 2.1.

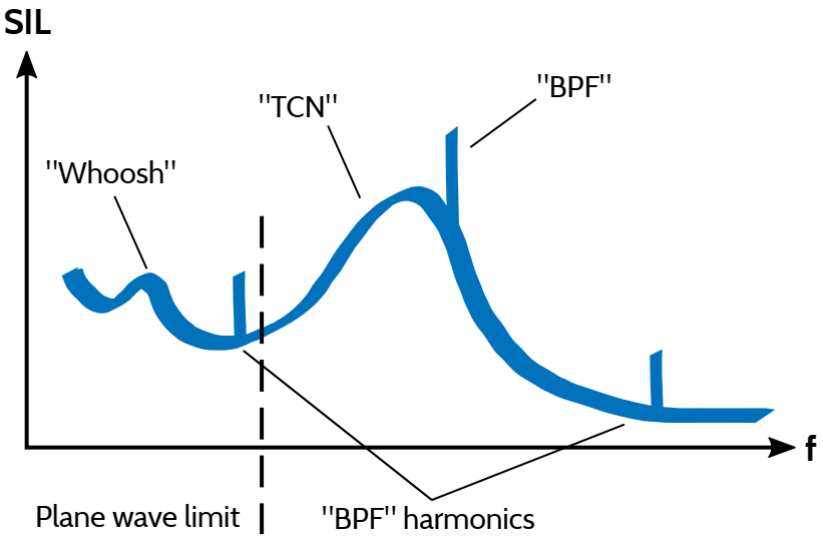

Figure 2.1: *Conceptual representation of centrifugal compressor noise components. Courtesy of Jorge García Tíscar [27].*

Regarding the identification of the noise sources in the literature, the interaction between the pressure discontinuities generated by the blades with static pressure disturbances, is proposed for tonal noise. As for broadband sources, stall and rotating instabilities are mentioned, but despite the data provided by the PIV and other measurements of the compressor local flow field, it is necessary to resort to numerical methods to obtain further insight.

2.3 Numerical study of the flow field

Early CFD studies of radial compressor acoustics used RANS turbulence models, as for example in the work of Lee et al. [43]. Although these models are capable of calculating average field characteristics, acoustic prediction is limited to the most prominent tonal noises.

The article by Mendonça et al. [44] pioneered the description of the numerical setup using scale resolving turbulence models, such as DES, a RANS-LES hybrid. These authors calculated the flow field near surge, showed the obtained spectra and analyzed the flow structures consistent with the observed frequencies. Unfortunately they did not provide any experimental noise measurements for validation. A tonal noise at 0.7 RO, the BPF and its harmonics, and two broad bands at high frequencies were identified. The flow field study shows rotating stall in the inducer and tip clearance flow. The rotating stall was proposed as the cause of the tone at 0.7 RO (although Raitor and Neise [26] claim that rotating instabilities produce broadband noise), and a helical mode is shown in the inlet duct at such frequency. At BPF, noise originating from the volute tongue is detected. Broadband noises are associated with detachment and reattachment at the blades.

In chapter 4 of the thesis by R. Navarro [24], a sensitivity study of the acoustic and performance prediction capabilities to the numerical setup was carried out. Different mesh sizes were tested, obtaining the best results with those that provide y^+ values in the viscous sub-layer, i.e., y^+ close to 1. The URANS and DES (specifically IDDES) turbulence models were tested, with different values of time step, corresponding to 0.5°, 1°, 2° and 4° of impeller rotation per time step. All settings provide accurate results for operating variables. In terms of acoustic response, both turbulence models offer similar predicting capabilities. Although DES is more precise in some frequency ranges, both are unable to capture high frequency broadband noise (TCN). Although the 1° time step is chosen, the 2° time step yields almost identical results in the range from 0 to 20 kHz, and the 4° is suitable for the low frequency range. The difference between segregated and coupled solvers was also studied. The latter offers better results in the presence of sonic conditions, although it is more expensive in terms of memory requirements.

Broatch et al. [45] calculated the flow field in a compressor operating in surge and marginal surge using DES with a time step of 1° and a mesh of $9{\times}10^6$ cells. They successfully reproduced the experimentally measured spectrum up to 5 kHz and identified the broadband whoosh noise. Near surge, they found rotating stall in the inducer flow field, while in the marginal surge point where the whoosh was more intense, the rotating stall was more important in the diffuser.

Sundström et al. [46] calculated the performance of a compressor with a ported shroud using LES, with a mesh of $9{\times}10^6$ elements, and a time step of 1°. The spectrum of the calculated pressure signals accurately corresponds to that measured experimentally. The dominant components of the spectrum are tonal or narrow band, there are no prominent broadband noises. At the

point close to surge, the compressor filling-emptying pattern was captured by surface FFT (fast Fourier Transform), and the velocity field was studied using POD and DMD modal decomposition. The mode corresponding to surge was identified, as well as four vortices in the inlet section caused by the outgoing flow from the ported shroud.

Later, Broatch et al. [47] simulated the operation of a compressor near surge, at marginal surge and at design point. They used DES with a time step of 1°. The numerically calculated spectra matched the experimental ones reasonably well in the plane wave range. At high frequencies the model failed to capture broadband noise. They compared URANS and DES models, and both showed similar acoustic prediction capabilities. The rotating stall in the diffuser observed at the point of marginal surge, was identified as the source of the whoosh noise. The disturbances caused by the jet-wake pattern at the impeller exducer were postulated as the cause of instabilities that produce this noise with higher or lower intensity at all operating points.

Semlitsch et al. [48] employed an implicit LES model with 5° per time step and wall functions to calculate the flow patterns that lead to surge. The operating variables accurately match the experimental ones. The acoustic flow field was not discussed, as the focus was set on the hydrodynamic field. POD and DMD were used to study compressor flow, and thus the surge cycle flow pattern was identified. The pressure increase in the volute, gives rise to reverse flow with swirl at the inlet. This increases the angle of incidence at the inducer, therefore reducing the aspirated flow, which in turn lowers the pressure in the volute. In this way, the backflow is reduced and so is the angle of incidence at the entrance, returning to the starting point.

Sharma et al. [22] tested different numerical setups to calculate a ported shroud compressor working close to surge. The URANS, DES, SBES and LES models were explored. All of them with time steps between 1° and 4° were able to predict the global variables of operation. The time step, however, influenced the acoustic prediction capability. With 2°, content above 10 kHz was attenuated, although the prediction was similar to that of 1°. With 4° there were very important discrepancies above 6 kHz. The acoustics were calculated with LES using a 2° time step. The noise level together with the broad band content at high frequencies were not correctly captured, which could be due to the difference in the location of the probe. The pressure field was decomposed by means of POD, finding spatial patterns associated with BPF and buzz-saw, in addition to broadband content in volute and diffuser.

Dehner et al. [49] used a k-ω DES model to calculate the flow field of a compressor at various operating points along an iso-speed line. They validated the velocity field at the inlet successfully using PIV. The SPL measurements in the 4 to 6 kHz bands, as well as the acoustic spectrum near surge match reasonably well the measurements. These authors identified content in the aforementioned frequency band in the reverse flow near the inducer. They proposed that the source of this noise is the interaction of the incoming flow with the backflow.

In conclusion, it has been proven that the simplest RANS models are capa-

ble of accurately calculating the average flow field and the operating variables with a low computational cost. For acoustic predictions involving broadband noise it is necessary to use scale resolving turbulence models, such as DES, SBES, or LES. These models are capable of capturing broadband noise, at least in the low frequencies. There are not many examples of broadband noise prediction at high frequencies (such as TCN) because not all compressors tested present them, and not all numerical setups are capable of capturing them.

The incorporation of numerical calculations into the compressor noise investigation has made it possible to clearly identify certain flow structures in relation to some components of the observed noise. Rotating stall in both inducer and exducer, and backflow in the inlet duct have been linked to whoosh noise. The pressure disturbance in the volute tongue is related to tonal noise at the BPF and its harmonics, and the filling-emptying pattern characteristic of surge has been associated with the content at very low frequencies.

2.4 Noise source analysis

Since the 1950s, when jet engines began to have civil application, the aerodynamic noise of these engines generated significant problems in urban areas with air traffic. This motivated the study of aeroacoustics, where Sir James Lighthill published the theory on aeroacoustic noise sources [36], [37]. Later, Ffowcs Williams and Hawkings adapted Lighthill's theory to account for moving walls in noise generation, leading to the acoustic analogy that bears their name [50].

Acoustic analogies allow for quantifying, locating in space, and studying the frequency content of different noise sources, as well as calculating their effect on receivers located in the far field. While the latter capacity has limited utility in the study of turbochargers, because free propagation is assumed, and the effect of compressor casing is not taken into account, the ability to characterize noise sources is very interesting.

An early example of the application of acoustic analogies for noise calculation in compressors is found in the article by Lee et al. [43]. The flow field in a compressor was calculated, probably with URANS using 1° time step, and the pressure field was used to estimate the dipole sources on the blades. Surface pressure fluctuation was found in the trailing edges as they pass through the pressure disturbance induced by the volute. This interaction is the origin of the tone at 2×BPF, i.e., the second harmonic of the BPF, as both the main and splitter blade trailing edges participate.

Sundström et al. [51] used the Ffowcs Williams and Hawkings (FW-H) acoustic analogy in the flow field calculated with the model described in [46]. The FW-H noise prediction corresponds well to the directly calculated far-field pressure spectrum, up to the frequency threshold allowed by the mesh resolution. The comparative of the SPL of the three types of sources shows that the dipolar are an order of magnitude greater than the monopole and quadrupole

sources. The SPL due to dipole sources matches the directly calculated total SPL, showing that this is the dominant source type. On the rotor surface, the dipole sources present greater intensity at the leading edge and on the pressure side of the trailing edge. Monopolar sources present greater intensity on the suction side of the trailing edge, due to flow detachment. Quadrupole sources present higher intensity also in the detachment zone at the blades and at the channel outlet due to the flow mixing downstream of the blades.

It is important to make the distinction between a hydrodynamic flow pattern (macroscopic spatial and temporal configuration of velocity, pressure, vorticity, etc.) that may be coherent with a certain frequency or broad band measured in the acoustic spectrum, and the sources of aeroacoustic noise. The latter are the primary contributors for the acoustic disturbances, i.e. that propagate at the speed of sound by virtue of the elastic forces of the fluid, while the flow patterns generate both acoustic (exciting these sources) and, predominantly, hydrodynamic disturbances.

This paper establishes a relationship between the surge and rotating stall flow patterns, and the noise sources associated with them. By filtering the frequency of the dipole term and the velocity field, the surge phases and the location of the acoustic sources are shown in four instants of a cycle. Specifically, during the phase in which the angle of incidence is greater, flow detachment occurs on the blade pressure side, causing a high noise level.

In the case of the rotating stall, four counter-rotating vortices are described a the inducer. When the leading edges chop the vortices that rotate in the opposite direction to the impeller rotation, a pressure oscillation is produced and noise is generated, as well as in the outlet section of those channels. The turning frequency of the vortex pattern (0.5 RO) marks the dominant frequency of this noise. Other modes of the pressure dipole term are identified at the impeller outlet related to multiples of the RO.

Another example of the quantification of aeroacoustic sources in compressors is the article by Zhong et al. [52]. An LES model was used to calculate the effect of the tip clearance gap and the number of impeller blades on the noise. The FW-H analogy was used to calculate the noise, showing good agreement with the experimental spectrum. The acoustic power on the rotor surface was shown for the different configurations, although the frequency content was not studied. The flow patterns proposed for noise generation are the outlet jets of the impeller, the flow detachment in the case with fewer blades, and the vortex shedding at the blade leading edge. However, details of the flow field are not shown that would allow to identify of these flow patterns.

The literature on the application of acoustic analogies in radial compressors is scarce. Papers relating aeroacoustic sources with flow patterns are even scarcer. However, this type of analysis is very important to understand the mechanisms of noise generation in compressors. In the present work, these techniques are applied to quantify the effect of the inlet duct geometry and operating conditions on the noise generation of radial turbochargers.

2.5 Impact of inlet duct geometries

Turbochargers in automotive vehicles are assembled in engine compartments where space is very limited. Thus, the use of inlet ducts with tortuous geometries such as 90º elbows and ducts with section changes is needed. This type of ducts give rise to uneven flow conditions at the compressor inlet.

Researchers have observed for decades that inlet flow non-uniformity caused by these inlet lines impairs compressor performance. From the beginning of the research in turbocharger noise, the presence of "turbulence" or "flow detachment" has been related to the generation of noise. Evans et al. [31] pointed out the possible contribution to the noise of the inlet duct in case it generated this type of disturbances upstream of the inducer.

The objective of this thesis is the study of the influence of the inlet geometries on the compressor noise. The type of geometries that this study focuses on are ducts commonly found at the inlet of compressors in automotive vehicles. 90° elbows and section changes are quite frequent. Other specific devices such as the ported shroud, focused on improving performance near the surge limit, are out of the scope; and both the properties of the flow field and their acoustic response have been discussed in other works, see for example [28], [25].

In the literature, there are several interesting studies of the flow caused by elbows at the inlet of compressors and its impact on performance.

Kim et al. [53], measured the degradation of performance of a compressor when changing the straight inlet duct for a 90° elbow. The loss of efficiency is due to the distortion of the inflow, where a secondary flow is established by virtue of the radial pressure gradient. This is due to the difference in centrifugal force between the flow particles on the major and minor radii of the elbow. As a result, two counter-rotating vortices are formed known as Dean vortices that alter the angle of incidence of the incoming compressor flow. The installation of guiding vanes with different spacing was tested to achieve greater flow uniformity.

Wang et al. [54], evaluated the effect of two 90° elbows at different axial distance from the compressor inlet. They observed a reduction in performance that increased with the rotation speed. They found out that the elbow generates a pressure disturbance in the inducer plane, more extensive the greater the axial distance, which in turn causes fluctuations in the blade loading that would generate noise. The high pressure zone generated by the elbow at the impeller inlet interacts with the high pressure zone induced by the volute downstream.

Zhao et al. [55] studied the effect of the relative orientation of a 90° elbow with respect to the volute tongue. At certain angles, the zone of low axial velocity in the inducer, caused by the elbow, coincides with the high pressure in the exducer under the volute tongue. This favors the stall onset, and the deterioration of the compressor performance.

Hou et al. [56] studied the effect of two consecutive 90° elbows with different assembling angles. The distortion generated by such ducts induces

bulk-like or twin counter-rotating vortices depending on the relative orientation between elbows, which cause pressure and efficiency losses. The intensity of those losses is reported to be strongly related to the relative rotating directions of vortices and rotor. They also found that the unsteady flow rate at individual impeller channels is affected by the interaction of the volute high pressure and the inlet distorted pressure distribution.

Zhang et al. [57] measured the pressure field along the casing of a compressor with different configurations of bent torsional inlet ducts. The effect of the positive and negative swirl induced by the ducts on the performance and the available operating range was investigated. Circumferential pressure distortion causes a loss of compressor performance, especially near the choke limit. The negative swirl is capable of extending the operating range close to surge although it has worse consequences at high mass flow rates than the positive swirl.

Serrano et al. [58] tested 90° elbows with different radii of curvature, with and without inlet guide vanes (IGV). They assessed the performance of these pipes regarding flow uniformity and the pressure drop. For low mass flow rates, the use of IGV provided good uniformity with low pressure drop, but at high mass flow the latter increased and a duct with maximum radius and no IGV was preferable.

Galindo et al. [59], designed a swirl generator device with a radial inlet to overcome packaging limitations and the flow distortion effects on compressor performance. They tested several vane angles for different operating conditions. While the device had a positive impact for low flow conditions, an important pressure drop was caused at higher mass flow rates.

Although the flow patterns that deteriorate performance usually yield the highest noise levels, it is convenient to study separately the influence of inlet geometries on performance and noise.

Teng et al. [33] tested the effect of pre-whirl generating devices and resonators on the inlet duct. While the negative pre-whirl reduced broadband noise, the devices caused a pressure drop that reduced the surge margin, thus discarding their viability. In contrast, a resonator tuned to 5-6 kHz in the inlet duct gave good results in terms of noise and performance, but was disregarded due to lack of packaging space.

Karim et al. [60] measured the effect on broadband noise (6 to 12 kHz) of an inlet duct with combinations of inlet grove or inlet step and swirl vanes. The inlet step offered the best results, as it allows the backflow not to obstruct the incoming flow. The inlet grove, for its part, generated cross flow that increased noise at medium mass flow. At low mass flow rates, swirl vanes guided the flow conveniently, but at higher rates, they created a wake that entered the compressor as a flow disturbance. The SPL in the 6-12 kHz band was calculated using computational aeroacoustics, but no detail was given on the location or quantification of the sources, other than proposing certain responsible flow patterns.

Figurella et al. [61] assessed the noise and performance of a compressor with and without IGVs. For high mass flow, the IGVs deteriorated the per-

formance and increased the emitted noise (up to 5 dBs). For low mass flow, but still above surge limit, the noise in the 5 to 12 kHz band was attenuated up to 5 dBs and the performance was not penalized.

Galindo et al. [62]. quantified the improvement in the surge margin of four inlet geometries. A straight tube, a tapered duct, a convergent-divergent nozzle and the convergent section alone of the same nozzle were tested at the compressor inlet. All the geometries improved the surge margin with respect to the straight tube, with the convergent-divergent nozzle being the most promising geometry at low mass flow rates. The low mass flow noise map of these ducts was also measured between 20 and 5000 Hz. The convergent nozzle showed the best results. Despite the good results at low mass flow, it was noted that the nozzle would reduce the choke limit.

Broatch et al. [63] tested four simple compressor inlet geometries: a straight duct, a resonator, a 90° elbow, and a tapered duct. They characterized the surge onset on an iso-speed line, and found that all geometries improved the reference surge margin of the reference straight duct. They measured the orifice noise in the inlet ducts under design conditions and near surge. The results were analogous at both operating points: the elbow exhibited a similar SPL to that of the straight duct, the tapered duct increased the SPL by up to 4 dB, and the resonator decreased it by up to 4 dB, showing narrow-band attenuation in the plane wave range. The ability of the elbow to improve surge margin besides being neutral in noise level, was highlighted as it is a commonly implemented solution due to space constraints. The possible disadvantages of these geometries in terms of performance, especially near choke, were not considered.

The noise and performance properties of 90° elbows were further studied by Broatch et al. [64]. They experimentally characterized the influence of the curvature radius of three 90° elbows at the compressor inlet. The noise in the band from 0.7 to 3 kHz, the circumferential standard deviation of the temperature in the inducer plane, the length of the inlet backflow and the isentropic efficiency were measured at points from surge to design for all compressor speeds. The results were compared with those of a straight inlet reported in [41]. The elbows caused an increase in noise that was bigger for the smaller curvature radii, especially at low mas flow rates. The temperature skewness also increased as the radius decreased, while the backflow length remained constant, approximately equal to the reference. Regarding isentropic efficiency, at low speeds and low flow, the elbow with the largest radius increased it by up to 2%. At higher mass flow, all elbows penalized performance, due to flow distortion.

Moritz et al. [65] experimentally measured the effect of a 105° bend upstream of the compressor on performance and radiated noise. The elbow generates the well-known Dean vortices pattern. The effects of negative and positive pre-whirl, a velocity gradient, and the combination of both to reproduce the Dean vortices were analyzed separately. Although in general the positive pre-whirl is more detrimental to performance (especially at high mass flow), it produces improvements in noise compared to the reference configu-

ration with axial inlet duct. Negative pre-whirl, on the other hand, worsens the acoustic response. The effect of the velocity gradient is to shift the map towards lower mass flow rates, for both surge and choke limits. This flow pattern reduces noise indirectly by operating farther away from the surge limit. Finally, when both effects are combined, the disadvantages of the swirl predominate, and it is concluded that a uniform flow presentation is desirable, and the use of inlet guide vanes is suggested.

The bibliographic review reveals that the effects of the inlet geometry have a very important magnitude that must be taken into account. In addition, these effects depend on variables such as the relative orientation with respect to the volute tongue, which can go unnoticed at the design stage. Elbows are the most studied geometry. These ducts create a flow distortion at the compressor inlet in the form of a radial pressure gradient and vorticity induced by a secondary flow. For 90°elbows, two twin counter-rotating vortices appear, while for bent-torsional inlet a bulk vortex appears occupying most of the section.

The effect of these non-uniformities is proportional to the flow velocity, and to the inverse of the elbow curvature radius. It therefore causes performance losses in the compressor for high mass flow. At low mass flow rates, the surge margin can be increased as the effective section is reduced by the flow deviation, increasing the axial speed and thereby improving the angle of incidence on the blades.

Regarding noise, the effect of the elbows is highly dependent on the operating conditions. Both, the mass flow rate and the compressor speed play an important role. As a rule of thumb, for low mass flow rates, higher noise levels are usually found, while at high mass flows, in general, the noise decreases. This may seem paradoxical, as the trend is opposite to what happens with performance. Thus, it would be unclear whether the increase in noise is due to the flow patterns induced by the elbow, exciting aeroacoustic sources in the compressor, or whether this flow only increases the propagation of the noise to the upstream duct.

Concerning other inlet systems such as swirl generator devices, they have proven to be effective in certain points of the compressor map, for improving both noise and performance, but when operating conditions change, their performance declines. Some authors, e.g. [59] suggest the need for active systems to adapt these geometries to the flow conditions.

As a summary, the impact of inlet geometry on the flow presentation to the compressor, as well as the interaction of this flow with that inside the compressor are well described in the literature. The influence of internal flow on performance is also discussed, but no studies are found on how this flow excites aeroacoustic sources. The present work aims to contribute to the understanding of this interaction.

2.6 Conclusions

In this chapter, the synthesis of the exhaustive literature review done on centrifugal compressor noise was presented.

The main components of the experimentally measured noise are the following:

- Tonal noise at frequencies multiple of the rotating order, including the BPF and its harmonics
- Sub-synchronous tonal noises at 0.5 to 0.7 RO related to rotating stall
- Broadband noise in the plane wave range called whoosh. Its origin is commonly related to the rotating stall in the inducer and diffuser.
- Broadband noise at high frequencies, labeled under the term TCN, although it is unclear whether this is the actual generation mechanism.

The different setups of numerical calculations have been studied. In order to reproduce broadband noise, it is necessary to use scale-resolving turbulence models that capture at least the inertial sub-range of turbulent eddies. A time step corresponding to 2° of impeller rotation is the minimum required to resolve the audible noise, although the recommended value is 1°. The convective Courant number must be close to 1 in the regions resolved with LES, and a minimum of 15 mesh cells per wavelength are needed to properly propagate acoustic waves. Numerical models with this setup have shown good noise predictive capabilities, although they sometimes fail to capture broadband noise at high frequencies.

The use of acoustic analogies to quantify and locate noise sources has made it possible to study how the observed flow patterns produce noise at different frequencies. The dipole sources due to fluctuating pressure load on the walls are the most important in turbocharger compressors.

Non-uniformity in the incoming flow caused by inlet geometries can lead to a loss of performance and an increase of noise, but more research is needed to establish applicable design criteria throughout the compressor map. The excitation of aeroacoustic sources due to the flow patterns induced by these geometries has not been sufficiently studied.

3

Computational models

Contents

3.1 Introduction

This chapter describes the numerical models used to calculate the flow field in two centrifugal compressors. The first section shows the characteristics of the analyzed compressors and discusses the selection of inlet geometries and operating conditions. The second section describes the numerical methods and the physical models, emphasizing the treatment of turbulence and the acoustic properties of the computational mesh.

3.2 Studied configurations

The calculated configurations are combinations of three elements: compressor, inlet geometry, and operating point. Each of these elements is described in detail in this section. Specifically, there are two different compressors with two sets of inlet geometries: the first are the reference straight ducts (abbreviated as rsd), and the second is a set of different geometries with industrial interest. Both compressors work at three operating points: near surge (nsg), highest pressure ratio (hpr), and best efficiency point (bep).

3.2.1 Compressors

The two radial compressors analyzed in this thesis (called c1 and c2, to avoid commercial nomenclature) are currently used in passenger cars. They are two compressors of similar dimensions, an impeller with 6 main and 6 splitter blades, and a vaneless diffuser. Table 3.1 lists the most relevant dimensions of each one.

Compressor	c1	c2
Inlet duct diameter (D_i)	42.0	42.0
Outlet duct diameter (D_o)	31.6	47.0
Impeller inducer diameter	36.1	41.4
Impeller exducer diameter	48.6	53.0
Trim	55%	61%
Impeller blades (main / splitter)	6/6	6/6
Diffuser inlet diameter	52.2	58.8
Diffuser outlet diameter	82.1	85.8
Diffuser inlet height	2.5	3.1
Diffuser outlet height	2.3	3.0

Table 3.1: *Dimensions of compressors in* mm.

The table above shows that the dimensions of both compressors are very similar. However, there are some differences. The inducer diameter of c1 is smaller than that of c2, so the inducer area of c1 is 24% smaller than that of c2. In addition, the trim of c2 is slightly larger. Figure 3.1 shows both compressors. It can be seen how the inlet duct, which has the same diameter

in both cases, narrows just upstream of the inducer in compressor c1. Some minor differences can be seen as well. For instance, the outlet ducts have a different inclination, and the direction of rotation of c1 is clockwise, while that of c2 is counterclockwise.

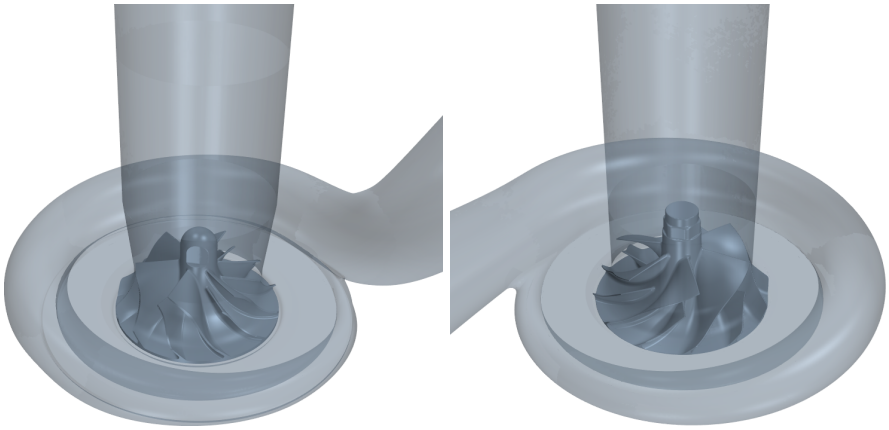

Figure 3.1: *CAD of compressors c1 (left) and c2 (right). The walls are made transparent to show the impeller.*

3.2.2 Inlet geometries

The following describes the inlet geometries used in the computational domain of both compressors. As mentioned above, first, the reference straight ducts configuration is described, and then, there is a second set of geometries, different for each compressor. The outlet ducts are always those used in the rsd configuration.

Compressor c1

For compressor c1, in the reference straight ducts configuration (abbreviated c1 rsd), inlet and outlet ducts of lengths $64D_i$ and $36D_o$ respectively are used. These lengths are selected to match the experimental setup, described in the next chapter.

The second set of inlet ducts for c1 consists of four geometries. Three surge margin enhancing geometries [63] and a straight inlet duct. This set will be referred to as the *simple geometries*. Every geometry is made of three elements. In the streamwise direction they are:

- A 195 mm long intake straight duct
- The characteristic geometry element: elbow, reservoir or tapered duct
- A $1D_i$ long straight part reaching the compressor inlet section

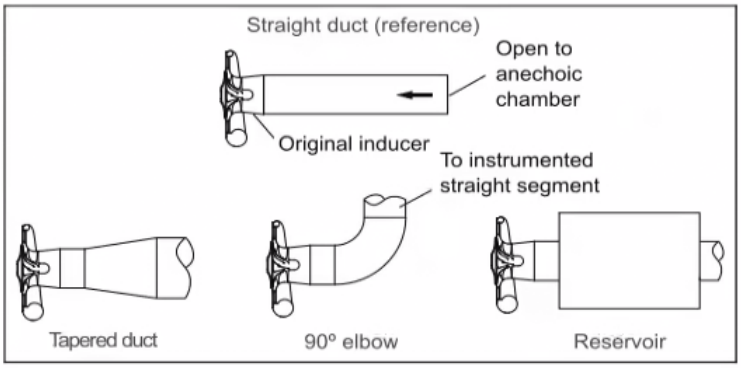

Figure 3.2: *Sketch of the simple geometries used with compressor c1. Courtesy of Jorge García-Tíscar [63]*

In every configuration, between the end of the inlet ducts and the impeller inducer, there is a $0.6D_i$ long convergent section to match the inlet duct diameter of 42.0 mm and the inducer diameter of 31.6 mm. The four simple geometries are schematically represented in figure 3.2.

The dimensions of the different elements are the following. The elbow has a diameter equal to D_i, a curvature radius of $1.36D_i$ (57 mm), and a 90° angle. The reservoir is $2.85D_i$ (120 mm) long with a diameter of $2.48D_i$ (104 mm). For the tapered duct, the tapered part has a minor diameter of D_i, a major diameter of $1.57D_i$ (66 mm), and an axial length of $1.66D_i$ (70 mm). The 195 mm straight duct section has a diameter of D_i in every case except for the tapered duct, where its diameter matches the major diameter of the tapered part ($1.57D_i$ i.e., 66 mm). For the elbow geometry, the relative orientation of the volute tongue and the axis of the inlet duct is depicted in figure 3.3. The outlet duct is the same for all four geometries, and equal to c1 rsd. Table 3.2 shows a summary of the inlet geometries of compressor c1.

Inlet geometry	Name
Reference straight ducts	*rsd*
90° Elbow	*elb*
Reservoir	*rsv*
Straight duct	*str*
Tapered duct	*tap*

Table 3.2: *Nomenclature of the compressor c1 inlet geometries.*

Compressor c2

Regarding compressor c2, there is as well a reference straight ducts configuration (c2 rsd) with inlet and outlet duct lengths of $47D_i$ and $45D_o$ respectively. The second set of geometries considered for this compressor consists of three

90° elbows. They have different curvature radii of 0.75, 1, and 1.5 times D_i. They are called e0D75, e1D and e1D5 respectively. All the elbows are preceded by the complete c2 rsd inlet duct. The c2 rsd outlet duct is kept for all c2 configurations. The angular position of the volute tongue with respect to the inlet duct is shown in figure 3.3.

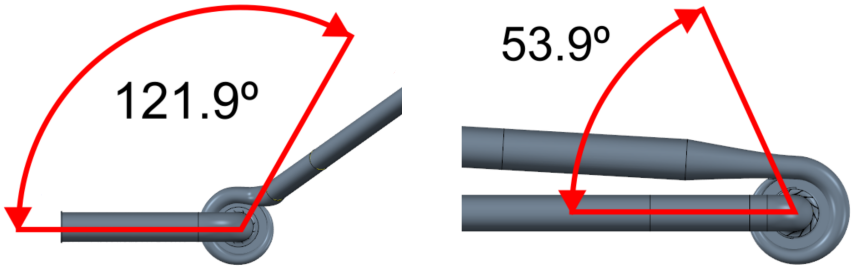

Figure 3.3: *Volute tongue orientation in compressors c1 (left) and c2 (right) with respect to the elbow inlet duct.*

In figure 3.4 The reference straight ducts and the three elbows of different curvature radii used in compressor c2 are displayed.

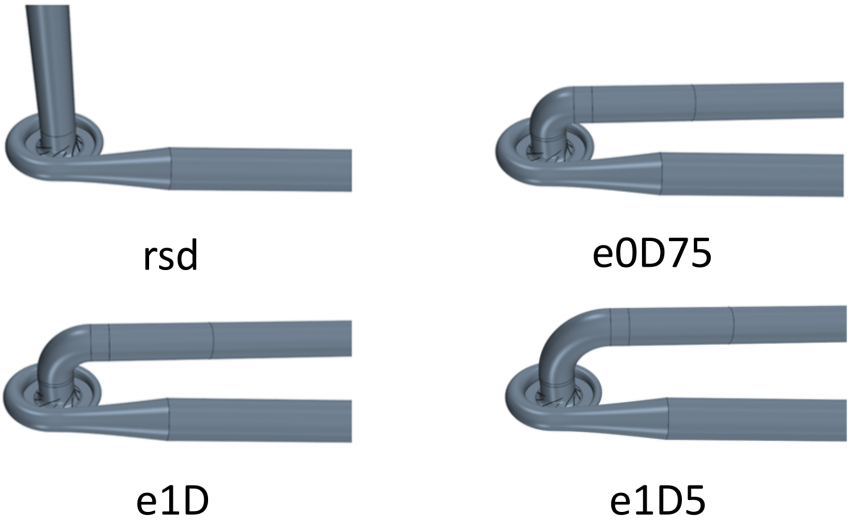

Figure 3.4: *Nomenclature of the inlet geometries for compressor c2. The complete duct length is not shown.*

Table 3.3 shows a summary of the inlet geometries of compressor c2

Inlet geometry	Name
Reference straight ducts	*rsd*
0.75D Elbow	*e0D75*
1D Elbow	*e1D*
1.5D Elbow	*e1D5*

Table 3.3: *Nomenclature of the c2 inlet geometries.*

Once the inlet geometries have been described, a few words are devoted to justifying the selection. The set of simple geometries of compressor c1 includes a straight reference duct, an elbow, a reservoir, and a tapered duct. The elbow and tapered duct are frequently used to accommodate the compressor in the engine compartment where space is limited, and ducts may have different sections. The reservoir is an element successfully employed in the literature [31], [33] to attenuate noise in specific frequency bands. Although its use is very limited in practice for space reasons, it is considered that the study of this geometry can provide relevant information on the noise problem in compressors. The set of three elbows used in compressor c2 was selected to carry out a parametric study on the curvature radius. The literature shows that elbows with smaller radii produce higher noise at low mass flow rates [41]. However, whether this is due to excitation from different aeroacoustic sources or to the convective enhancement of downstream noise is unclear. Therefore, studying the flow field and acoustic emission of these geometries will allow establishing design criteria to optimize the inlet ducts.

3.2.3 Operating conditions

The literature review presented in the previous chapter showed the noisiest points of the compressor operating map. Starting from the best efficiency point (bep) of an iso-speed line and restricting the mass flow rate progressively, the hpr (highest pressure ratio) is reached, where the slope of the iso-speed line is zero. The near surge (nsg) points are reached by further reducing the mass flow rate. At hpr, the flow starts to present instabilities, and the whoosh noise can be clearly distinguished [31]. As the operating point gets closer to surge, the instabilities, and the overall SPL level increase.

It follows from the above that the most interesting points for noise analysis are between hpr and nsg. Deep surge operation is outside the scope of this investigation, so the points of interest are limited to the near surge conditions. Both compressors are calculated at nsg, hpr, and bep points for the reference straight ducts (rsd) configuration. This selection covers the compressors' most representative operating conditions and acoustic sources. The simple geometries of compressor c1 are calculated at the nsg point and the bep to compare flow conditions and acoustic signature. The three elbows of different curvature radii of compressor c2 are calculated only in the nsg point

since they are the noisiest conditions and show more differences between the different elbows [41].

Regarding the iso-speed line, in Navarro's work [24], compressor c1 is calculated operating at 160 krpm. The results presented in that work provide a valuable benchmark for comparing the compressor results with different inlet geometries. For compressor c2, PIV measurements of the inlet flow field are available only on the 140 krpm line [66]. In addition, the mass flow and pressure ratio values on that line are very similar to those on the 160 krpm line of compressor c1, facilitating the comparison between both.

Figure 3.5 shows the operating maps of both compressors. The points selected for the numerical simulations are highlighted in red. All the calculated combinations of compressors, geometries and operating conditions are gathered in tables 3.4 and 3.5.

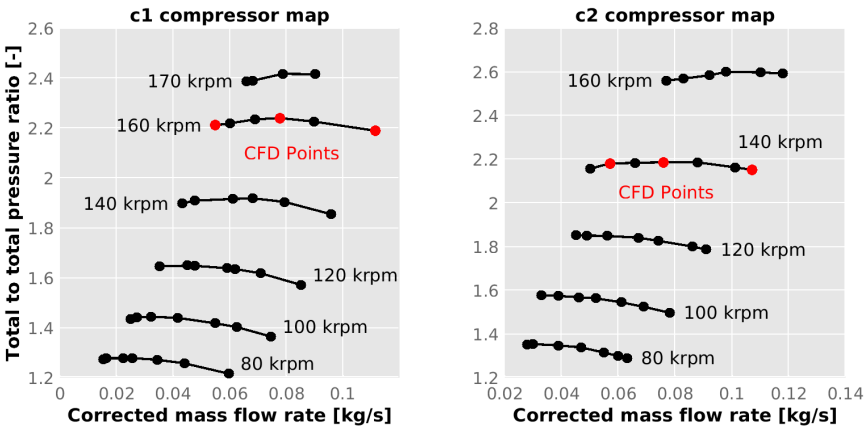

Figure 3.5: *Operating maps of compressors c1 and c2. The CFD points are signaled in red. In each map, the leftmost point is nsg, the center point is hpr, and the rightmost is the bep.*

Geometry	*nsg*	*hpr*	*bep*
rsd	*c1-rsd-nsg*	*c1-rsd-hpr*	*c1-rsd-bep*
elb	*c1-elb-nsg*	-	*c1-elb-bep*
rsv	*c1-rsv-nsg*	-	*c1-rsv-bep*
str	*c1-str-nsg*	-	*c1-str-bep*
tap	*c1-tap-nsg*	-	*c1-tap-bep*

Table 3.4: *Calculated configurations for compressor c1.*

Geometry	*nsg*	*hpr*	*bep*
rsd	*c2-rsd-nsg*	*c2-rsd-hpr*	*c2-rsd-bep*
e0D75	*c2-e0D75-nsg*	-	-
e1D	*c2-e1D-nsg*	-	-
e1D5	*c2-e1D5-nsg*	-	-

Table 3.5: *Calculated configurations for compressor c2.*

3.3 Numerical model

The aeroacoustic analysis carried out in this work is based on the numerical calculation of the flow field inside the turbomachine. In this section, the employed numerical models are described.

3.3.1 Numerical method

System of equations

The equations describing the motion of fluids are known as the Navier-Stokes equations. They are a system of non-linear partial differential equations.

The system is composed of five equations:

- Continuity equation
$$\frac{\partial \rho}{\partial t} + \nabla(\rho \mathbf{v}) = 0 \tag{3.1}$$
- Three momentum equations (in tensor notation)
$$\frac{\partial(\rho v_i)}{\partial t} + \frac{\partial(\rho v_i v_j + p_{ij})}{\partial x_j} = 0 \tag{3.2}$$
where
$$p_{ij} = p\delta_{ij} - \sigma_{ij} \tag{3.3}$$
- And the energy equation
$$\frac{\partial(\rho e)}{\partial t} + \frac{\partial(\rho e v_i + v_j p_{ij} + Q_i)}{\partial x_i} = 0 \tag{3.4}$$
where $\mathbf{Q}$ is the heat flux per unit area.

For calculating the viscous stresses, the air is assumed to be a Newtonian fluid and thus the expression
$$\sigma_{ij} = \mu \left(\frac{\partial v_i}{\partial x_j} + \frac{\partial v_j}{\partial x_i} - \frac{2}{3} \frac{\partial v_k}{\partial x_k} \delta_{ij} \right) \tag{3.5}$$
is used, where μ is the dynamic viscosity coefficient. For the heat flow $\mathbf{q}$, Fourier's law is used:
$$\mathbf{q} = -k \nabla T \tag{3.6}$$

where k is the thermal conductivity.

Thus there are five equations with seven unknowns: u, v, w, p, ρ, T, and e. There are three kinematic variables, and the other four are thermodynamic. The number of thermodynamic degrees of freedom can be reduced if the fluid is assumed to be in equilibrium. Then, it is meaningful to consider a thermodynamic state and to use two equations of state in order to close the system.

Air is assumed to behave as a perfect gas and hence:

$$p = \rho R T \tag{3.7}$$

Internal energy is assumed to be proportional to temperature:

$$e = c_v T \tag{3.8}$$

being c_v the specific heat at constant volume.

In this model, specific heats, viscosity and thermal conductivity are assumed to remain constant with temperature.

Although the system of equations is complete, no analytical solutions exist for a flow field as complex as that found inside a radial compressor. Therefore numerical methods have to be used to obtain a solution.

Turbulence modeling

Turbulence is a physical phenomenon that appears in flows where inertial forces dominate over viscous forces. It is an unstable flow regime where chaotic fluctuations of the flow variables occur. Although the very nature of turbulence precludes a simple description of the flow, there are certain patterns in turbulence that allow it to be decomposed into simpler phenomena. These are the turbulent eddies and the energy cascade.

In confined flows, the no-slip condition near the solid walls gives rise to a velocity gradient in the direction normal to the wall. The region affected by such gradient is known as the boundary layer. The relative importance of the viscous and inertial forces in the sub-regions that form the boundary layer defines the turbulent behavior. The non-dimensional wall distance y^+ is a useful parameter to establish the limits of the different near-wall layers. It is defined as

$$y^+ = \frac{u_\tau y}{\nu} \tag{3.9}$$

Where $u_\tau = \sqrt{\tau_w/\rho}$ is called the friction velocity, τ_w is the wall shear stress, y is the distance to the wall, and ν is the kinematic viscosity.

Close to the wall, where the minimum velocity is found, the flow is dominated by the viscous forces and does not depend on the free stream values. This region is called the viscous sub-layer, and it has a very small thickness normal to the wall, with $y^+ < 5$.

Next, further from the wall, there is a region called the buffer layer where the viscous forces are comparable to the inertial ($30 < y^+ < 500$). Finally,

above 20% of the boundary layer thickness, the flow is dominated by inertial forces in the so-called outer layer.

Out of the boundary layer, the velocity gradient caused by the solid wall ceases to exist. This free stream region interacts with the limit of the boundary layer by transferring momentum to the slower flow. Thus, in the turbulent part of the boundary layer, large eddies exist through which the free stream feeds the turbulence with energy.

The size of these eddies is of the same length scale as the main flow. They are anisotropic because they are distorted by the macroscopic motion of the flow. These big eddies yield energy to smaller and smaller eddies. While the biggest eddies are effectively inviscid, below a certain length scale known as the Taylor microscale, the dynamics of the eddies is affected by viscosity and they are more and more isotropic.

The energy transfer among eddies of the different length and velocity scales, from the biggest eddies interacting with the free stream, to the smallest eddies, which dissipate turbulent kinetic energy to viscous forces, is termed the energy cascade.

In figure 3.6 the turbulent kinetic energy content is represented as a function of the eddy wavenumber κ, which is a measure of their size. The largest eddies known as integral range are the most energetic. The dissipative Kolmogorov microscale eddies are the least energetic, and between the extreme length scales lays the inertial range, characterized by the $-5/3$ slope of the energy curve. They are driven by the inertia forces and effectively inviscid.

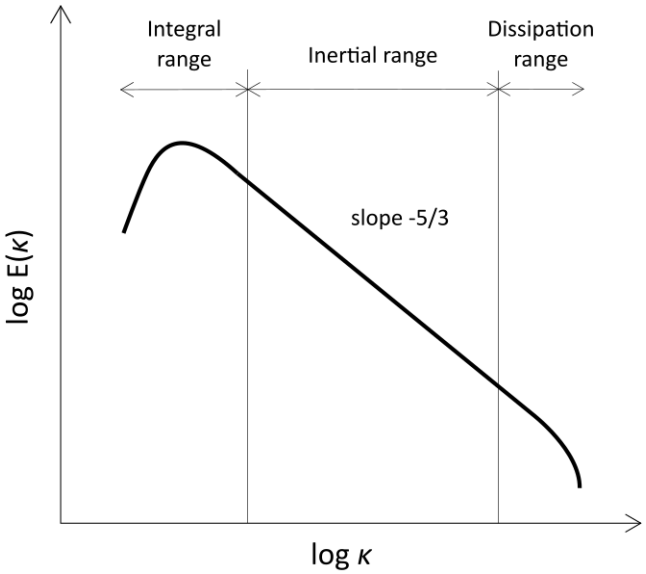

Figure 3.6: *Turbulent kinetic energy spectrum.*

The direct resolution of the Navier-Stokes equations would require a temporal and spatial discretization fine enough to capture the Kolmogorov mi-

croscales. The computational resources needed exceed those available for this investigation, and therefore, turbulence had to be modeled.

The method used to model turbulence is called Detached Eddy Simulation (DES). A Large Eddy Simulation (LES) is performed in those regions of the domain where the mesh is fine enough, and in the rest, an unsteady Reynolds-Averaged Navier Stokes (RANS) is implemented.

For the RANS method, the Reynolds averaging is performed on the Navier-Stokes equations. It consists of decomposing the flow variables in the mean value plus an oscillating part: $u(t) = \overline{u}+u'(t)$. New terms $\overline{u_i u_j}$ called Reynolds stresses appear in the equations as a result of the averaging. These new terms have to be calculated using a closure model. In this work Menter's $k-\omega$ SST model was used, where turbulent kinetic energy k and specific dissipation rate ω are used to calculate the Reynolds stresses.

LES methods resolve the largest eddy scales and model the smallest ones. A space filtering is performed in the flow domain such that the scales that can't be resolved with the smallest grid size are calculated with a sub-grid scale model (SGS). These SGS models calculate the dissipation effect of the smaller eddies by adding new sub-grid viscous stresses. Menter's $k-\omega$ SST model acts as a SGS model in the LES regions of the domain. The isotropic character of the smallest eddies, and their universal behavior, constitute an advantage of the SGS modeling. The interested reader can find more details in the book by Versteeg et al. [67].

Numerical scheme

In this thesis the finite volume method is used, where the integral flow equations are solved on a mesh of control volumes. This method is implemented in the commercial code Simcenter STAR-CCM+, which is utilized for all the CFD calculations. An implicit unsteady scheme is employed with second order precision for temporal discretization.

The Bounded Central Differencing (BCD) scheme is used for the convective and diffusive terms. This scheme consists of a hybrid between Central Differencing and the Upwind Differencing method. The first offers second-order accuracy, although it may present boundedness problems for high Peclet numbers, i.e., when for a given cell size, convection effects dominate over diffusion. The latter offers only first-order accuracy but guarantees boundedness for any Peclet number.

The BCD scheme is suitable for DES models because when the mesh is fine enough to have a low Peclet, Central Differencing is used, which offers higher accuracy and preserves the turbulent kinetic energy in the regions solved with LES. In regions where the mesh is not fine enough to employ that scheme, BCD switches to Upwind Differencing, which guarantees boundedness, in exchange for reducing the accuracy to first-order. It also may cause turbulent kinetic energy to decay unnaturally fast.

However, the spatial resolution requirements introduced by the acoustic analysis result in a fine mesh, where most of the domain of interest is solved

with second-order accuracy. The use of the BCD scheme is reported in other publications where the flow in radial compressors and their acoustics are studied: [46], [68], [48] and [69].

STAR-CCM+ offers segregated and coupled solvers. The segregated solver solves the flow equations sequentially, while the coupled solver solves them at the same time, and therefore has a higher RAM memory requirement. Although the coupled solver is more suitable for transonic flows [70], Navarro [24] made a comparison between both solvers, and concluded that the differences in prediction of operating variables were less than 1%, and the predictive capacities for the pressure spectra in the ducts were also equivalent. Furthermore, operating points are not going to be simulated near the choke limit of the compressor, where speeds are higher, and sonic conditions are reached. Therefore, the higher computational cost of the coupled solver is not justified, so the segregated solver is chosen.

Regarding temporal discretization, in the literature a time step corresponding to 1° of impeller rotation is often advised [24], [44], [71]. However, to capture the low frequency phenomena, it is necessary to record the solution of the flow field over a long time interval, in numerical terms. This fact, together with the number of different configurations considered in this thesis, makes it critical to use the largest possible time step, in order to reduce the computational resources required. In [24] a sensitivity study of the acoustic prediction with respect to the time step was carried out and it was concluded that below 20 kHz the time step of 2° is the maximum acceptable. Sharma et al.[22] also performed calculations with this time step value, obtaining good results. To check the sensitivity to this setting, both values are compared for the c2 rsd bep case.

First, operating variables such as total to total pressure ratio and isentropic efficiency are compared against experimental values in table 3.6. The temperature and total pressure used to calculate the operating variables are obtained by averaging over the flow cross-section at the experimental sensor location. No significant differences are found among the two tested time steps.

	Π_{tt} [-]	ε_R [%]	η_s [%]	ε_R [%]
Exp	2.13	-	72.56	-
1°/TS	2.14	0.7	72.23	0.5
2°/TS	2.15	0.9	72.76	0.3

Table 3.6: *Pressure ratio, isentropic efficiency and relative errors with respect to the measurements. The 1°/TS and 2°/TS configurations are tested for the c2 rsd bep case.*

Concerning acoustics, the spectra of pressure signals in the inlet and outlet ducts are compared in figure 3.7. The numerical models present specific differences with the measured signal, such as the overestimation of amplitude in the inlet from 200 to 6000 Hz or the underestimation in both ducts of the high-frequency broadbands. These differences will be discussed in detail in the next chapter, dedicated to experimental validation.

Regarding the comparison between the 1° and 2° cases, at the inlet, both spectra are identical up to 20 kHz, where the 2° case presents a slightly lower amplitude. However, it should be borne in mind that the human hearing range is from 20 Hz to 20 kHz, and frequencies outside of that range are of little interest in this study.

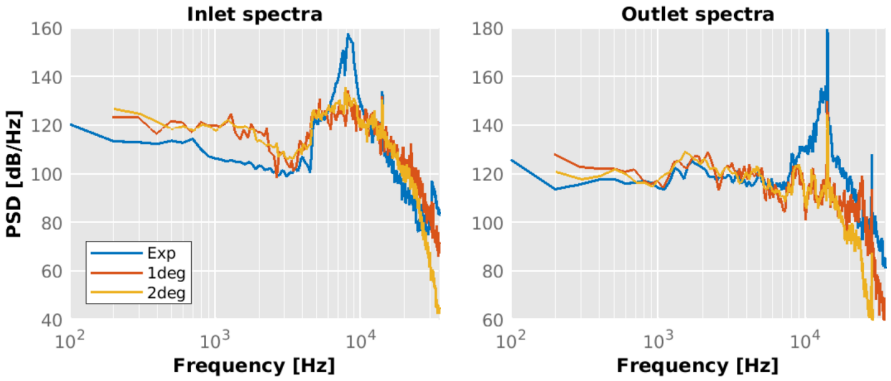

Figure 3.7: *Pressure spectra of the inlet and outlet ducts. The experimental spectrum is compared with computational models with 1°/TS and 2°/TS.*

In the outlet duct, the 2° case presents an underestimation of the amplitude with respect to 1° starting at 17 kHz. Between 17 and 20 kHz, the difference does not exceed 5 dB. Considering that the computational cost of the case with 2° is half of that with 1° and that the differences are appreciated in the very high frequencies of the audible spectrum, where the hearing sensitivity is lower, the 2° configuration offers a reasonable tradeoff.

In figure 3.8, the spectra of the axial velocity in the inlet duct, two diameters above the inducer plane, and at half duct radius from the wall are presented together with the -5/3 slope line, characteristic of the inertial range of turbulence. The two configurations show similar spectra, and both capture the inertial range. It can be concluded that both time steps provide similar results, and thus the 2° configuration is preferred, which gives a time step of $2.08 \times 10^{-6} s$ for c1 and $2.38 \times 10^{-6} s$ for c2.

3.3.2 Domain discretization

Geometric domain

The baseline region of the computational domain is composed of the rotor, diffuser, volute, and the first diameters of the inlet and outlet ducts; then, the remainder of the ducting was added. The impeller rotation is implemented by giving the rotor region a rigid body motion. Therefore, the interfaces with the inlet duct and the diffuser are sliding surfaces, and cell connectivity has to be recalculated every time step. The rotor domain of both compressors include the impeller tip clearance gap, but only for c1 the back plate region is present.

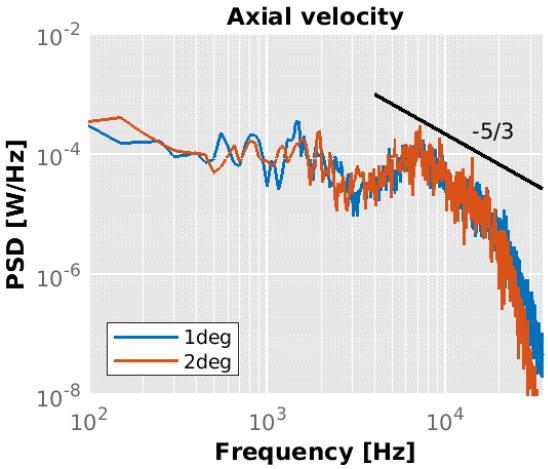

Figure 3.8: *Axial velocity spectra of the 1°/TS and 2°/TS configurations for c2 rsd bep. The -5/3 slope line is characteristic of the inertial range of turbulence.*

The inlet and outlet ducts have already been described, but in the simple geometries set there is an additional region. Since those inlet geometries are shorter than in the rsd configuration (a 195 mm straight duct versus a 2.6 m duct), the influence of atmospheric air intake is more significant in the inlet flow field. Therefore, a so-called atmospheric umbrella is placed surrounding the inlet duct intake. The shape of this region is a spheric sector of 340 degrees, with nine times the diameter of the inlet duct. The spherical shape was selected following [49], in order to avoid artificial numerical reflection.

Computational mesh

The mesh for compressor c1 is shown in figure 3.9. In the regions of the baseline model (rotor, diffuser, volute, and first diameters of inlet and outlet ducts) a polyhedral unstructured mesh was used. The rotor region features an inflation layer of 10 cells with a total width of 0.2 mm. This gives a y^+ close to 1 in all the rotor region. The wall y^+ value in the remainder of the baseline domain is below 3 except for the volute, where it reaches 10 at some spots. The first five diameters of the inlet and outlet ducts present a structured mesh in the core. For the extended straight ducts, the mesh was extruded towards the open ends, keeping y^+ values below 5 . The axial cell length was increased in a geometric progression from the initial length at the end of the baseline mesh to about 80 mm at the opposite ends. This way, a large volume could be added with a low cell count, as well as granting a numerical sponge capable of damping the waves reflected at the boundaries. The total cell count is about 11 million cells. In the work of Navarro [24] more details of the mesh properties can be found, as the baseline model was inherited from that research project. The mesh of the simple geometries kept the size of the baseline ducts, with y^+ values below 5. Regarding the atmospheric umbrella, the cell size was

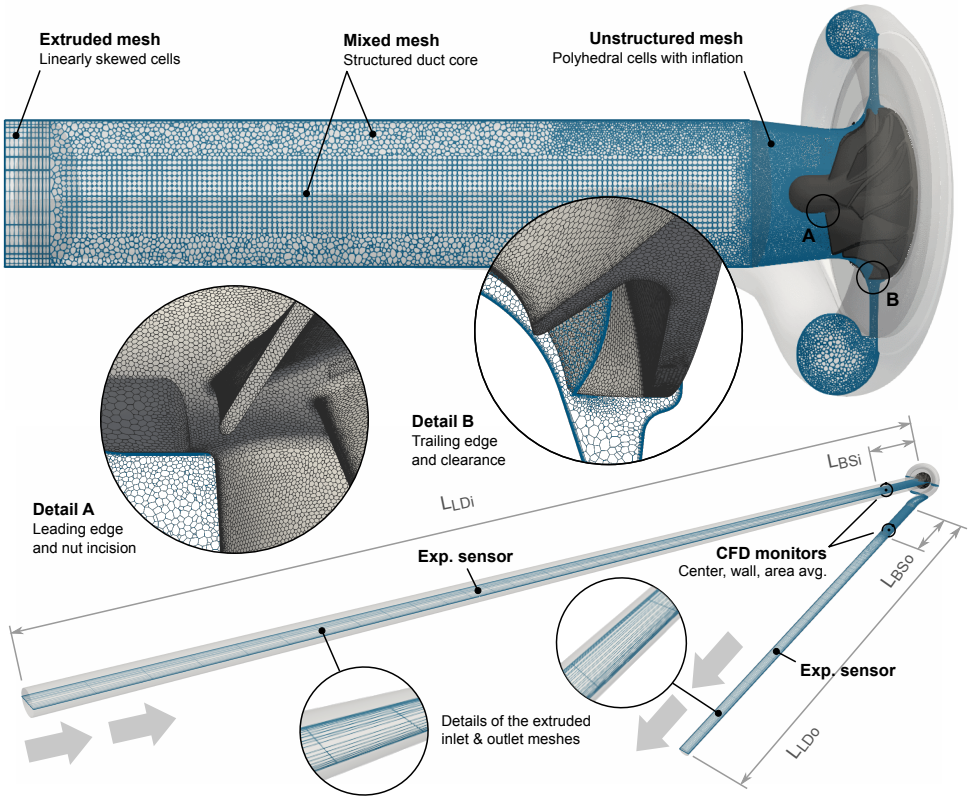

Figure 3.9: *Computational mesh of compressor c1. The baseline ducts length (L_{BS}) is shown together with the extended long ducts (L_{LD}) of the rsd configuration, with the extruded mesh. Figure courtesy of Dr. Jorge García-Tíscar [72]*

expanded in the radial direction to introduce additional numerical damping of the potential reflected waves. A picture of such mesh can be seen in figure 3.10.

As for compressor c2, since its dimensions are quite similar to those of compressor c1 (see table 3.1) the same meshing parameters as in c1 were used. In figure 3.11 it is shown how the values of y^+ coincide with those reported by Navarro [24] for compressor c1. In the rotor and diffuser regions, the values of y^+ are close to 1; in the ducts, those values are below 5, and in the volute, below 10 (not shown here). As a summary, the mesh of compressors c1 and c2 have both around 11 million cells, with y^+ values lying on the viscous sub-layer in every region except the volute, where the first cell belongs to the buffer layer. This, in conjunction with the "all y^+ wall treatment" selected in STAR-CCM+ [70] enables the flow resolution near the walls in the rotor and diffuser regions.

The Courant Number (CFL) is a relevant parameter to ensure a good

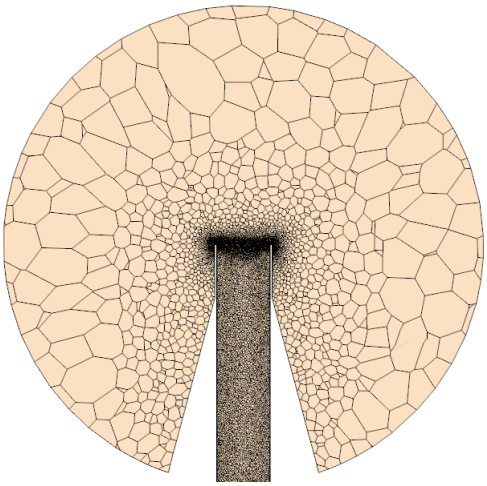

Figure 3.10: *Mesh at the atmospheric umbrella used in the simple geometries cof compressor c1. Cell size is increased in the radial direction.*

predictive capacity of the flow field in numerical models. Spalart et al. [73] recommend a value close to unity in the zones resolved with LES stating that " *[...] That leads to a local CFL number of 1. Again, it is based on rough accuracy estimates, not stability. Steps a factor of 3/2 or even 2 away in either direction from this estimate cannot be described as incorrect*".

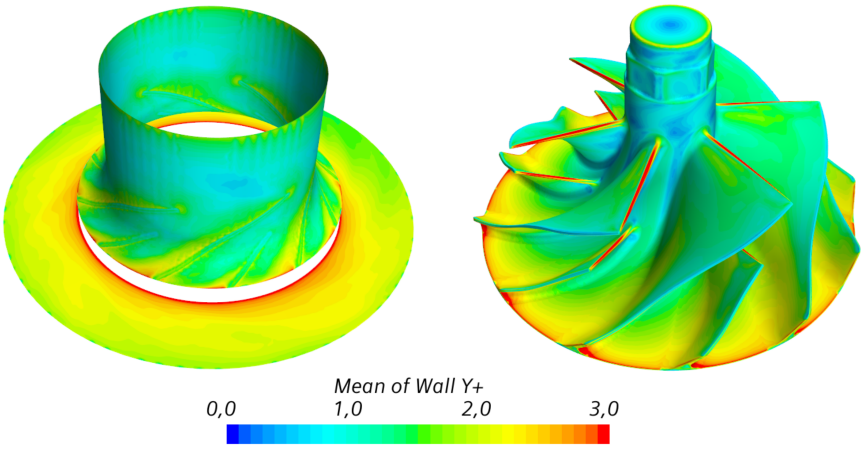

Figure 3.11: y^+ *values of the impeller shroud, diffuser and impeller walls of case c2 rsd bep.*

Figure 3.12 shows CFL values in the regions close to the rotor for the c2 rsd bep case with a time step corresponding to 1° and 2°. The black line

marks the isosurface of CFL = 1.

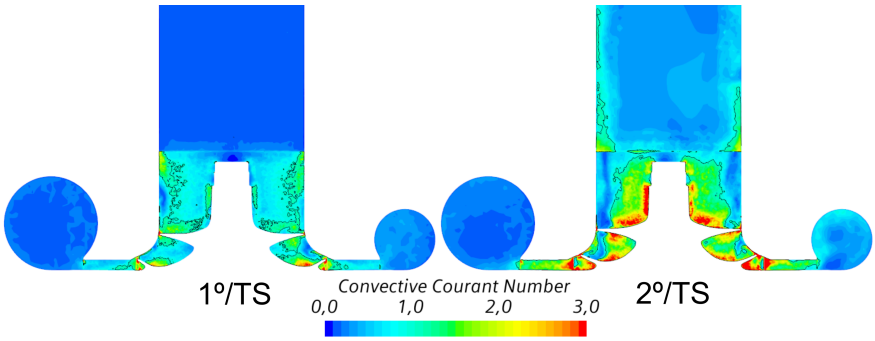

Figure 3.12: *Snapshots of the CFL number in the 1°/TS and 2°/TS configurations of the c2 rsd bep case. The black contour marks the isosurface of CFL = 1.*

It can be seen that for both cases the Courant number exceeds unity near the rotor walls. However, it must be taken into account that the zone resolved with LES does not reach the walls, and furthermore, the maximum CFL values are still of the order of magnitude of 1 in this region, and are below unity in the rest of the domain. To strictly comply with this condition, it would have been necessary to reduce the time step below 1° of rotation, which would result in a prohibitive computational cost given the number of geometries and operating points calculated. The computation time for a 100 ms signal on a 16-core machine with 56 GB of RAM is about 80 days.

Frequency properties of the extruded mesh

The ability of the extruded mesh to attenuate the reflected waves was measured by placing pressure monitors along the inlet duct. Figure 3.13 shows the location of the monitors over a schematic representation of the inlet duct extruded mesh, and the spectra of the recorded pressure signals. The spectra show that the pressure signals coincide for all the monitors up to certain frequency thresholds, where a noticeable attenuation begins to be introduced. These thresholds are at frequencies with fewer than 14 cells per wavelength.

Probe	in1	in2	in3	in4	in5
Axial cell length [mm]	2.5	5.4	25.9	66.9	82.0
Distance to inducer [m]	0.25	0.6	1.0	1.5	1.8

Table 3.7: *Cell size and location of the pressure probes at the inlet duct of c2 rsd bep.*

Table 3.7 shows the axial cell length and the position of the inlet duct probes analyzed in figure 3.13. From that figure it is deduced that the content above 1 kHz at the end of the duct is noticeably attenuated. To see in more detail the ratio between the pressure fluctuations emitted by the compressor

and reflected at the end of the duct in the low frequency range (below 1 kHz), the pressure signal has been decomposed by means of beamforming. An array of three pressure monitors in the inlet duct is used to perform Linearly Constrained Minimum Variance (LCMV) beamforming, as described by Piñero et al. [74]. Figure 3.14 shows the spectra of the emitted and reflected signal, and a minimum difference of 10 dB is observed below 1 kHz.

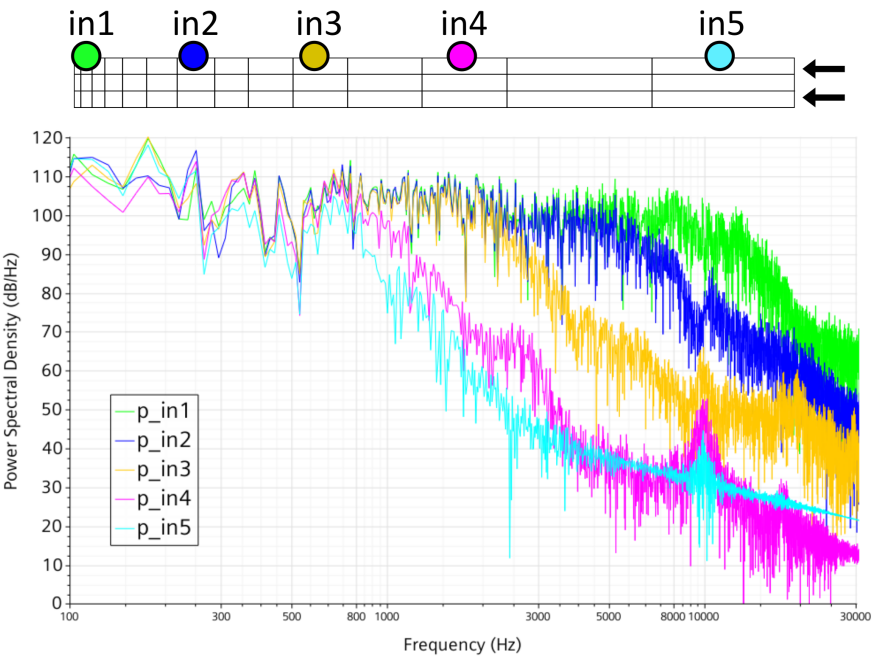

Figure 3.13: *Pressure spectra along the inlet duct extruded mesh for c2 rsd bep. The location of the monitors is displayed over a schematic representation of the mesh. The black arrows signal the flow inlet.*

3.3.3 Boundary conditions

The boundary conditions utilized are mass flow inlet and pressure outlet as described by Broatch et al. [75], or Sundström et al. [68] for instance. For the simple geometries, due to the presence of the atmospheric umbrella, a free stream inlet and mass flow outlet were used following [51]. The specific values were selected to match the experimental measurements of pressure, temperature, and mass flow in each operating point. The pressure outlet boundaries run with the unsteady non-reflecting option which "prevents spurious acoustic reflections in unsteady, compressible, and non-isothermal simulations" according to [70]. The Acoustic Suppression Zone (ASZ) tool from Simcenter STAR-CCM+ was tested for both inlet and outlet ducts, but all the values tested for the setup parameters produced unstable flow oscillations that ultimately led

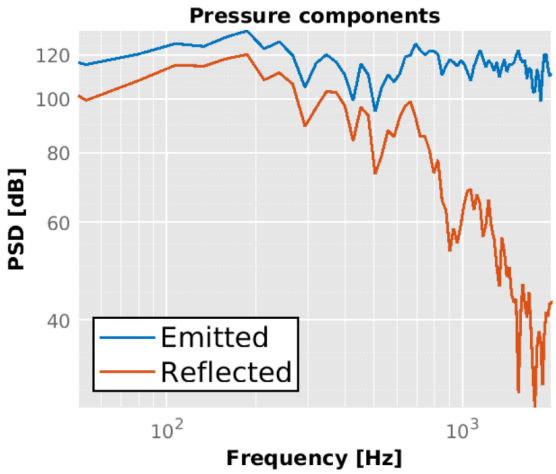

Figure 3.14: *Inlet duct pressure components decomposed by the beamforming method: emitted from the compressor, and reflected from the duct end. Data from the c2 rsd bep case.*

to calculations divergence. Thus the ASZ tool was not used, and the spurious reflections removal relies on the extruded mesh and the non-reflecting pressure condition. As for the rest of the walls delimiting the domain, all of them were treated as adiabatic smooth surfaces with no-slip condition.

4

Experimental validation

Contents

4.1 Introduction

This chapter presents the experimental validation of the numerical calculations. The first section shows the experimental setup used to characterize the compressor c1 and then the location of the analogous monitors of the numerical model is presented. The compressor operating points are validated through the main variables: mass flow rate, pressure ratio, and isentropic efficiency. Finally, the pressure spectra in the inlet and outlet ducts are compared with the measurements to validate the acoustic output of the compressor. This validation methodology is described in detail in [75]. In the second section, the same steps are followed with compressor c2. An additional subsection describing acoustic predictions using the Ffowcs Williams and Hawkings analogy is presented, and local flow field measurements are used to thoroughly validate the compressor c2 model. Finally some conclusions are drawn on the overall validation results.

4.2 Validation of compressor c1

4.2.1 Experimental setup

The compressor c1 was experimentally characterized on a rig mounted in an anechoic chamber described in [45]. Figure 4.1 shows said experimental setup and the measurement points of the main acoustic and operating variables for the c1 rsd configuration. In the inlet duct, the mass flow rate, the inlet pressure, and the temperature were measured. In addition, an array of three piezoelectric sensors separated 50 mm from each other was placed to carry out the decomposition of waves through the beamforming method, as described in [9]. Pressure and temperature were measured in the outlet duct, and another array of piezoelectric sensors was used to analyze the acoustic signals.

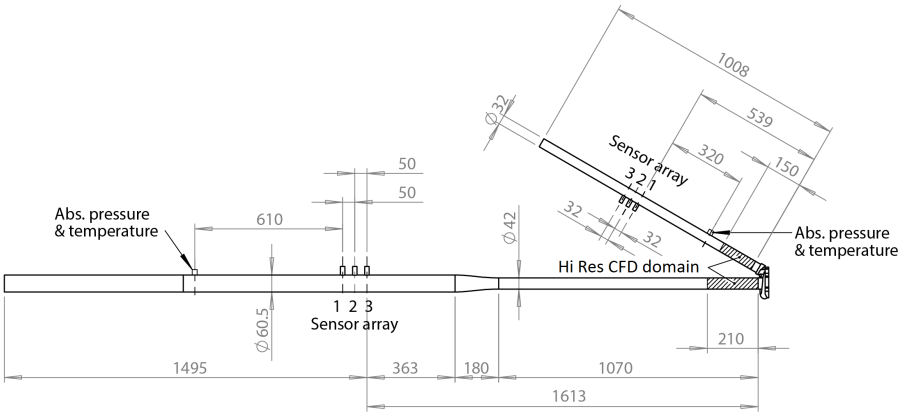

Figure 4.1: *Experimental setup for compressor c1 rsd.*

For the simple geometries, the same instrumentation as in rsd was used

in the outlet duct. At the inlet duct, the inlet pressure and temperature were measured in the ambient air, and the inlet sensor array was placed in the 195 mm straight duct preceding each geometry. However, due to the short length of this fragment, the flow is not fully developed when it reaches the array, and decomposition techniques cannot be applied. However, the temporal pressure signal inside that duct can be compared with its numerically calculated counterpart.

4.2.2 Numerical setup

The mass flow rate is imposed as a boundary condition in the numerical model. The pressure and temperature values at the inlet and outlet are taken at the same place where they were measured experimentally. As for the piezoelectric sensor arrays, in the rsd case, they are located closer to the compressor than in the experimental setup. This is because the mesh in the ducts increases in size, moving away from the compressor, as described in Chapter 3. Thus, there is an insufficient spatial resolution for all frequencies of interest at the experimental location. Figure 4.2 shows the location of the sensor arrays in the rsd case. In the simple geometries, the outlet duct configuration is identical to the rsd. As mentioned above, an array of three sensors is placed in the straight section in the inlet duct, but it is only used to compare the raw spectrum. Figure 4.3 shows the location of both arrays for the c1 elb case of the simple geometries. The atmospheric umbrella and the full outlet duct length are not shown.

Figure 4.2: *Numerical domain and location of the pressure probes for compressor c1 rsd.*

4.2.3 Operation variables

The compressor working map is defined by the mass flow rate and the total-to-total pressure ratio, with the isentropic efficiency curves superimposed. The equations 4.1 and 4.2 define these variables as a function of the magnitudes measured in the test rig described in section 4.2.1. Table 4.1 shows the numerical and experimental results of the operating variables for compressor c1 together with the relative error.

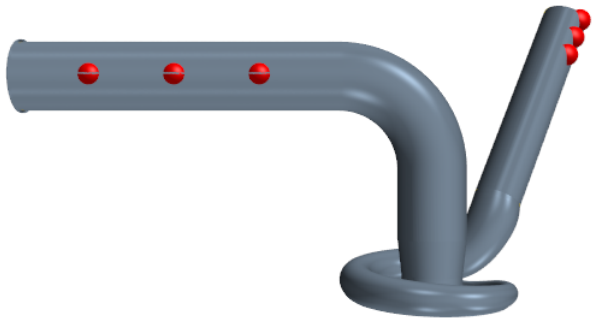

Figure 4.3: *Pressure monitors location for c1 elb. The full outlet duct is not shown.*

$$\Pi_{tt} = \frac{p_{out,T}}{p_{in,T}} \tag{4.1}$$

$$\eta_s = \frac{T_{in,T}(\Pi_{tt}^{\frac{\gamma-1}{\gamma}} - 1)}{T_{out,T} - T_{in,T}} \tag{4.2}$$

$$\varepsilon_R(\phi) = \frac{|\phi_{Exp} - \phi_{CFD}|}{\phi_{Exp}} \times 100 \tag{4.3}$$

Figures 4.4 and 4.5 show the pressure ratio and the efficiency of the points on the isoline of 160 krpm measured experimentally. The corresponding numerical values are represented superimposed, accompanied by the error bars that represent the temporal standard deviation of said values. The magnitude of the bars is five times the standard deviation so that they are visible on the graph scale.

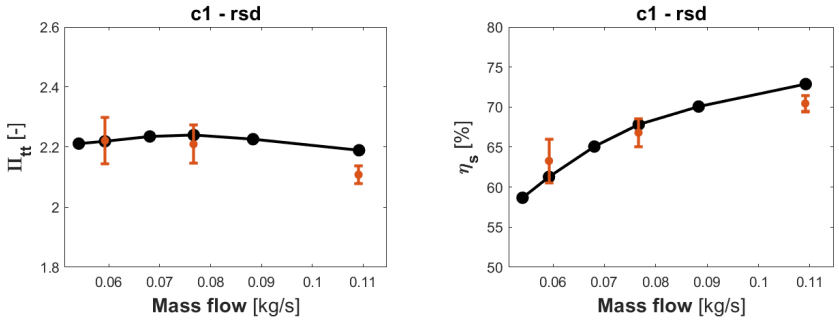

Figure 4.4: *c1 rsd 160 krpm iso-speed line. Measurements are displayed in black, and numerical calculations in red. The error bars length is five times the standard deviation of the time signal.*

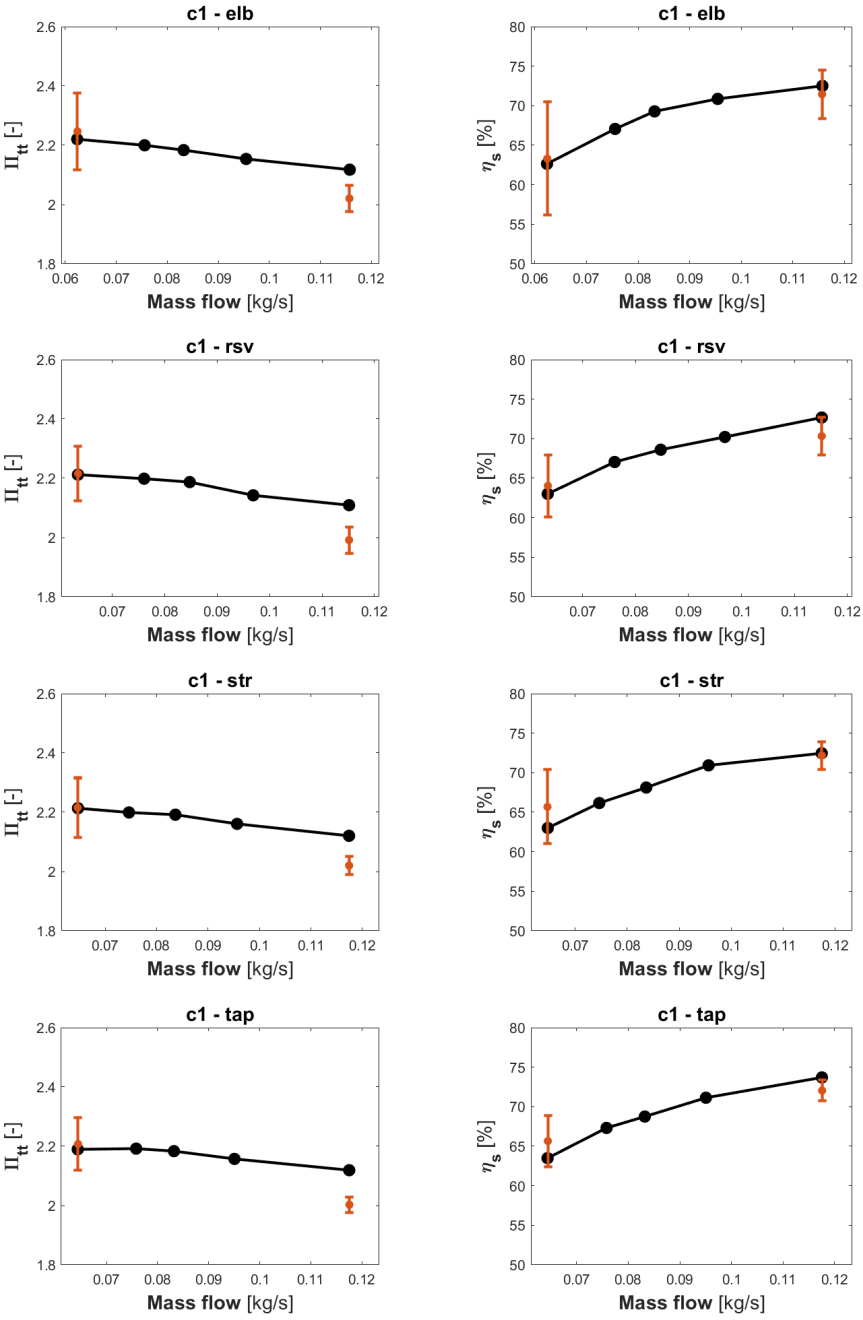

Figure 4.5: *c1 simple geometries working points along the 160 krpm iso-speed line. Measurements are displayed in black, and numerical calculations in red. The error bars length is five times the standard deviation of the time signal.*

In table 4.1 and figure 4.4 the values of the operating variables of the rsd cases can be seen. The bep case has the highest error with a 3.7% of pressure ratio deficit. The efficiency is also underpredicted, suggesting that the model could be excessively dissipative at the maximum flow velocity condition. However, the error values are admissible, considering the uncertainties in the boundary conditions and the models used.

Case	Point	Π_{tt} Exp	Π_{tt} CFD	ε_R [%]	η_s Exp	η_s CFD	ε_R [%]
rsd	bep	2.19	2.11	3.7	72.9	70.5	3.3
	hpr	2.24	2.21	1.4	67.8	66.8	1.5
	nsg	2.20	2.22	0.1	61.3	63.3	3.3
elb	bep	2.12	2.02	4.6	72.5	71.6	1.3
	nsg	2.22	2.25	1.2	62.7	63.3	1.0
rsv	bep	2.11	1.99	5.6	72.7	70.3	3.3
	nsg	2.21	2.22	0.2	63.0	64.1	1.7
str	bep	2.12	2.02	4.7	72.5	72.1	0.4
	nsg	2.21	2.22	0.1	63.0	65.7	4.3
tap	bep	2.12	2.00	5.5	73.7	72.0	2.3
	nsg	2.19	2.21	0.8	63.5	65.7	3.4

Table 4.1: *Measured and numerical operating variables for all c1 configurations.*

The same trend of underestimating pressure ratio and efficiency is observed in the bep cases of simple geometries, although the errors are slightly larger, reaching 5.6% in the c1 rsv bep case. The main difference between the flow field of rsd and simple geometries is that the latter includes air intake at the ducts. This factor could be a source of error, especially in bep, where the mass flow rate is higher, which justifies the increase of error in simple geometries with respect to rsd.

In the right column of figure 4.5, the isentropic efficiency is shown. A slight tendency to overestimate performance the points close to surge can be observed, although its magnitude is small. Additionally, it is observed that the standard deviation is greater at the points closest to the surge due to the characteristic instabilities at these operating conditions.

Despite the errors found at some operating points are of a certain magnitude, the main goal for this study is that the relevant noise-generating flow structures are accurately captured. This will be verified in the following subsection by comparing the numerical and measured pressure spectra.

4.2.4 Acoustic validation

The PSD of the pressure signals is estimated using Welch's method [76]. In this method, the time signal is divided in blocks with a certain degree of overlap (a 50% overlap is used throughout this work). The blocks are then windowed in the time domain using a Hanning window, and the discrete Fourier transform (DFT) is calculated. The individual periodograms are computed

by calculating the square of the DFT magnitude. Finally an ensemble average of the individual periodograms is performed to reduce the variance. In the numerical calculations, the time signal has a minimum of 66 ms for rsd cases, and 200 ms for the simple geometries. These signals are divided into a suitable number of blocks to obtain a frequency resolution of 100 Hz. This number is around 10 blocks for rsd and 50 for simple geometries. In the experiments, the signals were acquired during 1 s being sampled every 10^{-5} s. They are divided into 200 blocks to achieve the same frequency resolution as the numerical case.

In addition, beamforming decomposition of the signals in the ducts is carried out to examine only the pressure waves propagating at the speed of sound coming from the compressor [9] and dismiss the reflected waves at the open ends of the ducts. This method only allows studying the low frequencies since it is limited by the cut-on frequencies of the higher modes, as plane-wave propagation is assumed. All the beamformed spectra have a frequency resolution of 25 Hz, involving 2 averages for rsd cases, 10 for simple geometries and 50 for the experimental measurements.

Figure 4.6 shows the raw pressure spectrum and its corresponding decomposed signal by beamforming for the inlet duct of the rsd cases. The numerically calculated spectra reproduce their experimental counterparts quite well, except in some respects. At the bep and hpr points, between 2 and 4 kHz, an increase in the PSD is observed with respect to the experimental case. The plane wave limit, which can be seen as a steep increase in PSD above 4 kHz, is identified in all cases. However, the experimentally observed broadband around 10 kHz is not displayed by the calculations. Finally, the amplitude decay above said broadband is slower in the experimental case than in the numerical one. In all cases, the tonal content at the BPF (16 kHz) stands out. The beamformed signals follow a similar trend, although the negative slope around 1 kHz is steeper in the numerical model.

In the spectra of the outlet duct, shown in figure 4.7, a good agreement is observed, except for the band from 8 to 10 kHz, where the calculated PSD is underestimated for hpr and nsg cases. Also, again, above the BPF, the numerical spectrum decays more slowly than the experimental one. The beamformed signals correctly follow the experimental measurements in their frequency range, which is limited by the spatial Nyquist limit (around 3 kHz at the inlet and 5 kH at the outlet).

In figure 4.8, the spectra of the inlet duct for the simple geometries (both bep and nsg) are displayed. Due to the reduced length of the duct, the beamforming technique cannot be applied, so only the raw spectra are compared. In general, a very good agreement between the experimental and numerical spectra is observed, except in the broadband near 10 kHz, which cannot be reproduced numerically. For the c1 elb nsg case, a higher amplitude at low frequencies stands out in the numerical spectrum, which may be due to conditions closer to surge in the model than in the experiments. In the c1 rsv (bep and nsg), the peaks corresponding to the natural frequencies of the reservoir stand out in the low frequencies, and are accurately captured by the numerical

model.

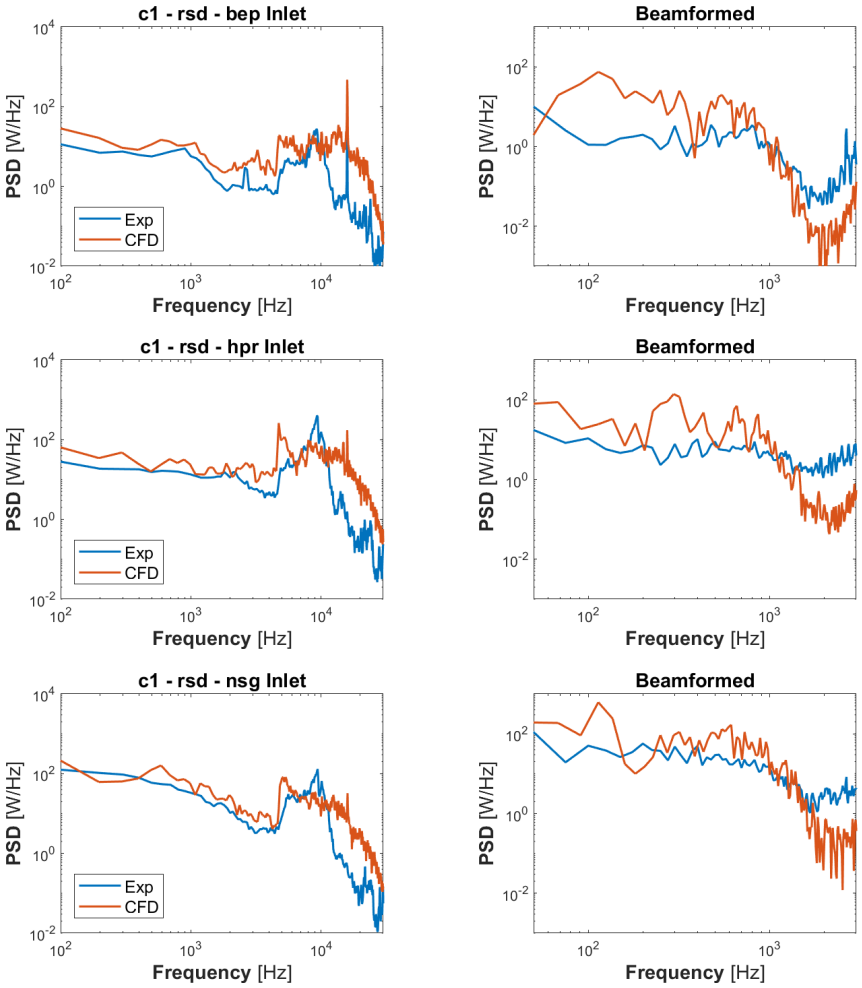

Figure 4.6: *PSD of the raw and beamformed pressure signals of the c1 rsd's inlet duct.*

In figure 4.9, the outlet duct spectra corresponding to the best efficiency point of the simple geometries are shown. The beamforming spectra are included, as this technique can be applied at the outlet straight duct. The agreement at this location is not as good as at the inlet duct. The main discrepancies are a higher overall level in the numerical case and the lack of a low amplitude band from 2 to 5 kHz. These same differences are also observed in the beamformed signals.

The spectra corresponding to the nsg point are shown in figure 4.10. The situation is similar to the bep case: the numerical spectra do not reproduce the low amplitude in the band from 2 to 5 kHz and have a slightly higher

level in the whole frequency range. Interestingly, they appear to be capable of reproducing the broadband around 10 kHz.

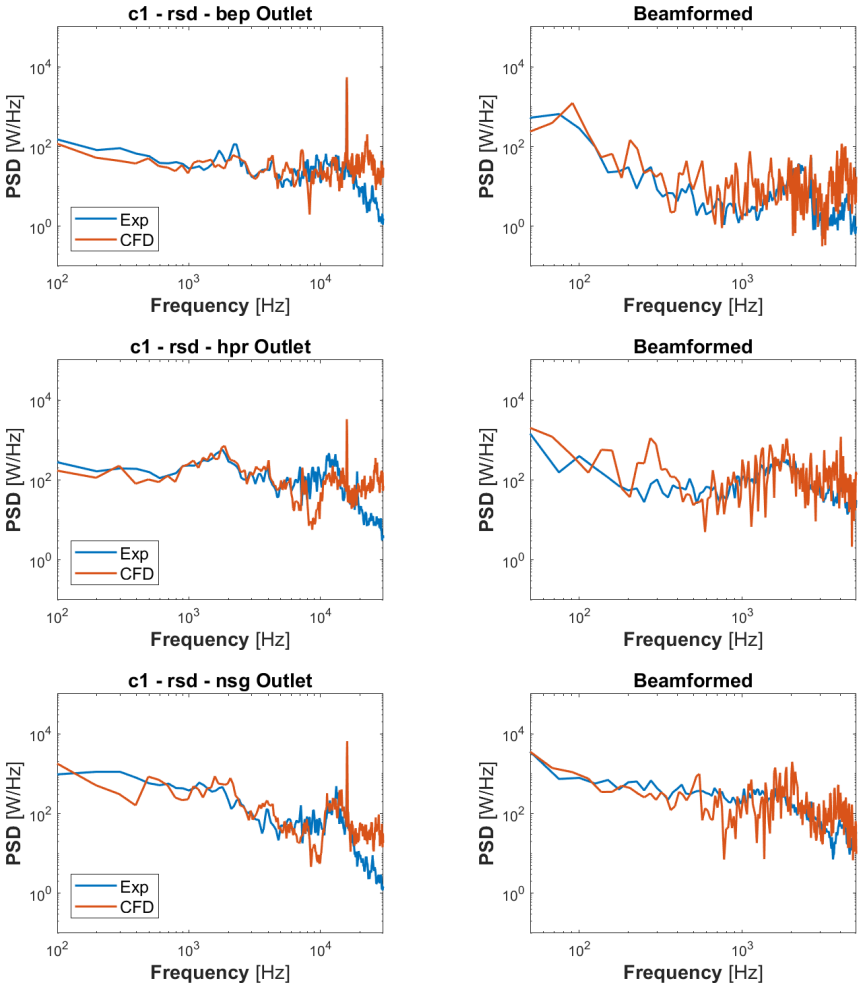

Figure 4.7: *PSD of the raw and beamformed pressure signals of the c1 rsd's outlet duct.*

In table 4.2 the sound pressure level (SPL) from 20 Hz to 20 kHz, of the raw pressure signals of all the c1 cases is presented. The numerical and experimental values in dB of both inlet and outlet ducts, together with the relative error in % are displayed. It can be seen that despite the discrepancies found in specific features of the spectra, the noise level is well captured by the numerical model. The biggest errors are around 4% at the inlet and 5% at the outlet. They have a similar in magnitude to the errors found in the operation variables (table 4.1).

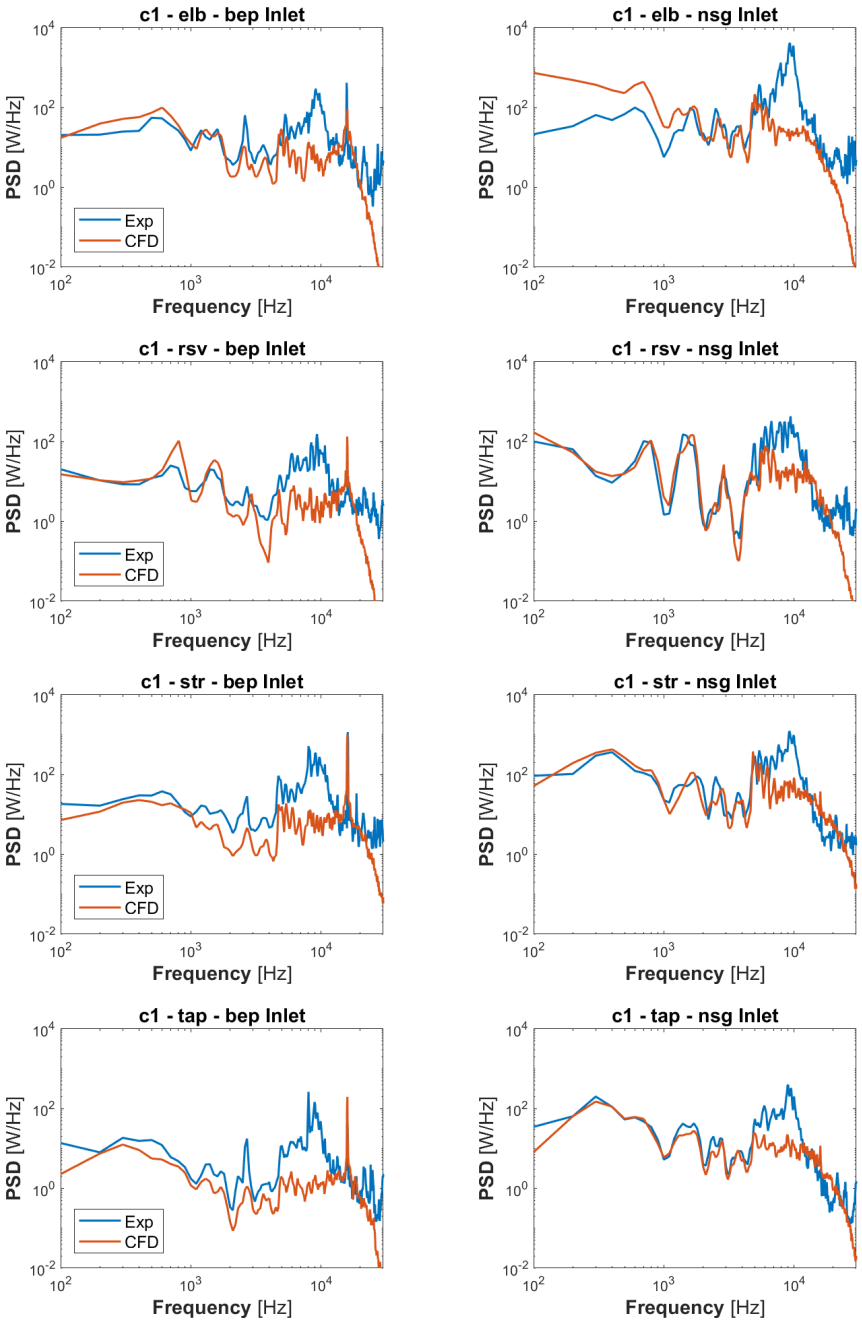

Figure 4.8: *PSD of raw pressure signals of the c1 the simple geometries' inlet duct.*

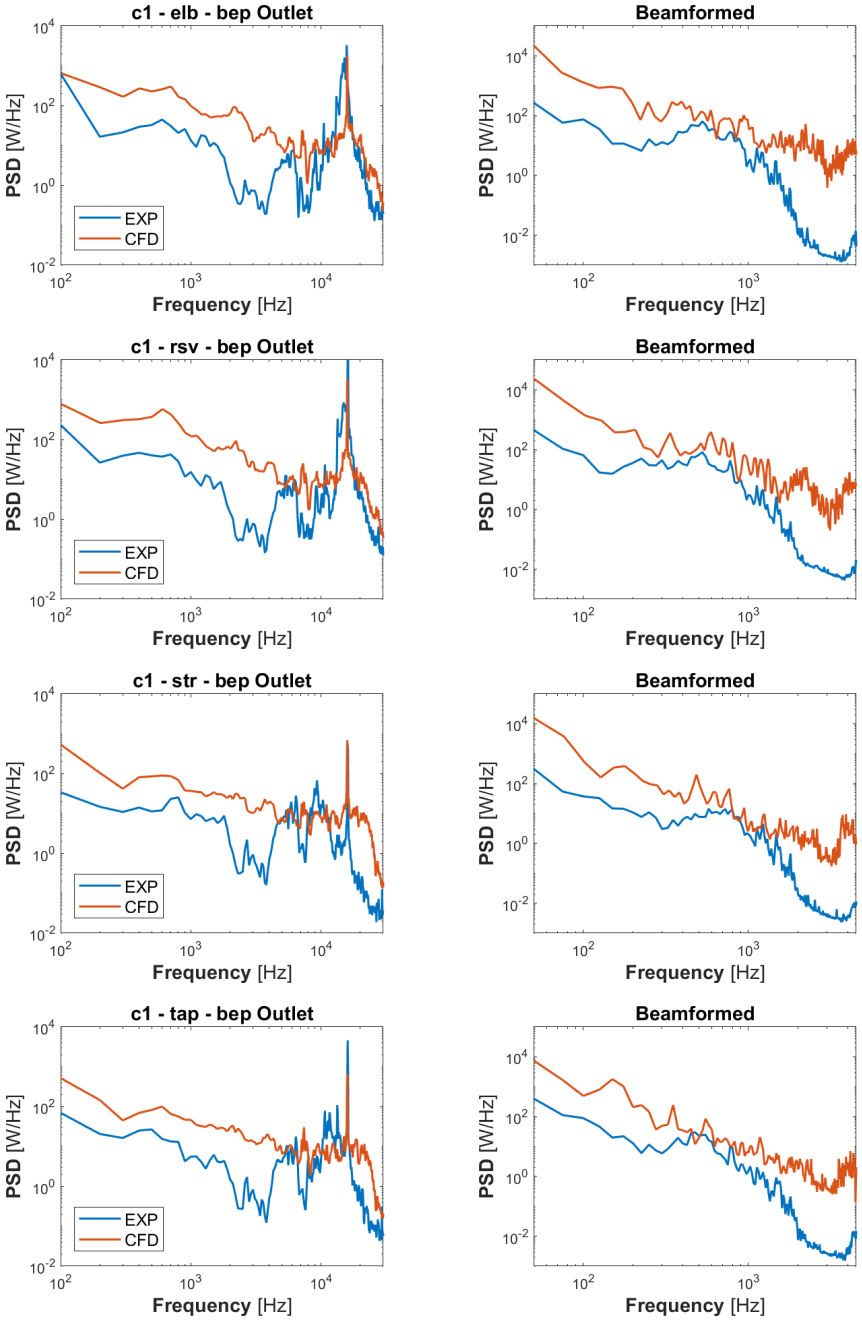

Figure 4.9: *PSD of the raw and beamformed signals of the c1 simple geometries' outlet duct at the best efficiency point.*

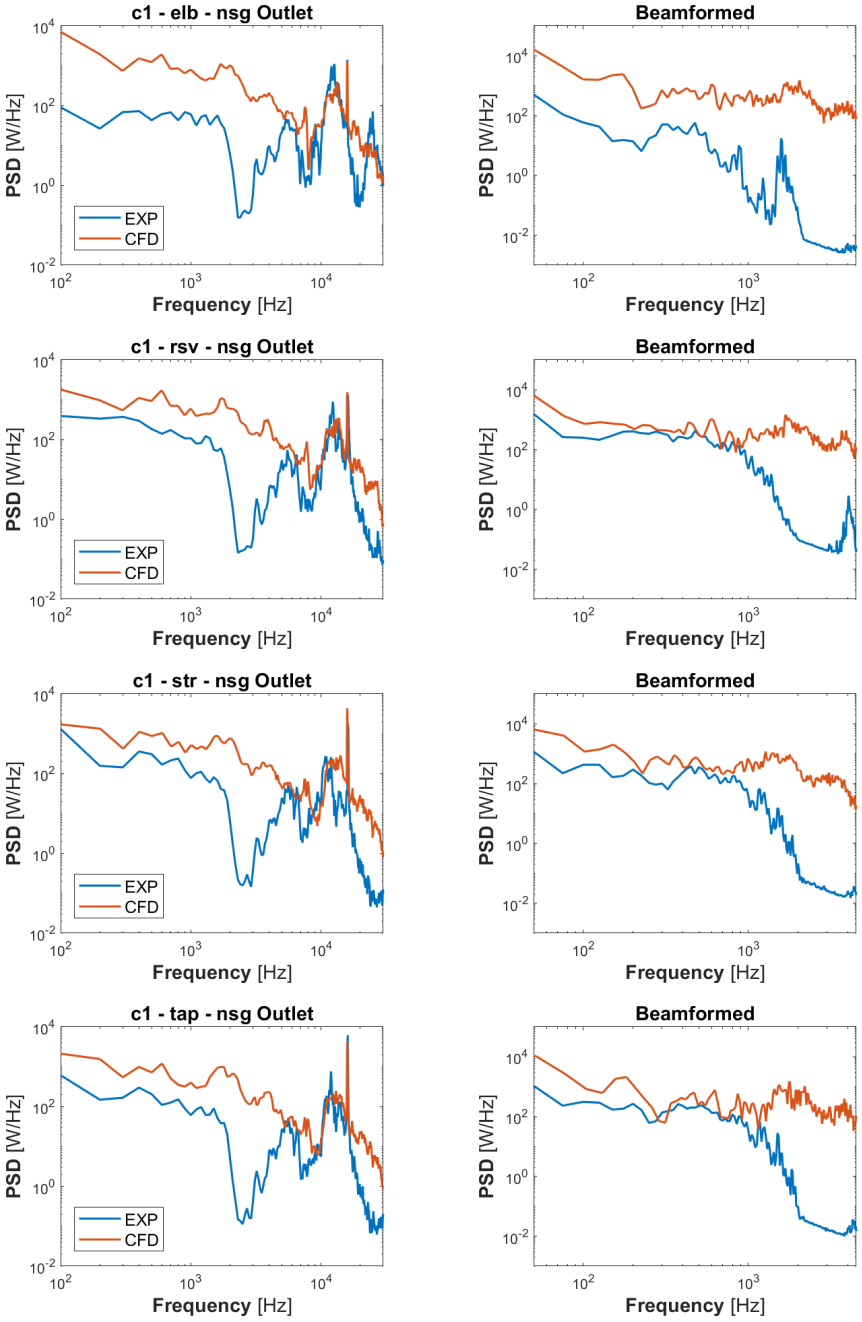

Figure 4.10: *PSD of the raw and beamformed signals of the c1 simple geometries' outlet duct at the near surge point.*

Geom	point	Inlet CFD	Inlet Exp	Inlet ε_R [%]	Outlet CFD	Outlet Exp	Outlet ε_R [%]
elb	bep	148.8	152.4	2.4	154.3	157.9	2.3
elb	nsg	155.7	160.7	3.1	161.2	156.8	2.8
rsv	bep	149.1	151.0	1.3	155.6	163.5	4.8
rsv	nsg	149.8	154.4	3.0	159.7	163.4	2.3
str	bep	147.8	154.2	4.2	155.1	158.9	2.4
str	nsg	152.7	157.7	3.2	159.8	155.5	2.8
tap	bep	141.9	138.4	2.5	154.5	163.2	5.3
tap	nsg	147.2	143.9	2.3	159.3	167.6	5.0
rsd	bep	148.5	142.8	4.0	157.4	155.8	1.0
rsd	hpr	152.8	152.1	0.5	159.7	158.6	0.7
rsd	nsg	150.7	149.6	0.7	160.2	158.3	1.2

Table 4.2: *Compressor c1 SPL (20 Hz to 20 kHz) of the raw pressure signals in dB, and relative error in %.*

4.3 Validation of compressor c2

4.3.1 Experimental setup

Figure 4.11 shows the experimental setup for compressor c2 in the rsd configuration. The instrumentation is the same as compressor c1, and the measurements were carried out in the same facility. The mass flow rate was measured at the inlet duct. Temperature and pressure were measured in the ducts with piezoresistive sensors and thermocouples, respectively, located at the positions displayed in the figure. Two separate piezoelectric sensor arrays were used to decompose the pressure signal in the ducts.

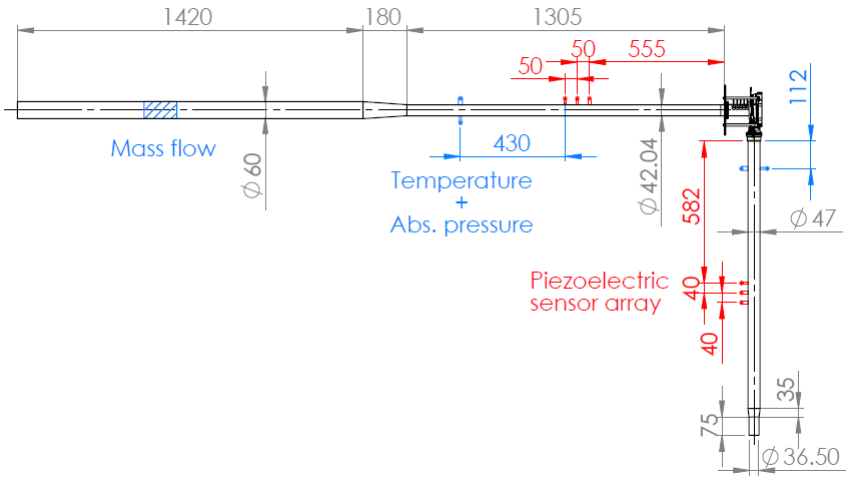

Figure 4.11: *Experimental setup for compressor c2 with the reference straight ducts.*

4.3.2 Numerical setup

In the numerical model of compressor c2, the experimental location of the arrays was maintained. The mesh in the ducts keeps the minimum required size to guarantee a frequency resolution up to 3 kHz so that the beamforming results can be directly compared to the experimental ones. Two monitors were placed closer to the compressor, where the mesh is fine enough to resolve frequencies up to 20 kHz, to compare the raw spectra across the entire audible frequency range. In figure 4.12, the location of the two arrays and the two sensors close to the compressor can be seen.

Figure 4.12: *Numerical domain and location of the pressure probes for compressor c2 rsd.*

4.3.3 Operation variables

The operating variables are calculated, using equations 4.1 and 4.2. In table 4.3, the values are shown together with the relative error defined by equation 4.3.

Case	Point	Π_{tt} Exp	Π_{tt} CFD	ε_R [%]	η_s Exp	η_s CFD	ε_R [%]
rsd	bep	2.12	2.14	0.9	72.6	72.7	0.2
	hpr	2.18	2.26	3.7	62	66.7	7.6
	nsg	2.16	2.26	4.6	53.4	60.8	13.9
e0D75	nsg	2.18	2.28	4.7	54.4	61.9	13.9
e1D	nsg	2.17	2.27	4.6	53.6	61.8	15.3
e1D5	nsg	2.18	2.27	4.4	53.7	61.6	14.7

Table 4.3: *Measured and numerical operating variables for all c2 configurations.*

In the left column of figure 4.13, the numerical and experimental pressure ratios on the 140 krpm iso-speed line are presented. In the right column, the isentropic efficiency on the 140 krpm iso-speed line is represented. Numerical points include an error bar of length five times the temporal standard deviation.

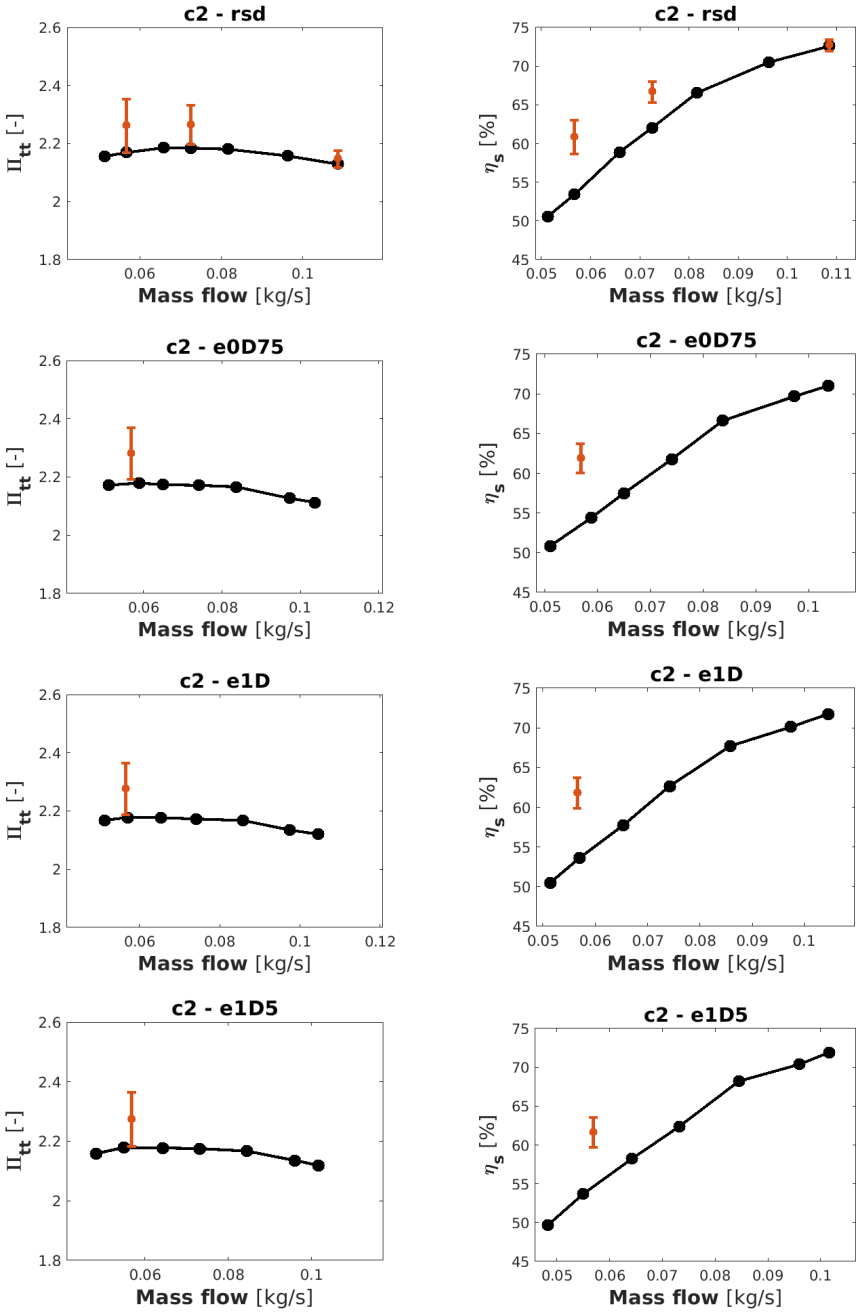

Figure 4.13: *c2, all geometries, working points along the 140 krpm iso-speed line. Measurements are displayed in black, and numerical calculations in red. The error bars length is five times the standard deviation of the time signal.*

Looking at the values of the global variables, there is a tendency to over-

estimate the pressure ratio in the near surge conditions. The mean pressure ratio of the near surge points is 4.6% above the experimental value. This value is considerable but still within what can be expected for DES models.

Isentropic efficiency is also overestimated near surge. However, the error is much higher in this case, reaching 15% in the worst case. Equation 4.2 shows that an increase in the pressure ratio produces an increase in efficiency. The denominator of said equation is the actual total enthalpy increase, represented by the temperature rise due to the impeller work. This temperature increase is more prominent as the compression process moves away from the ideal isentropic evolution. In the case of model c2, the temperature increase is less than the experimental one. This indicates that the modeled process is less irreversible than what occurs in reality. The model underestimates the efficiency loss due to flow instabilities. Errors in pressure ratio and total temperature rise add up to give a significant bias in isentropic efficiency. In the first row of figure 4.13, it can be seen that efficiency decreases as it approaches surge, as expected; however, it does not reduce as much as it should. There are other examples of state-of-the-art numerical models of compressors in the literature where performance is also overestimated at points close to surge. See for example [68], [48] and [69].

4.3.4 Acoustic validation

In this section, the frequency content of the pressure signals in the compressor ducts is analyzed. The PSD of the raw and the beamformed signals at the arrays location are shown. The pressure probes shown in figure 4.12 between the compressor and the inlet and outlet arrays are called the "close probes". The numerical raw pressure signals analyzed in this section are recorded at those probes, as the mesh resolution allows capturing frequencies up to 20 kHz. The numerical signals from the beamforming array and close probes have a minimum of 180 ms and 100 ms, respectively. The experimental signal is 1 s long. They are divided into 10, 20, and 200 blocks respectively to obtain a frequency resolution of 25 Hz for beamformed and 100 Hz for raw signals.

In figures 4.14 and 4.15, corresponding to the spectra of the inlet signal, it can be seen that the numerical signal adjusts reasonably well to the experimental one, except for the broadband around 10 kHz. The numerical spectrum shows a slightly higher level than the experimental one in the entire low-frequency range, below the plane wave cut-off frequency (around 5 kHz). This difference appears in the beamformed signal as well. The peaks of the BPF and the 2 $\times$BPF can be observed at 14 and 28 kHz. The latter stands out more in the experimental case for some configurations. Above 20 kHz, the numerical signal decays faster than the experimental one, although this frequency range is of little importance in the acoustic analysis.

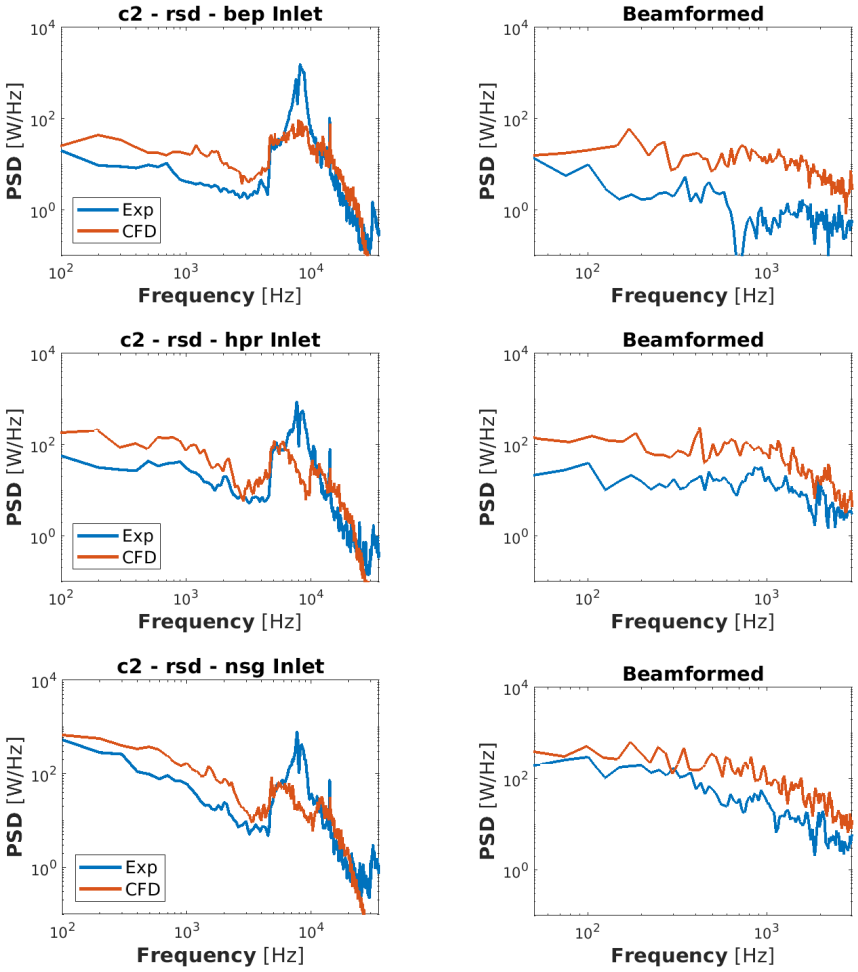

Figure 4.14: *PSD of the raw and beamformed signals of the c2 rsd geometries' inlet duct.*

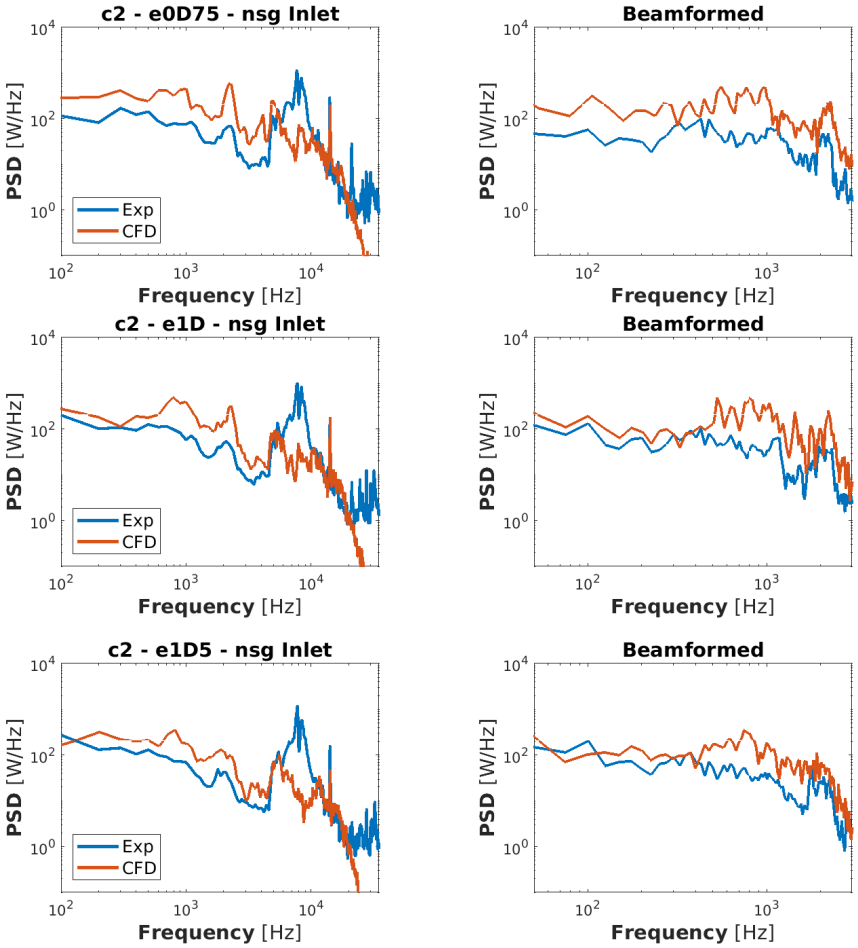

Figure 4.15: *PSD of the raw and beamformed signals of the c2 e0D75 e1D and e1D5 geometries' inlet duct.*

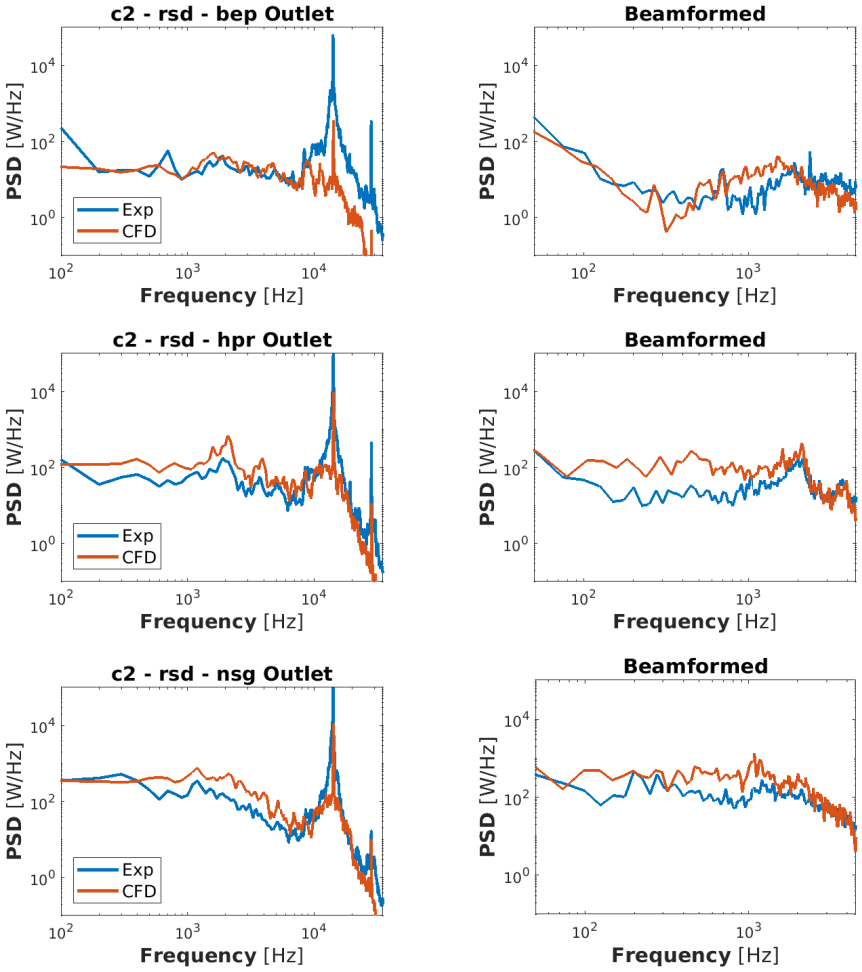

Figure 4.16: *PSD of the raw and beamformed signals of the c2 rsd geometries' outlet duct.*

Regarding the spectra of the outlet signals (figures 4.16 and 4.17), the coincidence between numerical and experimental signals is also good. In this case, the level at low frequencies is the same for the numerical model and the measurements. At high frequencies, the numerical model has a broadband increase, although it does not reach the same level as the experimental one. The numerical bep case in particular shows a remarkable attenuation above the BPF. The SPL of the raw signals is displayed in table 4.4. It can be seen that the predicted values match the experimental measurements with a very small error.

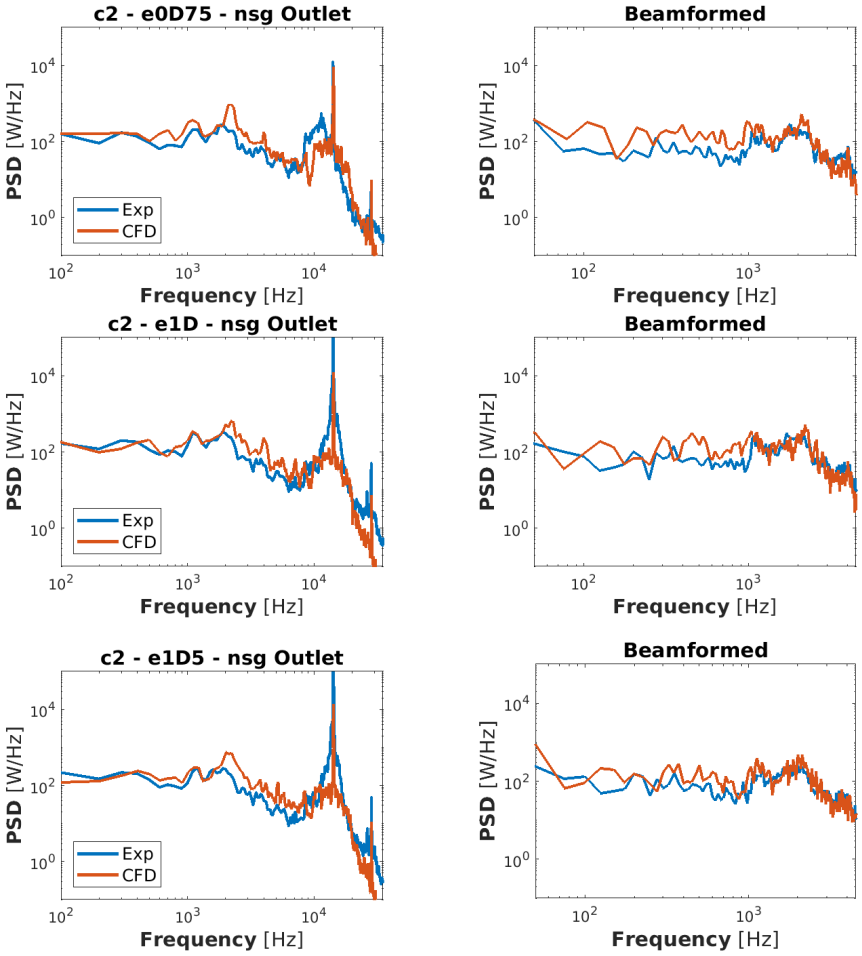

Figure 4.17: *PSD of the raw and beamformed signals of the c2 e0D75 e1D and e1D5 geometries' outlet duct.*

Case	Inlet CFD	Inlet Exp	Inlet ε_R [%]	Outlet CFD	Outlet Exp	Outlet ε_R [%]
bep	150.5	154.9	2.8	148.9	154.1	3.4
hpr	152.0	154.2	1.4	159.1	160.9	1.1
nsg	153.0	154.1	0.7	160.1	159.0	0.7
e0D75	155.2	155.8	0.4	159.4	160.0	0.4
e1D	153.5	154.1	0.4	159.1	161.0	1.2
e1D5	152.2	154.0	1.2	159.5	160.8	0.8

Table 4.4: *Compressor c2 SPL (20 Hz to 20 kHz) of the raw pressure signals in dB, and relative error in %.*

4.3.5 Aeroacoustic analogy

To complement the acoustic calculations shown above, this subsection presents the results of the Ffowcs Williams and Hawkings (FW-H) acoustic analogy in the c2 rsd cases.

Ffowcs Williams and Hawkings analogy

The Lighthill equation is obtained by deriving the continuity equation 3.1 with respect to time and subtracting the divergence of the momentum equation 3.2. This yields an inhomogeneous wave equation, where the inhomogeneous term represents the acoustic sources. The FW-H equation is an extension of the Lighthill equation, where the generalized derivative (see chapter 5 of reference [77]) is used to account for moving surfaces in the region of the acoustic sources.

Using the FW-H equation (4.4), the acoustic pressure oscillation at an observer's position due to the various sources can be calculated.

$$p'(\mathbf{x},t) = p'_T(\mathbf{x},t) + p'_L(\mathbf{x},t) + p'_Q(\mathbf{x},t) \tag{4.4}$$

The term p'_T represents the contribution of the monopole sources caused by fluctuating flow volume. The subscript T refers to "thickness" since the thickness of the passing blade causes this phenomenon in turbomachinery, especially when sonic conditions are reached [35].

The term p'_L represents diopole sources caused by fluctuating surface loading (hence the subscript L).

$$p'_L(\mathbf{x},t) \approx \frac{x_i}{|\mathbf{x}|}\frac{1}{c_\infty^2}\frac{\partial}{\partial t}\int_{S_o}\left[\frac{p_{ij}n_j}{4\pi|\mathbf{x}||1-M_r|}\right]_{\tau=\tau^*} dS \tag{4.5}$$

where $\mathbf{x}$ is the position vector of the observer relative to the source, c_∞ is the far field speed of sound, S_o is the source surface, p_{ij} is the pressure tensor, n_j is the surface normal vector, M_r is the relative Mach number, and τ^* is the time of emission.

In equation 4.5, the expression of dipole sources for the case of impermeable surfaces, such as impeller blades, is presented. The paper by Sündstrom et al. [51] shows that dipolar sources are dominant in centrifugal compressors.

Finally, the term p'_Q represents the quadrupole sources due to free turbulence. This term is important, for example, in high Mach number jets as those described in [78]. However, it is of minor importance in radial compressors.

Numerical setup

The FW-H analogy does not consider the effect on noise propagation of the compressor housing and ducting. For this reason, the inlet duct of the c2 rsd configuration was chosen to locate the FW-H receiver, as sound can propagate relatively unimpeded from the impeller. The location of the FW-H receiver is the same as that of the numerical pressure probe used for the inlet duct

spectra shown in the previous section, i.e., 1.74 D upstream of the impeller leading edge, and flush-mounted to the inlet duct wall. Figure 4.18 shows the location of this probe.

Figure 4.18: *Numerical location of the pressure and FW-H probe at the inlet duct of c2 rsd geometry.*

The FW-H module available in Simcenter STARCCM+ was used to estimate the acoustic contribution of the dipolar sources (p'_L), with the Dunn Farassat Padula 1A formulation [79] suitable for turbomachinery. The compressor housing walls and the impeller blade surfaces where selected as source surfaces for the FH-W model.

Figure 4.19 shows the experimental, CFD (directly from the calculated pressure field, as in the previous section), and FW-H spectra. Dashed lines mark the BPF and 2×BPF. A solid red line marks the plane wave (PW) cut-off frequency, i.e., the frequency below which the pressure disturbances only propagate as plane waves through the inlet duct.

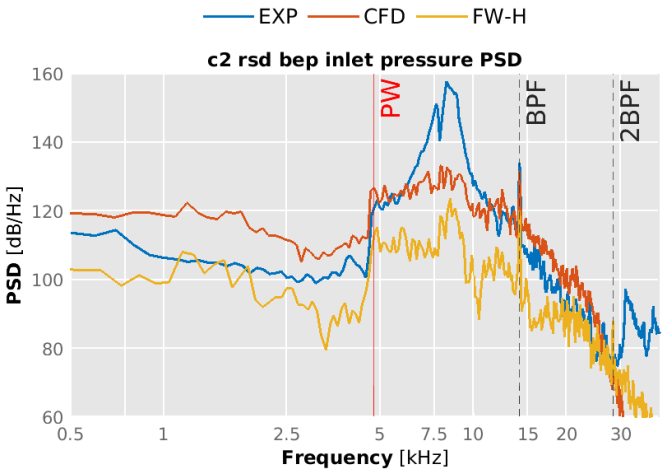

Figure 4.19: *Experimental, CFD and FW-H pressure spectra at the inlet duct of c2 rsd bep. The solid red line marks the plane wave frequency limit.*

The blue and red curves in figure 4.19 are the same as those in the first image in the right column of figure 4.14. The yellow line corresponding to

the FW-H spectrum follows the same shape as the red line of the raw CFD spectrum but with an offset of slightly less than 20 dB. The smaller amplitude of the FW-H spectrum is because the acoustic power propagates as a spherical wave rather than being confined in the inlet duct, as is the case with the CFD and experimental spectra pressure waves.

Two aspects of the FW-H plot are particularly relevant. The first is that the offset with the CFD spectrum is considerably reduced in the band between 7.5 and 10 kHz, corresponding to the high-frequency TCN broadband. This suggests that acoustic sources at these frequencies are indeed present on the surfaces but are not detected by the CFD duct probe due to an artificial attenuation introduced by the mesh. The pressure oscillations due to the FW-H dipole term propagate analytically to the receiver, so they are not subject to the propagation constraints introduced by the mesh.

The second interesting aspect is that the FW-H model captures the amplitude increase at the plane wave limit marked by the solid red line. In [41], it was noted that the lower frequency limit of the TCN band matches the plane wave cut-off frequency of the ducts. The FW-H model is not affected by the duct's cut-off frequency and displays the same lower frequency limit. It can be concluded then that the lower frequency limit of the TCN band is determined by the generating phenomena and not by the duct's propagation properties.

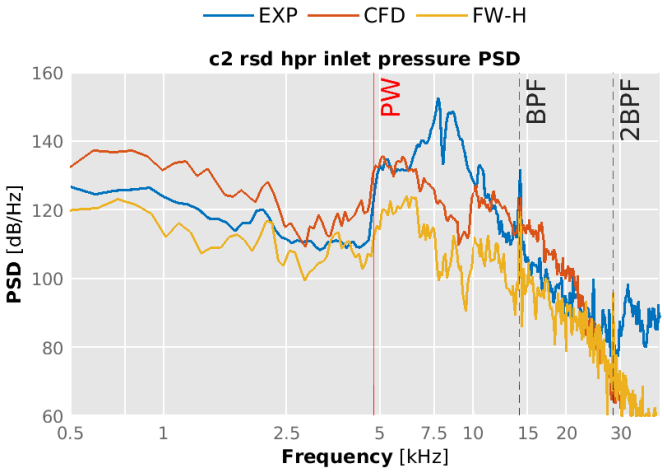

Figure 4.20: *Experimental, CFD and FW-H pressure spectra at the inlet duct of c2 rsd hpr. The solid red line marks the plane wave frequency limit.*

Figure 4.20 shows the spectra corresponding to the c2 rsd hpr case. The situation is similar to that shown in Figure 4.19. All three spectra show an increase in amplitude at the plane wave cut-off frequency, and the offset between the CFD and FW-H spectra is appreciably reduced between 7.5 and 10 kHz. Again, it appears that part of the CFD underprediction of the TCN

band is due to the attenuation caused by the mesh and not solely to the inability of the CFD model to reproduce the flow phenomena responsible for the noise in that frequency band.

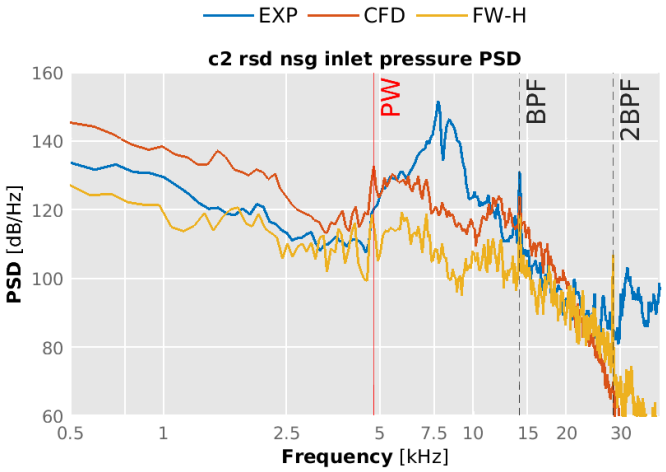

Figure 4.21: *Experimental, CFD and FW-H pressure spectra at the inlet duct of c2 rsd nsg. The solid red line marks the plane wave frequency limit.*

Figure 4.21 shows the spectra corresponding to the c2 rsd nsg case. In this figure, however, there is no decrease in the offset between the CFD and FW-H spectra in the 7.5 to 10 kHz band. This suggests that the phenomena responsible for the noise in this band appear in the CFD model more intensely in the bep and hpr cases than in nsg.

4.3.6 Local flow field validation

To further validate the flow field inside the turbomachine, additional available measurements of compressor c2 were used. In this section, the experimental setup used to measure the backflow extension at the inlet, the axial velocity distribution in the last section of the inlet duct, and the frequency content of the pressure field in the diffuser are described. The experimental and numerical results are compared, and the ability of the model to correctly reproduce the local flow field is assessed.

Inlet backflow temperature

Figure 4.22 shows the thermocouple array arranged in the axial direction in the inlet duct and a circumferential array above the inducer plane. The pressure probes placed in the inducer and the diffuser are also shown. In reference [41], the experimental rig and the measurement procedure are described in detail.

The linear array for backflow measurement is located on a line parallel to the axis of the inlet duct, at a radial distance of D/4. The first thermocouple is

14 mm upstream of the impeller leading edge, and the other five thermocouples are also 14 mm apart. The circumferential array of thermocouples coincides with the first probe of the linear array; i.e., it is 14 mm above the leading edge, also at a radial distance of D/4, and consists of eight thermocouples. This array was placed for quantifying the circumferential distortion of the temperature profile.

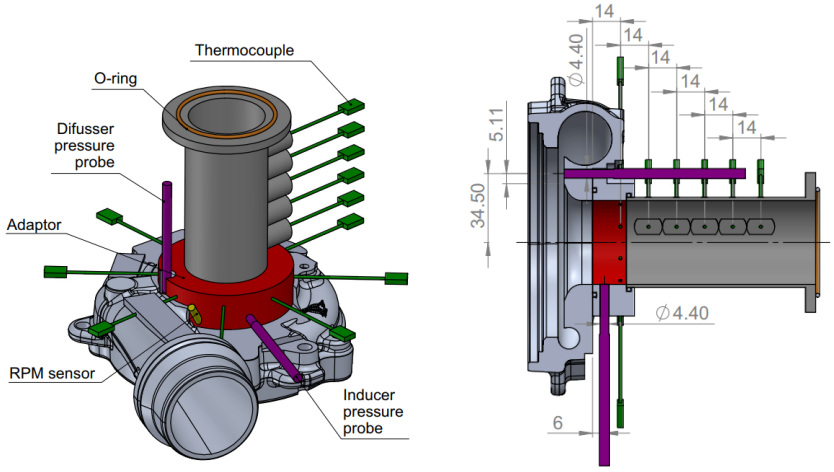

Figure 4.22: *Experimental setup for inlet backflow temperature, and local pressure measurements on compressor c2. Images courtesy of Jorge García-Tíscar [41].*

Figure 4.23 shows the temperature measurements in the rsd cases. Besides the experimental data, the temperature calculated in the longitudinal section of the inlet ducts is presented. The location of the numerical probes, which coincide with the experimental thermocouples, is marked with red dots. The "temperature rise" shown in this figure is defined as the difference between the temperature at the beginning of the inlet duct (1m upstream of the inducer) and the local temperature.

The iso-line corresponding to a temperature rise of 3 K has been added, following [41]. In that paper, the 3 K threshold was established to consider that a thermocouple is affected by backflow. A certain discontinuity can be observed in the 3 K iso-line a few millimeters upstream of the impeller axis nut (especially in the nsg case). This occurs because the rotor region is mobile, and therefore the time average has been taken using its rotating reference frame.

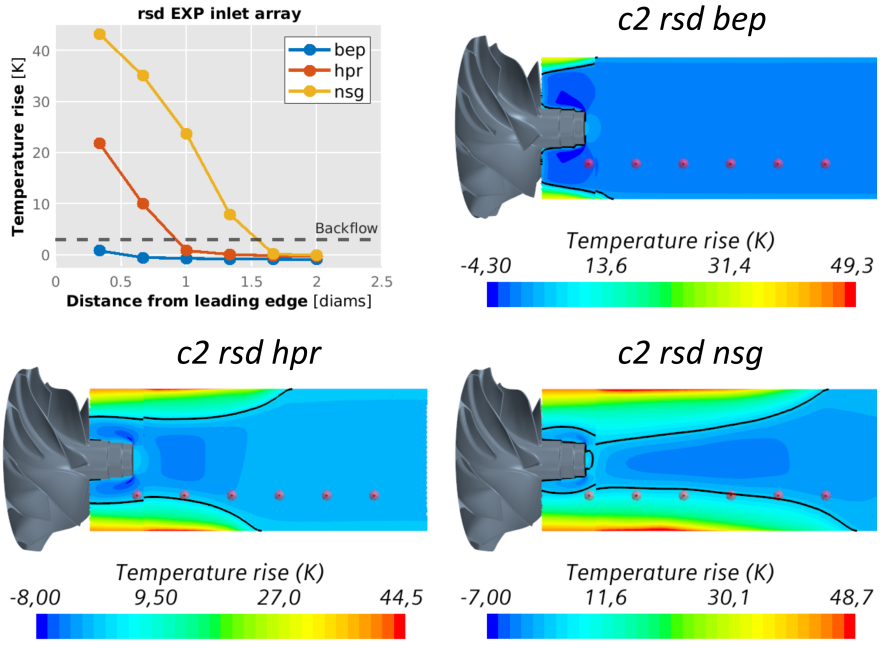

Figure 4.23: *Experimental and numerical distribution of temperatures for cases c2 rsd. The isoline of 3 K temperature rise is plotted in black.*

The numerical results reproduce the experimental ones in the sense that a 3 K temperature rise would be detected by the same numerical and experimental sensors. That is, in the bep case, no sensor would detect backflow, in the hpr case, the first two would see it, and in the nsg case, all thermocouples except the last two would be affected by backflow. However, the numerical model disagrees with the experimental results in the magnitude of the temperature increase, i.e., the numerical backflow is much colder than the experimental one.

This is due to two factors. The first is the lower temperature increase in the flow caused by lower irreversibility in the compression process, as mentioned in section 4.3.3. For this reason, the reverse flow is at a lower temperature than in the experiments. The second factor might be due to residual heat transmission from the duct wall to the flow or thermocouples in the experimental rig.

Figure 4.24 shows the images recorded during the experiments by the thermographic camera [41] at the operating points bep and nsg. The instrumented inlet of figure 4.22 is depicted in the top row, showing the surface temperatures. The same sections of figure 4.23 corresponding to the calculated flow field at these operating points are represented in the bottom row.

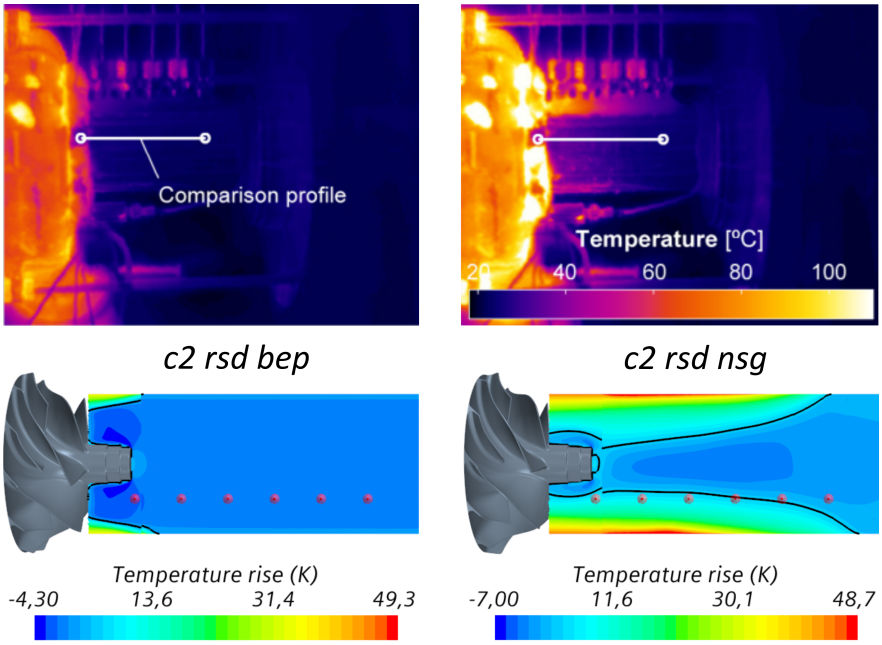

Figure 4.24: *Thermnographic camera images of the inlet temperature at bep and nsg points. Thermographic images courtesy of Jorge García-Tíscar [41].*

The high-temperature of the compressor casing can be seen at the left, while the inlet duct extends horizontally to the right. At the top of the image, the vertical lines of the thermocouples appear. It can be seen that the temperature of the casing, the thermocouple supports, and the surface of the inlet duct is notably higher at the nsg point.

It could be the case that the high temperature of the compressor casing could lead to an overestimation of the thermocouple readings by heating the probes themselves or the backflow, which has a low axial velocity in that area.

As for the circumferential thermocouple array shown in figure 4.22, the calculated backflow does not reach the radial position (D/4) of the probes. Therefore there is no feedback on the circumferential skewness of the temperature distribution predicted by the models compared to the experiments.

Figure 4.25 shows the results corresponding to the geometries e0D75, e1D, and e1D5 operating at the nsg point. The location of the thermocouples is on an arc of circumference concentric with the elbow curvature.

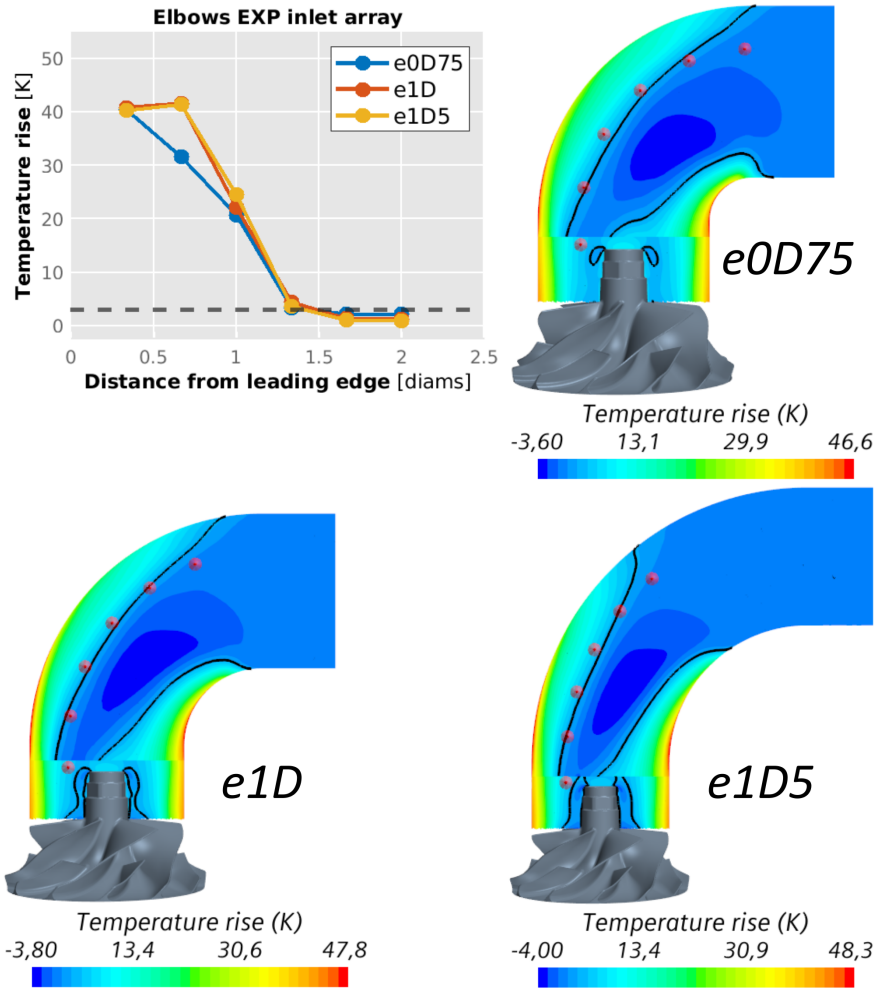

Figure 4.25: *Experimental and numerical distribution of temperatures for cases c2 e0D75, e1D and e1D5. The isoline of 3 K temperature rise is plotted in black.*

The radial distance remains D/4, and the thermocouples are separated from each other and with the leading edge the same arc length of 14 mm. In this case, the discontinuity of the 3 K temperature rise iso-line is more evident than with the rsd cases. At the top left, the experimental results are shown together with the threshold line of 3 K temperature rise. Again, the backflow extent affects the same sensors in the numerical and experimental cases, but the backflow temperature is lower, and consequently, so is the detected temperature rise.

It is interesting to note how the upstream extension of backflow at the minor radius of the e0D75 elbow reaches the upstream horizontal duct. As the elbow radius increases, the backflow no longer reaches the upstream horizontal

duct.

Inlet flow PIV

The velocity field upstream of the inducer was measured by means of PIV. A section of glass duct was placed in the experimental setup, and a longitudinal laser sheet was used to measure the axial velocity. The experimental setup and the measurement method are described in detail in [66].

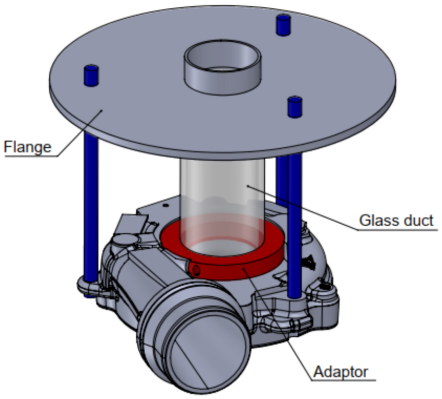

Figure 4.26: *Experimental setup for PIV measurement of the flow upstream of the inducer on compressor c2. Figure courtesy of Jorge García-Tíscar [66].*

Figure 4.26 shows a schematic of the experimental setup with the transparent section. Figure 4.27 shows the location of the longitudinal laser sheet. The operating points where the measurements were taken are also highlighted. These points do not coincide exactly with the points of the 140 krpm iso-speed line previously used to validate the operating variables. This is because the mass flow rate was not measured in the inlet duct during data collection for PIV. However, the mass flow was estimated using the measured velocity field, giving rise to two points called "low flow" and "high flow" (see figure 4.28). The first point is located between the nsg and hpr CFD points, while the second is close to the bep, but with a slightly lower mass flow rate. In the lower row of figure 4.27, the calculated axial velocity of the c2 rsd hpr and bep cases is shown.

The c2 rsd nsg upstream backflow extension shown in figure 4.27 is longer than in the PIV "low flow" point (90 mm for the calculations vs. 55 mm for the experiments). The greater extension of the backflow is consistent with the fact that in the numerical case, the mass flow rate is lower than in the experimental one. In the radial direction, the calculations show lower thickness than the experiments. They have also a lower temperature than in the experimental case, and thus the density will be higher. Therefore the same recirculated mass flow would occupy a smaller section.

In the "high flow" experimental case, a small region at the left end of the laser sheet presents backflow. In the numerical bep case, there is a thin backflow region as well in the left end of the section. In the high flow numerical and experimental cases, the 50 m/s iso-line is at a similar distance to the wall. This distance is a little smaller in the numerical case, but this is consistent with the higher mass flow of the numerical point. The averaging time of the numerical cases is longer than in the PIV measurements. This justifies the greater smoothness of the numerical flow field.

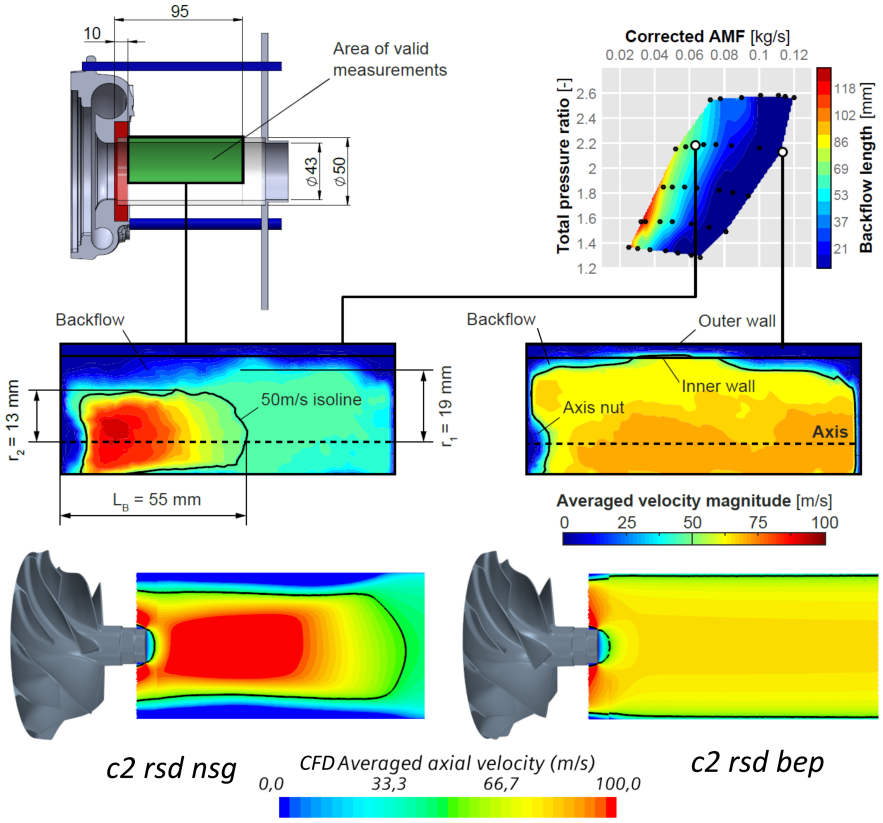

Figure 4.27: *Experimental setup and PIV measurements of axial velocity upstream of the inducer in compressor c2. CFD results are shown on the bottom row. The black line marks the 50 m/s iso-line. PIV images courtesy of Jorge García-Tíscar [66].*

In figure 4.28, the average axial velocity at the inlet duct axis is displayed. The horizontal part of the curves, upstream of the leading edge, allows the mass flow rate of the numerical points to be compared with the experimental ones. Again, the largest extent of the reduced cross-section zone is seen in the numerical nsg case. On the other hand, the maximum speed reached experimentally is lower. However, this may be due to the asymmetry of the experimental speed profile shown in 4.27, where it is seen that the maximum speed zone does not coincide with the central duct axis represented by the dashed line.

Besides the differences due to the backflow temperature, and considering that the short duration of the experimental sample offers a less smooth velocity distribution than in the numerical case, it can be concluded that the numerical model reproduces the velocity field reasonably well.

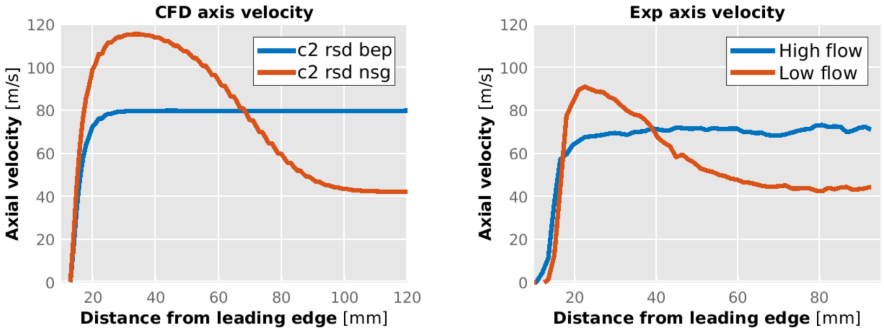

Figure 4.28: *Comparison of the numerical and PIV axial velocity at the inlet duct axis.*

Diffuser pressure signal

Figure 4.22 shows the location of two piezoelectric sensors inserted to measure the local pressure inside the compressor. The numerical model incorporates pressure monitors at the exact experimental locations. Unfortunately, it seems that the inducer probe in the numerical model was interfered by the passage of the blades and was out of the numerical domain in some time steps. For that reason, the signal is corrupted and is not plotted.

The PSD of the pressure signal in the diffuser is shown in figure 4.29. The numeric signal has a minimum duration of 150 ms. The measured signal lasts 1 s. Both are averaged 30 and 200 times respectively to achieve a frequency resolution of 100 Hz.

Again, a good coincidence between the numerical and experimental spectra is observed, except in the high-frequency broadband centered at 20 kHz. However, the underprediction of this broadband (whose frequency is significantly higher than the TCN) was expected since the mesh shows attenuation in all cases above 20 kHz. Additionally, in the rsd cases, the experimental spectra show narrowband noise at low frequencies, which the numerical model has not reproduced.h

4.4 Conclusions

In compressor c1, the operation variables were calculated with an acceptable error. Regarding acoustics, it can be considered that the numerical spectra reasonably reproduce their experimental counterparts, with the main exception of the broadbands at high frequencies. This shortcoming was already anticipated in Chapter 2, where more examples of DES models that are not capable of correctly capturing these broadbands are presented. The most significant discrepancies have been found in the outlet duct of the simple geometries. The SPL of the numerical calculations agree with the measurements with a similar error level as the operation variables. In conclusion, it is reasonable to think that the numerical flow field will include the most impor-

tant noise-generating mechanisms except perhaps those of the high-frequency broadband.

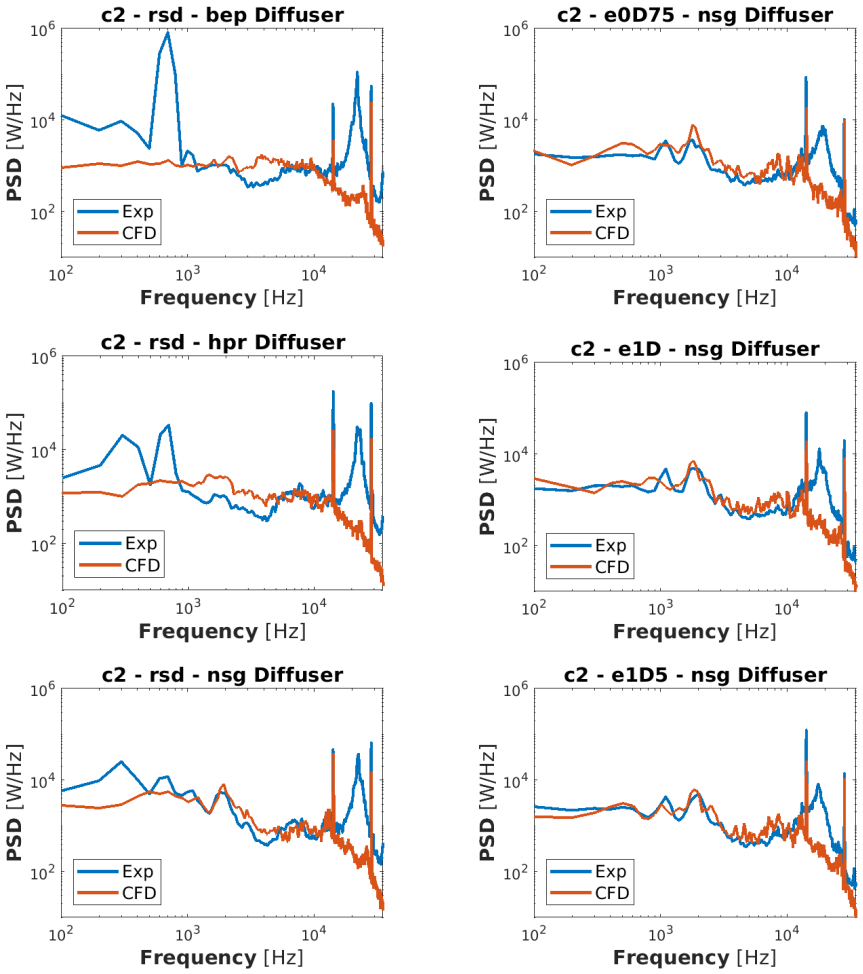

Figure 4.29: *PSD of the diffuser pressure probe in all the c2 cases.*

In compressor c2, the numerical model underestimates the level of irreversibility introduced by the unstable flow in the compression process near surge. This is reflected by an overestimated isentropic efficiency and a cooler backflow. On the other hand, the backflow upstream extension is well calculated, and the inlet velocity field is similar to the experimental one. Moving away from the surge point, the discrepancies with the experimental measurements vanish. Regarding the acoustic field, the spectra of the raw and decomposed signals, both in the ducts and in the diffuser, show a good agreement with the experimental measurements, except for the broadbands at high frequencies. Given the resemblance of the flow field and the good coincidence

of the pressure signals, it is determined that all relevant noise generation mechanisms will be present in the numerically calculated flow field, with the exception, again, of the high-frequency broadbands, which the model underpredicts. However the FW-H model suggests that part of the underprediction is related to mesh attenuation rather than absence of the noise sources in the flow field.

5

Frequency analysis of the flow field

Contents

5.1 Introduction

This thesis aims to improve the understanding of the effect of inlet duct geometry on the acoustics of radial compressors. The starting point is the experimental characterization which allows associating a pressure spectrum to each geometry. In this chapter and the next, a systematic methodology will be presented to include the intermediate link of the flow field between the geometry and the duct spectra. Thus, a chain of causality is established between the observed spectrum, the flow field, and the inlet duct geometry.

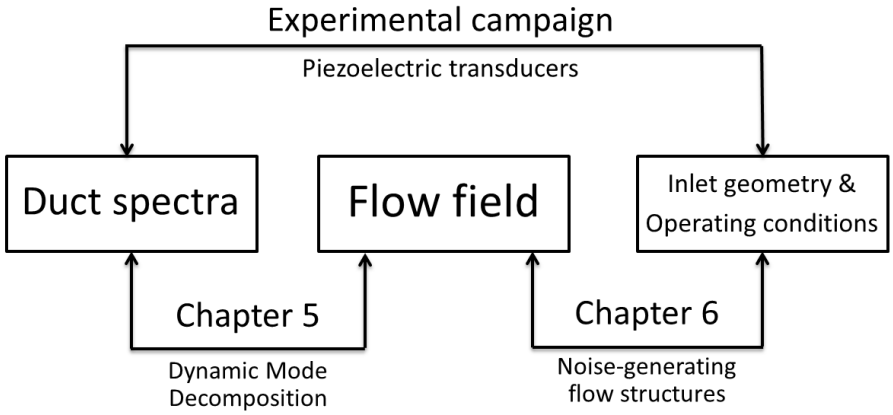

Figure 5.1: *Schematic reminder of the methodology explained in Chapter 1. In this chapter the DMD tool will be used to link the measured duct spectra with the flow field.*

In this chapter, the Dynamic Mode Decomposition (DMD) tool will be used to relate different space regions with the acoustic spectrum frequencies. The influence of the inlet duct geometry will first be assessed through the differences in the measured duct spectra. Then, these differences will be compared with the spectra of DMD modes to check which effects are captured by the numerical model. Finally, the modes associated with the spectral components of interest will be analyzed. The next chapter will identify the flow structures corresponding to the DMD modes and how the different geometries and operating points induce them.

5.2 Flow field modal decomposition

The introduction and mathematical development of the DMD method applied in this chapter are presented in subsections 5.2.1, 5.2.2, and 5.2.3. These sections are part of the paper in reference [72], of which the author of the present thesis is also an author.

5.2.1 Introduction

Analysis methods for turbomachinery acoustics originated in the field of aeronautics. The introduction of the jet engine in civil aviation after WWII led to noise problems in overflown residential areas, which motivated the study of turbomachinery aeroacoustics.

It is in this historical context where the seminal work of Tyler and Sofrin [19] was presented. They sought to offer a complete analytical understanding of axial compressor acoustics, from the source pressure distribution to the duct propagation and ambient radiation. Their studies highlighted the role of rotating acoustic modes that were, at the time, regarded as phenomena of secondary importance [80].

While the analytical spinning mode approach has been used abundantly along the years in both numerical and experimental investigations of aircraft engine noise [81, 82], most of these investigations have been focused on axial turbomachinery. Studies regarding the modal decomposition of the acoustic field produced by radial machines have remained, on the other hand, relatively scarce in comparison [26].

As radial compressors feature flow phenomena that differ from those found in axial machines [83], it becomes necessary to investigate how these, in particular, relate with the generation and propagation of noise at different frequencies. While at design condition tonal noise at the Blade Passing Frequency (BPF), caused by the rotation of pressure patterns associated to the aerodynamic blade loading, behaves similarly in both kinds of compressor, stall and surge dynamics of radial machines are still less understood [84, 85].

Particularly, non-axisymmetric volutes that create pressure differences along the angular coordinate [86] cause non-uniformities in the flow field and have been found to influence the location of shock waves in the passages, leading edge spillages and tip leakage flow trajectories [87].

In turn, these unstable flow phenomena related to the geometric characteristics are linked to the spectral signature of the compressor noise [88]. This opens the door to geometry improvements that optimize both flow stability and acoustics, such as the use of hub [89] or shroud [90, 91] cavities.

In this thesis, a better understanding of the relationship between the radial compressor geometry, its unstable flow features, and the corresponding acoustic phenomena is sought by means of modal decomposition techniques applied to a numerical simulation of the system operating at different points, including the mild surge region where unstable flow features start to manifest.

5.2.2 Analytical spinning modes

In order to facilitate the mathematical treatment of the compressor acoustics, Tyler & Sofrin proposed [19] a modal decomposition of the acoustic field into rotating pressure patterns referred to as 'spinning modes'. Propagation of these analytical modes was studied by first considering simplified media such as thin rectangular ducts and narrow annular ducts which could be understood as 2D cases, and then an annular duct typical of axial turbomachinery.

5.2. Flow field modal decomposition

However, this analysis primarily concerned tonal noise caused by the rotor only and by the rotor-stator interaction, disregarding other broadband noises of aerodynamic origin. In particular, a steady aerodynamic loading of the blades rather than unstable vortex-shedding or partially detached regimes was considered. This steady loading was found to create 'lobed' circumferential distributions of pressure.

Several authors [80, 92, 93, 94] have developed this analytical model over the years, showing that in the case of a uniform circular duct of radius R with axially uniform mean flow at Mach M_0, it is indeed possible to write the well-known convected wave equation

$$\left(\frac{\partial}{\partial t} + M_0 \frac{\partial}{\partial x}\right)^2 p = \nabla^2 p \tag{5.1}$$

in such a way that a solution for the pressure field can be obtained as a superposition of Tyler–Sofrin spinning modes in polar coordinates (r, θ, x) and time t:

$$p(r,\theta,x,t) = \mathrm{Re}\left\{\sum_m^\infty \sum_n^\infty A_{mn}^{\pm} J_m\left(\kappa_{mn}\frac{r}{R}\right) e^{im\theta} e^{-i\omega t} e^{ik_{x_{mn}}^{\pm} x}\right\} \tag{5.2}$$

Subscript $m \in \ldots, -2, -1, 0, 1, 2, \ldots$ refers to the azimuthal order of the mode, this is, the number of wavelenghts of the 'lobed' distribution in the circumferential direction. In a compressor without stator blades it is expected that the main orders are those of $m = hn_b$ with $h \in 1, 2, \ldots$ and n_b being the number of rotor blades, this is, those corresponding to the Blade Passing Frequency (BPF) and its harmonics.

On the other hand, subscript $n \in 0, 1, 2, \ldots$ refers to the radial order, this is, the number of zeros across the radius. Alternatively, m and n can be seen, respectively, as the number of nodal lines and nodal circles within a cross-section, with the special case $(m, n) = (0, 0)$ representing a plane wave.

Inspecting Eq. 5.2, $A_{mn}^{\pm}$ is seen to represent the unknown amplitude of each (m, n) mode in both positive and negative axial propagation direction. J_m is the Bessel function of the first kind and order m, whereas κ_{mn}, the radial wavenumber, satisfies the imposed boundary condition of an acoustic hard wall at the outer radius $r = R$ by requiring the first derivative of the Bessel function $J'_m(\kappa_{mn})$ to be zero. An illustrative visual example of this requirement in connection with the (m, n) order of the modal shapes can be found in Figs. 2 and 3 of Eriksson's 1980 paper [42].

Whereas the first two exponential terms $e^{im\theta}$ and $e^{-i\omega t}$ in eq. 5.2 are easily understood as related to the azimuthal 'lobed' structure of the mode and the driving frequency $\omega = 2\pi f$ of the mode spinning, it is important to carefully consider the axial wavenumber found in the last exponential term, as it is related to the propagation of the signal along the duct:

$$k_{x_{mn}}^{\pm} = \frac{k}{1 - M_0^2}\left(-M_0 \pm \sqrt{1 - (1 - M_0^2)\left(\frac{\kappa_{mn}}{kR}\right)^2}\right) \tag{5.3}$$

Here, $k = \omega/c_0$ is the acoustic wavenumber, with c_0 being the speed of sound, and the $\pm$ superscript again indicating that a certain mode can propagate in either axial direction with a corresponding $A^{\pm}_{mn}$ amplitude. Analyzing this expression, one can identify a specific 'cut-off' frequency at which the argument of the square root becomes zero:

$$f^{co}_{mn} = \kappa_{mn} \frac{c_0}{2\pi R} \sqrt{1 - M_0^2} \tag{5.4}$$

Taking into account the role of $k^{\pm}_{mn}$ in Eq. 5.2, it can be seen that for a driving frequency $f < f^{co}_{mn}$, the downstream propagation term $\mathrm{Re}\{e^{ik^{+}_{x_{mn}} x}\}$ has a decaying component $e^{-\mathrm{Im}\{k^{+}_{x_{mn}}\}x}$, and thus mode (m, n) is said to be 'cut-off', damped, or evanescent, since it will vanish at a certain distance from the source.

On the other hand, for values of the driving frequency $f > f^{co}_{mn}$ the mode is 'cut-on', as the real part of the downstream propagation term in Eq. 5.2 takes oscillatory values $\cos\left(k^{+}_{x_{mn}} x\right)$ and thus the mode propagates unattenuated. A visual representation of the physical meaning of the cut-off criterion can be found in Fig. 2 of Morfey's 1964 paper [80].

An example of the pressure distribution of a Tyler–Sofrin mode is given in Fig. 5.2, where mode $(6, 1)$ according to Eqs. 5.2 and 5.3 is represented. The rest of the parameters have been arbitrarily chosen so that $f > f^{co}_{6,1}$ and thus the mode propagates along the duct. The physical meaning of the cross-section pressure pattern in relation to the aerodynamic loading of the compressor blades is apparent.

Thus, in order to find the unknown modal amplitudes $A^{\pm}_{mn}$, one can either conduct experimental measurements or numerical simulations of $p(t)$ at different locations and then perform a least-squares fitting following the procedure recommended by Moore [95]. In his experimental rig, a single microphone

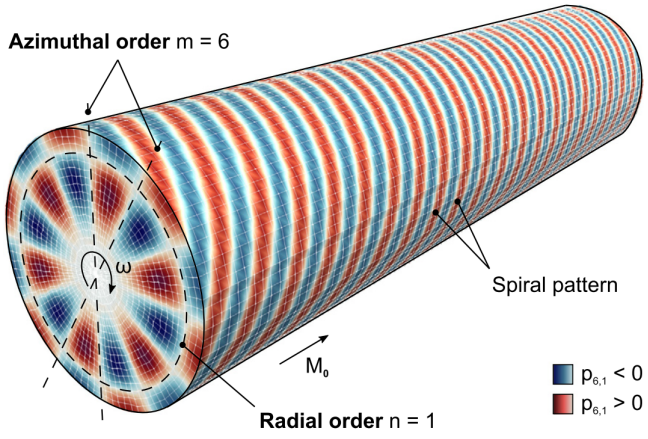

Figure 5.2: *Example of the Tyler–Sofrin mode* $(6, 1)$ *numerically evaluated with arbitrary values chosen so that* $f > f^{co}_{6,1}$

was motorized so it could reach different radial and circumferential positions at the measurement plane.

Later, authors such as Raitor & Neise [26] implemented these techniques in the experimental characterization of centrifugal fans and turbocompressors. Most recently, Limacher, Banica et al. investigated the sound field of centrifugal turbochargers through the least-square fitting of select blade passing frequencies to Tyler–Sofrin modes from both numerical [96] and experimental [97] points of view.

While these works successfully demonstrate that the pressure distribution of the expected Tyler–Sofrin modes $(hn_b, 0)$ is found in the measurement sections for the frequency corresponding to the BPF tone and its harmonics, this approach is not without drawbacks, especially in centrifugal compressors.

Besides the restriction of the shape of the modes themselves, which must adhere to Eq. 5.2, several assumptions are used. Excitation is introduced in an 'actuator disk' manner, and then equally propagated up and downstream. Especially the latter is questionable in centrifugal compressors, in which the outlet, contrary to the inlet, does not directly 'see' the rotating blade pressure distribution as the perturbations must first travel through the complex flow in the volute.

Furthermore, while uniform, unidirectional flow is assumed, it is known that between the onset of the marginal surge conditions to the deep surge limit, recirculating backflow at high temperature is present in the inlet section [41]. Also, while evanescent modes may not fully propagate beyond a short distance, both these local phenomena near the compressor may induce vibroacoustic excitation on the pipes, often made of rigid plastic materials to save weight and cost, and thus still radiate noise.

It can be seen in the aforementioned studies [26, 96, 97] that when noise phenomena other than BPF harmonic tones are decomposed in this way, a large number of mode orders become excited, this is, a large sum along the m and n orders is required in order to explain the observed pressure pattern at the measured cross-section.

A large sum of modes with similar amplitudes $A^{\pm}_{mn}$ makes difficult to understand the spatial distribution of the phenomenon, indicating that the actual pressure pattern is not particularly similar to any specific mode. Thereby, it is possible that the Taylor–Sofrin analytical model may not be the optimum decomposition in these particular situations.

5.2.3 Dynamic Mode Decomposition

A very different alternative to the analytical solution lies in the use of *data-driven* numerical decompositions, such as the classical Proper Orthogonal Decomposition (POD) [21] which was pioneered by Lumley in 1967 for detection of spatial coherent patterns in turbulent flows [98] and has since been used widely in aeronautical research [99, 100, 101, 102, 103].

A recent alternative, better suited for the identification of acoustic phenomena at particular frequencies, is the Dynamic Mode Decomposition (DMD)

[104], a technique which aims to group coherent spatial features into modes of a single temporal frequency [105, 106]. It has been used in recent investigations of, for instance, cavity flow [107], airfoil buffeting [108], fan [109] combustion [110, 111] and landing gear [112] noise, and turbocharger acoustics [68, 48], among others.

This decomposition method is based in estimating the eigenmodes and eigenvectors associated to the Koopman operator of a given system, an infinite-dimensional but linear operator which is used to describe the dynamics of finite-dimensional but non-linear systems [113]. DMD eigenvalues obtained in this way contain a single frequency, together with the growth or decay rates associated to their associated mode. This allows the identification of transient modes that may be short-lived or low-energetic in nature but still coherent [114].

In general, the evolution of a field such as in this case the pressure field $p(r, \theta, x, t)$ can be described by a temporal sequence $\mathbf{V}_1^N$ of vectors $\mathbf{v}_t(\mathbf{x})$, each one containing the pressure data at a certain spatial position $\mathbf{x} = \{r, \theta, x\}$ and at a certain discrete time step $t \in 1, 2, \ldots, N$:

$$\mathbf{V}_1^N = \{\mathbf{v}_1, \mathbf{v}_2, \ldots, \mathbf{v}_N\} \tag{5.5}$$

This representation fits naturally flow field characterizations offered by experimental techniques such as Particle Image Velocimetry (PIV), as well as those obtained through Computer Fluid-Dynamics (CFD) simulations. In both cases data is obtained as several 'snapshots' of the flow variables (velocity, pressure, density, species, etc.), that could be put intuitively in column vector form, and then assembled in a matrix $\mathbf{V}$ describing the overall evolution of the selected variable.

By following the original procedure introduced by Schmid [104], DMD can be applied to the snapshot matrix $\mathbf{V}_1^N$ of Eq. 5.5. If we assume that the snapshots $\mathbf{v}_i$ which conform the matrix are linearly related by an unknown matrix $\mathbf{A}$:

$$\mathbf{v}_{i+1} = \mathbf{A}\mathbf{v}_i \tag{5.6}$$

Then the eigenvalues and eigenvectors of this matrix will characterize the evolution of the flow. Even if the system is non-linear, this will provide a linear tangent approximation of the flow evolution. We can combine Eqs. 5.5 and 5.6 to write:

$$\mathbf{V}_2^N = \mathbf{A}\mathbf{V}_1^{N-1} \tag{5.7}$$

While some authors solve this eigensystem by QR decomposition of the associated companion matrix [115, 105, 116], a more robust alternative makes use of the Singular Value Decomposition (SVD) $\mathbf{V}_1^{N-1} = \mathbf{U}\mathbf{\Sigma}\mathbf{W}^{\mathrm{T}}$ [104, 117, 118, 106]. Plugging the SVD decomposition into Eq. 5.7 we obtain:

$$\mathbf{V}_2^N = \mathbf{A}\mathbf{U}\mathbf{\Sigma}\mathbf{W}^{\mathrm{T}} \tag{5.8}$$

5.2. Flow field modal decomposition

We now build a matrix $\widetilde{\mathbf{S}}$, which is defined exclusively in terms of known matrices but is constructed in a way that ensures *matrix similarity* with $\mathbf{A}$:

$$\widetilde{\mathbf{S}} \triangleq \mathbf{U}^{\mathrm{T}}\mathbf{V}_2^N\mathbf{W}\mathbf{\Sigma}^{-1} = \mathbf{U}^{\mathrm{T}}\mathbf{A}\mathbf{U} \tag{5.9}$$

As a consequence of this similarity, the eigenvalues λ_i of the reduced-size $\widetilde{\mathbf{S}}$ match those of the larger $\mathbf{A}$, with the DMD modal shapes being computed by mapping the eigenvector matrix $\mathbf{Y}$ of $\widetilde{\mathbf{S}}$ into the non-reduced space through $\mathbf{U}$, which we can recognize as being the POD basis of $\mathbf{V}_1^{N-1}$:

$$\mathbf{\Phi} = \mathbf{U}\,\mathbf{Y} \tag{5.10}$$

However, since many numerical routines normalize the resulting eigenvectors, it is necessary to recover the modal amplitudes α_i, which we can intuitively do by solving the reconstructed flow field multiplied by the unknown amplitudes against, for instance, the first snapshot of the flow [119]:

$$\mathbf{V}_1 = \mathbf{\Phi}\,\boldsymbol{\alpha} \implies \boldsymbol{\alpha} = \mathbf{\Phi}^{-1}\,\mathbf{V}_1 = \mathbf{Y}^{-1}\,\mathbf{U}^{*}\,\mathbf{V}_1 \tag{5.11}$$

Where we have taken advantage of the fact that $\mathbf{U}$ is unitary and thus its conjugate transpose $\mathbf{U}^*$ is also its inverse, in order to solve the system by inverting $\mathbf{Y}$ instead of the higher order $\mathbf{\Phi}$. Now, the full evolution of the flow described by the snapshot matrix at discrete time steps t_k, can be reconstructed by the linear superposition of the DMD modes:

$$\mathbf{V}(\mathbf{x}, t_k) = \mathrm{Re}\left\{\sum_{i=1}^{N-1} \mathbf{\Phi}_i(\mathbf{x})\,\alpha_i\,\lambda_i^{k-1}\right\} = \mathrm{Re}\left\{\mathbf{\Phi}\,\mathbf{D}_{\mathbf{iag}}(\boldsymbol{\alpha})\,\mathbf{V}_{\mathbf{and}}(\boldsymbol{\lambda})\right\} \tag{5.12}$$

Here, $\mathbf{D}_{\mathbf{iag}}(\boldsymbol{\alpha})$ is the diagonal matrix of modal amplitudes and $\mathbf{V}_{\mathbf{and}}(\boldsymbol{\lambda})$ is the Vandermonde matrix of the eigenvalues. Furthermore, from the eigenvalues we can recover the single frequency associated to each mode, by taking into account the time step Δt between each consecutive snapshot:

$$f_i = \frac{\omega_i}{2\pi} = \frac{\mathrm{Im}\{\ln(\lambda_i)\}}{2\pi\Delta t} \tag{5.13}$$

Finally, the computed modes need to be ranked in importance. While the most direct approach consists in computing the energy of the eigenvectors augmented by the amplitude coefficients [119], Kou & Zhang [120] have recently proposed a simple criterion which integrates the influence of each dynamic mode on the whole sampling space:

$$E_i = \sum_{j=1}^{N} \left|\alpha_i\,\lambda_i^{j-1}\right| \,\|\mathbf{\Phi}_i\|_F^2\;\Delta t \tag{5.14}$$

5.2.4 Implementation

In this thesis, the DMD will be used to analyze the frequency content of the pressure field inside the compressors. This tool provides valuable information

about coherent flow structures at the same frequency, which can be easily related to the components of the experimental spectrum. On the other hand, it is not the ideal tool for identifying broadbands in the spectrum since the time evolution of the modes is harmonic (at a single frequency). This limitation, however, does not preclude the identification of different modes within the broadbands, coherent in space, as will be seen in the following sections.

The DMD code was developed by the author in collaboration with Dr. Jorge García-Tíscar. For the DMD calculation, a random sample of 10^6 probes located in the center of the grid cells was used in compressor c1. The DMD requires that the spatial coordinates of the probes used are constant. Therefore, the sample was taken over the entire computational domain except for the volume swept by the impeller blades. Since the cell density is not uniform throughout the domain, the sample will have more probes in the regions of smaller cell sizes. No probes were taken within the prism layer, where the mesh has the maximum cell density, to help reduce the bias.

A snapshot (x, y, z and pressure in each probe) was stored every 7 time steps. The sampling frequency is, therefore, 68.7 kHz. Taking into account the Nyquist criterion, the maximum available frequency is 34.35 kHz, so the 2×BPF of approximately 32 kHz is included. For this compressor, 3440 snapshots were stored, covering a time interval of 50 ms and yielding a lower frequency limit of 20 Hz.

For compressor c2, a sample of 1.3×10^6 probes was selected over the entire domain, excluding again the volume swept by the impeller blades and the prism layer. A snapshot was stored every 7 time steps, yielding a sampling frequency of 60 kHz. Taking into account the Nyquist criterion, the upper frequency limit of 30 kHz contains the 2×BPF, which is at 28 kHz. A total of 1502 snapshots were stored, covering a signal duration of 25 ms and thus a lower frequency limit of 40 Hz.

One way to measure the DMD quality is to check that the eigenvalues λ_i lay in the unit circle when plotted in the complex plane.

In figures 5.3 and 5.4 almost all the eigenvalues are shown to lay in the unit circle, including the ten most relevant modes. Furthermore, all such modes lay in the upper semi-circumference, as only positive frequencies were considered for such modes.

Another way to assess whether a sufficient number of snapshots have been used in the DMD is to check that the residuals divided by the number of snapshots converge to a finite value [23].

These residuals are defined in [119] as the maximum difference between the snapshot matrix reconstructed by the modes and the original snapshot matrix.

$$\Delta = \mathrm{Re}\left\{\mathbf{\Phi}\,\mathbf{D_{iag}}(\boldsymbol{\alpha})\,\mathbf{V_{and}}(\boldsymbol{\lambda})\right\} - \mathbf{V}_1^{N-1} \tag{5.15}$$

$$r = max|\delta_{i,j}| \tag{5.16}$$

where $\delta_{i,j}$ are the coefficients of matrix Δ.

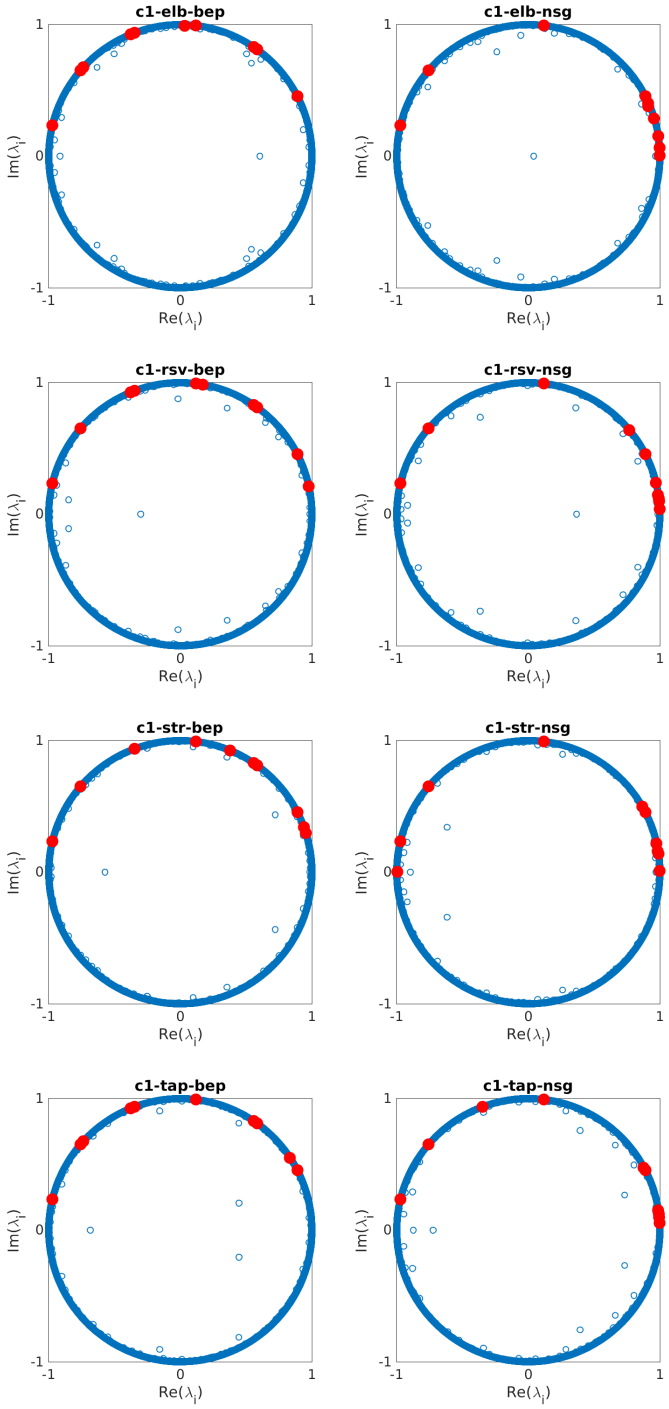

Figure 5.3: *Complex plane representation of the DMD eigenvalues for all cases of compressor c1. The red dots signal the ten most relevant modes.*

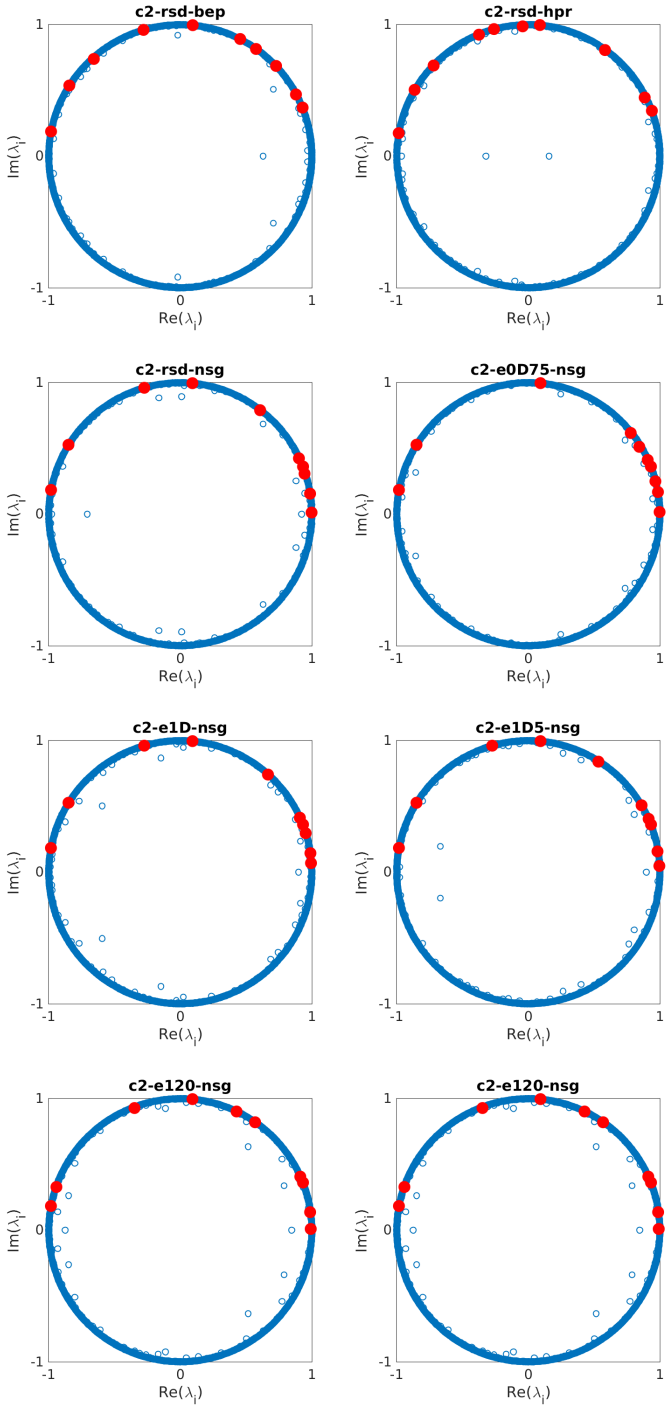

Figure 5.4: *Complex plane representation of the DMD eigenvalues for all cases of compressor c2. The red dots signal the ten most relevant modes.*

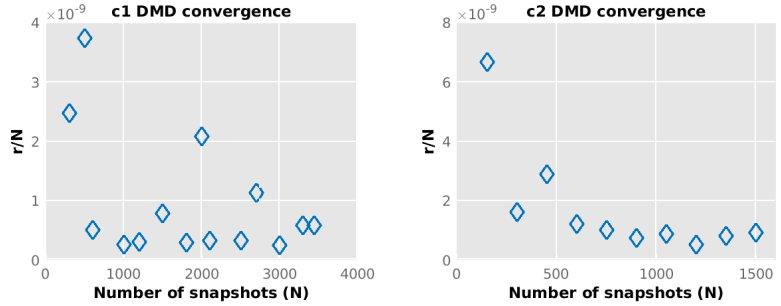

Figure 5.5: *DMD residuals divided by the number of snapshots of case c1 str nsg (left) and c2 rsd nsg (right). Both residuals converge for the number of snapshots used in each compressor.*

The test results for the two compressors is shown in Figure 5.5. In both cases, it is observed that the residuals converge for the number of snapshots used.

Since the DMD modes will be compared to in-duct pressure measurements, the transient or evanescent modes are not of interest for the task of identifying the most energetic and thus relevant modes. Therefore, the Kou & Zhang criterion (Equation 5.14) is selected to rank the DMD modes.

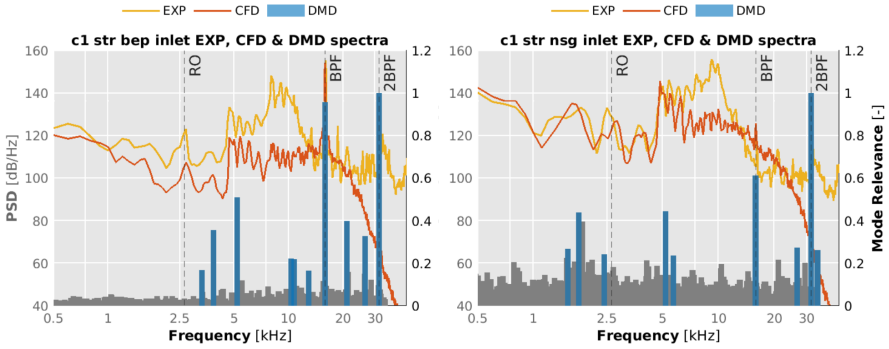

Figure 5.6: *Experimental and CFD PSD in the inlet duct vs. DMD mode relevance metric E_i. The 10 most relevant and prominent modes are highlighted in blue over the complete DMD spectra depicted in gray.*

Figure 5.6 shows the PSD spectra of the experimental and CFD inlet duct pressure signals and the normalized relevance of the DMD modes E_i. All the DMD modes (as many as snapshots) are displayed in gray, and the ten most relevant modes are shown in blue. The selection has been made not only by the magnitude of the E_i metric but also by its prominence, i.e., how much a mode stands out compared to the other nearby modes.

The shown cases: c1 str bep and nsg are paradigmatic of both operating points. At the best efficiency point (bep), the most prominent modes stand

out clearly against a low-magnitude background. The modes of the cases operating near surge (nsg) have a higher average magnitude. Thus, some selected modes stand out less clearly or have even lower E_i than some unselected modes. The followed criterion ensures that the most diverse possible modes are studied with an easily programmable selection method. In addition, the frequency bands of greatest interest in the DMD spectrum are well represented by the selected modes.

Some interesting conclusions can be drawn from the presented spectra. First, the highest amplitude frequencies of the PSD spectra do not always correspond to the most relevant DMD modes. That may happen because the relevance of the modes is a measure of the frequency coherence of all points in space, while the spectra are a local measure of pressure. Secondly, mode 2×BPF is the most prominent, although, in that frequency range, it is clear that the CFD model introduces an artificial frequency attenuation due to the mesh size in the ducts. This indicates that modes can be identified at their origin without the computational cost of propagating them to the experimental probe locations in the ducts

The following sections will show the DMD spectra of all cases. For clarity, only the ten most relevant modes of each case are shown. The absence of modes at particular frequencies does not necessarily mean that there is no relevant content but that it has less prominence than the selected modes. Conversely, the presence of prominent "nearby" modes, such as the three lowest frequency modes in the right image of Figure 5.6, may indicate that discrete frequencies represent a broadband. The spatial coherence of the nearby modes can confirm whether they are compatible phenomena.

5.2.5 Visualization of the DMD modes

Before concluding the section devoted to the description of the dynamic modal decomposition, it is worthwhile to dwell on the discussion of the graphical representation of the modes.

Some aspects of the DMD development presented in the previous sections will be summarized to highlight the information contained in the modes ($\mathbf{\Phi_i}$). The DMD allows expressing the time evolution of the pressure at any point in the probe cloud as a sum of modes:

$$p(x, y, z, t) = \sum_i p_i(x, y, z, t) \tag{5.17}$$

where modal pressures p_i follow the expression

$$p_i(x, y, z, t) = \alpha_i \, \mathbf{\Phi_i}(x, y, z) \, e^{j\omega_i t} \tag{5.18}$$

where α_i is the modal magnitude, and has pressure units (Pa). $\mathbf{\Phi_i}$ is a complex-valued function, representing the space distribution of mode i. The harmonic time evolution at the modal angular frequency ω_i is expressed by $e^{j\omega_i t}$, given by the eigenvalue λ_i, which, as seen in figures 5.3 and 5.4, is a

complex number with a unitary modulus. At any probe k (x_k, y_k, z_k) the value of $\mathbf{\Phi_i}$ is

$$\mathbf{\Phi_i}_{,k} = \mathbf{\Phi_i}(x_k, y_k, z_k) = \phi_{i,k}\, e^{j\xi_{i,k}} \tag{5.19}$$

i.e., a complex number with modulus $\phi_{i,k}$ and argument $\xi_{i,k}$. Thus, the expression of the pressure due to mode i at the probe k has the form

$$p_{i,k}(t) = Re\{\, \alpha_i\, \phi_{i,k}\, e^{j(\omega_i\, t + \xi_{i,k})}\, \} = \alpha_i\, \phi_{i,k}\, cos(\omega_i\, t + \xi_{i,k}) \tag{5.20}$$

Computationally, the function $\mathbf{\Phi_i}(x, y, z)$ is represented by a complex vector with one element for each probe. This vector has a unitary norm and describes the relative weight of each probe in the mode through their modulus $\phi_{i,k}$. The argument $\xi_{i,k}$ indicates the initial phase of each probe k. Figure 5.7 shows one such vector as an example. The cloud of normalized, dimensionless complex numbers rotates around the origin with the angular frequency ω_i of mode i.

The highest amplitude indicates the region where the oscillation is generated, and the phase shows the spatial distribution of the mode. To visualize this information, the regions with the highest amplitude percentiles can be shown, as well as volumes containing points in phase or within a range of phases.

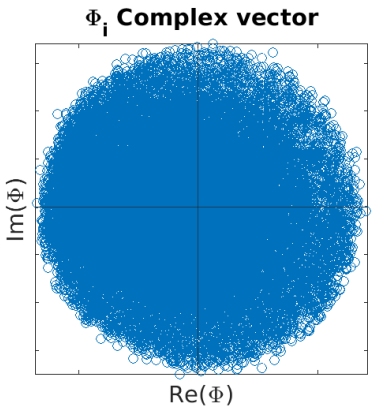

Figure 5.7: *Complex plane representation of a generic DMD mode* $\mathbf{\Phi_i}$*. Each dot shows the relative amplitude and initial phase of one pressure probe. The point cloud rotates around the origin with angular frequency* ω_i*.*

In figures 5.8, 5.9 and 5.10, the BPF mode of c1 str bep is used to demonstrate the information each type of graph provides. It can be seen that snapshots of a combination of amplitude and phase often provide this information in a very compact form.

Figure 5.8 shows in green the volume occupied by the 10% of points with the highest amplitude of the BPF mode of one case of compressor c1. That information is independent of the chosen instant.

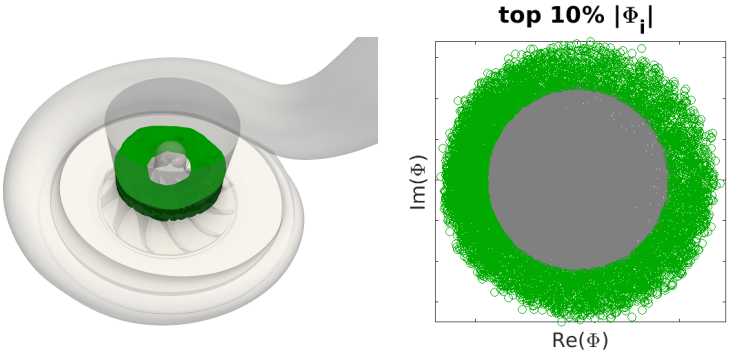

Figure 5.8: *Maximum amplitude representation. The 10% of the probes with maximum relative modal amplitude are signaled in green in the right figure. In the left, the physical location of those probes is represented by the green region.*

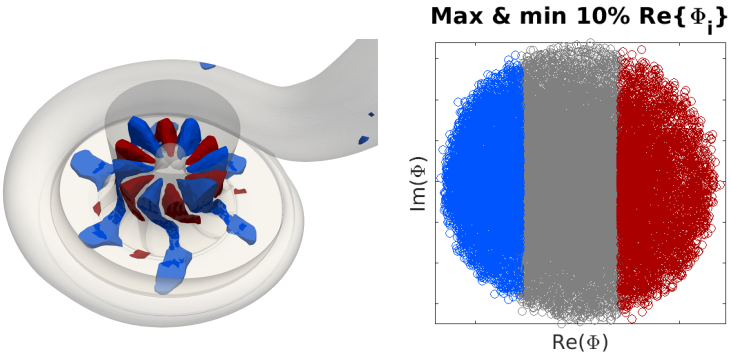

Figure 5.9: *Modal shape representation. The 10% probes with maximum and minimum real part are signaled in red and blue in the right figure, they are in phase opposition and show the mode shape. In the left, the physical location of those probes is represented by the red and blue regions.*

Figure 5.9 shows the points of the maximum (red) and minimum (blue) 10% of the real part. This figure shows information valid for the initial instant when the point cloud's rotation angle is 0°. However, this image gives an idea of the shape (phase) of the mode in the region of greatest amplitude. The blue circles are clustered around the −180° phase, while the red ones have a phase "close" to 0°. The pattern formed by the red and blue regions is easily recognized as the pressure increase due to the blade's leading edge and the pressure decrease due to the blade's wake. In addition, the blue region extends through the tip clearance until it reaches the diffuser, where six low-pressure stripes are formed, consistent with the trailing edge jets.

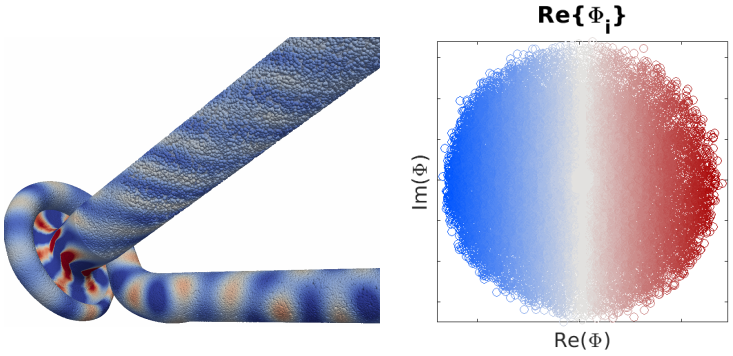

Figure 5.10: *Mode propagation representation. The real part of every probe is colored in the blue-to-red range. The points of the same color (blue or red) are in a close phase, while the color intensity (bright to dim) signals the amplitude. In the left, the physical location of the probes is represented. The alternating patterns in the ducts show the mode propagation.*

Figure 5.10 shows the outer surface colored according to the real part of the mode at the initial instant (0° angle). This image provides information on the phase through the color (red, centered at 0°, blue centered at −180°) and on the amplitude through the color intensity: brighter colors have the highest amplitude, and whiter colors have a lower amplitude. This graph compactly provides information about the shape of the mode and its amplitude over the whole domain, although it is a snapshot (0° angle).

In the following sections, these types of figures will be used for illustrating the characteristics of each mode. Green color will be used for the highest amplitude region, blue and red for phase points near −180° and 0°, respectively. It is worth noting again that these plots show normalized and dimensionless modes. The instantaneous pressure values could be obtained directly by projecting the complex numbers onto the real axis and multiplying by the modal magnitude α_i.

5.3 Spectral and modal analysis

In this section the experimental spectra and the DMD modes associated with the most relevant spectral components are analyzed. For this purpose, the geometries studied are divided into four groups:

- c1 bep {elb, rsv, str, tap}
- c1 nsg {elb, rsv, str, tap}
- c2 rsd {bep, hpr, nsg}
- c2 nsg {rsd, e0D75, e1D, e1D5}

Note that all groups are composed of different geometries in a constant operating point except group c2 rsd, where the geometry is the same and the operating points are changed. The c1 rsd cases were used to test the numerical setup but are not considered in this analysis.

With the division of the four groups mentioned above, the influence of the inlet geometry and the operating point will be studied. The dominant components of the spectra will also be identified. Then it will be identified which of the main components of the experimental spectra are captured by the DMD modes. Finally, the spatial characteristics of the most relevant modes will be described in detail.

The following sections extensively use acronyms referring to CFD cases and compressor parts. In table 5.1 abbreviations for compressor parts and spectral features are presented as a reminder. At the beginning of every subsection, the nomenclature of the compressor geometry and operating points analyzed is recalled as well.

Compressor parts		Spectral features	
LE	Leading Edge	RO	Rotating Order
TE	Trailing Edge	PW	Plane Wave
TC	Tip Clearance	TCN	Tip Clearance Noise
VT	Volute Tongue	BPF	Blade Passing Frequency

Table 5.1: *Reminder abbreviations for compressor parts and spectral features.*

All the spectra presented in this section have certain auxiliary elements in common. The frequencies of the rotating order (RO), blade passing frequency (BPF), and 2×BPF are marked in dashed lines. The remainder multiples of the RO are marked in solid black lines. In addition, the cut-on frequency of the mode (1,0) of the ducts is marked as f_{PW} because it is the upper limit of the range where only the plane wave mode (PW) propagates. Its mathematical expression is found in equation 5.21, proposed by Eriksson [42] for the specific values of wavenumber $\kappa_{1,0}$ from equation 5.4.

$$f_{PW} = f_{1,0}^{co} = 1.84 \frac{c_0}{2\pi R} \sqrt{1 - M_0^2} \tag{5.21}$$

In addition to the discrete frequencies, red, green, and blue shading signal the broad bands of interest in the experimental spectra. The right Y-axis shows the normalized mode metric (E_i) of the DMD modes, which are represented by bars of the same color as the corresponding measured spectra.

5.3.1 c1 bep

Table 5.2 shows the nomenclature of the cases analyzed in this sub-section.

Name	Compressor	Inlet geometry	Operating point
c1 elb bep	c1	Elbow	Best efficiency point
c1 rsv bep	c1	Reservoir	Best efficiency point
c1 str bep	c1	Straight duct	Best efficiency point
c1 tap bep	c1	Tapered duct	Best efficiency point

Table 5.2: *Reminder of abbreviations for c1 bep cases.*

Figure 5.11 shows the spectra of the c1 bep cases in the inlet duct. All four geometries present spectra with almost identical shapes. The main components are two broadbands, marked in red and green, a tone at the RO, a high-frequency broadband marked in blue, and the BPF tone. The broadband marked in green corresponds to the *whoosh* noise reports in the literature (see Figure 2.2 of reference [27]). The most relevant components in terms of amplitude are the high-frequency blue band and the BPF tone, although the green band and the RO tone appear in the maximum human hearing range (from 1 to 10 kHz).

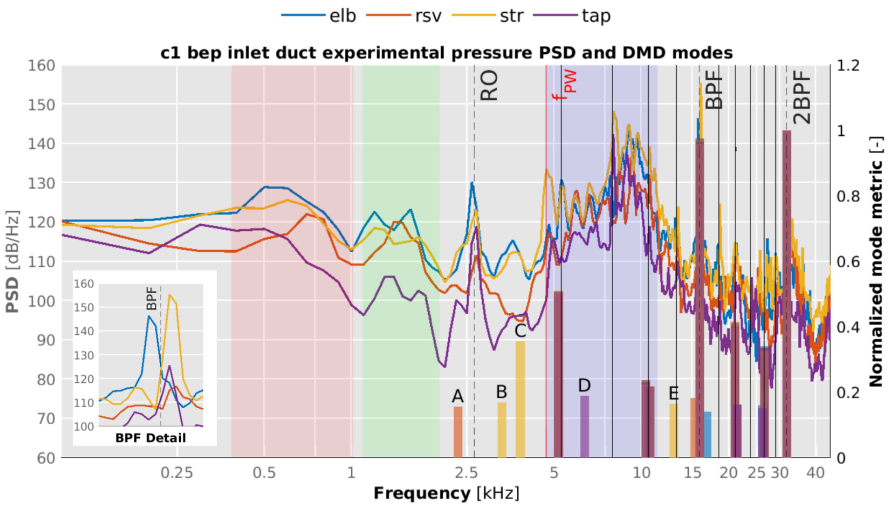

Figure 5.11: *DMD and experimental inlet duct spectra for compressor c1 operating at bep. Solid black lines signal multiples of the RO. f_{PW} is the plane wave limit. Red, green and blue bands signal broadbands of interest.*

As for differences due to geometry, in the BPF tone, as seen in the detail, the str geometry has the highest amplitude, followed closely by elb. More than 20 dB below, tap appears, and finally rsv, with a minimal prominence. In the RO tone, the rsv case remains the one with the lowest amplitude. The purple line corresponding to the tap case has the lowest amplitude in almost the entire frequency range. The BPF and RO tones mentioned above are notable exceptions.

Since all geometries present the same components, although with some

differences in amplitude, it can be concluded that the effect of these geometries is not to excite different aeroacoustic sources in the compressor but to attenuate to a greater or lesser degree the sound generated downstream.

In particular, the tap geometry seems to transmit worse at all frequencies except tones, where the rsv geometry has the lowest amplitude. The difference in the frequency of the BPF tones seen in the figure is due to minor ($< 1\%$) differences in regime of the measured operating point.

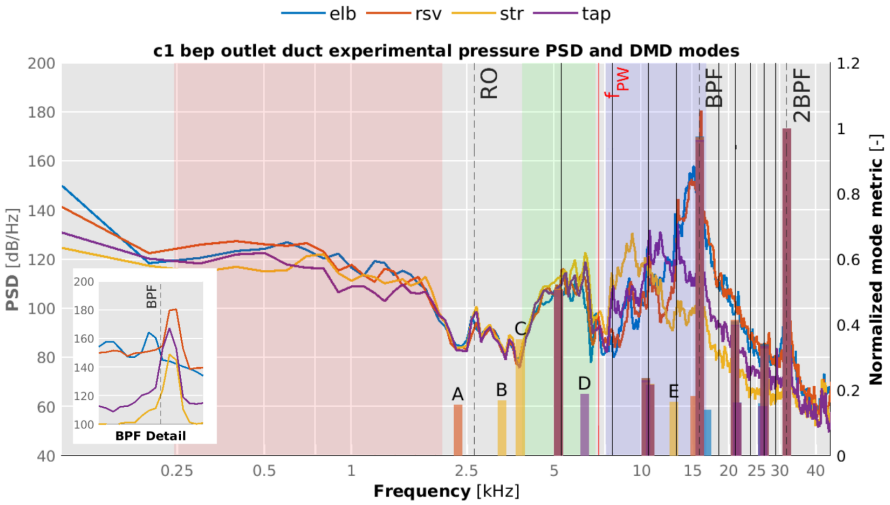

Figure 5.12: *DMD and experimental outlet duct spectra for compressor c1 operating at bep. Solid black lines signal multiples of the RO. f_{PW} is the plane wave limit. Red, green and blue bands signal broadbands of interest.*

In the outlet duct, shown in figure 5.12, the common features of the spectra are two broadbands in the plane wave range (red and green, although the latter now appears above the RO), a high-frequency broadband in blue, and the BPF tone. In this case, the plane wave limit is higher due to the smaller diameter and higher temperature of the outlet duct. The blue broadband seen at the inlet appears to be cut by the f_{PW} into two distinct parts, below (green) and above (blue) the plane wave limit. The RO tone has lost the relevance it had in the inlet duct.

The most obvious difference among geometries in this case, is that the high-frequency broadbands (blue) have a different bias for each case. The str case has in this band its maximum amplitude near the plane wave frequency f_{PW}. The elb and rsv cases have the maximum amplitude interval adjacent to the BPF tone (as seen in the detail) and about 25 dB above the other two cases. The tap case has its maximum amplitude between the abovementioned extremes and a magnitude similar to str. An interesting detail is that the rsv case, at the inlet, presented minimum values in the RO and BPF tones (the latter below 120 dB). At the outlet it has the maximum amplitude of all BPF tones with 160 dB. This shows that the tone is indeed present in

that pressure field, but the inlet geometry (the reservoir) is responsible for its reduced amplitude at the inlet spectrum.

The DMD spectrum is shown in both figures to observe the correlation with both ducts measured spectra. Several modes appear in brown, indicating that modes of all four geometries appear superimposed at these frequencies. They will be called the common modes. They appear at every even multiple of the RO. The 2×BPF mode has the highest metric, followed by BPF and 2×RO. The 2×BPF mode in all cases of all compressors has the highest metric, although, in most measured spectra, it either does not stand out or has a second-order amplitude. Moreover, it is always above the threshold of human hearing. However, in this thesis, its characteristics will be analyzed given that for 6-blade compressors, this mode will be audible at speeds below 100 krpm.

The modes appearing alone, i.e., without modes of other cases at the same frequency, will be called isolated modes. In figures 5.11 and 5.12, they are marked with the letters A to E. Some of them are interesting for different reasons. Mode C of the str case corresponds in the inlet to a narrow band where the elb and str cases have higher amplitude than rsv and tap. Mode D appears under the high-frequency broadband and is not a multiple of the RO. In this thesis, the DMD modes at frequencies multiples of the RO (including BPF and 2×BPF) will be called "synchronous", and the others, "asynchronous". Mode D (as well as A, B, and C) is, therefore, an asynchronous mode.

The modes of the c1 bep {elb, rsv, str, tap} cases are analyzed in the following. The plots described in section 5.2.5 will be used to identify the origin of the oscillations (10% points with the highest amplitude, in green), the spatial distribution of the mode (10% maximum and minimum real part of the mode, in blue and red respectively) and their propagation through the ducts (coloring the real part of all probes gradually from blue to red).

Synchronous modes

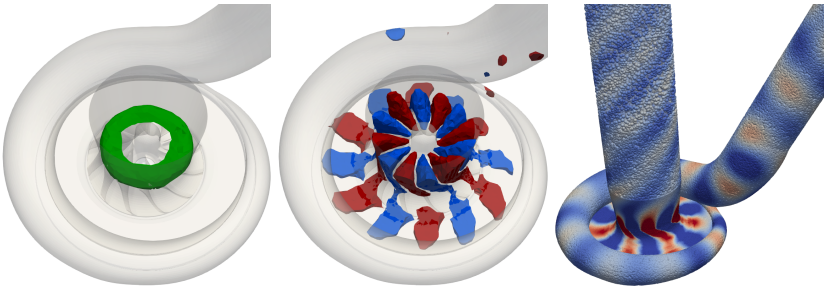

Figure 5.13: *Maximum amplitude, modal shape and propagation of the BPF mode of c1 str bep. The mode is the same in all four geometries.*

Figure 5.13 shows the BPF mode. This mode is identic in all geometries. The zone of maximum amplitude is on the impeller leading edge from the middle of

the blade radius to the tip. The mode has six red and six blue wedge-shaped lobes on the LE, with greater height above the LE tip and lower near the hub. In the diffuser, six other lobes of each color connect with the previous ones through the tip clearance.

The right image shows that the mode propagates through the inlet duct following a helical pattern similar to the analytical modes in Figure 5.2. The mode propagates in the volute and the outlet duct, following a more irregular pattern. The right image shows the highest amplitude of the mode in the LE tip, followed by the TC and the diffuser. The outlet duct shows greater amplitude (more intense colors) than the inlet duct.

To understand the temporal evolution of the mode, the spatial and temporal periodicities are considered. The BPF mode (central image) has symmetry around the impeller axis. In the circumferential direction, 6 lobes of each color appear. After half a period of oscillation ($T_{BPF}/2$), the blue lobes will occupy the position of the red lobes, which are in phase opposition. After one full period, the blue lobes will occupy the position of the next blue lobe. Since there are 6 lobes, the angular displacement will be $\Delta\theta = 1/6\, rev$. Since the mode frequency is BPF = 6×RO, the period will be $\Delta t = T_{BPF} = 1/6\, T_{RO}$. The angular velocity of the lobes will therefore be $\Omega_{BPF} = \Delta\theta/\Delta t = 1\, rev/T_{RO} = \Omega_{RO}$. For all the axisymmetric modes the following general equation holds:

$$\Omega_i = \frac{\Delta\theta}{\Delta t} = \frac{\frac{1}{N_{lobes}}\, rev}{\frac{f_{RO}}{f_i}\, T_{RO}} = \frac{f_i/f_{RO}}{N_{lobes}}\, \Omega_{RO} \tag{5.22}$$

In this way, the BPF mode moves in unison with the impeller, and its distribution is easily identified with the pattern of high and low pressures accompanying the impeller blades: high pressure on the blade pressure side and low pressure on the suction side. In the diffuser, a jet and wake pattern is formed with respectively low and high pressure.

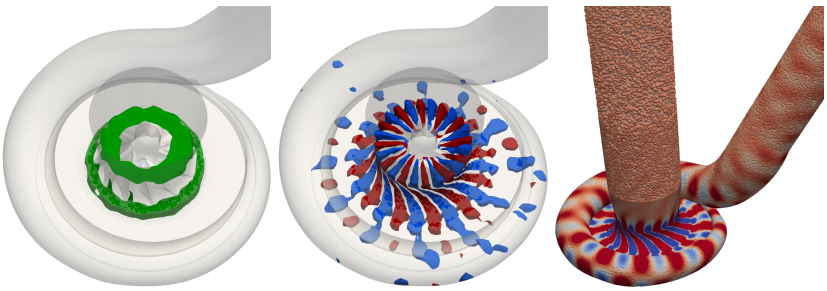

Figure 5.14: *Maximum amplitude, modal shape and propagation of the 2×BPF mode of c1 str bep. The mode is the same in all four geometries.*

Figure 5.14 shows the 2×BPF mode. Again, this mode is identical in all

geometries of this group. The highest amplitude zones of the mode are located at the impeller LE and TE. The spatial pattern is the same as in the BPF mode but with twice the spatial periodicity: 12 lobes of each color. Since the frequency, 2×BPF is 12×RO, and there are 12 lobes, the angular velocity of the mode is, again, equal to the rotational speed of the impeller. The right image shows how the mode propagates through the scroll in an alternating pattern that becomes irregular as it reaches the outlet duct. In the inlet duct, the shape of the mode is not distinguishable, indicating that it has a very low amplitude.

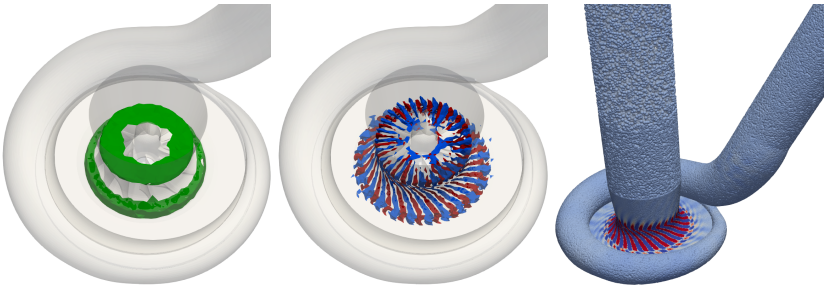

Figure 5.15: *Maximum amplitude, modal shape and propagation of the 2×RO mode of c1 str bep. The mode is the same in all four geometries.*

The 2×RO mode is shown in Figure 5.15. It can be seen that it is very similar to the 2×BPF mode. It has its maximum amplitude at the impeller LE and TE. It features 24 lobes, which, together with its frequency of 2×RO, gives an angular velocity of $1/12\,\Omega_{RO}$. The mode does not propagate through the ducts.

Figure 5.16 shows modes 4, 8, and 10×RO. They all have the same characteristics as the 2×RO mode but with different frequency and spatial periodicity.

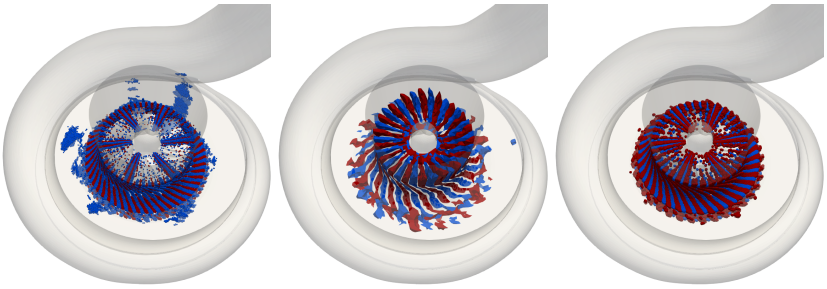

Figure 5.16: *Modal shape of the 4, 8 and 10×RO modes of c1 bep. They present 48, 18, and 36 lobes of each color around the impeller channels.*

The 4×RO mode has 48 lobes, and rotates with $\Omega_{4RO} = 1/12\,\Omega_{RO}$. The 8×RO mode has 18 lobes, which gives $\Omega_{8RO} = 4/9\,\Omega_{RO}$. Finally, the 10×RO

mode has 36 lobes, and $\Omega_{10RO} = 5/18\,\Omega_{RO}$. As was the case with 2×RO, these modes also do not propagate through the ducts (not shown here).

From the above, some conclusions about the synchronous modes can be drawn. All cases have identical modes at even multiples of the RO. The BPF mode is easily related to the properties of the compressor flow field. The 2×BPF mode presents a variation: high amplitude at the TE. The trailing edges of the main and splitter blades are equal. Therefore, a perturbation in the diffuser pressure field, for example, the presence of the volute tongue (VT), would result in an interaction that would occur 12 times per impeller revolution. Hence the relevance of this region in the 2×BPF mode. These two modes propagate through the ducts, especially the outlet one, and are therefore perceived externally, which justifies their interest.

The other even multiples of the RO are of less relevance. Especially the 4, 8, and 10, since 2×RO does at least correlate with important components of the spectrum. These modes are second-order harmonics of phenomena excited by the BPF and 2×BPF. They capture the effects of phenomena such as vortex shedding and flapping at blade edges since several of their wavelengths appear in their wake. Although they are phenomena with high spatial coherence that appear in all cases, they have weak propagation in the ducts. Similar modes appear in the remaining groups of geometries and operating points, so they were described here in some detail as a reference for the following sections.

Asynchronous modes

Next, the isolated asynchronous modes will be examined. A simplified version of the spectra in Figures 5.11 and 5.12 are shown again in Figure 5.17 to recall the location of these modes.

In the low frequencies, modes A, B, and C appear. Mode C correlates at the inlet with maximum local amplitude. It cannot be compared with modes from other geometries, but it will provide information on the predominant flow structures at these frequencies, as will be seen later.

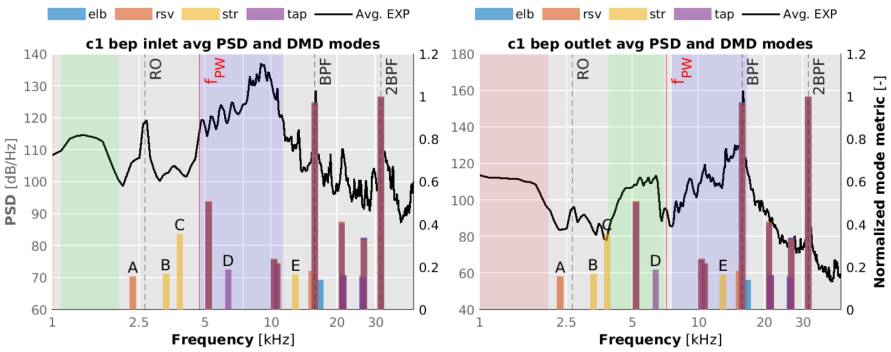

Figure 5.17: *Reminder of the DMD and experimental duct spectra for compressor c1 operating at bep. The black curves are the average of the four geometries PSD. The isolated modes are marked with letters A to E.*

The most interesting is mode D, which corresponds to the tap case. This mode is the only one within the high-frequency broadband that is not close to a multiple of the RO (asynchronous). Moreover, as shown in the previous chapter, the CFD calculations reproduced this broadband well in the frequency interval immediately above the plane-wave limit. Mode D lies in that range; thus, it can provide some information about the phenomena responsible for broadband noise at high frequency.

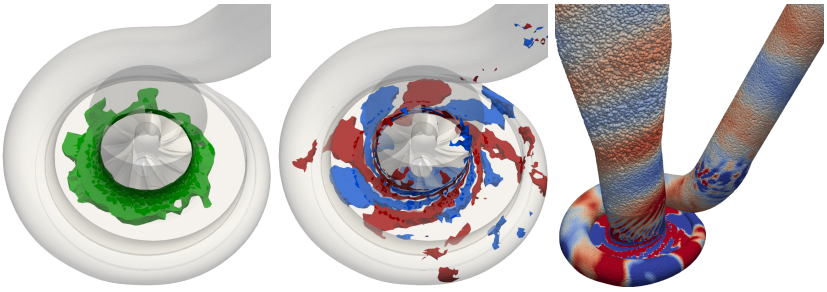

Figure 5.18: *Maximum amplitude, modal shape and propagation of isolated mode D of c1 tap bep. It shows the maximum amplitude region around the TC, in agreement to its frequency band called TCN in the literature*

The left image of Figure 5.18 shows the maximum model amplitude from the TC (downstream of the LE) to the middle of the diffuser. In fact, this broadband is associated in the literature with the so-called tip clearance noise (TCN) [27]. The central image shows the shape of the mode at its origin: helical lobes that spring at the tip clearance and propagate downstream to the diffuser.

Noticeably, the rotation direction of these lobes is clockwise, contrary to what happened with the modes seen above, related to the impeller channels. In the case of mode D, there are five lobes. In the right image, the propagation of the mode through the ducts is clearly distinguished. At the inlet, it has a helical shape, while at the outlet, it presents the plane wave pattern (the surfaces of equal phase are planes perpendicular to the axis of the outlet duct).

The different propagation shape in the inlet and outlet ducts is because the mode frequency is below the plane wave limit at the outlet and above it at the inlet, as seen in figure 5.17. Around the inducer, above the TC spirals, some thin tilted shapes can be distinguished as well. The flow mechanism related to the observed pattern is not obvious but it is clear that it has the greatest amplitude in the tip clearance and propagates through the ducts. In the last section of this chapter some additional insight will be given on the origin of these “TCN modes”.

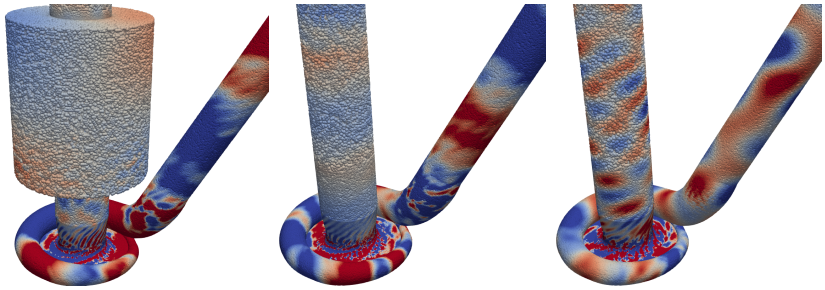

Figure 5.19: *Propagation figures of isolated modes A, C and E (from left to right) of c1 bep.*

Figure 5.19 shows the isolated modes A, C, and E. In the tip clearance zone, it can be seen how all of them present a helical pattern similar to that of mode D. In fact, all of them have the same shape and zone of maximum amplitude as this mode (not shown here). In all cases, the modes propagate through the ducts, especially the outlet. Modes A and C are in the plane wave range in both ducts. Such modes propagate as a plane wave, except at the inlet of mode A. In the reservoir a pattern with four blocks appears. The frequency of mode E is above plane wave in both ducts. In the right image, the complex propagation patterns of this mode are displayed.

In summary, the flow field of these cases is dominated by the synchronous modes, particularly BPF and 2×BPF, which propagate in the ducts, especially in the outlet. The rest of the even multiples of RO are of minor importance and do not propagate in the ducts. Finally, all the isolated modes have the same shape: a helical pattern in the tip clearance, which propagates in the ducts. Regarding the noise components identified in the spectra, the BPF tone is the most important and is correctly reproduced by the modes. The second most important component is the high-frequency broadband, which is scarcely reflected by some isolated modes, although it is known that this component is not well reproduced by the numerical model. The remaining components of interest, such as the RO tone and the low-frequency broadbands, do not appear in the DMD modes. The differences in PSD average amplitude or RO and BPF tones displayed by tap and rsv cases are not reflected by the modes. They are attributed to the different sound transmission properties of the ducts.

5.3.2 c1 nsg

In this section the spectra and modes belonging to the group c1 nsg {elb, rsv, str, tap} will be studied. The nomenclature is reminded in table 5.3.

Name	Compressor	Inlet geometry	Operating point
c1 elb nsg	c1	Elbow	Near surge point
c1 rsv nsg	c1	Reservoir	Near surge point
c1 str nsg	c1	Straight duct	Near surge point
c1 tap nsg	c1	Tapered duct	Near surge point

Table 5.3: *Reminder of abbreviations for c1 nsg cases.*

Figure 5.20 displays the inlet measured PSD spectra together with the DMD normalized mode metric E_i.

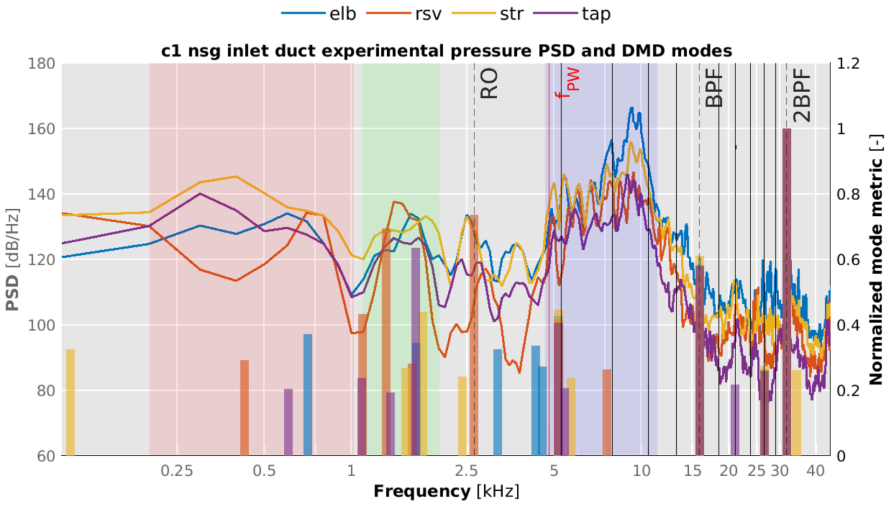

Figure 5.20: *DMD and experimental inlet duct spectra for compressor c1 operating at nsg. Solid black lines signal multiples of the RO. f_{PW} is the plane wave limit. Red, green and blue bands signal broadbands of interest.*

The four geometries show very similar plots. Two broad bands appear at low frequencies, colored red and green. Just above the plane-wave boundary f_{PW} is the high-frequency broadband marked in blue. The BPF tone that dominated the bep spectrum is, in contrast, absent at the nsg point. That is the most remarkable difference between the two operating points. In this case, the green band, which, as indicated above, corresponds to the *whoosh* noise, gains relevance in the absence of the BPF tone and because, unlike the red band, it is located in the maximum human hearing range.

Specific differences between the four geometries can be identified. The rsv case has four local minima at low frequencies between 250 and 5000 Hz. They are caused by the resonance frequency of the reservoir. In the blue band, between 3 and 4×RO, the elb case has an amplitude up to 20 dB higher than the other cases. That is the most significant difference due to the geometries, although unfortunately, it appears in the range worst reproduced by the numerical model. The tap case, in purple, shows the lowest amplitude

throughout the spectrum, except at the rsv resonance frequencies.

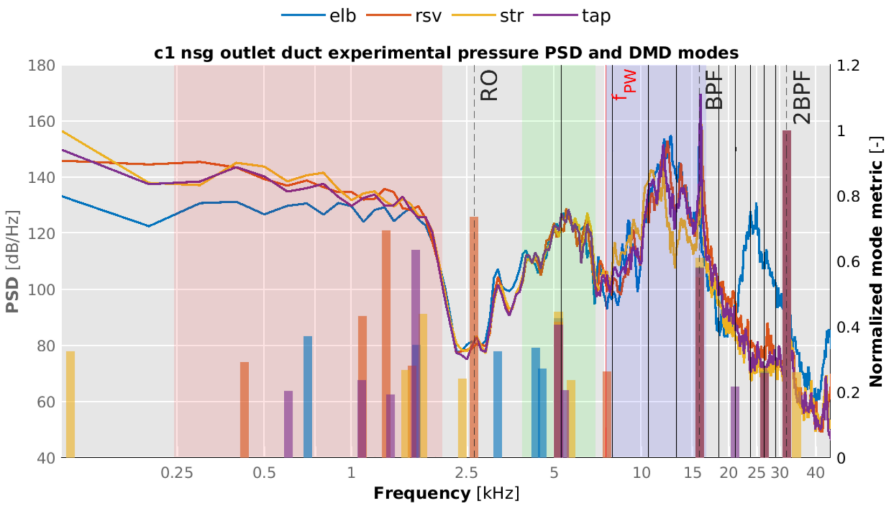

Figure 5.21: *DMD and experimental outlet duct spectra for compressor c1 operating at nsg. Solid black lines signal multiples of the RO. f_{PW} is the plane wave limit. Red, green and blue bands signal broadbands of interest.*

The outlet duct spectra are shown in figure 5.21. The spectrum is dominated by the BPF tone and a broadband above the plane wave, marked in blue. Just below the plane wave boundary appears another broadband marked in green. Below the RO, which again does not stand out in the spectrum, the low-frequency broadband appears in red. The spectra of the different geometries are very similar. The only notable differences are a smaller amplitude of elb at low frequencies and a broad band of this same case above 20 kHz.

The dominance of the BPF tone at the outlet is noteworthy, as it is absent at the inlet. This indicates that this tone has different generation mechanisms for each duct. The thermodynamic conditions in the inlet duct are similar in the bep and nsg cases, so the absence of the BPF tone at the inlet in the nsg cases may not be due to attenuation by the ducts but to the absence or lower intensity of its generation mechanism.

On the other hand, the local minima in the rsv amplitude at low frequencies are not reproduced in the outlet spectrum. It confirms that the cause is the attenuation by resonance in the inlet duct.

The DMD in these cases also exhibits some common modes: BPF, 2×BPF, 2×RO, and 10×RO. The BPF mode is still second in metric in all cases but has a noticeably lower magnitude than in the bep cases, in agreement with the experimental spectra.

There is an asynchronous common mode around 1500 Hz, albeit with some frequency difference between geometries amplified by the logarithmic scale. As for the isolated modes, one of them, from the rsv case, appears in the blue band corresponding with the TCN at the inlet. It will offer interesting in-

formation about this region of the spectrum. The rest are scattered below the plane wave frequency. In particular, both low-frequency broad bands are well represented by the isolated modes, specially the inlet green band corresponding to *whoosh* noise. At the RO an outstanding rsv mode can be seen. Although it is a synchronous mode in terms of frequency, it will be seen that the spatial mode structure agrees with the asynchronous modes instead. The small number of common modes suggests that the flow phenomena responsible for the higher noise in near-surge conditions are more fluctuating and distributed in frequency than in the bep case.

Synchronous modes

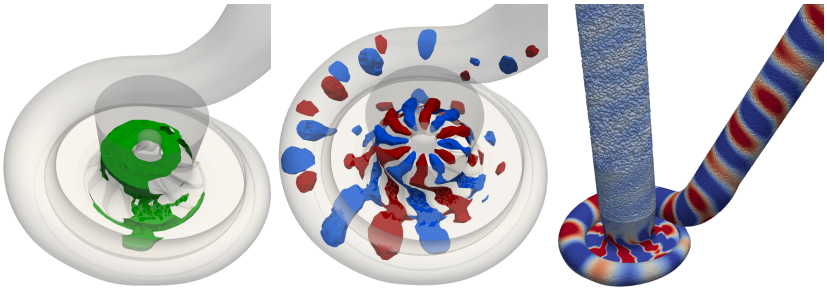

Figure 5.22: *Maximum amplitude, modal shape and propagation of the BPF mode of c1 str nsg. The mode is the same in all four geometries.*

Figure 5.22 shows the BPF mode, which is identical in all geometries. The structure of the mode is similar to that shown in the bep. It has six lobes moving in unison with the blades. However, some differences can be observed. The maximum amplitude is no longer concentrated exclusively in the circular crown in the LE from blade mid-radius to tip. In fact, part of this region is missing in the left image, and instead, the amplitude increases in part of the TC, TE, and beginning of the diffuser. The central image also shows that the height of the lobes in the LE tip has been significantly reduced. The content in the diffuser and volute has increased with respect to bep. As for the propagation, a very clear and high amplitude helical pattern is observed in the outlet duct. Helical propagation is also observed at the inlet but much more faint. These differences can be related to what was seen in the spectra in figure 5.20. The LE tip region has lost relevance in this mode, leading to a significant decrease in mode amplitude in the inlet duct. Meanwhile, the impeller TE, volute, and outlet duct show a larger amplitude. That reinforces the hypothesis that the BPF mode generation mechanisms are different at the inlet and outlet: at the inlet, they are located in the impeller LE tip and at the outlet in the TE and diffuser.

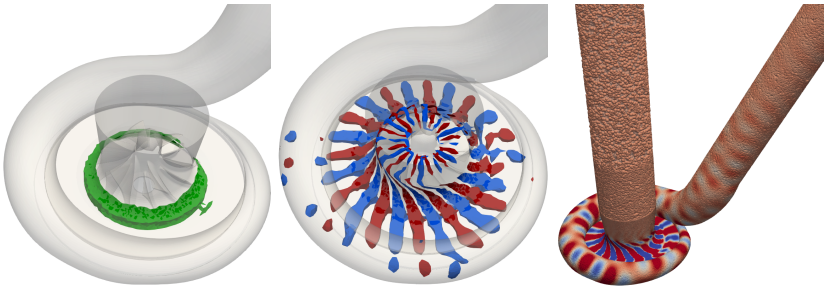

Figure 5.23: *Maximum amplitude, modal shape and propagation of the 2×BPF mode of c1 str nsg. The mode is the same in all four geometries.*

In Figure 5.23 the 2×BPF mode can be seen. Again, it has a 12-lobe structure, similar to the one seen in the bep. However, a decrease in the inducer section relevance is observed since in the amplitude image, the surface above the LE seen in the bep does not appear. The central image also shows the decrease in the height of the LE lobes, especially in the outer radius, near the tip. As for the propagation, it is not much affected because, as in bep, this mode is more relevant in the diffuser and outlet duct and has little presence at the inlet.

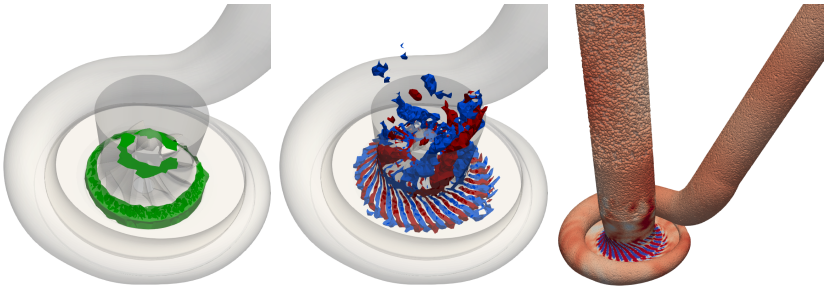

Figure 5.24: *Maximum amplitude, modal shape and propagation of the 2×RO mode of c1 str nsg. There are 24 lobes around the blade channels. The mode is the same in all four geometries.*

The 2×RO mode is shown in Figure 5.24. Again, it has the same shape as in bep but has two important differences. The first is the aforementioned decrease in amplitude near the LE tip. The second is the appearance of backswept lobes upstream of the LE, which occupy a circular crown over the major radii of the inducer. The lobes appearing around the blade channels are 24, as in the bep. As for the duct propagation, this mode still does not show remarkable propagation. The 10×RO mode is equal as at the bep: it has 36 lobes in the blade channels and does not propagate in the ducts (not shown here).

Asynchronous modes

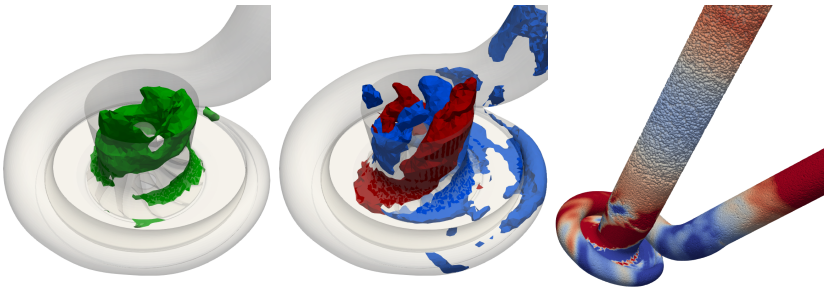

Figure 5.25: *Maximum amplitude, modal shape and propagation of the c1 str nsg mode at 1536 Hz. It appears in the green broadband of figure 5.20. The other geometries show similar modes in that band. They are termed "whoosh modes", as the green band corresponds to the whoosh noise.*

The last group of common modes, corresponding to the broadband of the *whoosh* noise marked in green in Figure 5.20 is shown in Figure 5.25. It is an asynchronous common mode, and as such, it presents some frequency dispersion. Although the modes in this band are irregular in nature, they follow the same pattern in all four geometries. In the maximum amplitude image (center), a high-amplitude region is observed upstream of the LE, at the outer duct radii. The TC and diffuser also have some high amplitude areas. Finally, all cases show a high amplitude region under the volute tongue (where the outlet duct separates from the scroll beginning). All these modes present on the LE two backswept lobes of each color, similar to those in the 2×RO mode. In the TC a spiral pattern following the slope of the inducer backswept lobes can be distinguished. In the right image, it can be seen how the mode propagates as a plane wave in both ducts, although it presents greater amplitude at the outlet.

In the literature [45], [51] there are reports of vortices appearing upstream of the LE, and they are sheared by the blades. This interaction favors detachment at the blade suction side. In the TE, low-velocity stalled cells detach and advance through the diffuser until they impact the volute tongue. The whole process leads to a phenomenon called rotating stall. The correlation between the diffuser pressure fluctuation caused by these stalled cells and the pressure in the outlet duct is confirmed in [45].

This flow mechanism is consistent with the high amplitude zones shown in Figure 5.25 and with the mode pattern. The two backswept lobes rotate around the impeller axis with a velocity close to 33% of Ω_{RO}, like the reported inducer vortices. The fluctuating zones in the diffuser also manifest in the volute. The mode propagation at the inlet is caused by the pressure oscillations resulting of the movement and interaction of the vortices. At the outlet duct, the oscillations are caused by the fluctuating pressure at the diffuser and VT.

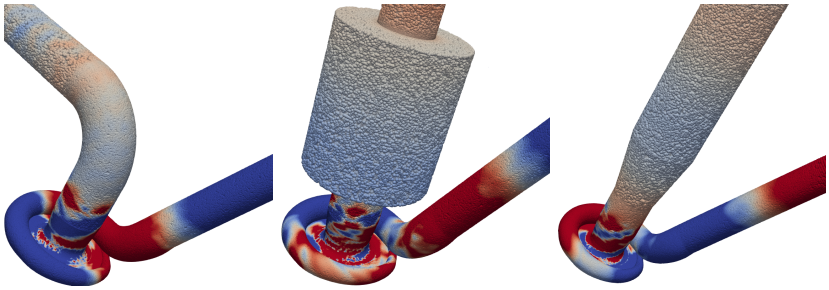

Figure 5.26: *Propagation of the "whoosh modes" of the remaining geometries of c1 nsg. They present a plane wave pattern in both ducts.*

Figure 5.26 shows the propagation of this mode in the remaining geometries, where it also presents a plane wave pattern, with more amplitude at the outlet than at the inlet.

Next, the isolated modes are analyzed. The tap mode at 8×RO will be excluded because it has an already known shape. Similarly, the str mode above 2×BPF is excluded because it is outside the frequency range of interest. The first str mode to appear, at 107 Hz, is also disregarded because it is too close to the lower frequency limit of 20 Hz.

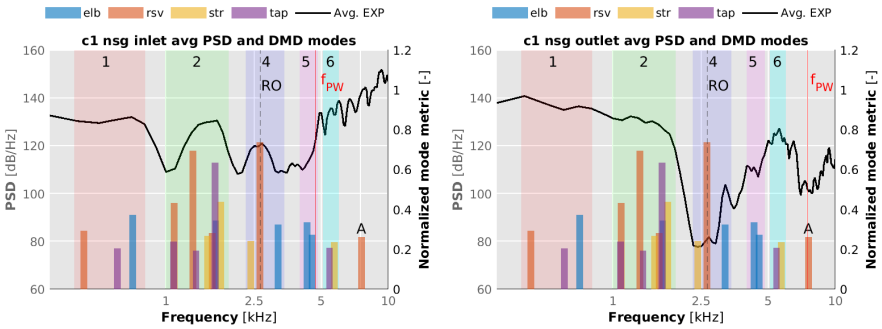

Figure 5.27: *Reminder of the DMD and experimental duct spectra for compressor c1 operating at nsg. The black curves are the average of the four geometries PSD. Only the asynchronous modes are shown. The frequency range depicts the low and medium frequencies to see these modes in more detail. The colored bands group modes with the same number of lobes. There is an outlier isolated mode marked with "A".*

Figure 5.27 shows the isolated modes. The synchronous modes were removed for clarity. All these modes have the same shape as the "whoosh mode" shown in figure 5.25 but with a different number of lobes. In figure 5.27 there are colored bands marked to indicate the number of lobes of the modes they contain. The increase of lobes with frequency causes the ratio of equation 5.22 to remain between 20% and 36% of Ω_{RO}. Figure 5.28 shows modes with 1, 2 and 4 lobes of the rsv case.

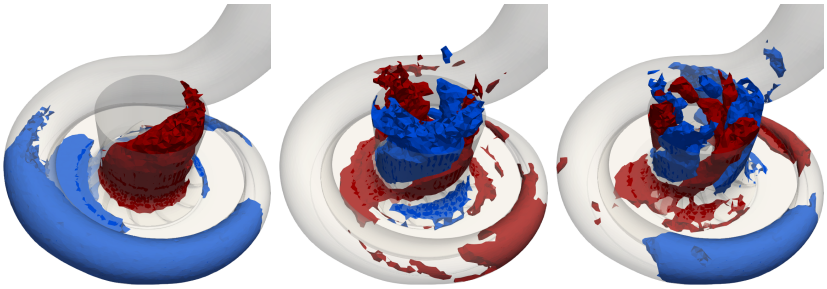

Figure 5.28: *Modal shapes corresponding to c1 rsv nsg "whoosh modes" with 1, 2 and 4 lobes of each color.*

What was discussed above clearly shows that the asynchronous spectral content below the plane-wave limit is consistent with a single pattern. The vortices associated with the *whoosh* noise [45], their interaction with the blades, the stall cells in the diffuser, and the VT, appear represented by modes with different spatial and temporal periodicity but always maintain the same recognizable pattern. The multiplicity of modes with a different number of lobes rotating at a similar speed is associated with the motion of two primary vortices from which smaller vortices are shed.

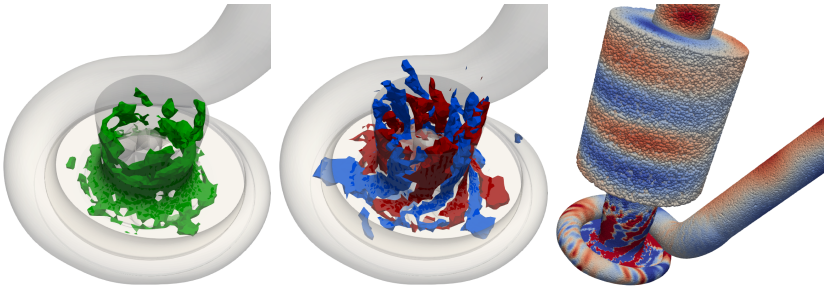

Figure 5.29: *Maximum amplitude, modal shape and propagation of the c1 rsv nsg isolated mode marked "A" in figure 5.27.*

The last mode to be discussed is the rsv mode at 7593 Hz, which appears in the high-frequency broadband of figure 5.27 marked with an A. It is shown in Figure 5.29. This mode presents 5 lobes but has two fundamental differences from the modes described below the plane wave limit. The first is that the region of maximum amplitude is more displaced towards the tip clearance and the beginning of the diffuser than towards the volume upstream of the LE. The second is that it does not follow the lobe-to-frequency ratio of the other modes and has an angular velocity of 57% Ω_{RO}. It can be seen that since both ducts are above the respective plane wave limit, the propagation has complex patterns. This mode has in common with the high-frequency broadband modes seen in c1 bep (Figure 5.18) that the zone of maximum amplitude includes the entire tip clearance, and the TC pattern is also a

clockwise spiral, although with a slightly higher slope. It can be concluded that above the plane wave limit, a sub-type of the "whoosh modes" appears. They are modes with numerous thin lobes, with the largest amplitude concentrated around the TC, where they show the spiral pattern of lobes around the impeller blades. This sub-type will be called "TCN modes" throughout the chapter. Appearing above the plane wave limit, the "TCN modes" propagate through the ducts following complex patterns.

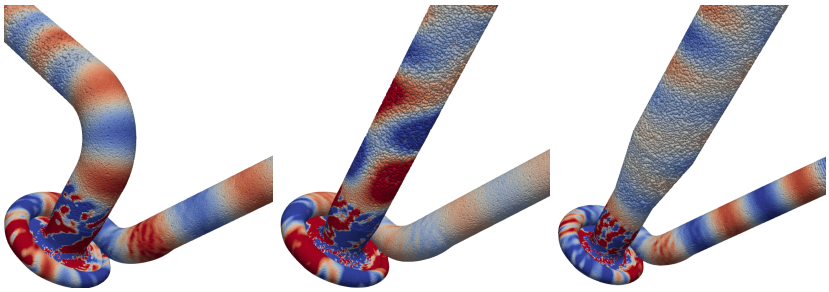

Figure 5.30: *Propagation of c1 nsg asynchronous modes. They correspond to the three modes immediately below mode "A" in frequency (Figure 5.27). They present plane wave propagation except at the inlet of geometries str and tap.*

Finally, figure 5.30 shows the propagation of the remaining asynchronous high-frequency modes shown in figure 5.27. They all propagate as a plane wave in the outlet duct. On the other hand, only the elb mode is within the plane wave range at the inlet. The other two present more complex patterns.

To summarize the results for the c1 nsg group, the following can be said: The synchronous modes are the same as in c1 bep, but with less importance of the LE in favor of the TE. In the 2×RO mode, backswept lobes appear for the first time. These shapes are characteristic of all asynchronous modes appearing below the plane wave limit. These modes exhibit a number of lobes increasing with frequency while maintaining a bounded rotational speed. They are consistent with the inducer vortices reported in the literature [45], [51], and their interaction with the vanes, diffuser, and volute. They propagate through the ducts, generally following the plane wave pattern, although they present more complex propagation patterns with increasing frequency. This result is relevant since it establishes a clear relationship between important spectral components, such as the *whoosh* noise and flow structures known in the literature, such as inducer vortices.

5.3.3 c2 rsd

In this section, the flow field of compressor c2, for rsd geometry, is analyzed at three operating points: nsg, hpr, and bep. The nomenclature is presented in table 5.4.

Name	Compressor	Inlet geometry	Operating point
c2 rsd nsg	c2	Reference straight ducts	Near surge point
c2 rsd hpr	c2	Reference straight ducts	Highest pressure ratio
c2 rsd bep	c2	Reference straight ducts	Best efficiency point

Table 5.4: *Reminder of abbreviations for c2 rsd cases.*

Figure 5.31 shows the inlet spectra and DMD modes.

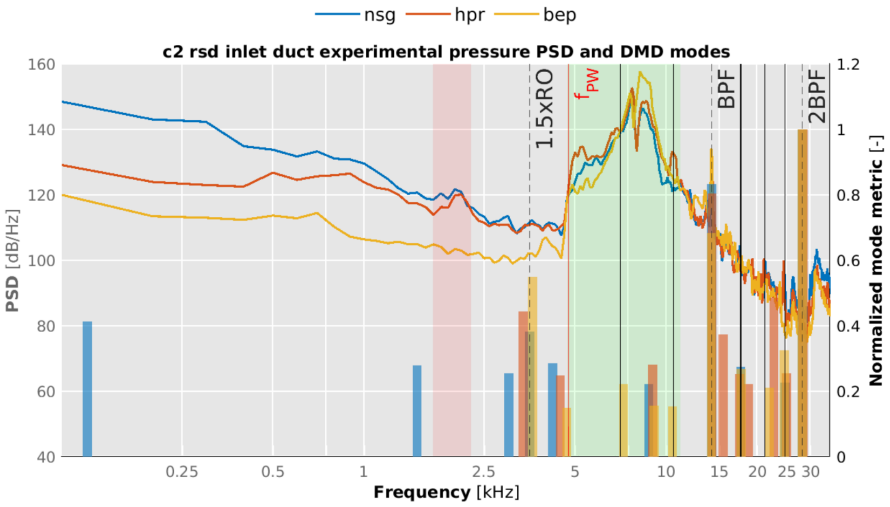

Figure 5.31: *DMD and experimental inlet duct spectra for compressor c2 rsd operating at nsg, hpr and bep. Solid black lines signal multiples of* $1.5\times RO$*.* f_{PW} *is the plane wave limit. Red and green bands signal broadbands of interest.*

There is a change in the auxiliary lines considered in the previous sections. The first dashed line is placed at 1.5×RO instead of RO. The solid black lines are placed on multiples of 1.5×RO: 2×1.5RO, 3×1.5RO etc. The frequencies BPF and 2×BPF are multiples 4 and 8×1.5, respectively. This change is because the synchronous modes of compressor c2 appear at 1.5×RO, and its multiples, instead of RO and its multiples, as in compressor c1.

In the inlet duct, the spectra are dominated by a high-frequency broadband highlighted by the green stripe. The BPF tone is the second most prominent spectral component. At low frequency, the red band corresponding to the *whoosh* noise stands out in the nsg and hpr cases.

The most important differences between the three operating points are the following: in the high-frequency broadband, between 2 and 3×1.5RO, the bep case stands out. In the band between f_{PW} and 2×1.5RO, the bep has a lower amplitude than the other points. On the other hand, below f_{PW}, the points closer to surge have a higher average amplitude and also present the *whoosh* band, which is not seen in the bep.

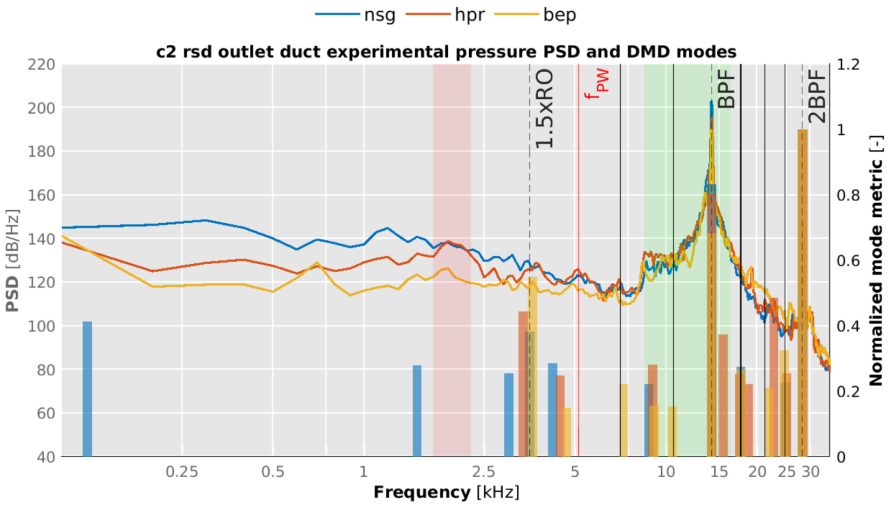

Figure 5.32: *DMD and experimental outlet duct spectra for compressor c2 rsd operating at nsg, hpr and bep. Solid black lines signal multiples of* $1.5\times RO$*.* f_{PW} *is the plane wave limit. Red and green bands signal broadbands of interest.*

The BPF tone dominates the outlet spectrum shown in figure 5.32. Around this tone is a broad band with an abrupt decay at 9 kHz. In the low frequencies, the *whoosh* band appears. In the bep, there is only a small prominence in that band. In the hpr case, it can be clearly observed, and in nsg, it is masked by the rest of the low-frequency noise characteristic of this operating point. The most noticeable difference between operating points is the higher amplitude at low frequencies of the points closer to surge (hpr and nsg).

As for the DMD, common modes appear at the synchronous frequencies of 1.5×RO, BPF, 5 and 7 × 1.5RO, and 2BPF. In addition, there are two groups of common asynchronous modes, between 1.5×RO and 2 × 1.5RO, and between 2 and 3 × 1.5RO. The second of these groups (around 9 kHz) coincides with the maximum amplitude of the high-frequency broadband at the inlet. The bep isolated modes appear at synchronous frequencies in the high-frequency broadband. The hpr isolated modes appear at asynchronous frequencies above the BPF. Finally, the nsg case presents isolated modes in the lower frequencies at asynchronous spots.

Synchronous modes

In the following, the shape of the DMD modes will be analyzed: first, the common synchronous modes, then the asynchronous and isolated modes.

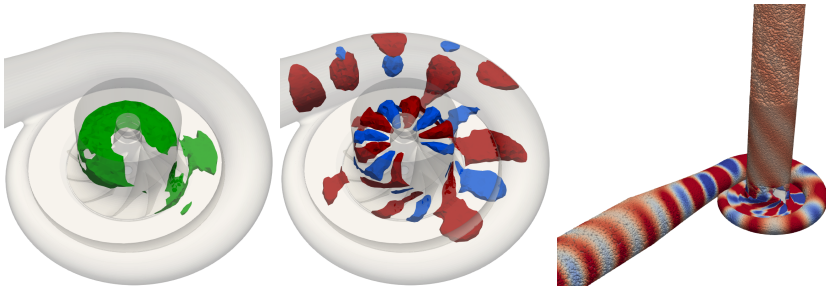

Figure 5.33: *Maximum amplitude, modal shape and propagation of the BPF mode of c2 rsd bep.*

Figure 5.33 shows the BPF mode of the c2 rsd bep case. The maximum amplitude appears over the blade leading edge, plus a small region at the TE and diffuser. In the central figure, the six well-known lobes move together with the impeller, representing the static pressure pattern relative to the impeller. In the right-hand image, it can be seen that the mode propagates helically at the inlet, although with reduced amplitude. In the outlet duct, it also propagates helically, with greater amplitude, although it decreases away from the volute. The lack of a wedge-shaped region in the impeller LE zone stands out in these figures. The data corresponding to that small area was lost due to a storage error. That does not compromise the validity of the DMD in the rest of the domain.

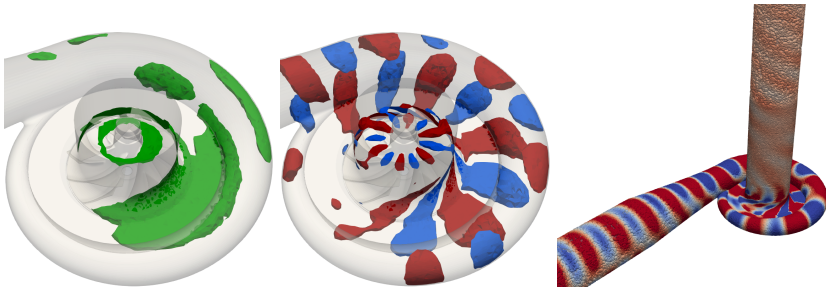

Figure 5.34: *Maximum amplitude, modal shape and propagation of the BPF mode of c2 rsd hpr.*

In the hpr case shown in figure 5.34, the same evolution is observed as in compressor c1 when reducing the mass flow rate. The area in the larger radii of the LE loses relevance in favor of the diffuser and volute. The asymmetry observed in the diffuser is noteworthy. The mode has a small amplitude downstream counterclockwise of the VT, where the lobes do not show up. The mode propagates in both ducts. In the inlet duct, it has a reduced amplitude, as was the case in the bep, and in addition, the helix has a smaller inclination than in that case.

Figure 5.35: *Maximum amplitude, modal shape and propagation of the BPF mode of c2 rsd nsg.*

Figure 5.35 shows the BPF mode of the c2 rsd nsg case. The same changes as in hpr are observed but more pronounced: in the left image, the ring around the hub at the LE is barely visible. In the central image, the LE lobes are restricted to the first half of the blade radius, and they have a lower height than in the bep case. The mode propagates through the ducts with the same patterns as in the two previous cases. The inlet helical pattern has a lower slope than in the bep case.

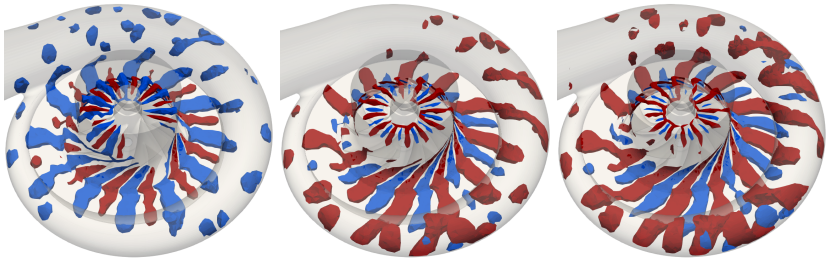

Figure 5.36: *Modal shape of the 2×BPF modes of c2 rsd bep, hpr and nsg, respectively from left to right.*

Figure 5.36 shows the 2×BPF mode of the bep, hpr, and nsg cases. It has the known 12-lobe pattern that rotates along with the impeller. Like the BPF mode, it has lower amplitude in the LE tip and higher amplitude in the diffuser and volute at the points with lower mass flow rate. The mode presents smaller lobes downstream counter-clockwise from the VT, as in the BPF modes. The mode propagates helically and only in the outlet duct, as in compressor c1 (not shown here).

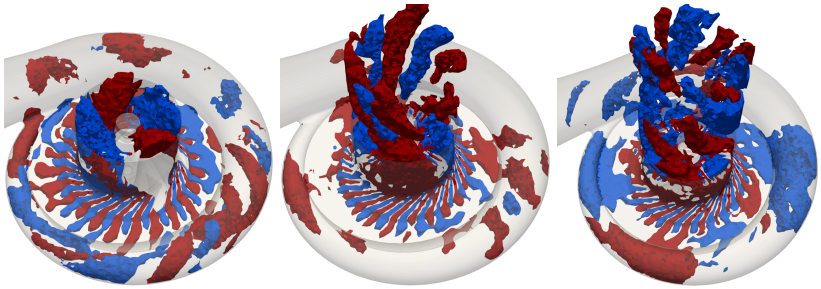

Figure 5.37: *Modal shape of the* $1.5\times RO$ *modes of c2 rsd bep, hpr and nsg, respectively from left to right. There are 24 lobes around the blade channels.*

The 1.5×RO mode is shown in figure 5.37. As was the case in the 2×RO mode of the c1 nsg cases, the mode has two parts. Around the impeller channels, there are 24 lobes rotating at a rate of $1/16\,\Omega_{RO}$, and upstream of the inducer appear the backswept lobes. The presence of these lobes, although small in size, in the bep case is a novelty with respect to the c1 compressor. None of these modes propagate through the ducts (not shown here).

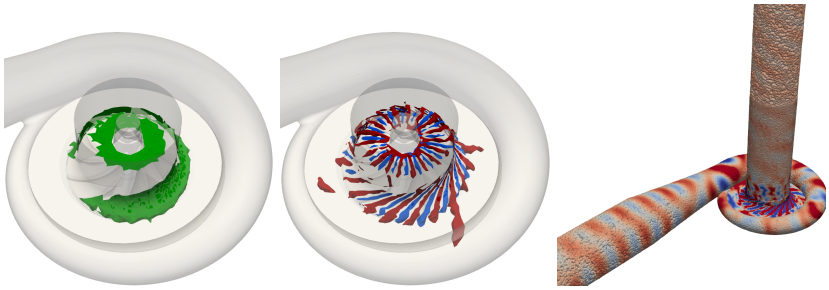

Figure 5.38: *Maximum amplitude, modal shape and propagation of the* $5 \times 1.5RO$ *mode of c2 rsd nsg. The other operating points show similar modes at this frequency. There are 18 lobes around the blade channels.*

The last synchronous mode is shown in figure 5.38, it is the 5×1.5RO mode. The figure shows the mode corresponding to the c2 rsd nsg case. The mode is the same in the hpr and bep cases, although with slightly higher amplitude in the LE tip. This mode has 18 lobes in the impeller channels, which rotate at $5/12\,\Omega_{RO}$. The right image shows how it propagates through the ducts in a complex helical pattern. The 7×1.5RO mode (not shown here) also appears in all cases of the c2 compressor. It has 36 lobes, rotates at $7/24\,\Omega_{RO}$, and does not propagate through the ducts. It is also outside the human hearing range, at 24.7 kHz.

Asynchronous modes

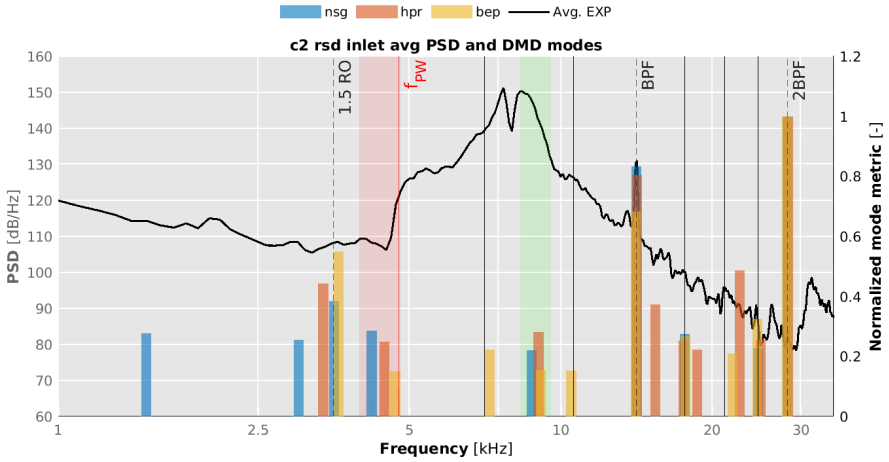

Figure 5.39: *Reminder of the DMD and experimental inlet duct spectra for compressor c2 rsd operating at nsg, hpr and bep. The black curve is the average of the three operating points PSD. The red and green bands mark the common asynchronous modes.*

Figure 5.39 shows, as a reminder, the spectrum in the inlet duct along with the modes of the c2 rsd: nsg, hpr, and bep cases. All common synchronous modes have already been analyzed. Two common asynchronous modes are marked with the red and green bands. The first appears just below the plane wave limit f_{PW}, and the second appears within the high-frequency broadband, coinciding with the highest amplitude interval of the whole spectrum.

The bep case presents two isolated modes at 2 and 3×1.5RO and the asynchronous frequency of 21.9 kHz. The hpr case has three isolated asynchronous modes above BPF. The nsg isolated modes are found at the low frequencies: 122 Hz (not shown), 1.5, and 3 kHz. They are examined below. First the common asynchronous modes will be discussed, and then the isolated modes.

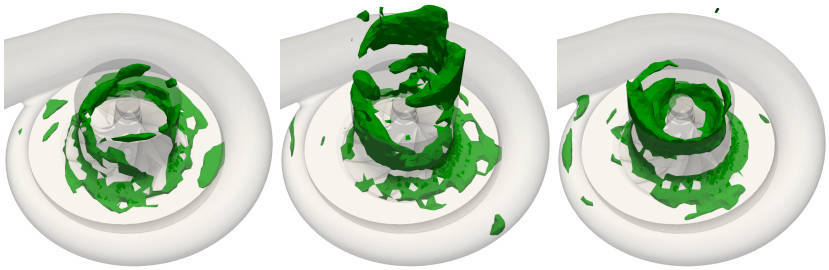

Figure 5.40: *Maximum amplitude for the common asynchronous modes shown in the red band of figure 5.39. From left to right: bep, hpr and nsg.*

Figure 5.40 shows the amplitude of the asynchronous common mode below f_{PW}, for the three c2 rsd cases: bep, hpr and nsg. A similar pattern is observed in all three cases: high amplitude at the outer radii upstream of the impeller, at the TC, and some points on the diffuser. There are also small areas of high amplitude near the VT.

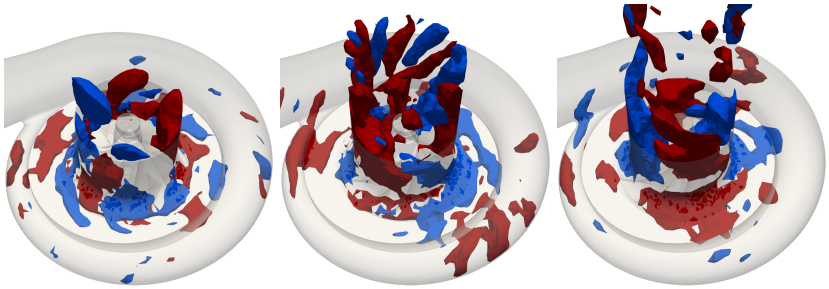

Figure 5.41: *Modal shape for the common asynchronous modes shown in the red band of figure 5.39. From left to right: bep, hpr and nsg.*

The distribution of these modes is shown in Figure 5.41. The shape of these modes and their area of maximum amplitude corresponds to the "whoosh modes" seen in the c1 nsg cases. There are lobes upstream of the LE, extending through the TC, and downstream through the diffuser and volute. In compressor c1, there was no mode of these characteristics at the bep. However, it does appear in compressor c2.

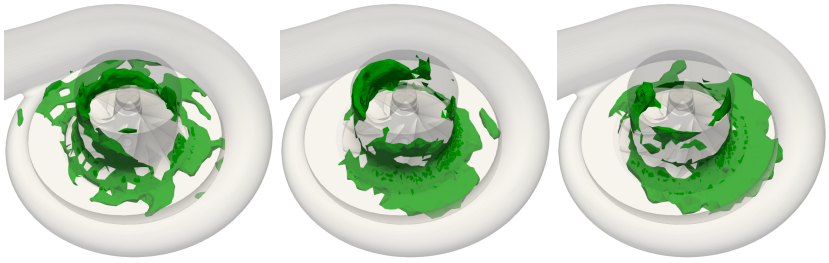

Figure 5.42: *Maximum amplitude for the common asynchronous modes shown in the green band of figure 5.39. From left to right: bep, hpr and nsg.*

Figure 5.42 shows the amplitude of the second asynchronous common mode, in this case, in the high-frequency broadband, of the bep, hpr, and nsg cases. It can be seen that the high-amplitude region gathers around the TC and the diffuser.

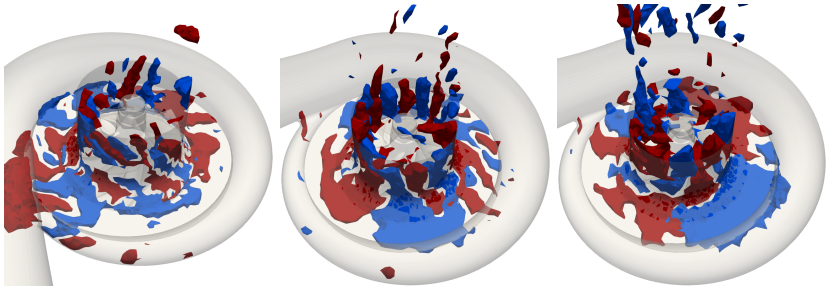

Figure 5.43: *Modal shape for the common asynchronous modes shown in the green band of figure 5.39. From left to right: bep, hpr and nsg.*

The shape of these modes is shown in figure 5.43. The left image has been rotated 90° to appreciate the mode structure better. The modes present numerous thin lobes around the impeller. In the TC, the pattern shows the same slope of the inducer lobes and opposite to the impeller blades. The modal shape and the maximum amplitude zones around the TC shown in figure 5.42 allow concluding that they are modes of the TCN sub-type seen in compressor c1: in Figure 5.18 for bep and Figure 5.29 for nsg.

Finally, the isolated modes of the three c2 rsd cases are analyzed. As seen in Figure 5.39 the bep case has two synchronous isolated modes in 2 and 3×1.5RO, which have the same shape as the 5×1.5RO shown in Figure 5.38, but with 48 and 30 lobes respectively. They are not shown here. The third isolated bep mode and the three hpr modes appear at asynchronous frequencies above BPF (two above 20 kHz). They all have the same the TCN characteristics shown in figure 5.43. They will not be shown here either. The isolated modes of the nsg case are displayed below.

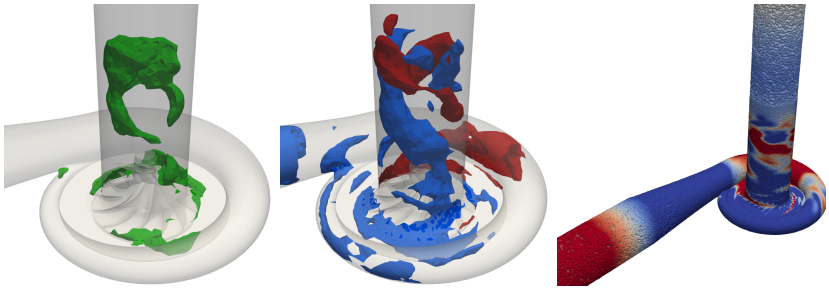

Figure 5.44: *Maximum amplitude, modal shape and propagation for the c2 rsd nsg "whoosh mode" at 1500 Hz.*

Figure 5.44 shows the whoosh-like mode appearing at 1.5 kHz. Its maximum amplitude is distributed in the usual way for these modes: upstream of the inducer, in the TC, diffuser and VT. It has two lobes of each color, which gives a rotating rate of 32% Ω_{RO} and propagates as a plane wave in both ducts.

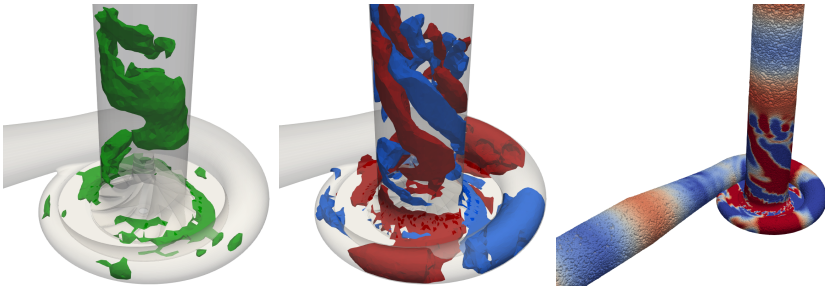

Figure 5.45: *Maximum amplitude, modal shape and propagation for the c2 rsd nsg "whoosh mode" at 3000 Hz.*

Figure 5.45 shows the other isolated nsg mode. It is a whoosh mode at twice the frequency of the previous one: 3 kHz. In this case, it has 5 lobes, a rotational velocity of 26% Ω_{RO}, and propagates as a plane wave in both ducts as well.

A summary of the c2 rsd modes is offered next. The DMD modes of the compressor c2, with the rsd geometry at three operating points: bep, hpr, and nsg, have been studied to analyze the influence of the operating point while maintaining the geometry. The bep flow field is dominated by the synchronous modes: multiples of 1.5×RO (1, 2, 3, 4, 5, 7, and 8), with 4 and 8 being the BPF and 2×BPF modes. However, unlike the bep cases of the c1 compressor, in c2 rsd bep, some modes more typical of lower mass flow points appear. The lowest frequency synchronous mode 1.5×RO has some backswept lobes upstream of the inducer, as was the case in the 2×RO mode of c1 nsg. In addition, three asynchronous modes appear, with the shape of the whoosh and TCN modes seen in the c1 compressor at the nsg point. In conclusion, the bep of compressor c2 presents the main features seen in c1 bep, but with some incipient features of the nsg flow field.

The hpr and nsg points have very similar modes. The main synchronous modes: BPF, 2×BPF, and multiples 1, 5, and 7 of 1.5×RO appear, but with smaller amplitude near the LE impeller tip and greater importance in the diffuser and outlet duct, as was the case in c1 nsg. The asynchronous modes have the characteristics of the whoosh and TCN modes. As for the isolated modes, those of hpr appear at high frequencies in the form of TCN-type modes, and those of nsg appear at low frequencies as whoosh-type modes. There is a correlation between the higher amplitude of the nsg spectrum below plane wave and the presence of whoosh-like modes.

It has also been pointed out that the TCN modes appearing in the higher amplitude interval of the high-frequency broadband are the same as those seen in that band for the c1 bep and nsg cases.

5.3.4 c2 nsg

Finally, the experimental spectrum and DMD modes of the c2 nsg group will be analyzed. In this group are all the cases of compressor c2 operating at the nsg point, i.e., rsd, e0D75, e1D, and e1D5 (note that the c2 rsd nsg case is repeated in this section from the previous one). The nomenclature is reminded in table 5.5. The analysis of these cases will allow a better understanding of the effect of changing the straight inlet geometry by three elbows of a different curvature radius for the same operating point.

Name	Compressor	Inlet geometry	Operating point
c2 rsd nsg	c2	Reference straight ducts	Near surge point
c2 e0D75 nsg	c2	0.75 D Elbow	Near surge point
c2 e1D nsg	c2	1 D Elbow	Near surge point
c2 e1D5 nsg	c2	1.5 D Elbow	Near surge point

Table 5.5: *Reminder of abbreviations for c2 nsg cases.*

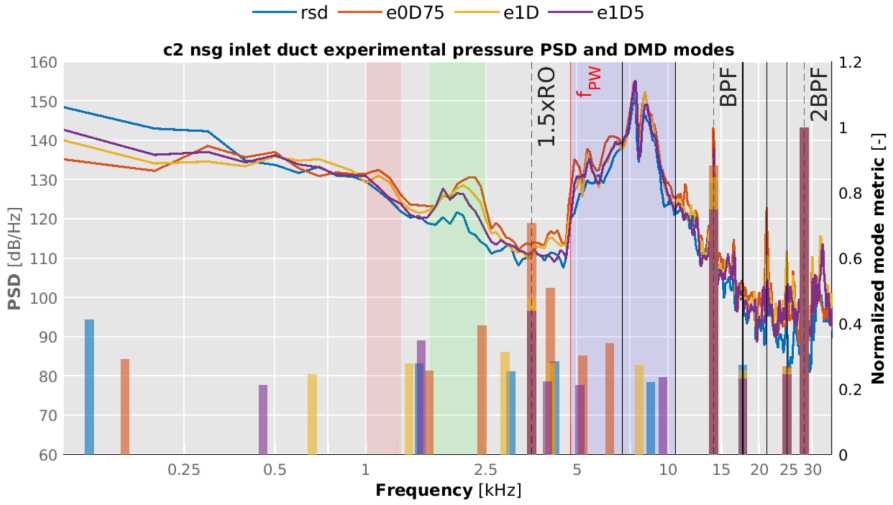

Figure 5.46: *DMD and experimental inlet duct spectra for compressor c2 operating at nsg. Solid black lines signal multiples of the* $1.5\times RO$. f_{PW} *is the plane wave limit. Red, green and blue bands signal broadbands of interest.*

Figure 5.46 shows the experimental and DMD spectra of the cases in this group. This figure shows a dashed line corresponding to the 1.5×RO frequency and solid black lines corresponding to its natural multiples, as in the previous section.

The inlet duct spectra are dominated by a high-frequency broadband (above f_{PW}), marked in blue. The second principal component is the tone at the BPF. Low frequencies (below 1 kHz) are the following greatest amplitude

range, although human hearing has lower sensitivity in this range. For that reason, the two bands, green and red, compatible with the *whoosh* noise, are the third most important spectrum feature, as they appear in the maximum human hearing sensitivity range (1 to 10 kHz).

The most significant difference between the various geometries appears in the red and green bands. In particular, in the green band, it is observed that the amplitude follows an inverse trend to that of the curvature radius: the e0D75 case, with the smallest radius, has the highest amplitude. The rsd case, on the other hand, has the smallest amplitude. The two cases with the smallest radii also have the largest amplitude in the red band. Moreover, in the high-frequency broadband, between the f_{PW} line and the 2×1.5RO line, the e0D75 case also has the highest amplitude, at some points even 10 dB higher than the reference rsd case.

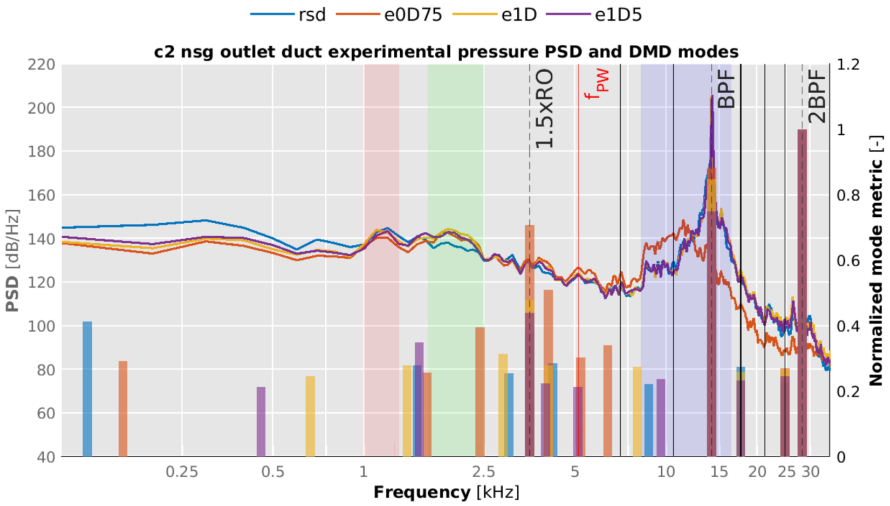

Figure 5.47: *DMD and experimental outlet duct spectra for compressor c2 operating at nsg. Solid black lines signal multiples of the* $1.5\times RO$. f_{PW} *is the plane wave limit. Red, green and blue bands signal broadbands of interest.*

Figure 5.47 shows the outlet duct spectra. It can be seen that they are very similar to that of c2 rsd nsg, already shown in the previous section. The spectrum is dominated by the BPF, followed by a high-frequency broadband around that tone. In the mid-frequencies, the red and green bands of the *whoosh* noise appear. As for the differences between geometries, the most important is the one presented by the e0D75 case in the blue broadband. This case is clearly distinguished from the others. It has a higher amplitude in the lower-frequency half of the blue band and a lower amplitude from the middle of the band to the high frequencies. Even the BPF tone has an amplitude 20 dB lower than the other cases, although it is not visible in the figure. This difference is surprising, considering that the rest of the geometries present practically identical spectra. Furthermore, one would expect the largest dif-

ferences to happen in the inlet spectrum since the four cases have different inlet geometries, while the outlet is identical. As the previous chapter shows, the numerical model does not capture this anomalous behavior. Concerning the rest of the spectrum, the three elbows show a slightly higher amplitude than the reference rsd case in the green band. Below 1 kHz, the rsd case is the one with a slightly higher amplitude.

As for the modes, the same synchronous frequencies appear as in the c2 rsd nsg: multiples 1, 5, and 7 of 1.5×RO, the BPF, and the 2×BPF. The remaining modes appear at asynchronous spots at low frequencies and high-frequency broadband (blue). The common mode around 1.5 kHz appears between the red and green broadbands. Although this mode's frequency does not coincide with the broadbands, one has to bear in mind that the asynchronous phenomena captured by the DMD represent flow structures with fluctuating frequencies. At 2.5 kHz, an e0D75 mode is observed, matching the highest amplitude in the green band. It will provide information about the mode shape at the exact frequency of the broadband.

In this subsection, the shape of the DMD modes of the c2 nsg case group is analyzed. First, the synchronous modes are shown. Then the different groups of asynchronous modes, which have the form of the well-known whoosh-like modes below the plane-wave limit, are analyzed. The focus will be on the effect of the elbow curvature radii on the modes. The objective is to obtain useful information to understand the cause of the differences observed in the measured spectra. Some modes have already been described in the previous sections. Therefore only the most relevant modes will be shown.

Synchronous modes

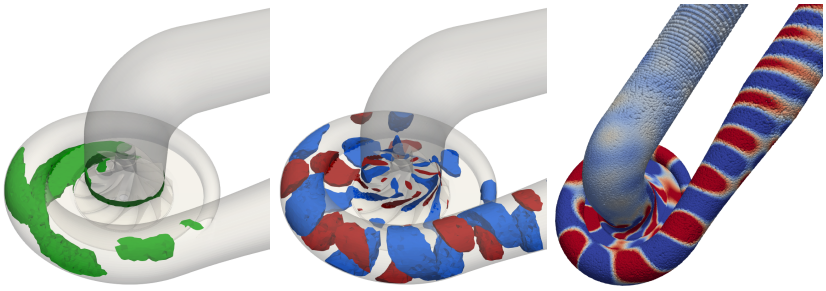

Figure 5.48: *Maximum amplitude, modal shape and propagation of the BPF mode of c2 e0D75 nsg.*

Figure 5.48 shows the BPF mode for the c2 e0D75 case. It can be seen that it has the same shape as in the c2 rsd nsg case shown in the previous section. The only difference appears in the propagation at the inlet duct. The presence of the elbow distorts the helix seen in the straight duct case. The other elbows display an identical BPF mode. The 2×BPF mode also has the same form as in c2 rsd nsg and is not shown here.

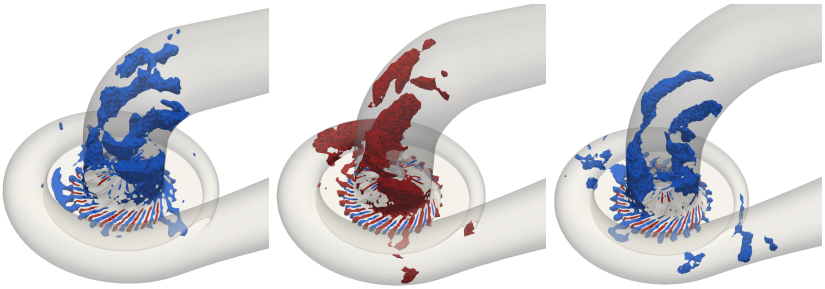

Figure 5.49: *Modal shape of the* 1.5×*RO modes of c2 nsg. From left to right: e0D75, e1D and e1D5. There are 24 lobes around the blade channels.*

Figure 5.49 shows another synchronous mode: the 1.5×RO. The mode has the same shape observed in the previous two sections: a lower part, with 24 lobes of each color located around the impeller channels, and an upper part, upstream of the inducer where back-swept lobes appear. The upstream lobes lean towards the horizontal inlet duct due to the elbow curvature. The other synchronous modes, 5 and 7 × 1.5RO, are the same as in the rsd cases and are not shown here.

Asynchronous modes

Figure 5.50 presents the inlet duct spectra up to the high-frequency broadband to show the asynchronous mode groups in more detail, although the common synchronous mode at 1.5×RO can also be seen. The first group of common modes at low frequencies is shown in red. Despite the logarithmic frequency scaling, all four modes are within a 500 Hz range. The two lowest frequency modes (122 and 159 Hz) are too close to the lower limit of 40 Hz to be reliable. However, they present shapes very similar to the other modes in the group. They are single-lobe whoosh modes. More whoosh modes appear in the green, blue, and magenta bands. The c2 rsd nsg modes of these three bands were shown in the previous section.

As will be seen below, the curvature of the inlet duct introduces distortion in the upstream backswept lobes, which makes it difficult to count their number. However, it will be seen that as the frequency increases, so does the number of lobes. Thus, the rotational velocity relative to the impeller is bounded, in the same range as for straight inlet ducts: between 20% and 36% of Ω_{RO}. In the blue band, a mode marked with "A" matches the e0D75 maximum amplitude at the *whoosh* band.

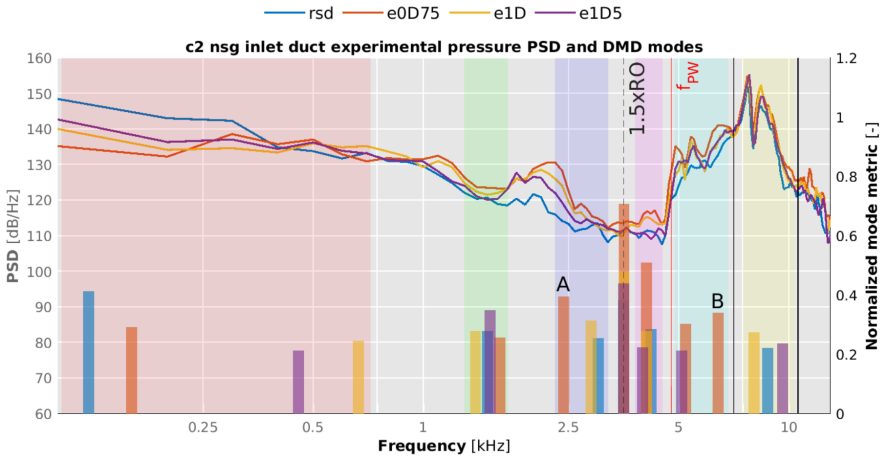

Figure 5.50: *Reminder of the DMD and experimental inlet duct spectra for compressor c2 operating at nsg. The frequency range was selected to show the asynchronous modes in detail. The red, green and magenta bands mark common asynchronous modes. The blue, cyan and yellow bands gather isolated modes. The two modes marked with "A" and "B" match local amplitude maxima at the e0D75 spectrum.*

Finally, the high-frequency broadband modes appear in cyan and yellow, where another e0D75 mode matching an outstanding amplitude maximum is marked with "B". The characteristics of these modes will be discussed in the following.

Figure 5.51: *Modal shape of c2 nsg "whoosh modes" around 1500 Hz (green band at figure 5.50). From left to right: 0D75, e1D and e1D5.*

Figure 5.51 shows the modes from the green band of previous figure. They have the familiar shape of the "whoosh modes" with lobes upstream of the inducer and content in the diffuser and the volute. These modes gather structures at the frequencies of the *whoosh* noise broadbands shown in the spectrum above. In the modes of the smaller curvature radii elbows, the lobes are more distorted since the geometry forces them to rotate around the elbow axis of curvature. The lobes of such modes penetrate the horizontal inlet duct. On the other hand, the elbow with the largest radius has lobes whose main axis of

twist is the vertical axis of the impeller, and they do not reach the horizontal section of the inlet duct.

Figure 5.52: *Modal shape of c2 nsg "whoosh modes" around 4000 Hz (magenta band at figure 5.50). From left to right: 0D75, e1D and e1D5.*

The modes corresponding to the magenta broadband in Figure 5.50 are shown in Figure 5.52. As stated above, these higher frequency modes present a larger number of lobes. The difference in the curvature of the modes toward the horizontal inlet duct is more evident than in the previous figure.

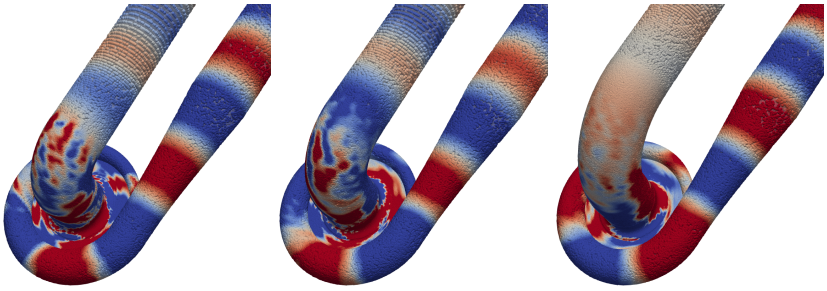

Figure 5.53: *Propagation of the c2 nsg "whoosh modes" around 4000 Hz. From left to right: 0D75, e1D and e1D5. The inlet duct of the greater elbow radius (right figure) shows the lowest amplitude.*

Figure 5.53 shows the propagation of the magenta band modes. As expected, they propagate in both ducts as a plane wave. It is noteworthy that the two cases of smaller radii have a higher amplitude in the inlet duct than the elbow of larger radius. It can be seen that these modes are more distorted by the curvature of the elbow and penetrate the horizontal inlet duct. These amplitude differences at the inlet are consistent with those shown in the measured spectra. The interaction of the lobes of the left and central images with the upper elbow wall is apparent.

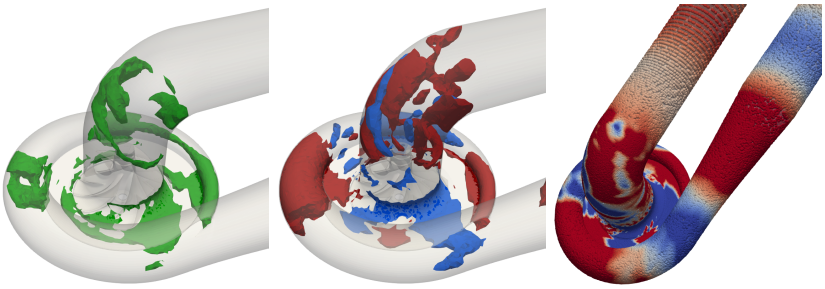

Figure 5.54: *Maximum amplitude, modal shape and propagation of mode c2 e0D75 nsg, marked "A" in figure 5.50. This is clearly a "whoosh mode" and appears at the frequency of the whoosh noise band.*

The mode depicted in Figure 5.54 belongs to the blue band in Figure 5.50 marked with "A". It is the case e0D75 and coincides in frequency with the highest amplitude of the measured *whoosh* noise band. It is clearly a whoosh mode, with the maximum amplitude in the lobes upstream of the inducer, the diffuser, and the VT region. It propagates through the ducts as a plane wave. This again confirms the correlation of this type of mode with the *whoosh* noise observed in the spectra.

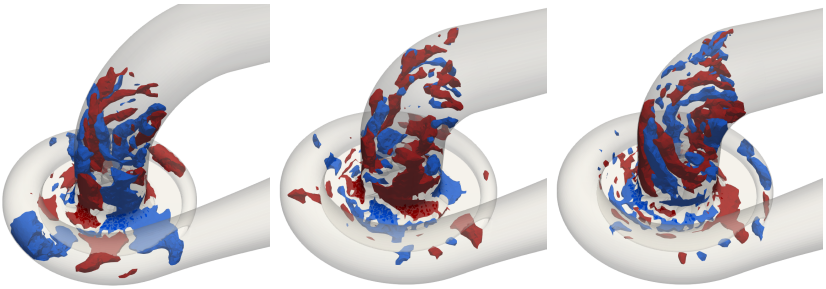

Figure 5.55: *Modal shape of the c2 nsg modes at the cyan band of figure 5.50, inside the high-frequency broadband. The first mode (left) belongs to geometry e1D5. The other two belong to e0D75. The third mode (rignt) is marked "B" in the mentioned spectrum.*

The three modes of the high-frequency broadband in cyan are shown in Figure 5.55. Their shape is similar to the whoosh modes seen previously. Central and right-hand images, corresponding to the elbow of the smallest curvature radius, present more distorted modes that reach the horizontal inlet duct. They have a high number of narrow lobes. The mode in the right image coincides with a local maximum in amplitude at the high-frequency broadband marked with "B". In this e0D75 case, there is a good correlation between the local maxima of the measured spectrum and the most relevant DMD modes.

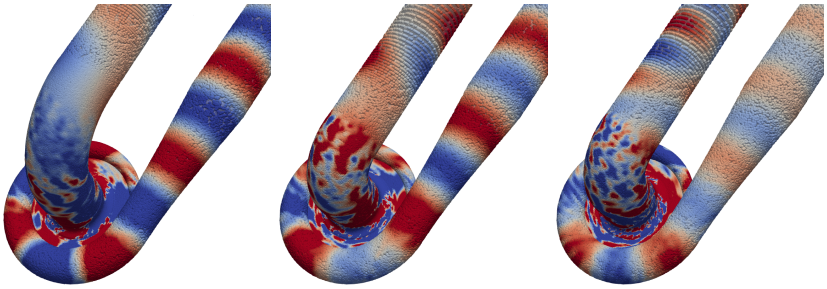

Figure 5.56: *Propagation of the c2 nsg modes at the cyan band of figure 5.50. The first mode (left) belongs to geometry e1D5. The other two belong to e0D75. The third mode (right) is marked "B" in the mentioned spectrum.*

The duct propagation of the above analyzed modes is shown in Figure 5.56. The outlet duct shows almost plane wave propagation, as the modes are only slightly above the theoretical frequency limit. At the inlet, the pattern is more complex. The influence of the lobes from the previous figure is clearly seen in the elbows. The central and right-hand images show how the lobes interact with the upper elbow wall.

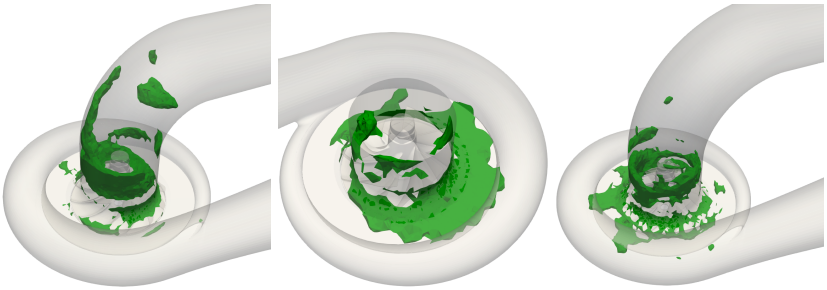

Figure 5.57: *Maximum amplitude of the c2 nsg modes at the yellow band of figure 5.50, under the high-frequency broadband. Left to right: e1D, rsd and e1D5.*

Figure 5.57 shows the amplitude of the three high-frequency broadband modes in the yellow band, in increasing order of frequency. The first mode has a profile more characteristic of the whoosh modes, with an elongated lobe upstream of the inducer. The other two modes, especially the one in the central image, (already seen in the previous section, in figure 5.42) has greater amplitude at the TC and diffuser. This feature is characteristic of the TCN modes found in other cases in the high-frequency broadbands.

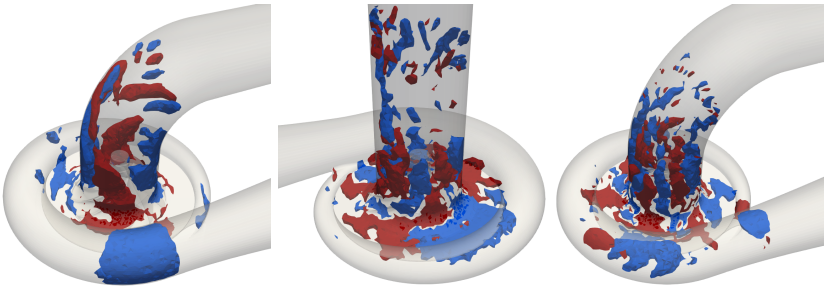

Figure 5.58: *Modal shape of the c2 nsg modes at the yellow band of figure 5.50, under the high-frequency broadband. Left to right: e1D, rsd and e1D5.*

Figure 5.58 shows the shape of the previously discussed modes. The left image shows wider lobes. The central and right images show narrower and more numerous lobes. In addition, the shape of these modes completely covers the TC. From this figure and figure 5.57, where the maximum amplitude was shown, it can be concluded that the left mode has characteristics more similar to the whoosh modes, while the central and right modes are of the TCN subtype.

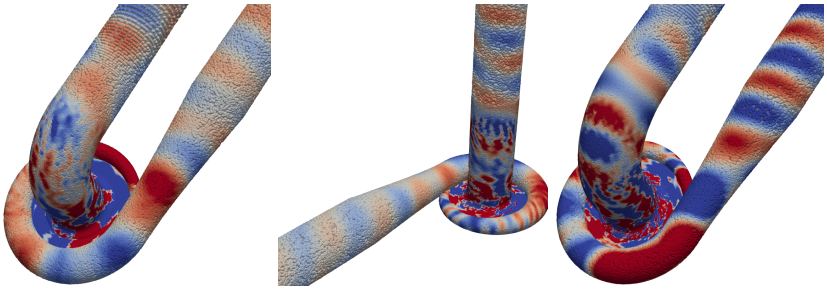

Figure 5.59: *Propagation of the c2 nsg modes at the yellow band of figure 5.50, inside the high-frequency broadband. Left to right: e1D, rsd and e1D5.*

The propagation in the ducts of these modes is shown in Figure 5.59. It can be seen how all modes have the complex wave patterns in both ducts characteristic of high-frequency modes.

A summary of the analysis performed on the c2 nsg modes is herein presented. A set of four geometries of the compressor c2 operating near surge has been studied: the straight inlet duct (rsd) and three elbows of different curvature radii: e0D75, e1D, and e1D5. The measured inlet spectrum was dominated by the high-frequency broadband, followed by the BPF tone and whoosh noise bands. These bands had an amplitude inversely proportional to the inlet duct curvature radius.

As in the c1 nsg cases, a few synchronous modes appear, subordinated to the BPF and 2×BPF. The rest of the modes are asynchronous. All asynchronous modes below the plane wave frequency f_{PW} are of the whoosh type.

The correlation of these modes with the *whoosh* noise broadbands has been demonstrated. Modes were found to reproduce the trend seen in the amplitude of the *whoosh* noise versus the curvature radii of the inlet ducts. Reducing the radius causes the lobes upstream of the inducer to distort, interacting with each other and with the upper wall of the elbow. In addition, the upper boundary of these lobes penetrates the horizontal inlet duct.

The proposed hypothesis is that the higher amplitude presented by these modes is due to the interaction of the lobes with each other. In addition, the space restriction to these lobes generates interaction with the surfaces of the duct and the impeller. The presence of such lobes at the end of the horizontal inlet duct may contribute to a better propagation of the pressure oscillations resulting from their interactions but is not the main cause of the high amplitude. The inlet duct of the rsd case is fully exposed to the lobes and does not have as high amplitude in the whoosh bands. That is because, in the straight duct case, the lobes rotate in an orderly manner around the impeller axis without interacting with each other. The interaction with the walls is also weaker than in the case of reduced radius elbows. On the other hand, the largest radius elbow is located halfway between the smaller elbows and the straight duct. Its lobes are distorted, although to a lesser extent, and do not reach the horizontal inlet duct.

Finally, modes with a greater number of narrower lobes are observed in the high-frequency broadband. They also have more amplitude in the TC and diffuser than the low-frequency whoosh modes. They are similar to TCN modes shown in the high-frequency broadband of the previous sections.

5.4 DMD analysis of the impeller flow field

The DMD analysis presented in the previous sections was carried out with a probe cloud over the entire computational domain except for the volume swept by the blades. In this section, the modes inside the rotating region will be studied. It will improve the understanding of the modes described above, their interaction with the impeller, and their relation to the acoustic sources.

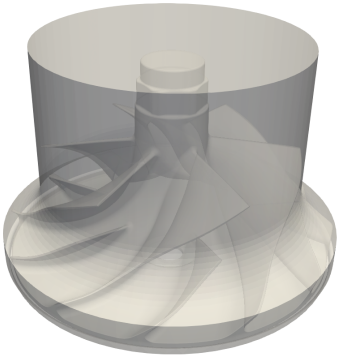

Figure 5.60: *CAD representation of the rotating impeller region of compressor c2.*

Pressure data analogous to those used for the DMD analysis in the previous sections were stored in compressor c2 but in the rotating impeller region. This region is shown in Figure 5.60 and includes the volume swept by the blades, the first 18 mm upstream of the LE, the tip clearance, and a 2 mm radius at the TE to the diffuser inlet.

All parts of this region except the volume swept by the blades were already

part of the point cloud analyzed in the previous sections. However, in this section, the probes rotate along with the impeller, so they are static in the moving reference frame.

The objective of this section is not to perform an exhaustive analysis of the modes in the rotating region. Only those modes which allow a deeper understanding of the flow field and its structures analyzed in the previous section will be shown. Analogous to what was seen in the preceding sections, the difference between operating points is the kind of modes that appear. Near the bep, there are more synchronous modes, and near surge, there are more asynchronous modes, but the shape of such modes is very similar among operating points. Also, the different geometries do not appreciably affect the shape of the modes in the rotor region.

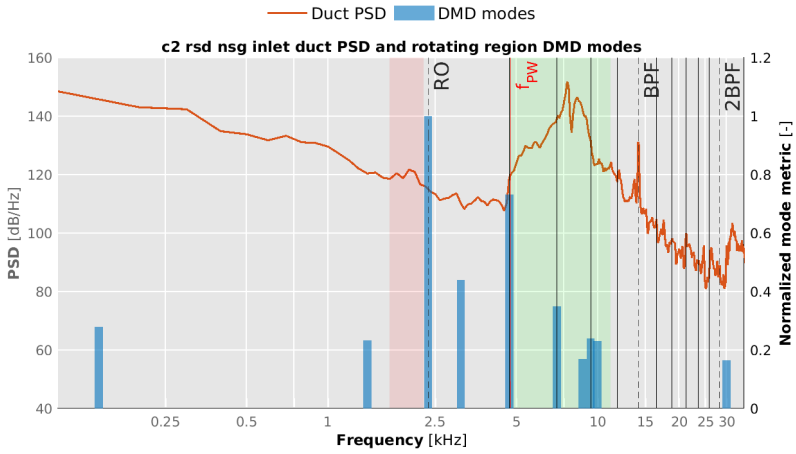

Figure 5.61: *Rotating impeller region DMD, and experimental inlet duct spectrum for c2 rsd nsg. Solid black lines signal multiples of the RO. f_{PW} is the plane wave limit. Red and green bands signal broadbands of interest.*

Figure 5.61 shows the rotating region DMD spectrum of the c2 rsd nsg case. The rest of the cases show similar spectra. The most relevant modes appear at the first multiples of the RO, while the rest are at asynchronous frequencies, most of them lower than the BPF. The first striking change is that the BPF and 2×BPF frequencies that dominated the static domain modes do not even appear in these spectra.

In the previous sections, it was seen that the BPF and 2×BPF modes correspond to the static pressure pattern rotating along with the impeller. For this reason, the DMD modes, which have a harmonic time evolution, do not reflect such a static pattern. However, the modes corresponding to the RO and its multiples show a relationship with the BPF and the 2×BPF.

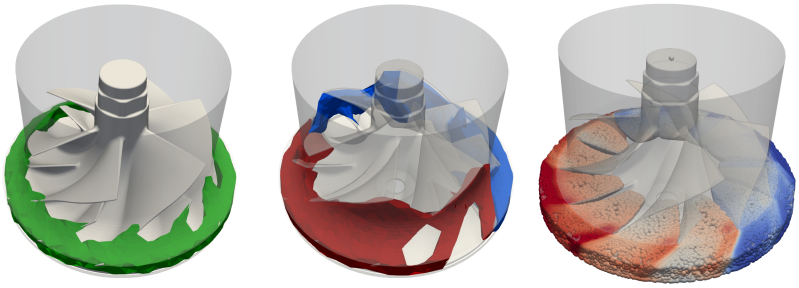

Figure 5.62: *Maximum amplitude, modal shape, and mode distribution for the RO mode of c2 rsd nsg, in the rotating impeller region.*

Figure 5.62 shows the RO mode of the c2 rsd nsg case. It can be seen that the largest amplitude appears in the TE region. The mode divides the rotor into two halves in phase opposition. The right image shows the channels from the splitter blade LE to the TE. It can be seen how each channel between main blades (every two splitter blade channels) is in a different phase. From one main channel to the next, there is an offset of $T/6$, being T the mode period. There is phase opposition ($T/2$ offset) three main channels away from the initial one.

The mode has one lobe of each color, and its frequency is 1×RO. The equation 5.22 results in a rotation rate equal to Ω_{RO}. The mode moves around the "static" impeller with an angular velocity of Ω_{RO}. Alternatively, this is a static perturbation in the circumferential pressure profile of the diffuser that the impeller "sees" once every revolution.

The probes in each of the 6 impeller main channels oscillate at the RO but with a $T/6$ offset. Each time the impeller makes one revolution, 6 offset oscillations are completed. The frequency at which a static observer perceives these oscillations is 6×RO, i.e., the BPF. The trailing edge region interaction with the VT pressure perturbation to generate a tone at the BPF is known as the "clocking" effect of the volute tongue.

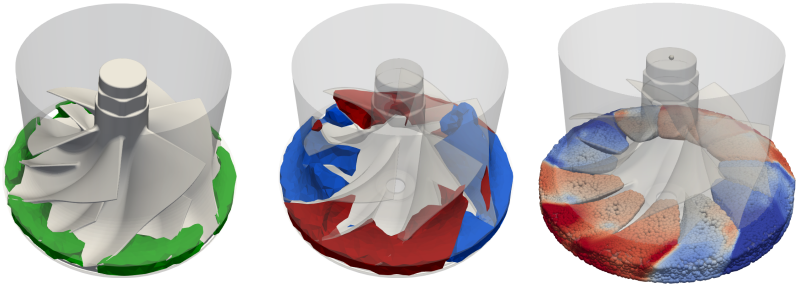

Figure 5.63: *Maximum amplitude, modal shape, and mode distribution for the 2×RO mode of c2 rsd nsg, in the rotating impeller region.*

Figure 5.63 shows the mode corresponding to the 2×RO frequency, which

has two lobes of each color. The offset between individual splitter channels is $T/6$, and for every impeller revolution, two periods are completed, thus giving rise to a tone at the 2×BPF by the same mechanism described above.

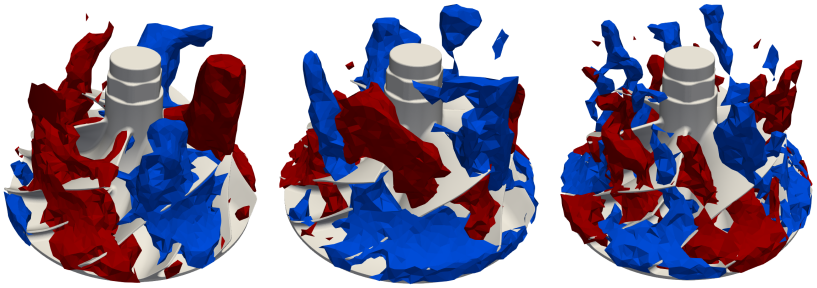

Figure 5.64: *Modal shape of asynchronous modes at the rotating impeller region of c2 rsd nsg. The characteristic "whoosh mode" lobes appear and are chopped by the blades.*

Figure 5.64 shows some of the asynchronous modes of the rotating region of c2 rsd nsg. All asynchronous modes exhibit a similar pattern of backswept lobes. These are the same lobes that appeared in the whoosh modes of the stationary domain. The blades chop down the lobes because their rotational speed is lower than that of the impeller. The resulting spatial pattern corresponds to that observed in the TC of the whoosh modes.

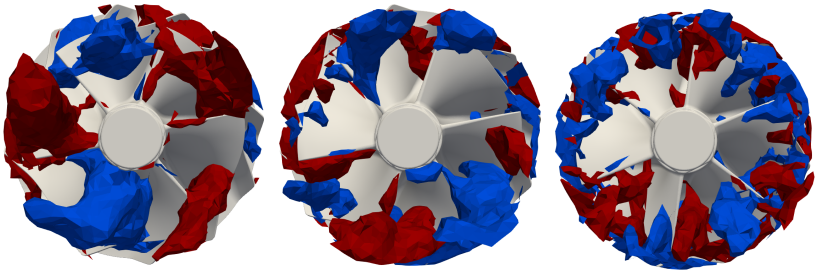

Figure 5.65: *Top view of the modal shape of asynchronous modes at the rotating impeller region of c2 rsd nsg.*

Figure 5.65 shows the top view of the above modes. It can be seen that their location is on the outer radii, close to the blade tip.

The whoosh modes described in the previous sections exhibited a rotational velocity between 20% and 36% of Ω_{RO}. The absolute rotational velocity of the lobes in the rotating region can be obtained with the relation $\Omega_{abs} = \Omega_{rel} + \Omega_{frame}$. The absolute velocity is that seen by the static observer (20% to 36% of Ω_{RO}), the relative velocity is that of the lobes with respect to the impeller in the moving reference frame, and the velocity of the reference frame is Ω_{RO}.

According to the above relationship, in the moving reference frame, the modes should have a relative velocity between 64% and 80% of Ω_{RO}, and in the opposite direction, to correspond to the whoosh modes observed in the stationary domain. The mode in the right image in figure 5.64 has 6 lobes and a frequency of 8768 Hz. The equation 5.22 gives a rotational speed of 62.6% of Ω_{RO}. The lower frequency and lower lobe number modes show similar values.

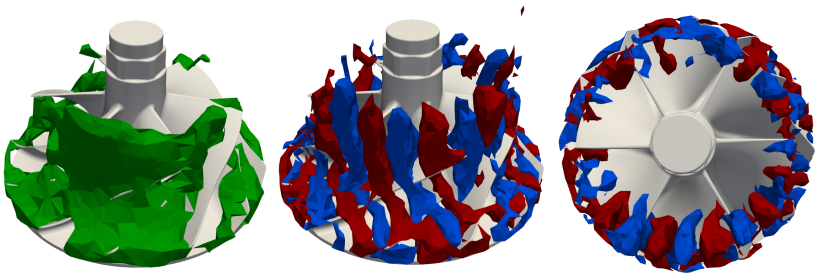

Figure 5.66: *Maximum amplitude, modal shape, and top view of a c2 rsd bep TCN mode. The maximum amplitude region is placed around the TC. There are numerous thin lobes presenting a slope opposite to the blades in the TC.*

A higher frequency mode corresponding to the TCN band of the c2 rsd bep case is shown in Figure 5.66. This mode has a relative velocity of 76% Ω_{RO}. It can be seen that it has thinner and more numerous lobes. They are practically vertical in the inducer, and in the TC, they have a slope opposite to the blades. This pattern corresponds to that shown by the TCN modes in the tip clearance. It shows the thin lobes being cut by the impeller blades. The right-hand image displays how the mode is distributed near the blade tip and TC.

Dipolar acoustic sources

The force on the impeller surfaces was also stored to calculate the acoustic sources. As described in section 4.3.5 of the previous chapter, the acoustic analogy of Ffowcs Williams and Hawkings [50] provides the expression for dipolar acoustic sources, which are the main contributors for centrifugal compressor noise [51].

$$p'_L(\mathbf{x},t) \approx \frac{x_i}{|\mathbf{x}|}\frac{1}{c_\infty^2}\frac{\partial}{\partial t}\int_{S_o}\left[\frac{p_{ij}n_j}{4\pi|\mathbf{x}||1-M_r|}\right]_{\tau=\tau^*} dS \tag{5.23}$$

Disregarding the effects of propagation to the observer, the amplitude of the dipole sources is proportional to the time derivative of surface loading. The DMD of the impeller surface loading time derivative was carried out. It will allow evaluating the effect on the dipole acoustic sources of the structures observed in the modes described previously.

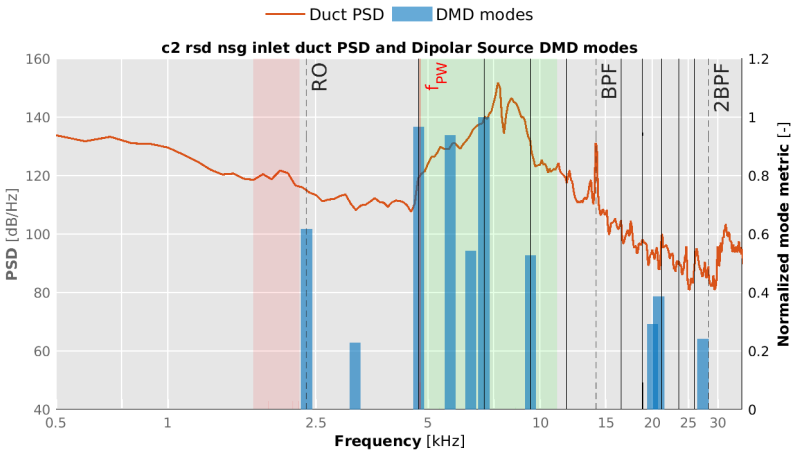

Figure 5.67: *Dipolar source DMD, and experimental inlet duct spectrum for c2 rsd nsg. Solid black lines signal multiples of the RO. f_{PW} is the plane wave limit. Red and green bands signal broadbands of interest.*

The spectrum of the dipolar sources for the case c2 rsd nsg is shown in Figure 5.67. It is similar to the pressure spectrum in the impeller rotating region shown in figure 5.61. The spectrum has synchronous modes in multiples 1 to 4 of the RO. The rest of the modes are asynchronous. The most relevant ones are in the mid-frequencies (green band). Since these data are stored in the rotating reference frame, tones at the BPF and 2×BPF do not appear.

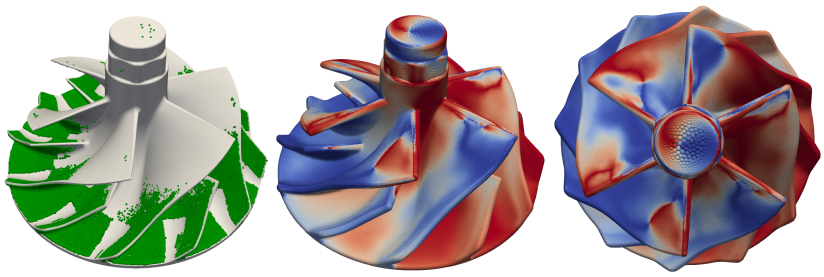

Figure 5.68: *Maximum amplitude, modal distribution, and top view of the dipolar sources at the impeller surface of the RO mode of c2 rsd nsg.*

Figure 5.68 shows the mode corresponding to the RO. The maximum amplitude is concentrated at the trailing edge region. Its distribution is the same as in the RO mode in the rotating impeller region seen in figure 5.62. This mode corresponds to the static pressure perturbation of the volute tongue, "rotating" around the impeller. In its rotation, it generates six tones offset by $T/6$, which give rise to the BPF tone perceived by the static observer.

The central figure clearly shows how the two splitter channels that form

each main blade channel are in the same phase, as they present the same tonality. For this reason, the "clocking" effect of the volute tongue gives rise to the BPF tone.

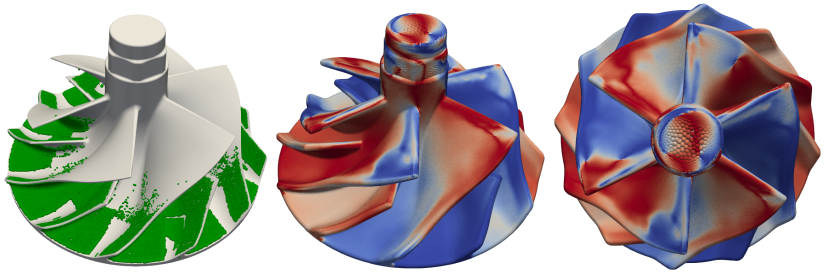

Figure 5.69: *Maximum amplitude, modal distribution and top view of the dipolar sources at the impeller surface of the 2×RO mode of c2 rsd nsg.*

Figure 5.69 shows the 2×RO mode. The maximum amplitude appears near the impeller TE. The mode distribution presents two static pressure perturbations interacting with the trailing edge, giving rise to the 2×BPF tone perceived by the static observer. The generation mechanism is the same described for the impeller rotating region: in each impeller revolution, a set of six offset tones completes two oscillations.

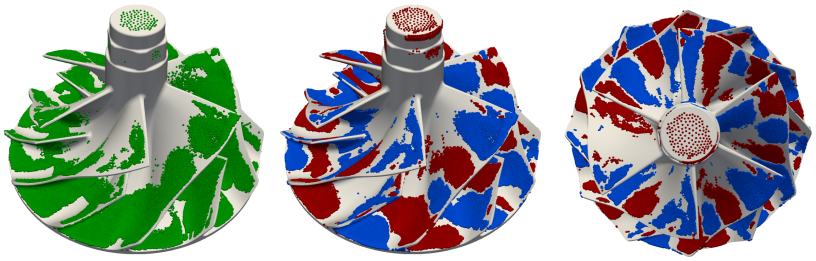

Figure 5.70: *Maximum amplitude, modal shape and top view of the dipolar sources at the impeller surface of an asynchronous mode of c2 rsd bep.*

Figure 5.70 shows one of the asynchronous modes of the c2 rsd bep case. It is an oscillation of the surface loading whose maximum amplitude is distributed at the largest radii of the blade. The mode shows a pattern of alternating bands on the surface, which coincides with the different-colored lobes cut by the blade.

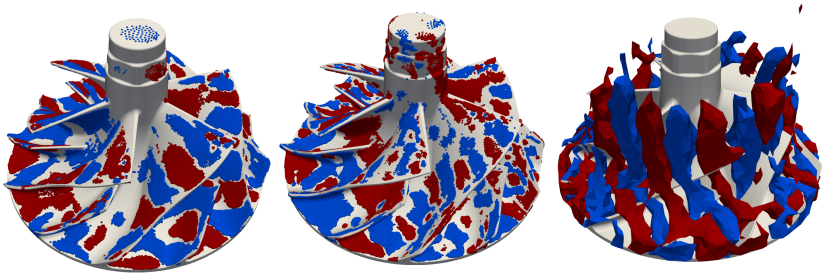

Figure 5.71: *Modal shapes of two asynchronous modes of the dipolar sources, and a TCN mode of the rotating impeller region. The alternating bands on the impeller surface match the alternating lobes interacting with the blades.*

Other examples of asynchronous modes of dipolar sources are shown in figure 5.71. The same pattern can be observed, but with a different number of bands of each color. The right image shows one of the pressure modes in the rotating impeller region, which exhibits the lobes being chopped by the vane.

The analysis of the dipolar source modes has made it possible to relate the flow structures described throughout the chapter to the most relevant acoustic sources. The pressure perturbations at the diffuser interact with the impeller trailing edges to produce tones at the BPF and 2×BPF. For their part, the whoosh-mode lobes cut by the blades produce blade loading oscillation near the blade tip.

5.5 Conclusions

The objective of this chapter was to relate the ducts measured spectra to the properties of the pressure field using DMD. Three main components dominate the analyzed spectra: the tone at BPF, a broad band of high frequencies (TCN), and broadbands below plane wave (*whoosh* noise). The DMD modes have provided relevant information on the generation mechanisms of these spectral components.

The tones at BPF (and 2×BPF) are generated by the static pressure pattern in the impeller LE. Moreover, the interaction between the TE and the pressure perturbations in the diffuser, such as that caused by VT, also excite these tones.

In the low-frequency broadbands, so-called “whoosh modes” have been found. These modes have alternating lobes upstream of the inducer and show pressure oscillation in the TC, the diffuser, and near the VT. These modes correspond to the vortices associated with the rotating stall in the literature. It has been shown how such vortices rotate at a lower velocity than the impeller and are chopped by the blades.

Above plane wave, the “TCN modes” are variants of the “whoosh modes” with a larger number of thinner vortices and present the largest amplitude

concentrated in the TC. The interaction of the small high-frequency vortices with the impeller blades generates the greatest pressure oscillations in these modes.

It has been shown how the described modes generate unsteady surface loading on the impeller blades thus exciting the dipolar acoustic sources. The synchronous tones excite the TE by interacting with the static pressure perturbations in the diffuser, while the asynchronous modes (whoosh and TCN) interact with the larger blade radii when they cut the vortices.

Throughout the chapter, the influence of the inlet geometries on the measured noise has been analyzed. In compressor c1, the different inlet geometries alter the noise by their ability to transmit the noise generated downstream. The tapered duct (tap) reduces the average amplitude across the spectrum, while the reservoir (rsv) attenuates the tonal noises in the bep and reduces the low-frequency noise in nsg through resonance.

In compressor c2, an inverse relationship is found between the elbow curvature radius and the amplitude in the *whoosh* noise bands and the lower half of the TCN band. The modes show how the vortices upstream of the inducer are distorted due to the elbow curvature. This distortion increases the interaction between vortices and with elbow walls, and produces an amplitude increase in the broadbands mentioned above.

Finally, the influence of the operating point on noise generation has been studied. The pressure field at the bep point is dominated by synchronous phenomena. The BPF and 2×BPF tones show the maximum intensity at the impeller LE. As the mass flow rate is reduced and the nsg point is reached, asynchronous whoosh modes appear. The BPF and 2×BPF tones show less intensity in the LE impeller, and the excitation mechanism in the TE is the main one.

The c2 rsd bep case shows intermediate behavior between those seen in c1 bep and c1 nsg. It has a large number of synchronous modes but presents some whoosh-like modes.

6

Study of the noise-generating flow structures

Contents

6.1 Introduction

This chapter completes the analysis methodology described previously by analyzing the flow structures responsible for the spectral components of interest.

In the previous chapter, the DMD method revealed specific spatial patterns of the pressure field related to the frequencies of the duct spectra. In this chapter, the conventional flow field, i.e., velocities, pressure, and other thermodynamic conditions in the time domain, will be studied to identify which flow structures correspond to the DMD modes of interest.

Once these flow structures have been identified, the effect of inlet duct geometry and operating conditions on them will be studied.

The first part of the chapter will be devoted to analyzing the average flow field in three regions of the compressor: upstream of the inducer, the impeller, and the diffuser. In the second part of the chapter, unsteady flow structures will be studied. Finally, conclusions are drawn on the relationship of geometry and operating conditions to the flow structures of interest.

The geometries and operating conditions analyzed are the same as in the previous chapter: the four simple geometries of compressor c1 operating at bep and nsg, the reference straight ducts (rsd) of compressor c2 operating at bep, hpr, and nsg, and the three elbows of different radii of compressor c2 operating at nsg.

6.2 Inducer mean flow field of compressor c1

In this section, the analysis of the mean flow field upstream of the inducer of compressor c1 is performed. The average was taken from at least 20 impeller revolutions in each case.

The inlet geometries str, rsv, and tap of compressor c1 are axisymmetric, and their average flow field in the inducer is practically identical. Therefore, the c1 str cases are shown alone as the paradigm for axial inlet geometries. The flow field of the str cases is compared with that of the elb cases to study the influence of the inlet elbow.

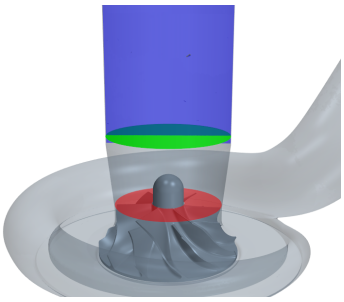

Figure 6.1: *Inlet sections for compressor c1. In blue the "long1" section, in green "upstream1", and in red "inducer1".*

Figure 6.1 shows the sections used for the inlet flow field analysis. There are two cross-sections and one longitudinal. The longitudinal section, in blue, is in the symmetry plane of the inlet duct and reaches down to the rotating impeller region. The green section is located at the end of the straight section of the inlet duct, 25 mm (0.6 diameters) upstream from the impeller leading edge (LE). Downstream of the green section begins the the rotating impeller region. The red section is in said region, 1 mm upstream of the LE. It rotates along with the impeller, thus the average

flow field in that section is expressed in the rotating reference frame. Throughout the chapter, the blue longitudinal section will be referred to as "long1", the green section, as "upstream1" and the red section as "inducer1". The velocity components tangential to any given section will be named "secondary velocity".

6.2.1 Straight inlet duct

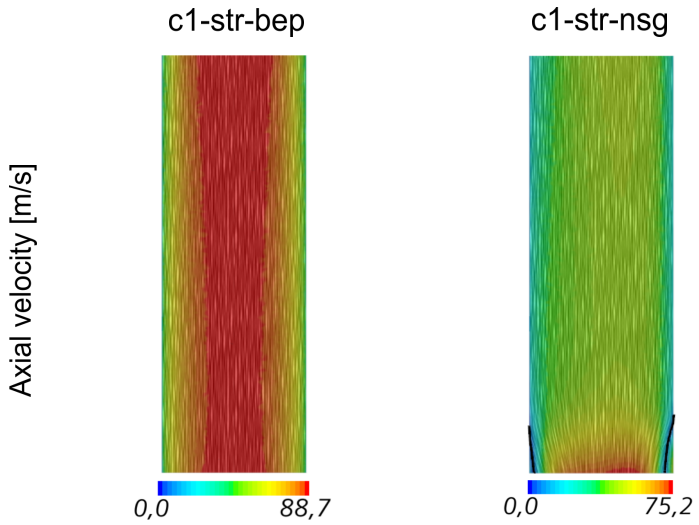

Figure 6.2: *Average velocity field in the long1 section. The black line marks the zero axial velocity isosurface. The LIC of the velocity is represented over the axial velocity contours.*

In figure 6.2 the velocity field is displayed at the long1 section of the straight duct cases (str) of compressor c1. The line integral convolution (LIC) technique is used to visualize the streamlines by adding a static random pattern of dark and light paint sources. At the best efficiency point (bep), the velocity is axial and uniform. At the near surge point (nsg), the velocity field is uniform until backflow appears in the bottom section of the duct. This causes two phenomena. On the one hand, the passage section is narrowed, which causes an acceleration of the axial flow, and on the other hand, the reverse flow has a high angular momentum transferred by the impeller.

In figure 6.3 the secondary velocity on the upstream1 section is shown. In the bep, the secondary velocity has a very weak radial center-wise pattern. The maximum secondary velocity is 1.2% of the peak axial velocity at the section center. For its part, the secondary velocity at the nsg point is dominated by the backflow angular velocity. The reverse flow is at the periphery of the section, outside the black line with zero axial speed. It has a high rotational velocity.

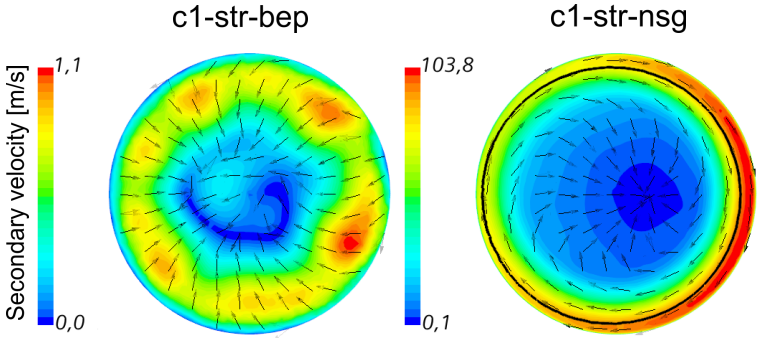

Figure 6.3: *Secondary velocity field in the upstream1 section. The black line marks the zero axial velocity isosurface. The contour shows the magnitude of the secondary velocity, and the vectors show the direction.*

The flow on the other side of the black line inherits this angular velocity due to viscous friction. Near the center of the section, a center-wise radial velocity can be seen due to the narrowing of the passage section caused by the reverse flow. In this case, the secondary velocity is of the same order of magnitude as the axial velocity.

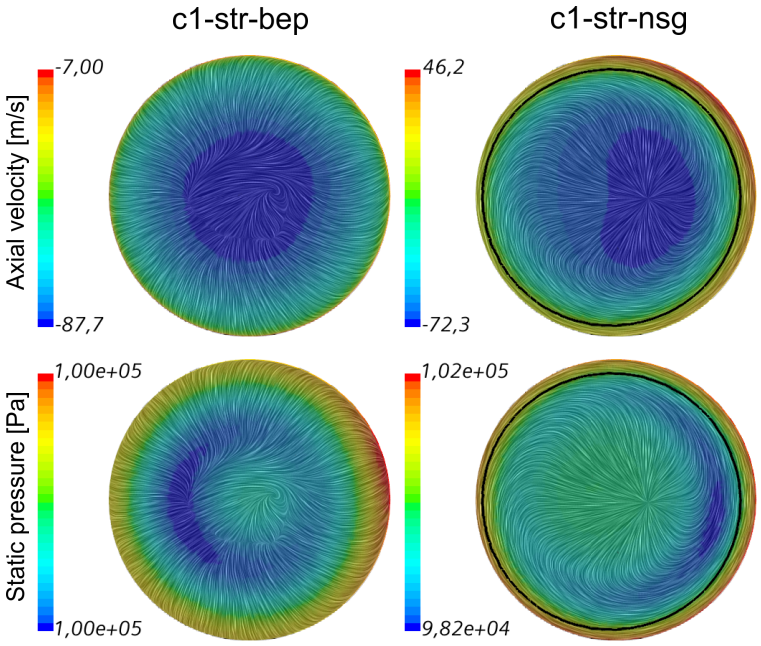

Figure 6.4: *Axial velocity and static pressure contours over LIC of the secondary velocity in the upstream1 section. The black line marks the zero axial velocity isosurface.*

In the first row of figure 6.4, the axial velocity of the c1 str cases at the

upstream1 section is displayed. It can be seen that the spatial distribution in both cases is eminently axisymmetric (despite a certain eccentric deviation in the nsg case) and is dominated by the axial component in the bep case. Near surge, the section center is dominated by the axial velocity, while in the periphery, there is a strong swirl due to backflow. Regarding pressure, in the bep case, the pressure is practically uniform (changes below 0.5%). In the nsg case, as the backflow is made up of compressed air, it has a higher pressure than the incoming flow. The minimum pressure is not found in the center of the sections but in an annulus around it. That is caused by the presence of the impeller nut downstream, which yields a circular crown-shaped passage section.

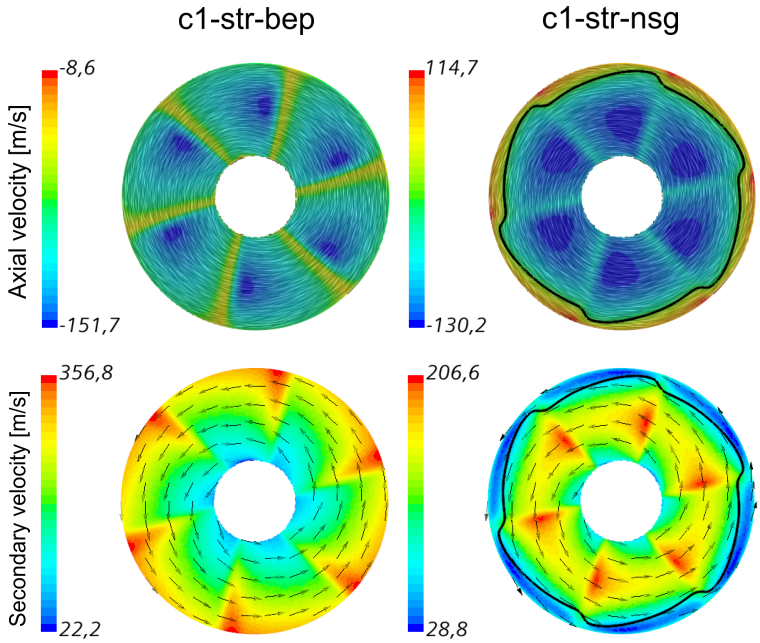

Figure 6.5: *Average velocity field in the rotating inducer1 section. The first row shows the axial velocity over the LIC of the secondary relative velocity. The contours indicate the magnitude. At the second row the contours show the relative secondary velocity magnitude, while the arrows mark the direction. The black line represents the zero axial velocity isosurface.*

Figure 6.5 shows the time-averaged velocity field in the rotating inducer1 section. In the first row, the axial velocity can be seen. Since the reference frame of the post-processing section inducer1 rotates with the impeller, the blades are static from the point of view of the inducer1 section. In the bep case, the blade leading edges appear in yellow as the areas of lowest axial velocity (keeping in mind that the velocities are negative as they are downward on the Z-axis). The highest axial velocity appears in the channels, just behind the blade LE. In the nsg case, there is positive axial velocity (upward) at the

outer radii due to the backflow. In the center of the section, on the other side of the zero axial velocity black line, the axial velocity has a more uniform distribution than in the bep due to the smaller available section.

The second row shows the secondary velocity, i.e., tangent to the inducer1 section. In these sections, the relative velocity is shown. The observer is placed on the impeller, rotating in the clockwise direction. As seen in the previous sections, the flow arriving at the inducer has a vertical downward velocity, with no rotational component of relevance (except in the backflow). The mobile observer sees the flow rotating in the counter-clockwise direction. The relative secondary velocity follows the expression $v_{abs} = v_{rel} + v_{frame}$. Since v_{abs} is close to zero, the relative velocity is $-v_{frame} = -\Omega_{frame} \times r$, where r is the radius. In the bep case, the velocity trajectory is formed by concentric circles, and its magnitude, denoted by the contours, grows linearly with the radius. The maximum velocity appears at the blade tips. In the nsg case, the situation is the same in the first half of the blade radii. However, in the blade tip, the backflow region has a low relative velocity because it carries the angular momentum of the impeller. The low relative velocity of the backflow causes the maximum secondary velocity to be reached approximately in the middle of the blade radius.

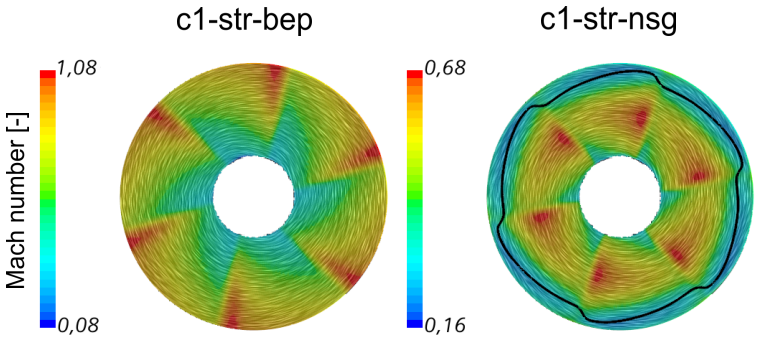

Figure 6.6: *Average Mach number in the rotating inducer1 section. The contours indicate the magnitude. The LIC displays the direction of the secondary velocity. The black line represents the zero axial velocity isosurface.*

Figure 6.6 shows the Mach number relative to the impeller over the LIC of the relative secondary velocity. The magnitude of the Mach number shows the same distribution as the relative secondary velocity seen in the previous figure. In the bep case, the maximum Mach appears at blade tips, where sonic conditions are reached. In the nsg case, due to the angular velocity of the backflow, the maximum Mach appears in the middle of the blade radius, and sonic conditions are not met.

Reaching sonic conditions implies a qualitative change in the noise-generating capability of the flow field. This fact is well documented in the literature, where, for example, Raitor and Neise [26] show how tonal noises dominate the acoustic spectrum of compressors where sonic conditions are reached.

Indeed, in the spectra shown in the previous chapter (Figures 5.11 and 5.20) it is shown how the inlet duct spectrum of c1 str bep is dominated by the BPF tone, while in c1 str nsg, this tone does not appear. Thus, the sonic conditions in the blade LE or its inhibition due to the backflow are very relevant flow structures in the noise generation in radial compressors.

The effects of the above conditions on the pressure field in the inducer1 section are shown in figure 6.7. In the bep case, there is a great pressure difference between the pressure side (PS) and suction side (SS) of the LE, especially at the tip, of approximately 30 kPa. At the nsg point, the maximum pressure jump between the PS and the SS occurs in the middle blade radius and has a magnitude of about 15 kPa. The maximum pressure in the nsg case appears in the backflow region, at the external radius, between the blades.

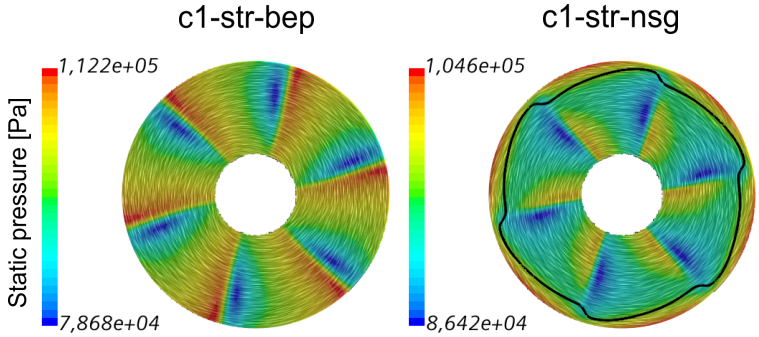

Figure 6.7: *Average pressure in the rotating inducer1 section. The contours indicate the magnitude. The LIC displays the direction of the secondary velocity. The black line represents the zero axial velocity isosurface.*

The pressure pattern shown in figure 6.7 coincides with the inducer region of the BPF mode in the c1 bep and nsg cases (Figures 5.13 and 5.22 of the chapter 5). The alternating lobes in the bep case had their maximum height at the LE tip, whereas in the nsg points, these lobes appeared only in the first half of the blade radius and with a markedly lower intensity. This way, the flow mechanism behind the most relevant difference in the synchronous sources of the bep and nsg spectra has been identified.

6.2.2 Elbow inlet duct

In this section,the average flow in the inlet of the c1 elb cases operating in the bep and nsg conditions will be analyzed. Figure 6.8 shows the nomenclature of certain geometrical characteristics of the inlet elbows that will be used throughout the chapter.

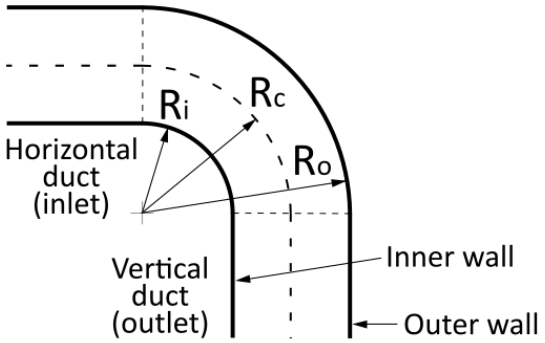

Figure 6.8: *Schematic elbow geometry with nomenclature. R_i stands for "inner radius", R_c for "curvature radius", and R_o for "outer radius".*

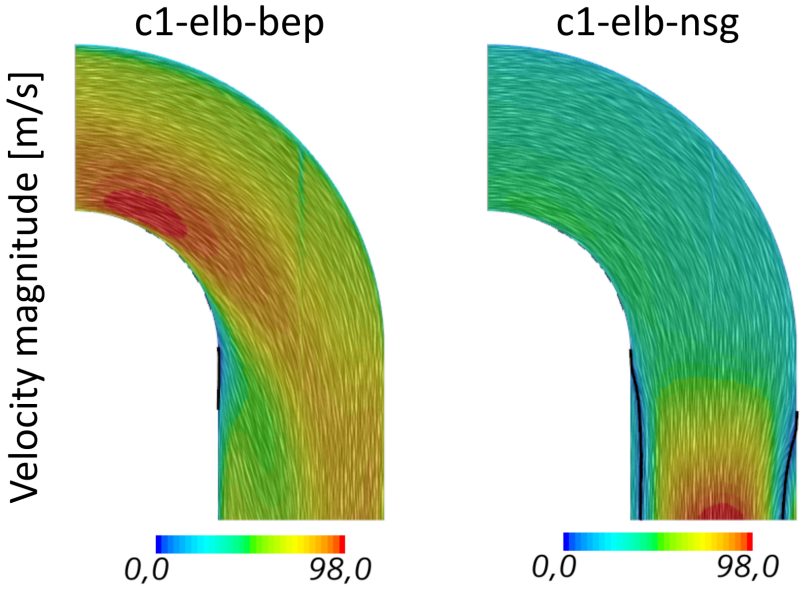

Figure 6.9: *LIC of the average inlet velocity in the long1 section. The contours show the velocity magnitude. The black lines mark the zero axial velocity isosurface.*

The velocity field in the long1 section is shown in figure 6.9. At the bep, the flow through the elbow is dominated by the inertia of the air from the horizontal duct. The change in direction imposed by the elbow generates a zone of low velocity in the outer radius of the duct where the horizontal flow hits the wall. At the inner radius, the horizontal velocity of the flow moves the air away from the inner wall. The flow speed is greater in this area, and a jet is formed that starts at the inner radius and ends at the bottom of the outer wall. The velocity in the vertical section following the inner radius is

smaller. This results in an uneven axial velocity profile in the last portion of the vertical section.

As for the nsg conditions, since the mass flow rate is lower (62 g/s compared to 116 g/s in the bep case), the flow enters the elbow with a lower velocity. Therefore, the effect of the direction change is less severe, and the flow in the vertical duct is dominated by backflow effects rather than inertial effects from the horizontal duct. The characteristics of the flow at the elbow outlet resemble those of straight ducts: acceleration due to section narrowing and vorticity induced by the reverse flow.

Figure 6.10 shows the average static pressure in the long1 section of the c1 elb cases. The left image shows the low pressure at the inner radius, where the velocity is maximum, and the high pressure at the outer radius, where the flow hits the wall. In the right image, corresponding to the nsg case, the radial pressure gradient also exists, but it is milder due to the lower flow velocity. In the vertical duct, pressure decreases when the flow is accelerated as the backflow reduces the cross-section. It is observed that the extent of the upstream backflow on the inner wall is more significant because, in this zone, the pressure and flow velocity are lower than at the outer wall.

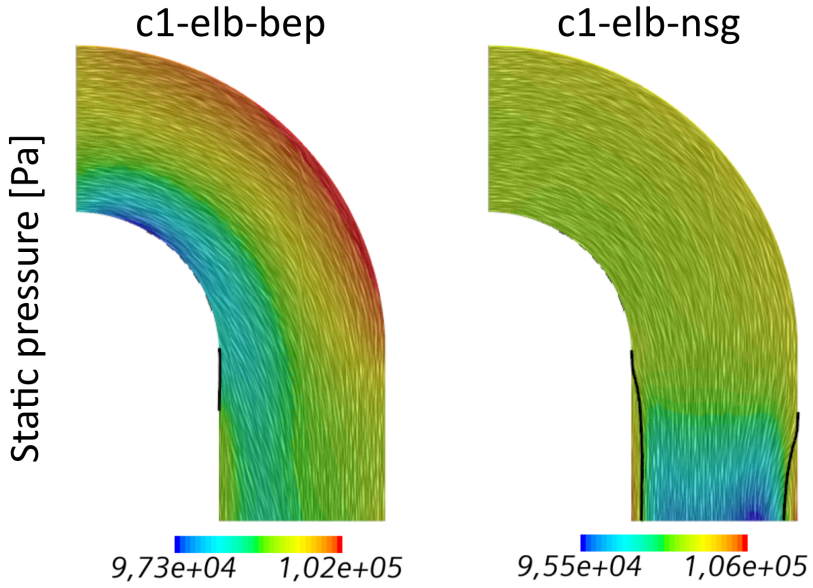

Figure 6.10: *Average static pressure over the LIC of the velocity in the long1 section. The black lines mark the zero axial velocity isosurface.*

In figure 6.11 the flow field in the upstream1 section of cases c1-elb is shown. The axis of the horizontal duct corresponds to the vertical direction in the figure. The lowest point of the section (at 6 o'clock) corresponds to the outer radius and the highest point (12 o'clock) to the inner radius.

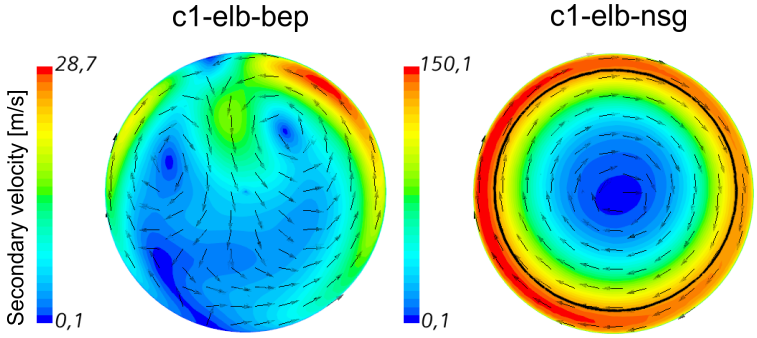

Figure 6.11: *Secondary velocity field in the upstream1 section. The black line marks the zero axial velocity isosurface. The contour shows the magnitude of the secondary velocity, and the vectors show the direction.*

In the bep (left figure), the pattern known as Dean vortices is observed in which two counter-rotating vortices are generated. This flow structure is described, for example, in [53]: "*In curved ducts, it is known that a pressure gradient is developed between the inner and the outer walls depending on the radius of curvature, the radius of the curved flow passage and the angle of the bend as well as the corresponding Reynolds number in the flow regime. The corresponding pressure gradient induces secondary flow because the particles near the inner wall of the curvature have higher velocity and are acted upon by a larger centrifugal force than the slower and higher pressure particles near the outer wall owing to the lack of the centrifugal force to overcome the pressure gradient over the cross-section in the curved section of the pipe. As a result, this pressure gradient driven secondary flow has a complicated flow structure consisting of the outer flow directed inwards along the wall and the inner flow directed outwards to fill up the deficit of the flow regime because of continuity.*"

The magnitude of the secondary flow in the c1 elb bep case is the largest found in all four c1 bep geometries, reaching up to 34% of the the axial velocity magnitude.

In the nsg point (right figure), a high secondary velocity region is seen in the area occupied by the backflow, outside of the black line. The backflow swirl is transmitted to the center of the section by the viscous friction. Therefore, the Dean vortices do not appear, or are overrun by the high vorticity induced by the backflow.

Figure 6.12 shows the average axial velocity and static pressure in the upstream1 section of the c1 elb cases. The LIC shows the Dean vortices described above in the left column corresponding to the bep. The axial velocity has the highest values in the inner radius (12 o'clock) and between the Dean vortices. At the bottom of the section, a crescent-shaped zone shows the minimum velocity near the outer wall. The static pressure is minimum between the vortices and maximum at the outer wall.

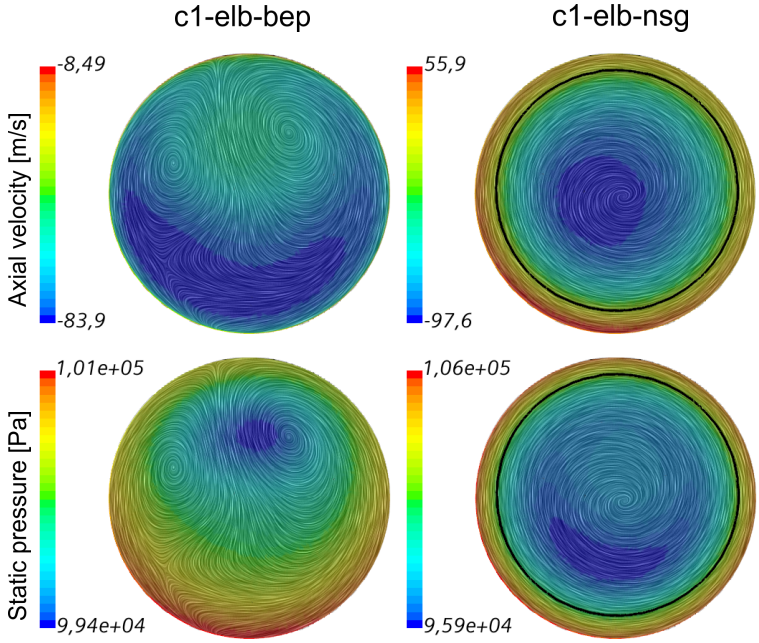

Figure 6.12: *Flow field in the inlet1 section. In the first row, the direction of the secondary flow is shown by the arrows, and the magnitude by means of the contours. The LIC of the other images correspond to the secondary flow direction. The black lines mark the zero axial velocity isosurface. The generatrix of the inner elbow radius is located at 12 o'clock, and that of the outer radius is at 6 o'clock.*

The right column corresponding to the nsg point shows a different pattern. The LIC describes concentric circles due to the swirl of the backflow. The axial velocity is maximum (negative because it is downward) in the center of the section. The backflow has a high velocity magnitude in the upward direction. The pressure presents a pattern similar to that shown in c1 str nsg: maximum value in the already- compressed backflow and minimum pressure in a circular crown around the section center. The presence of the impeller nut downstream of this section increases the pressure in the center of the section. In the nsg case, the flow field does not show the Dean vortices from the bep and is dominated by the backflow vorticity, as in c1 str nsg.

To conclude with the inducer mean flow field of the compressor c1, the rotating section inducer1 of the cases c1 elb will be analyzed. Figure 6.13 shows the average of secondary relative velocity, Mach number, and static pressure at inducer1. The patterns observed for both operating points of the c1 elb geometry are the same as those observed in c1 str. In the bep, the secondary relative velocity describes concentric circles and presents an increasing magnitude with the radius that reaches its maximum value at the LE tip. The Mach number follows the same pattern, reaching sonic values at LE tip. Static pressure, on the other hand, presents maximum values in the blade PS and minimum values in the blade SS. The largest pressure jump

appears on both sides of the LE at the blade tip. As mentioned above, this static pressure pattern coincides with the BPF mode in the inducer.

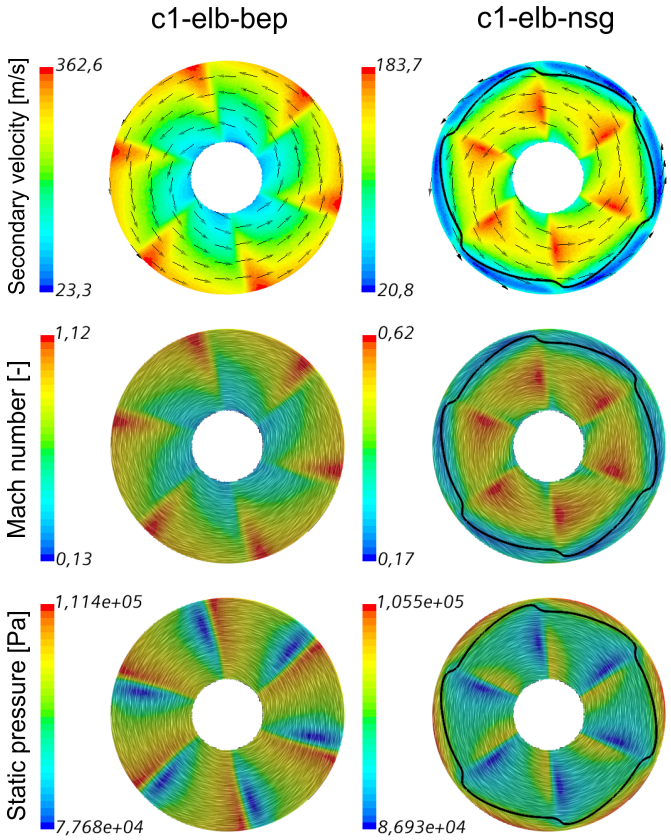

Figure 6.13: *Average flow field in the rotating inducer1 section of the c1 elb cases. The arrows and the LIC show the direction of the secondary velocity. The contours indicate the magnitude. The black line represents the zero axial velocity isosurface.*

At the nsg point, outside the black line of zero axial velocity, the backflow presents a very low velocity relative to the impeller as it rotates along with it. Inwards of the black line, the relative velocity pattern increases with the radius to the middle blade span. From the middle radius, it decreases back to the area occupied by the backflow. The Mach number shows the same pattern. Its maximum appears in the middle of the blade radius, where conditions are still subsonic. The static pressure presents its maximum jump in the middle of the blade radius, between the PS and the SS. The magnitude of this jump is much smaller than in the bep. Again, the pressure pattern corresponds to the BPF mode of the nsg cases shown in the previous chapter.

From the above, it is concluded that the Dean vortices formed downstream of the elbow at the bep do not change the average flow in the moving inducer1

section. Thus, the flow mechanism responsible for generating the tonal noise at the BPF is not altered by the presence of the upstream elbow. At the nsg point, the flow field in the upstream1 section of the elbow was identical to that presented by the straight inlet duct: axisymmetric distribution dominated by the swirl induced by the backflow. Consequently, the flow field in the rotating inducer1 section is also identical between the elbow and the straight duct operating at nsg.

In summary, in this first subsection, the static pressure pattern in the inducer has been identified as the flow structure causing the BPF tone. The sonic conditions at the bep points make this pattern very prominent in the blade tip and dominant in the acoustic spectrum. At the nsg point, the backflow in the blade tip region inhibits the sonic conditions. The resulting pressure pattern is weaker, and the BPF tone does not dominate the spectrum. The inlet geometry does not alter this noise-generating flow structures. At the bep, the elbow produces the Dean vortices, but the magnitude of their velocity is small compared to the relative velocity at the inducer and has no appreciable effect. At the nsg point, the backflow vorticity dominates over the effects of the change in direction introduced by the elbow. Therefore the str and elb geometries yield the same flow field at the inducer.

6.3 Inducer mean flow field of compressor c2

In this section, the mean flow field upstream of the inducer in compressor c2 is analyzed. The c2 cases are divided in two groups: reference straight ducts (rsd), and elbows. The c2 rsd group has three operating points: bep, hpr and nsg. The c2 elbow group has the e0D75, e1D and e1D5 operating at nsg point. The flow field averages were taken from at least 20 impeller revolutions.

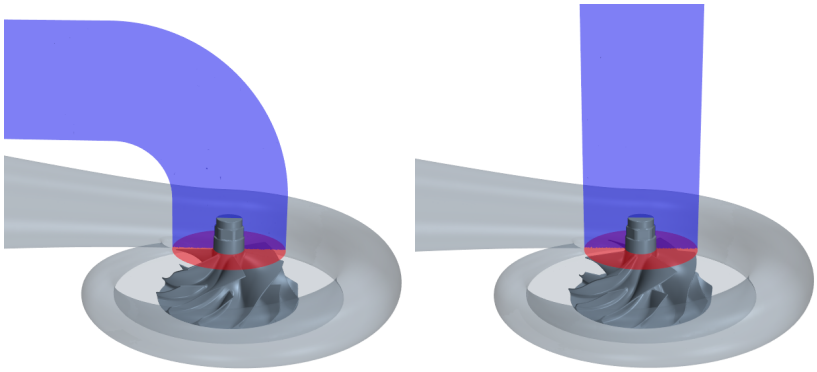

Figure 6.14: *Inlet sections for compressor c2. In blue the "long2" section, and in red the "inducer2" section, 1 mm upstream of the impeller LE.*

Figure 6.14 shows the sections used to analyze the incoming flow field at c2. The blue longitudinal section is the symmetry plane of the inlet duct,

it will be called "long2". The red section, called "inducer2", is located 1mm upstream of the impeller leading edge. These sections are similar to those used in compressor c1 but with some differences. The long2 section reaches the inducer2 section, i.e., its bottom portion is inside the impeller rotating region. However, the whole section remains static, and averages are taken in the static reference frame. The inducer2 section is the same as the inducer1 section. It moves along with the impeller, and averages are taken in the moving reference frame. A section analogous to upstream1 of compressor c1 does not appear in compressor c2. The greater proximity of the elbow outlet to the impeller inducer, and the extension of long2 down to the inducer plane means that the relevant flow information can be conveniently described with just the two sections, long2 and inducer2.

6.3.1 Straight inlet duct

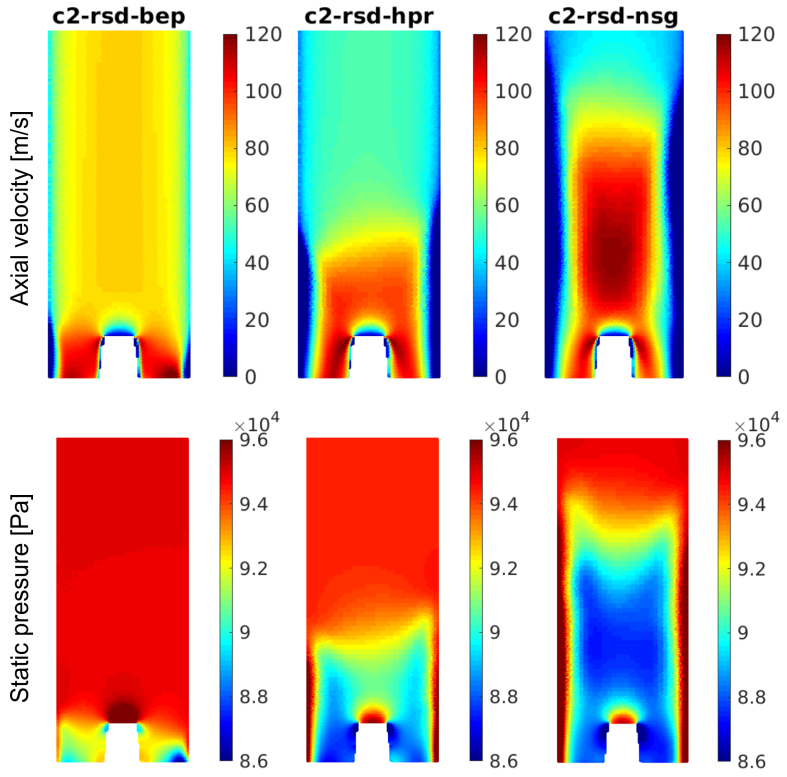

Figure 6.15: *Flow field at the long2 section for c2 rsd cases. On the bottom side, in white, the impeller nut outline can be seen. The color scale in the top row is limited to positive velocity values.*

Figure 6.15 shows the inlet flow field for rsd geometries. The flow is axial

and headed downwards. In the hpr and nsg cases, the backflow generates a section reduction and, therefore, a flow acceleration upstream of the impeller nut. Unlike in compressor c1, there is backflow at the bep point of compressor c2, as seen in the PIV shown in chapter 4 (Fig. 4.27). It can be distinguished in dark blue near the walls, although it does not exceed the impeller nut height. This difference may occur because the shroud between the upstream1 and inducer1 sections of compressor c1 (see figure 6.1) forms a convergent duct (because the inducer section is smaller), which increases the axial velocity and prevents backflow. In all three cases, the flat surface of the impeller nut produces stagnation of the flow immediately upstream.

The bottom row shows the average static pressure. Low pressure values are found at the maximum velocity regions, i.e., those where the cross section is reduced by the backflow. In the bep case the maximum pressure appears in the stagnation zone above the impeller nut. In hpr and nsg cases the compressed backflow presents the maximum pressure values.

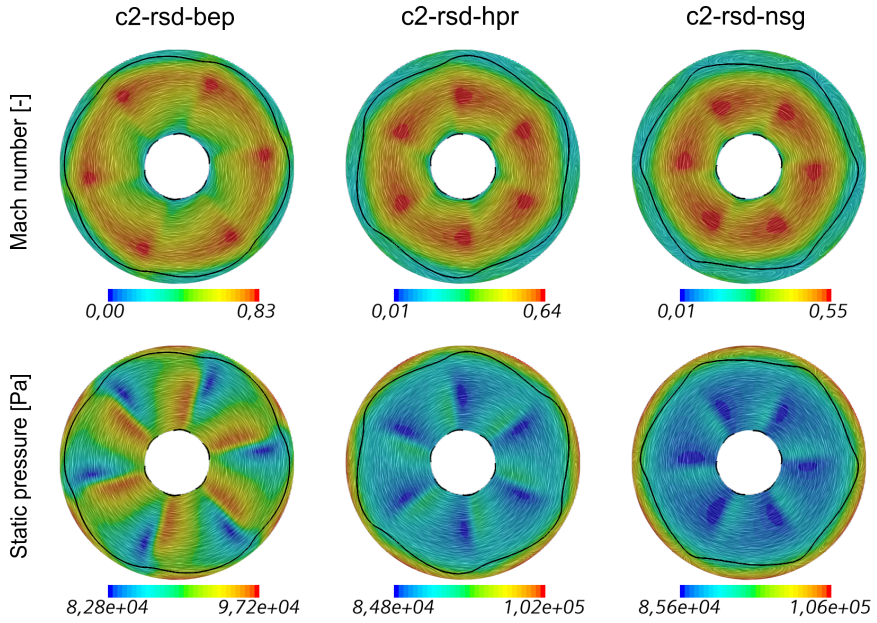

Figure 6.16: *Average flow field over the relative velocity LIC on the rotating inducer2 section. The black line marks the zero axial velocity isosurface.*

Figure 6.16 shows the average Mach number and static pressure in the inducer2 section that rotates together with the impeller, in the counter-clockwise direction.

This flow field is similar to that seen in c1 in the cases with backflow. The maximum Mach occurs on the leading edge in an intermediate radius between the tip and the hub. That happens because, in all cases, there is backflow with the same rotating speed as the impeller, and therefore the maximum relative

speed does not appear at the blade tip. Sonic conditions are not reached in any case.

It can be seen how the size of the region occupied by the backflow is inversely proportional to the mass flow rate. The narrower the backflow area, the more blade radius is available, and the greater the maximum Mach. In the bep, the maximum Mach is beyond the blade mid-radius. At hpr, it is approximately above the blade mid-radius, and at the nsg point, it appears at a radius smaller than the blade mid-radius.

The maximum pressure gradient coincides with the zone of maximum Mach in the change from the suction to the pressure side. In the hpr and nsg points the maximum pressure is found in the backflow region.

Regarding the noise-generating flow structures, the pressure pattern shown in figure 6.16 coincides with the BPF mode found in the previous chapter. The presence of backflow in the c2 rsd bep case confirms the relationship between sonic conditions at the blade LE and the predominance of the BPF mode in the spectrum. While in the c1 bep cases, sonic conditions were reached at the blade LE tip, and the BPF tone was the frequency of maximum amplitude in the spectrum, in the c2 bep case, the BPF tone appears but is not dominant. The spectrum shown in the figure 5.31 of the previous chapter shows how the high-frequency broadband reaches amplitudes up to 20 dB greater than the BPF at the c2 rsd bep case.

Furthermore, a relationship between the backflow and the asynchronous modes can be established. In the c1 bep cases, there were no asynchronous "whoosh modes". However, in the c2 rsd bep case, two whoosh-type modes appear, in addition to the backswept lobes in the mode at 1.5×RO. Thus, all cases displaying backflow at the inducer section show asynchronous "whoosh modes" as well.

6.3.2 Elbow inlet duct

The average flow in the c2 cases with inlet elbows is analyzed in the following. As a reminder, the three cases, e0D75, e1D, and e1D5, have 90° elbows with curvature radii of 0.75, 1, and 1.5 times the inlet duct diameter. In all the cases with elbow inlet geometry, the compressor c2 operates in the nsg point. The effect of the curvature radius on the average flow will be evaluated.

The objective of this subsection is not to give a detailed description of the flow field, which, as seen in the previous chapter, is highly three-dimensional and unsteady. The goal is to describe how the curvature radius affects the overall patterns of the mean flow and to evaluate the effect on the noise-generating flow structures.

Figure 6.17 shows the LIC of the average velocity at the inlet. The flow enters horizontally and turns inside the elbow until it exits in a downward vertical direction. The black line of null streamwise velocity indicates the backflow, which restricts the cross-section and causes the flow acceleration, marked in shades of red. The backflow forms a vortex at the inner radius with the incoming flow, as shown by the LIC lines.

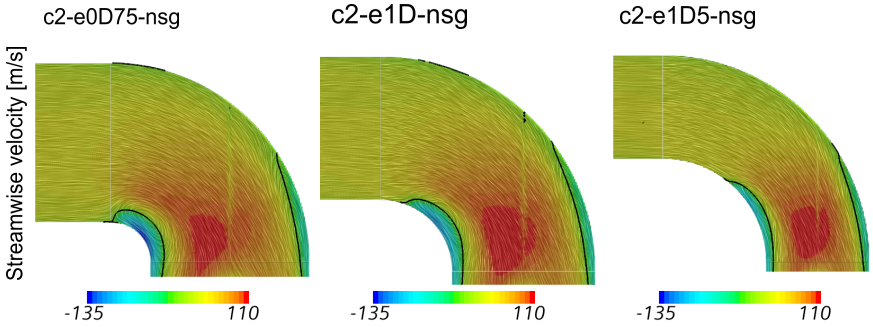

Figure 6.17: *Streamwise velocity contours over the LIC of the inlet velocity at the long2 section of c2. The black line marks the isosurface of null streamwise velocity. The streamwise direction is shown with a dashed line in figure 6.8.*

In case e0D75, the backflow at the inner radius obstructs part of the final section of the horizontal duct. The zone of maximum velocity appears immediately downstream of this obstruction. This zone is closer to the inner radius than to the outer radius. In case e1D, the backflow vortex in the inner radius does not interfere with the horizontal duct. The region of maximum streamwise velocity is closer to the inner radius than the outer radius. However, the bias is smaller than in the previous case. Finally, in the elbow with the largest curvature radius (e1D5), the incoming flow does not encounter the backflow until it is well inside the elbow. At this point, the acceleration caused by the section reduction produces a zone of maximum velocity centered in the duct.

The effect of elbow radius on the flow patterns matches that found in the previous chapter's DMD modes of these elbows. The smallest radius elbow exhibited flow structures going upstream, reaching the horizontal duct due to the proximity of the elbow inlet to the inducer. In addition, the smallest curvature radius resulted in a more distorted and biased flow towards the inner radius. Meanwhile, the e1D5 case shows a flow field analogous to the straight inlet duct case (c2 rsd nsg). Although the flow turns at the elbow, symmetry is maintained in the streamwise direction, and the backflow does not reach the horizontal duct.

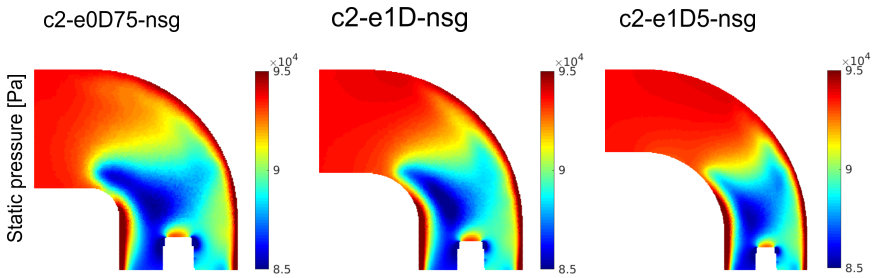

Figure 6.18: *Average static pressure in the long2 section of the c2 elbow geometries.*

6.3. Inducer mean flow field of compressor c2

Figure 6.18 shows the average static pressure at the elbows of compressor c2. The minimum pressure region in all three cases appears biased towards the inner radius. Specifically, the minimum pressure appears just downstream of the vortex formed by the backflow at the inner radius. The deflection caused by this vortex in the incoming flow gives rise to the minimum pressure. This minimum pressure region is larger the smaller the curvature radius. Furthermore, at e0D75, it extends upstream to the inlet of the horizontal duct. At e1D5, it does not reach the horizontal duct.

The observed pressure pattern is also consistent with the disturbances seen in the DMD modes: greater distortion in the inlet flow, the smaller the elbow curvature radius, and greater extension upstream to the horizontal duct.

The average flow field in the rotating inducer2 section is shown in Figure 6.19. The patterns found are identical to those of the c2 rsd nsg case. That is because the asymmetry in the flow at the elbow outlet has a small magnitude compared to the velocity and pressure jumps in the inducer.

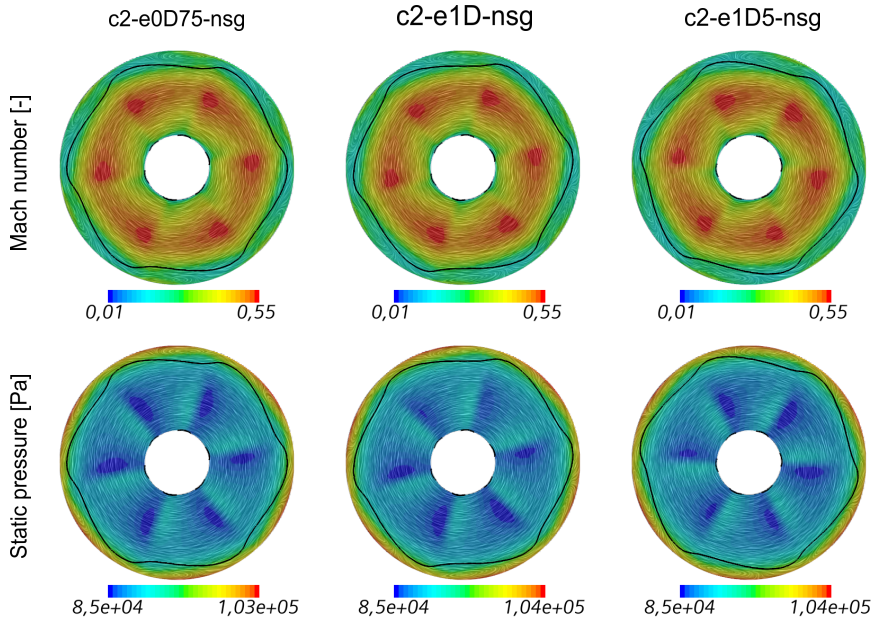

Figure 6.19: *Average flow field over the relative velocity LIC on the rotating inducer2 section. The black line marks the zero axial velocity isosurface.*

This shows how the inlet geometry has no appreciable influence on the flow structures generating the synchronous noise in the inducer. This conclusion is consistent with the experimental spectra and DMD BPF modes in the previous chapter, which showed no differences between the elbows and the straight inlet duct of compressor c2.

Although the mean flow field examined in this section does not provide much information on the unsteady flow structures, the evolution of the flow

patterns with the elbow curvature radius corresponds with what was seen in the previous chapter. Smaller curvature radii result in a flow field with higher distortion and structures that reach the horizontal duct. The largest radius elbow has a much more symmetrical and uniform flow, and the backflow does not reach the horizontal duct.

6.4 Impeller mean flow field

In this section, the average flow field at the impeller will be addressed. To do so, the isospan 50% surface (i.e., halfway between the shroud and the hub for each streamwise position) has been used as described in Appendix A of [24]. This surface belongs to the rotating impeller region and moves along with it. The averages are taken in the rotating reference frame, during at least 20 impeller revolutions.

Figure 6.20 shows the isospan 50% sections. The inducer and impeller sections are shown in blue and green, respectively. They will be developed on a meridional vs. circumferential plane to study the impeller flow field. The (m', theta) warp, available from Simcenter STARCCM+ [70], was used for such representation. The red surface spanning the diffuser and the volute inlet will be used in the next section.

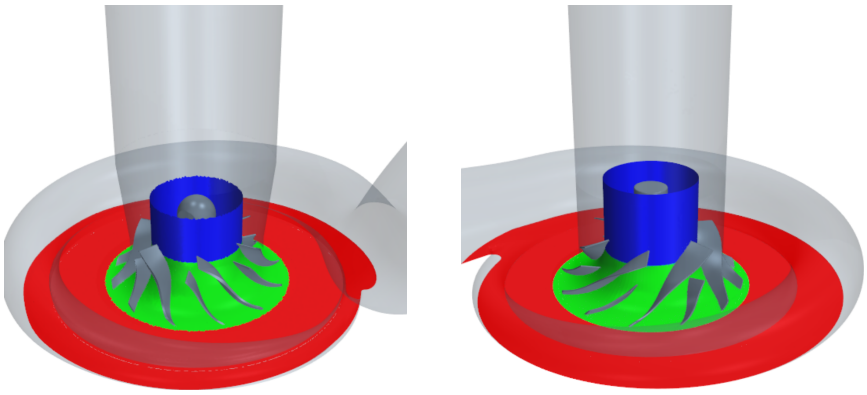

Figure 6.20: *Isospan 50% sections in compressors c1 (left) and c2 (right). In blue, the cylindrical section corresponds to the inducer. In green, the revolved arc of ellipse in the impeller. In red is the horizontal plane for the diffuser and volute.*

First, the average flow of the compressor c1 is analyzed. The same selection of geometries is made as in the previous sections: c1 str as the axial inlet paradigm is compared with c1 elb.

Figure 6.21 shows the average Mach number over the LIC of the velocity relative to the impeller at the bep. The spatial pattern is the same in both geometries.

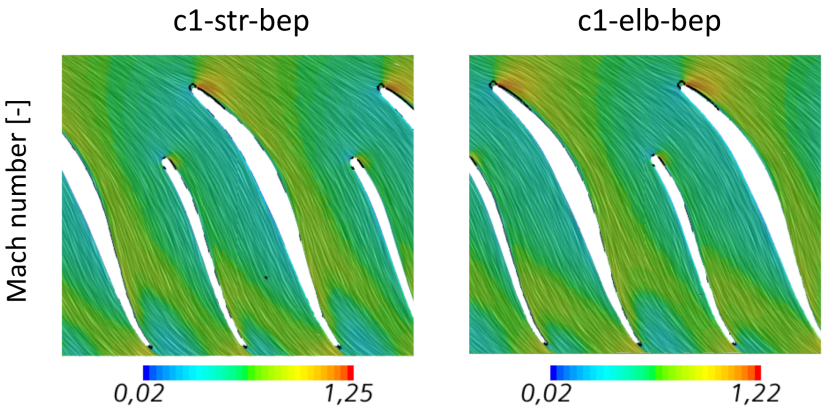

Figure 6.21: *Mean relative Mach number over the LIC of the relative velocity in the isospan 50% developed section. Blades move from right to left.*

The incoming flow arrives at the main blade LE. At the LE suction side (SS), the Mach is maximum, reaching sonic conditions (Ma ¿ 1.2). At the pressure side (PS), the Mach number is minimum, as the flow reduces its velocity as it impacts the blade.

Streamlines follow the main blade profile near the SS until just before the trailing edge (TE). The angle of the flow reaching the LE becomes more vertical at the blade mid-chord. Upon reaching the TE, it becomes more horizontal again. The contour shows that the magnitude of the Mach number in the region adjacent to the main blade SS is high.

Just before the TE, the high-Mach "jet" separates from the main blade and heads toward the TE of the splitter blade. In reference [24], this deflection is explained by means of the Coriolis force. This force diverts the flow in the opposite direction to the impeller rotation and favors the detachment of the suction side flow.

In the splitter blade, the flow pattern is similar to that of the main blade. The flow interaction in the LE is much less than in the main blade since the main blade has already guided the flow in the chordwise direction. When the flow reaches the splitter blade LE, the region adjacent to the SS shows high Ma. The high-Ma flow follows the SS until just before the TE, where, again, it separates and migrates to the TE of the following main blade.

Figure 6.22 shows the cases operating at nsg. The incoming flow to the blade LE also causes a maximum value of Ma in the SS and a minimum in the PS, although sonic conditions are not reached in this case. The flow follows the direction of the main blade down to the splitter blade LE streamwise position. At this point, the streamlines separate from the main blade SS due to the lower degree of channel filling. The high-Mach jet arrives at the splitter blade PS and follows it to the TE.

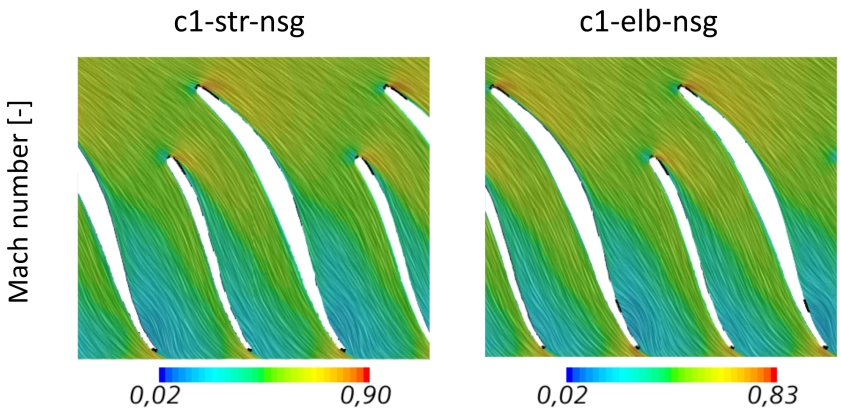

Figure 6.22: *Mean relative Mach number over the LIC of the relative velocity in the isospan 50% developed section. Blades move from right to left.*

The same happens in the splitter blade; the flow is attached in the first section of the SS, but then the high-Mach region is directed to the main blade PS. The detachment region in the main blade SS is much larger than in the bep, where it only occupies a small area next to the TE. In addition, lower Mach values (darker blue) are reached at nsg. Consequently, in the TE, the high Mach zone is narrow and is located in the PS. The rest of the channel is occupied by a low-velocity zone.

In summary, in the bep, the flow has a higher velocity in the blade SS, and before reaching the TE, there is a small separation zone. In nsg, the flow separates from the SS shortly after the LE, leaving a large zone of detached flow from the blade mid-chord to the TE. The high-velocity region inside the channel occurs at the blade PS.

From the point of view of noise-generating flow structures, the high Mach values at the LE give rise to the BPF tone. Higher Mach values appear in this isospan section than in the inducer1 section, which was 1 mm upstream of the LE. However, the difference between bep, where sonic conditions are reached, and nsg, where the flow is subsonic, remains.

The detached flow zone in the final section of the SS is related to the rotating stall and asynchronous noise sources, as will be seen at the end of this chapter. That zone was not influenced by the different inlet geometries as well.

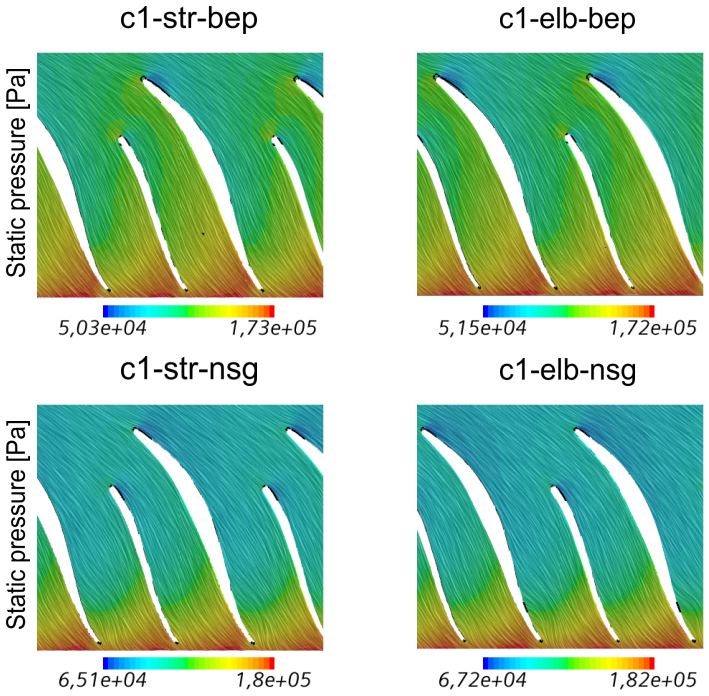

Figure 6.23: *Mean static pressure over the LIC of the relative velocity in the isospan 50% developed section.*

Figure 6.23 shows the average static pressure. The pressure pattern at both operating points has similar features. On the main blade LE, a high-pressure value appears at the PS and low pressure at the SS. Following the streamwise direction, the pressure increases. The maximum pressure region appears at the channel outlet. The pressure level curves are approximately perpendicular to the blades. Thus, near the TE, the PS has the maximum pressure, while in the SS, the pressure is lower.

While the pressure jumps in the main blade LE are clearly identified as the BPF pressure pattern in the inducer, the situation in the TE is different. There is a low and a high-pressure zone in the 12 channels defined by the main and splitter blades. The low pressure is in the blade SS and the high pressure is in the PS. This results in the 12 lobes of each color seen in the TE of the 2×BPF mode. Each channel has one lobe corresponding to the low-pressure zone and one to the high-pressure zone. The fact that no influence of inlet geometry or operating point is observed on the intensity of the pressure pattern in the TE shown in figure 6.23 is consistent with the 2×BPF mode pattern seen in the previous chapter. While in the inducer, the pattern lost intensity at nsg, in the TE, it remained unchanged for all geometries and operating points.

The BPF mode presented 6 lobes of each color in the TE. That pattern is to be understood as a sub-harmonic of the pressure pattern in the TE. The

superposition of the 6-lobe pattern with the 12-lobe pattern of the 2×BPF reflects minor differences in pressure magnitude between the main and splitter blade channels.

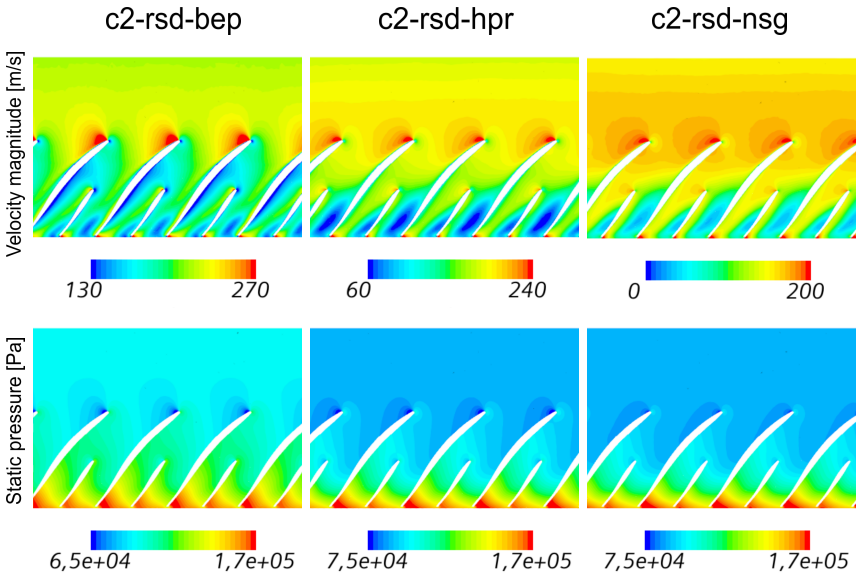

Figure 6.24: *Average relative velocity magnitude and static pressure in the isospan 50% section. Blades move from left to right.*

Figure 6.24 shows the average velocity and pressure in the impeller of the c2 rsd cases. It can be seen that in compressor c2, the same pattern explained above is followed. In all cases, there is a maximum velocity zone in the SS of the main blade LE and low velocity in the PS.

In the bep, the high-velocity zone in the channels is attached to the main blade SS until just before reaching the TE, where it passes to the splitter blade PS. This deflection gives rise to the small zone of detached flow near the TE.

At nsg, the high-velocity zone in the channels is attached to the PS as the flow separates from the SS before reaching the mid-chord position giving rise to a large zone of detached flow. The hpr flow characteristics are halfway between bep and nsg. Care must be taken when analyzing the velocity figures, as the color scale is different for each case, to maintain a good resolution in such disparate flow conditions.

The pressure distribution is also the same as in compressor c1. There is a minimum value in the SS of the LE and a high value in the PS. Towards the duct outlet, the pressure increases with level curves approximately perpendicular to the blade. The static pattern with alternating pressures in the LE and TE responsible for the BPF and 2×BPF modes, respectively, is also clearly seen in compressor c2.

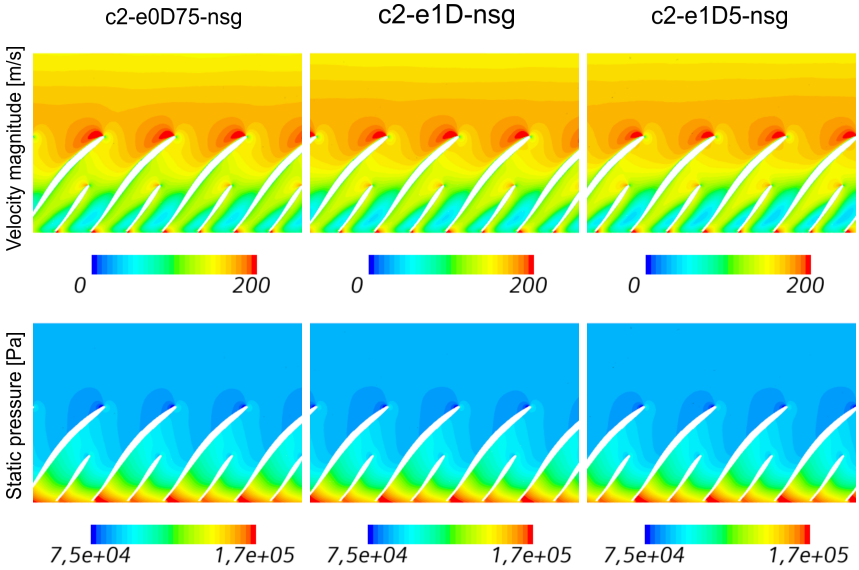

Figure 6.25: *Average relative velocity magnitude and static pressure in the isospan 50% section. Blades move from left to right.*

Finally, in figure 6.25, the average velocity and pressure in the impeller of the c2 cases with inlet elbow are shown. It can be seen that the pattern is identical to the c2 rsd nsg straight inlet case. There are also no noticeable differences between the elbows with different curvature radii.

As the conclusion of this section, it is possible to remark the static pressure patterns responsible for the BPF mode in the LE, and the 2×BPF mode in the TE. The inlet geometry has no influence on either compressor's flow pattern. The operating point, however, did show an influence on the pressure patterns intensity in the LE, where sonic conditions are reached at the bep (only in c1) but not at nsg. In the TE, however, there were no remarkable differences between the operating points.

At nsg point, there was a significant zone of detached flow in the blade SS, from the blade mid-chord to the TE. In the bep, this zone was smaller and located just upstream of the TE. The relationship of this flow pattern to asynchronous sources will be discussed in later sections.

6.5 Diffuser mean flow field

The mean velocity and pressure fields will be examined in the 50% isospan section in the diffuser and volute (red section in figure 6.20). The radial velocity component was chosen to analyze the flow stream from the diffuser to the volute.

The flow enters the diffuser from the section center. It follows a spiral path, with the rotation direction marked by the curved arrow, to the volute inlet indicated by the dashed circle. Once inside the volute, the outer wall causes the radial component of the velocity to vanish, and the velocity becomes tangential.

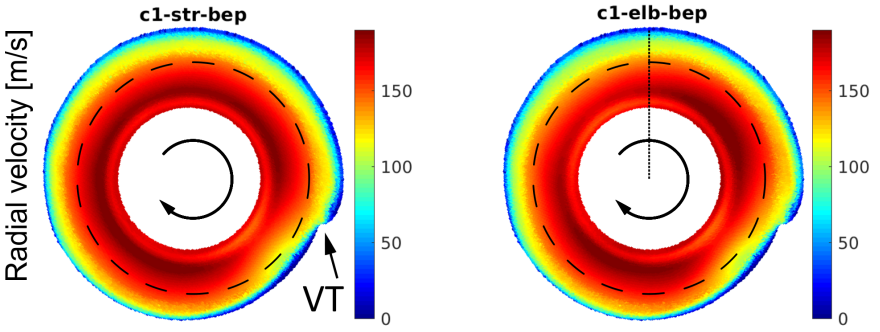

Figure 6.26: *Average radial velocity in the isospan 50% diffuser and volute section. The dotted line indicates the axis of the elbow inlet. The dashed circle indicates the volute inlet, and the impeller rotation direction is marked by a curve arrow.*

The figure 6.26 shows the radial component of the average velocity. There is an initial acceleration at the diffuser inlet, where the light red color changes to dark red. That is because the initial section of the diffuser is convergent. Further on, the increase in radius in the diffuser yields an increase in cross-section, which causes the velocity to decrease. Shortly after entering the volute, the radial velocity vanishes.

The velocity distribution is axisymmetric except for the perturbation caused by the volute tongue (marked VT in the figure). That is the point where the outer volute wall is closest to the diffuser inlet. The collision of the flow with the wall just downstream of the VT causes a zone of lower average velocity in the circular sector between 4 and 5 o'clock. The only difference between the two geometries is that c1 elb has a slight velocity deficit between 10 and 11 o'clock.

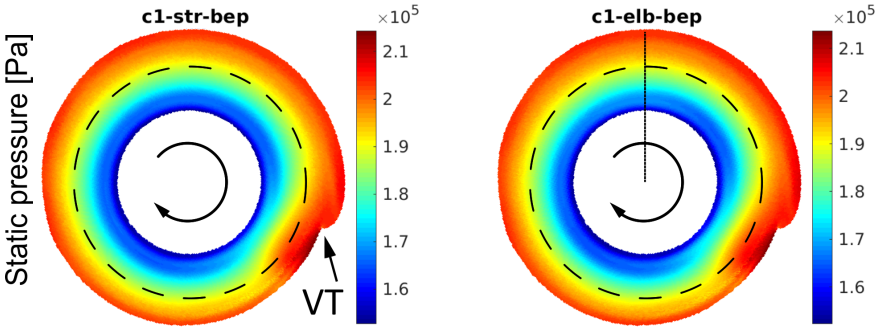

Figure 6.27: *Average static pressure in the isospan 50% diffuser and volute section. The dotted line indicates the axis of the elbow inlet. The dashed circle indicates the volute inlet, and the impeller rotation direction is marked by a curve arrow.*

The average pressure is shown in figure 6.27. The pressure grows with radius due to the increase in the cross-section discussed above. The only asymmetry is in the region downstream of the volute tongue. The impact of the flow against the wall causes an increase in pressure in the sector between 4 and 5 o'clock. The str and elb geometries show an identical pressure pattern.

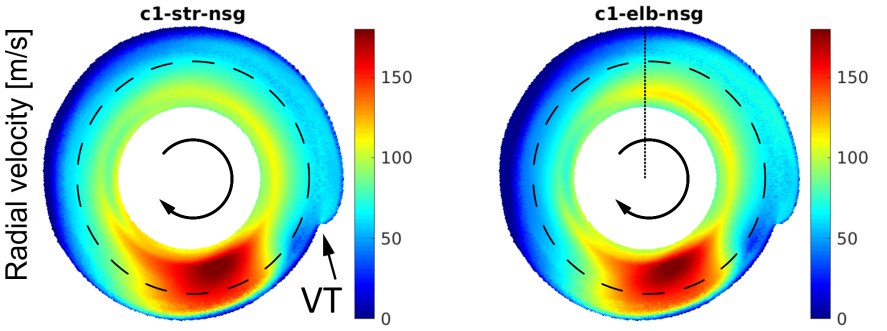

Figure 6.28: *Average radial velocity in the isospan 50% diffuser and volute section. The dotted line indicates the axis of the elbow inlet. The dashed circle indicates the volute inlet, and the impeller rotation direction is marked by a curve arrow.*

The average radial velocity is shown in figure 6.28 for the c1 nsg cases. In the region just downstream of the VT the velocity is very low as the flow impacts the outer wall. Downstream of this zone in the clockwise direction is a region of maximum radial velocity, extending from 5 to 7 o'clock. Continuing clockwise, the radial velocity decreases, becoming zero and even reversing at the outer radius of the volute. Since the color scale only goes down to 0, the dark blue areas represent the reverse radial flow. From 12 o'clock to the VT, the radial velocity in the volute experiences a slight increase.

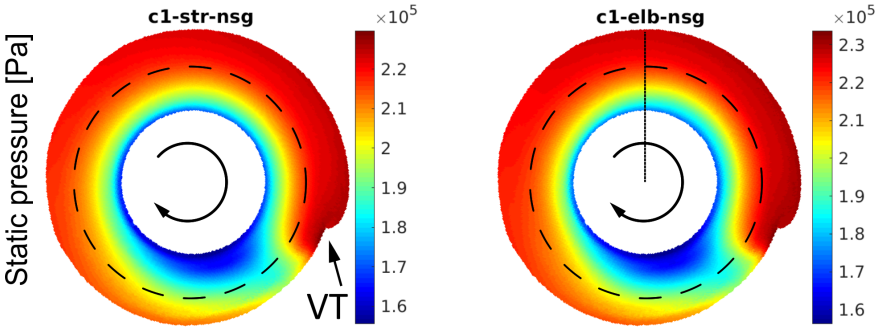

Figure 6.29: *Average static pressure in the isospan 50% diffuser and volute section. The dotted line indicates the axis of the elbow inlet. The dashed circle indicates the volute inlet, and the impeller rotation direction is marked by a curve arrow.*

The average pressure is shown in figure 6.29. The pressure grows with radius due to the increase in cross-section. The radial pattern is altered in the zone of maximum pressure under the volute tongue and the zone of minimum pressure from 5 to 7 o'clock, coinciding with the maximum radial velocity. In the outer radius of the volute, between 11 o'clock and the VT, a gradual pressure increase is observed in the circumferential direction. This increase is because the cross-section of the volute grows in the circumferential direction. The pressure and velocity patterns found in the nsg point agree with those reported by Navarro [24] and Sundström et al. [68].

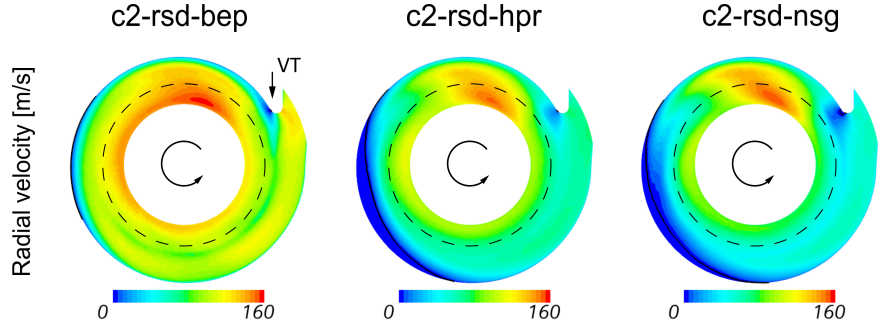

Figure 6.30: *Average radial velocity in the isospan 50% diffuser and volute section. The dashed circle indicates the volute inlet, and the impeller rotation direction is marked by a curve arrow. The solid black line marks the isosurface of null radial velocity*

Figure 6.30 shows the average radial velocity in the c2 rsd cases. The flow field at point nsg is similar to the same point of compressor c1. Under the VT there is a low-velocity region. Downstream (counterclockwise, at compressor c2), the region of maximum radial velocity appears. Continuing counterclockwise, at the volute's outer radius, the radial velocity is reduced and eventually reversed. The solid black line marks the isosurface of zero axial

velocity. Between 6 o'clock and VT, the radial velocity increases again. The hpr point shows the same pattern but with a higher average radial velocity (the green shades reach the volute inlet dashed circle, and the deep-blue zones are smaller). The bep point shows the same zones: low velocity under VT, maximum radial velocity around 12 o'clock, reduced radial velocity at the outer radius of the volute from 10 to 8 o'clock, and increasing radial velocity from 6 o'clock to VT. In this figure, it can be seen how in the c2 bep case, the flow field in the diffuser exhibits again features characteristic of lower mass flow operating points. It was seen above with the appearance of backflow in the inducer. In the diffuser, c2 bep shows again a flow field more similar to c2 nsg than c1 bep.

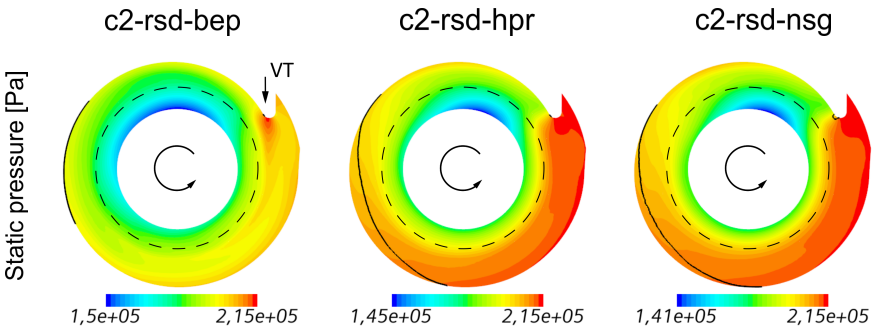

Figure 6.31: *Average static pressure in the isospan 50% diffuser and volute section. The dashed circle indicates the volute inlet, and the impeller rotation direction is marked by a curve arrow. The solid black line marks the isosurface of null radial velocity*

The average static pressure of the c2 rsd cases is shown in figure 6.31. The c2 rsd nsg case has a pressure pattern analogous to the nsg cases of compressor c1. Inside the diffuser, the pressure grows radially except for some perturbations listed in the following. The maximum pressure is next to the VT. Downstream in the counterclockwise direction appears the zone of minimum pressure coincident with the maximum radial velocity. At the volute's outer radii, a pressure gradient appears in the circumferential direction caused by the progressive increase of the volute cross-section. At the hpr point, the pressure distribution is similar. At the bep, the same pattern also appears, but the low-pressure zone due to the maximum radial velocity is more extensive. In addition, the circumferential pressure gradient in the volute is milder than at the lower mass flow points.

Figure 6.32 shows the average radial velocity and static pressure in the three c2 cases with inlet elbows. The average flow field is identical to the c2 rsd nsg described above. The only difference between the elbows with different curvature radii is the extent occupied by the reverse flow between 6 and 10 o'clock at the outer volute radius. However, there is no clear trend with the elbow radius since the case with the largest backflow is the intermediate radius c2 e1D. The following section will show that the backflow in that zone

is caused by unsteady flow structures.

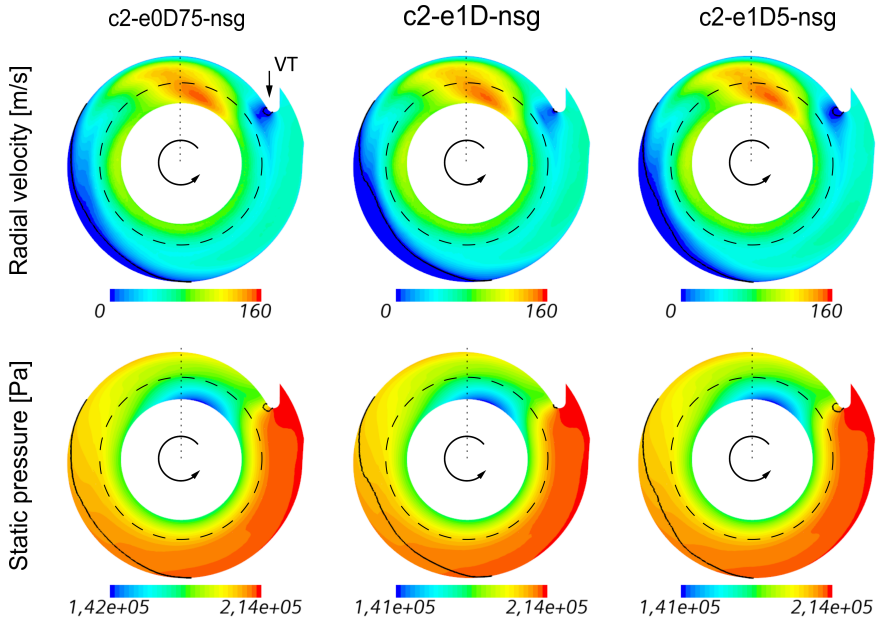

Figure 6.32: *Average radial velocity and static pressure in the isospan 50% diffuser and volute section. The dotted line indicates the axis of the elbow inlet. The dashed circle indicates the volute inlet, and the impeller rotation direction is marked by a curve arrow. The solid black line marks the isosurface of null radial velocity*

The following is an overview of the noise-generating flow structures in this region. The maximum radial velocity zone found in compressor c2 operating at hpr and nsg (rsd and elbows) coincides with the diffuser region where no BPF mode lobes appear in those same cases (Figures 5.34, 5.35, and 5.48). The low pressure in that region reduces the oscillation intensity of the BPF lobes.

However, the most important noise generation mechanism in the diffuser region is the interaction of the circumferential pressure profile with the TE of the impeller blades. The previous chapter showed how the interaction of the impeller blades with one and two pressure perturbations per revolution in the diffuser gave rise to oscillations at frequencies BPF and 2×BPF, respectively.

Figure 6.33 shows in yellow the average circumferential pressure profile at the volute inlet for the cases c1 str bep and c1 str nsg. The VT is located at angle 0°, and the angular coordinate advances clockwise. As seen in figure 6.27, at bep, the maximum pressure appears immediately downstream of VT, then drops and remains approximately constant until it reaches VT again. At nsg point (figure 6.29), the maximum pressure is at the VT, then drops sharply and gradually increases in the clockwise direction.

In its rotational motion, the impeller is periodically exposed to this pres-

sure profile. The harmonic content of the pressure disturbance seen by the impeller can then be analyzed utilizing the Fourier transform in the circumferential coordinate.

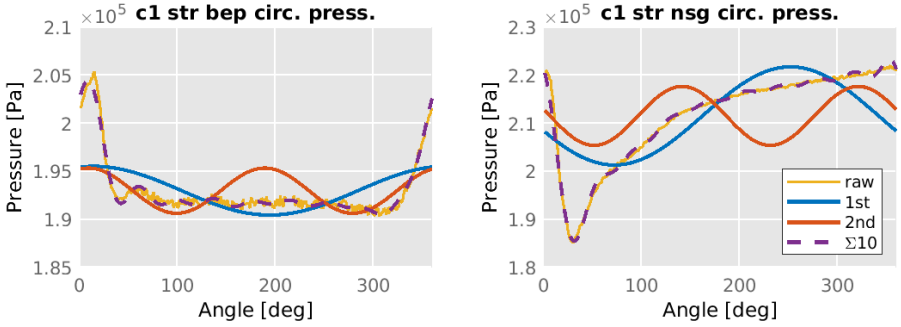

Figure 6.33: *Circumferential distribution of the average pressure at the volute inlet. The VT is located at angle 0°, and the angular coordinate advances clockwise. The blue and red lines are the first two harmonics of the circumferential FFT. The dashed purple line is the sum of the first 10 harmonics.*

Figure 6.33 also shows the first two harmonics of the circumferential pressure distribution in blue and red. These harmonics have wavenumbers of 1 and 2, respectively. The purple dashed line shows the sum of the first ten harmonics, and it can be seen that it reproduces the raw pressure very accurately.

The harmonics shown match exactly the one- and two-disturbance pressure profiles in the circumferential direction that appear in the TE of the impeller DMD modes. Figures 5.62 and 5.63 show these profiles in the DMD modes of the pressure in the impeller rotating region. In Figures 5.68 and 5.69, the same patterns appear in the TE of the DMD modes of the dipole term of the Ffowcs Williams and Hawkings equation.

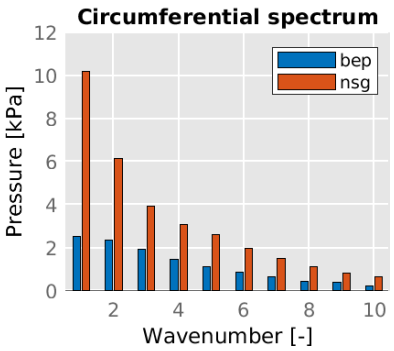

Figure 6.34: *Spectrum of the circumferential pressure profiles of c1 str bep and nsg cases at the volute inlet.*

Figure 6.34 shows the amplitude of the first ten circumferential harmonics of each case. The first two harmonics shown in figure 6.33 correspond to wavenumbers 1 and 2. It can be seen that the harmonics at the nsg point have a much larger amplitude than in the bep. In addition, the first two harmonics of the nsg point are considerably larger than harmonics 3 to 10. In the bep, on the other hand, harmonics 1 and 2 are not much larger than the following harmonics.

The high amplitude of the first harmonic in nsg is the reason why the BPF tone dominates the spectrum at the outlet of the c1 nsg cases (Figure 5.21),

whereas in the inlet spectrum (Figure 5.20) the BPF tone did not appear, because of the lack of sonic conditions in the impeller LE.

With the circumferential pressure spectrum calculation, it was possible to quantify separately the flow structure responsible for the BPF and 2×BPF tones in the impeller TE.

As a summary of this section, the pressure increase caused by flow impingement with the VT is the most important perturbation appearing in the diffuser averaged flow. At the near surge point, there is also a zone of maximum radial velocity just downstream of the VT and a pressure rise in the circumferential direction at the outer volute radius.

The most important noise-generating flow structure is the circumferential pressure disturbance. Its different harmonics have been quantified by circumferential FFT to distinguish those exciting the BPF and the 2×BPF. The inlet geometry has not shown to be relevant regarding these flow structures. On the other hand, the operating point has an evident influence. At the nsg point, the first circumferential pressure harmonics have more than twice the amplitude of those at the bep.

6.6 Unsteady flow structures

The goal of this chapter is to find the flow structures responsible for the spectral components highlighted in the previous chapter by means of the DMD modes. In the previous sections, the flow structures that generate the synchronous sources have been identified by analyzing the mean flow field.

In this section, the flow structures responsible for the asynchronous noise will be identified. First, a literature review is done about the known unsteady flow structures in radial compressors and their role in noise generation. Next, these structures are identified in the flow field of the compressors considered in this thesis, and their relationship with DMD modes is discussed. Finally, the influence of inlet geometry and operating conditions are analyzed.

6.6.1 Literature review

The main unsteady flow structures associated with noise generation found in the literature are grouped under the more generic phenomena of rotating stall and surge. The rotating stall consists of low-velocity regions in the impeller channels, which pass from one channel to the next through tip clearance. Surge is a filling-emptying pattern in which the compressor mass flow is periodically and violently reversed when the low incoming mass flow cannot overcome the high backpressure in the volute.

In the paper by Mendonça et al. [44], the rotating stall near the impeller inducer is shown. Its sub-synchronous rotation speed of 70% of RO is related to a narrowband noise in that frequency.

The rotating stall is associated with different flow structures upstream and downstream of the impeller. Broatch et al. [45] show low-pressure regions upstream of the inducer that interact with the impeller LE. It is known as

inducer rotating stall. It occurs both at the nsg and hpr points, although at the latter, it does not have as much upstream extension. In addition, from the mid chord of the blades on, low-momentum areas (stall) are shown on the suction side, which reach the trailing edge. Downstream of the trailing edge, these areas break off and pass into the following channels, stall them, and form the so-called diffuser rotating stall. Some of these stall cells detach from the impeller and progress through the diffuser. The detachment of these cells was found to be consistent with the pressure oscillations in the outlet section. This was identified as the *whoosh* noise-generating mechanism.

Two vortical structures upstream of the inducer at nsg are shown in [47] by Broatch et al. These vortices cause the inducer rotating stall. The vortices, in turn, were caused by the interaction of the incoming flow with the swirling backflow. In this paper, snapshots of the flow in the isospan 50% surface developed in the meridional vs. circumferential plane were presented. There were regions of low meridional (streamwise) velocity in the inducer, corresponding to the vortices mentioned above. These structures appear in nsg and hpr points but not in the bep. In the three operating points, detachment in the SS of the blades downstream from the mid-chord was observed.

In the paper by Sundström et al. [69], a pattern of two co-rotating vortices was found in the inducer. About the cause of the rotating structures, it is stated that "*The radial gradient of the radial velocity component generates the instability causing the vortices. The rotation of the co-rotating vortices around the impeller axis occurs due to radial gradient of the circumferential velocity component*". The intensity of the vortices changes with the angular position to the VT due to the uneven diffuser pressure. Stall cells break away from the impeller trailing edge and interact with the VT shear layer.

A connection between the inducer vortices and the acoustic dipole sources at the impeller leading edge is shown in another paper by Sundström et al. [51]. Four vortices with opposite rotation directions were found: alternating two clockwise and two counterclockwise. That pattern is influenced by the four ribs of the ported shroud. These vortices move with 50% of the impeller rotating speed. When the impeller blades cut these structures, pressure fluctuations and oscillation of the incidence angle are generated. The vortex interaction causes high levels of the acoustic surface loading term in the LE. Furthermore, high levels of the acoustic loading term were reported at the impeller trailing edge, on the suction side, associated with the separated flow in this zone.

In summary, the literature allows establishing a connection between the swirling backflow and the creation of vortices upstream of the inducer. These vortices interact with the impeller LE; they cause fluctuating pressure on the blade surface and impair the flow incidence angle. A high incidence angle favors the flow detachment on the suction side, promoting the rotating stall. Downstream of the blade mid-chord, flow detachment appears at all operating points but is aggravated in cases with rotating stall. The pressure fluctuation due to this phenomenon also generates noise near the trailing edge. Finally, when some stall cells detach from the impeller trailing edge, they advance

through the diffuser until they reach the VT. The low momentum cells cause fluctuations at the VT shear layer and pose another acoustic source.

6.6.2 Unsteady flow structures in compressors c1 and c2

The operating conditions considered in compressors c1 and c2 range from the bep to nsg. Typically, by reducing the mass flow rate from the bep, flow instabilities such as rotating stall begin to appear in hpr. By further reducing the mass flow rate, the surge limit is reached. The nsg operating point in both compressors is close to the surge limit but without experiencing the aforementioned mass flow inversion conditions. Therefore, rotating stall is the phenomenon that groups the flow instabilities expected in the studied compressors.

Figure 6.35 shows the instantaneous streamwise velocity on the developed isospan 50% surface for c2 rsd nsg. Impeller blades move from left to right. The structures described for the rotating stall phenomenon are present. Upstream of the inducer, low-velocity regions appear in white, corresponding to the vortices. Detachment occurs on the suction side downstream of the mid-chord position in the impeller passages. At the trailing edge, low-velocity bubbles detach towards the diffuser. In the diffuser, these stall cells advance until they reach the VT. Downstream of the VT, these zones disappear in the region of maximum velocity. The figure of c2 is shown first since the phenomena described are seen more clearly than in c1.

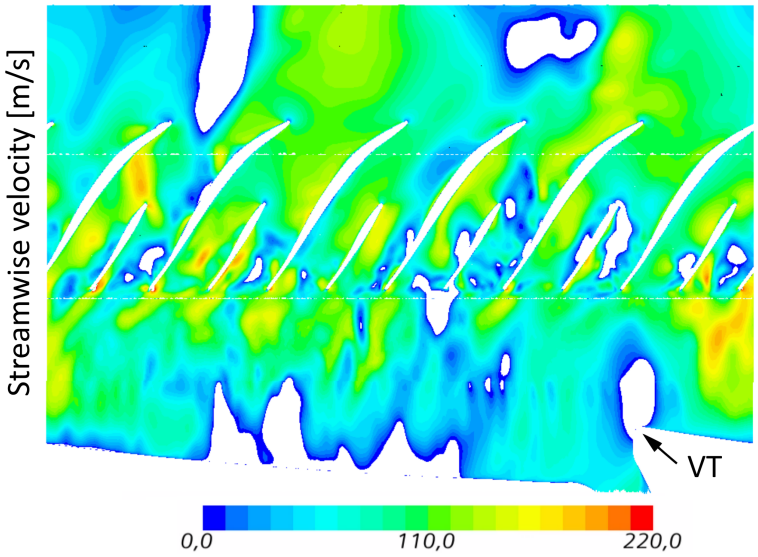

Figure 6.35: *Snapshot of stremwise velocity, in m/s, on the developed isospan 50% surface of c2 rsd nsg. Impeller blades move from left to right. The volute tongue is marked with the letters "VT".*

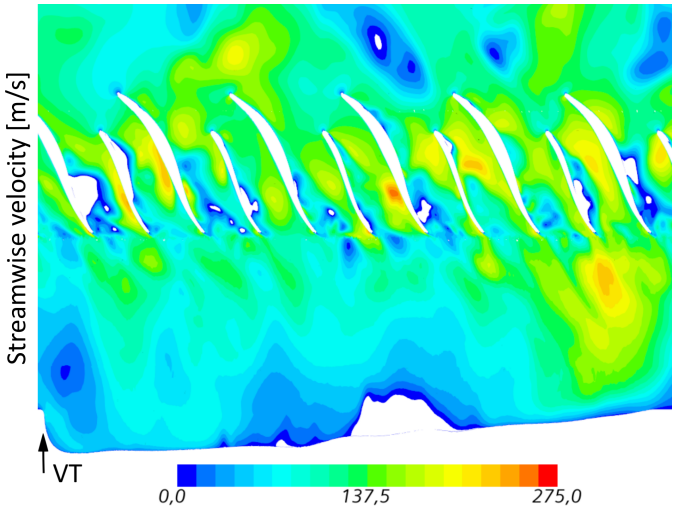

Figure 6.36: *Snapshot of stremwise velocity, in m/s, on the developed isospan 50% surface of c1 str nsg. Impeller blades move from right to left. The volute tongue is marked with the letters "VT".*

Figure 6.36 shows the same section of c1 str nsg, where the impeller blades move from right to left. The same flow patterns are observed, although the conditions are visibly more severe in compressor c2 than in c1 in terms of quantity and extension of stall cells.

The previous figures have shown the rotating stall flow structures in two nsg cases with straight inlet ducts of compressors c1 and c2. The following summarizes these flow structures in the other studied cases.

Rotating stall does not appear at the bep points of compressor c1. There is a slight flow detachment on the suction side of the impeller blades, but no vortices and no diffuser rotating stall are observed. There is rotating stall at every nsg point of compressor c1, as seen in figure 6.36. In compressor c2, all the points operating in nsg have conditions similar to those of figure 6.35: rotating stall with vortices, detached flow in the impeller channels, and diffuser rotating stall.

In the c2 rsd hpr case, there is also rotating stall. Vortices, passage stall, and diffuser rotating stall appear at that operating point, albeit in a lighter way than in nsg. As mentioned above, these instabilities are also characteristic of the hpr point [47]. Finally, contrary to what happened in compressor c1, there is rotating stall at the bep point of compressor c2 (c2 rsd bep). Again, weaker than in hpr and nsg, regarding extension and number of stall cells.

Figure 6.37 shows three snapshots of the inducer2 section and the 50% isospan section in the diffuser and volute of the c2 rsd bep case. In the time between each snapshot and the next, the impeller has rotated 60°, i.e., one main blade passing period. A low-velocity cell can be seen in white at the inducer, marked with a black arrow.

The round shape and the radial position suggests it might be the core of a vortex. In the time between the first and third snapshots, the impeller rotates 120°, while the low-velocity cell only rotates 60°. Thus, in this time interval, its speed is about 50% of the rotor. In the third snapshot the cell shape is stretched in the circumferential direction, as the impeller LE passes below its position.

In the diffuser, approximately at middle radius, a series of stall cells appear at 4 o'clock and progress to the VT. One of those cells is marked with a red arrow. As commented in figure 6.35, these cells advance until they collide with the volute tongue, causing surface loading fluctuations, thereby exciting the dipole acoustic sources.

The presence of rotating stall in the bep can be thus related to the also atypical presence of backflow in these operating conditions. The backflow swirl rolls the incoming flow generating inducer vortices as shown. These promote detachment in the impeller channels by impairing the incidence, resulting in stall cells detaching from the trailing edge that advance through the diffuser.

At this point the structures that compose the rotating stall have been shown in the isospan 50% section developed (figures 6.35 and 6.36) and their time evolution in the series of snapshots in figure 6.37. Snapshots of certain low-pressure isosurfaces are shown below to identify vortices in the inducer and establish relationships with the patterns observed in the asynchronous DMD modes.

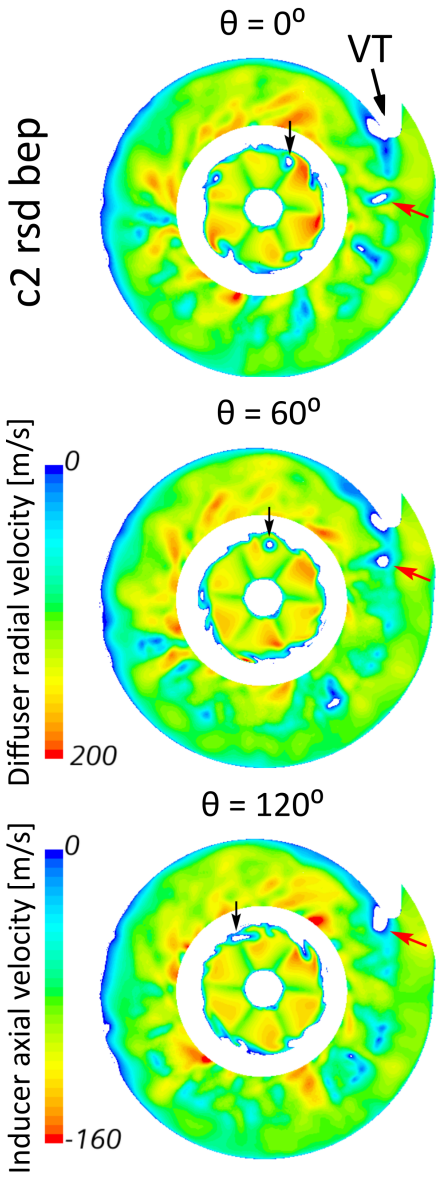

Figure 6.37: *Top view of the inducer2 and isospan 50% sections of the diffuser and the volute of c2 rsd bep. Streamwise (axial at the inducer, and radial at the diffuser) velocity contours are shown. The snapshots are separated by one main blade passing period, i.e., 60° of impeller counter-clockwise rotation.*

Figure 6.38 shows a snapshot of the 90 kPa isosurface in the c1 str nsg case. This surface forms backswept lobes that appear mostly on the major radii of the inducer and descend to the impeller blades. The left figure shows how the blades cut through these lobes. The right figure shows the LIC of the velocity on the pressure isosurface. It can be seen that the streamlines are perpendicular to the axis of the lobes, so the flow motion in those areas is vortical. In addition, the vortex surfaces closest to the largest radii have the maximum velocity. The vortex surfaces closer to the hub have lower velocities. That is consistent with the observations in [69] where it is explained that the radial gradient of the circumferential velocity causes the rotation of the inducer vortices.

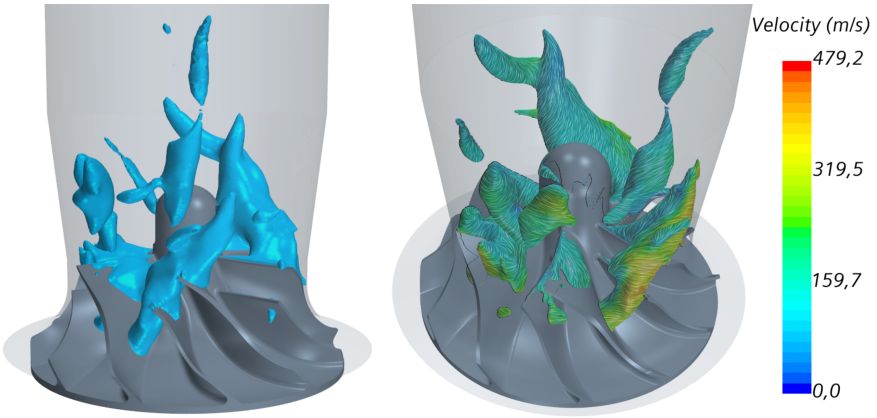

Figure 6.38: *Snapshot of the 90 kPa isosurface of c1 str nsg. LIC of the velocity is represented in the right figure.*

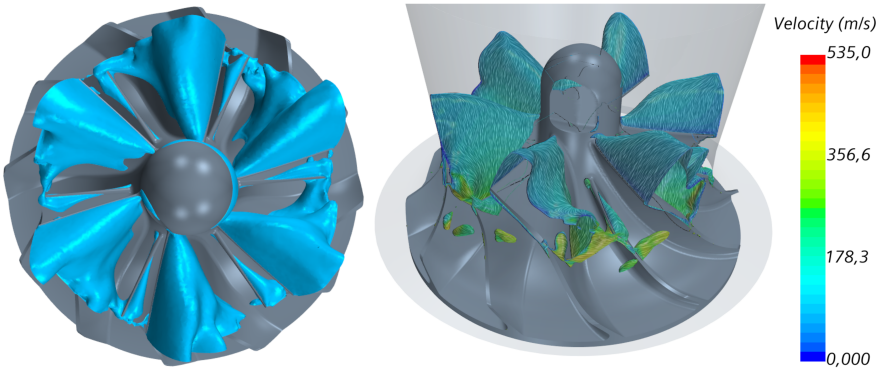

Figure 6.39: *Snapshot of the 95 kPa isosurface of c1 str bep. LIC of the velocity is represented in the right figure.*

The 95 kPa isosurface in the c1 str bep compressor is shown in figure 6.39. The surface describes six lobes in the SS immediately downstream of the LE

of the main blades. The left figure shows that small lobes also appear on the LE of the splitter blades. The shape of the isosurface is easily recognized as the lobes of the BPF mode described in the previous chapter. The right figure shows the velocity LIC over the pressure isosurface. It can be seen how the streamlines describe concentric circles around the impeller axis. As the previous chapter shows, no vortices appear at this operating point. All the modes found in the c1 bep cases correspond to synchronous frequencies (multiples of RO).

The two previous figures belong to the str case of compressor c1, but the rest of the geometries present similar isosurfaces (not shown here). In particular, the vortices of the c1 elb nsg case have the same shape as those of the c1 str nsg case. Due to the vertical duct span between the elbow and the inducer, the vortices do not reach the elbow, and thus no influence of the inlet geometry is observed.

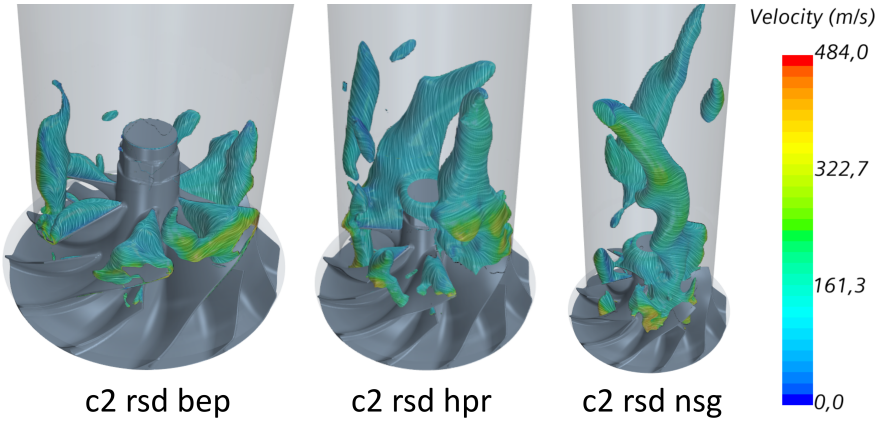

Figure 6.40: *Snapshot of the 88 kPa isosurface of c2 rsd cases. The LIC of the velocity is represented on the isosurface.*

Figure 6.40 shows the 88 kPa isosurface for the c2 rsd cases. In the bep, BPF lobes are observed above the main blades SS, but at the outer radius, backswept vortices appear. Although the vortices do not have much upstream extension, their appearance at the bep point is remarkable. That is associated with the presence of backflow in this case, as shown throughout the chapter. In the center of the figure appears the hpr case. Although some LE lobes can be distinguished, two large vortices and some smaller vortices are also observed. Finally, on the right is the nsg point. There two vortices with a large upstream extension can be seen. This shape is clearly associated with the "whoosh modes" of the previous chapter. In this figure, it can be seen that the inducer vortices appear at the three operating points of c2 rsd. It is clear how reducing the mass flow rate increases the upstream extension of the vortices.

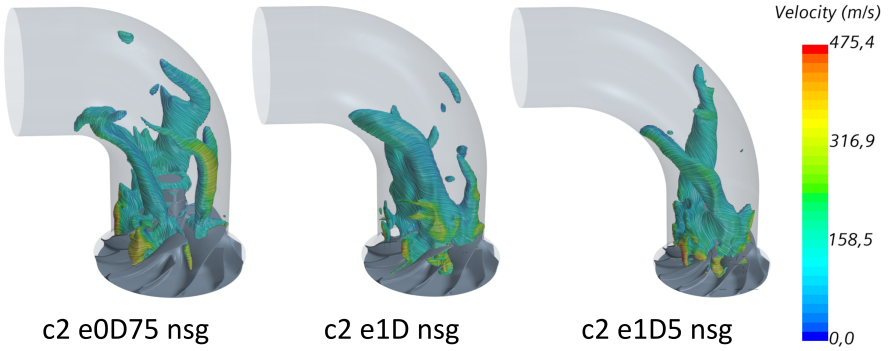

Figure 6.41: *Snapshot of the 88 kPa isosurface of c2 elbow cases. The LIC of the velocity is represented on the isosurface.*

Snapshots of the 88 kPa isosurface in the c2 cases with inlet elbow are shown in figure 6.41. The differences observed for the different elbow curvature radii are the same as in the whoosh modes of the previous chapter. The smallest radius case, e0D75, shows vortices stumbling against the outer elbow wall and being forced into the horizontal duct. That change of direction distorts the vortices and causes interaction with the elbow walls and other vortices. The interaction with the outer elbow wall is smaller in cases with larger curvature radii. The distortion of the vortices due to the inclination towards the horizontal duct is also less intense. In the case of the largest radius, e1D5, the vortices have the same tilt as in c2 rsd nsg. The outer elbow wall does not limit the upstream extension of the vortex. In addition, the vortices do not enter the horizontal duct.

In chapter 5 it was shown how vortex distortion and interaction with other vortices are directly related to the amplitude of the *whoosh* noise broadband.

6.7 Conclusions

The objective of this chapter was to identify the flow structures causing the modes associated with the spectral components of interest.

Synchronous sources

The most important synchronous spectral component is the BPF. Three flow structures have been found concerning the generation of the BPF tone. In order of importance, they are:

- Static pattern of pressure in the main blade LE. The sonic conditions in the main blade LE tip cause this flow mechanism to dominate the acoustic spectrum.
- Interaction of the TE with the circumferential pressure distribution in the diffuser. Specifically the first harmonic, with a wavenumber of 1.

- Static alternating pressure pattern at the outlet of the blades in the channels formed by the main blades.

The second most important synchronous component is the 2×BPF. The flow structures responsible for this tone are:

- The static alternating pressure pattern at the blades TE (both main and splitter blades).
- Interaction of the TE with the circumferential pressure distribution in the diffuser. Specifically the second harmonic, with a wavenumber of 2.
- Static pattern of pressure in the main and splitter blade LE.

The inlet geometry has not shown influence on the flow structures generating synchronous noise. Operating conditions do have an important influence on these flow structures. The presence of backflow at the outer inducer radius results in a low relative velocity at the blade tip and thus inhibits the sonic conditions. In all cases where inducer backflow was present, the BPF tone did not dominate the spectrum and, depending on the backflow thickness, was not even distinguishable. Also, the velocity at the blade tip is directly related to the Mach number in that zone; therefore, points with higher impeller rotational velocity achieve sonic conditions more easily.

The operating point did not influence the static pattern of pressure in the TE. On the other hand, the TE interaction with the circumferential pressure pattern in the inducer did change with the operating point. At the nsg points, the amplitude of the first two harmonics was more than twice as large as in the bep case and was also considerably larger than that of the successive harmonics.

Asynchronous sources

The most important asynchronous spectral components are two broadband noises. The TCN (tip clearance noise) above the plane wave limit, and the *whoosh* noise below that limit.

The *whoosh* noise is generated by the flow mechanism known as the "rotating stall". The inducer backflow gives rise to a radial circumferential velocity gradient that generates vortices upstream of the inducer. The vortices rotate around the impeller axis at a velocity lower than the impeller. The blades shear the vortices, and this interaction results in flow instabilities in the impeller channel that promote flow detachment in the blade SS. Stall cells near the TE cause diffuser rotating stall, passing from one blade to the next. Some of these cells detach and progress through the diffuser until they impact the volute tongue. They generate an unsteady loading on its surface and, thus, a dipolar noise source.

The vortices related to the rotating stall and the stall cells in the diffuser and VT were identified by the DMD modes in the previous chapter and by the flow snapshots in this chapter.

The inlet geometry does not influence this flow structure as long as it does not interfere with the vortices. In compressor c1, all inlet geometries have a one-diameter long straight duct section between the inlet geometry and the converging section leading to the inducer. Thus, the elbow is sufficiently separated from the inducer so that its presence does not affect the inducer vortices.

In compressor c2, on the other hand, the elbows considered do not incorporate the straight duct section between the elbow and the inducer. Thus, the elbows with smaller curvature radii interfere with the vortices. Interaction occurs between the vortices and the elbow walls, as well as between the various vortices. These interactions are directly proportional to the amplitude of the *whoosh* noise broadband. In addition, the vortices in these elbows enter the upstream horizontal duct, facilitating the propagation of pressure oscillations.

Larger curvature radii elbows exhibit vortices free of distortion and heavy interaction with the elbow walls, similar to the vortices found in the straight inlet duct (rsd). These geometries exhibit lower amplitude in the *whoosh* noise band than smaller radius elbows.

As for the operating conditions, vortices do not appear in the bep of compressor c1. In compressor c2, they appear at all points: bep, hpr, and nsg. It has been shown how the extent of vortices increases with decreasing mass flow rate, in line with the amplitude in the *whoosh* noise broadband. The presence of backflow is directly correlated with the presence of inducer vortices.

The backflow in the bep of compressor c2 is an important difference with respect to the flow field in compressor c1. In the latter, the inducer section is 24% smaller than in c2, increasing the axial velocity and preventing backflow. Thus, a reduced inducer section may influence noise generation by inhibiting backflow, although that feature may have a negative impact on the near-choke operation.

As for the high-frequency broadband (TCN), it has been shown how the interaction of the vortices with the blade surface generates noise at these frequencies. The previous chapter showed how the vortices in the tip clearance region were cut by the blades' outer radii and produced an unsteady blade loading that excited the dipole acoustic sources.

Thus, part of the noise in the high-frequency broadband can be associated with the interaction of the vortices with the blades in the TC region. However, this mechanism may not be the only one responsible for the noise in that broadband. In particular, the TCN broadband appears in the c1 bep cases, where no inducer vortices have been observed.

Numerical calculations with DES turbulence models are not able to accurately reproduce the TCN broadband. As seen in Chapter 4, both compressors underestimate the amplitude of the experimental spectrum in this frequency range. Therefore, some of the flow mechanisms responsible for the noise in this broadband are likely absent from the calculated flow field.

However, it has been shown that the interaction of the blade surface with the inducer vortices is an important contributor to the noise in this frequency range.

7

Conclusions and future works

Contents

7.1 Introduction

This last chapter is devoted to the conclusions of the thesis. The objective of a doctoral thesis is to expand the frontier of knowledge in a particular area of research. Thus, this chapter will discuss how the results obtained in this thesis contribute to the state of the art in compressor noise research and the achievement of the objectives stated in the first chapter.

First, the conclusions about the numerical model and the analysis methodology are discussed, and then the results about the noise-generating flow structures and the influence of the operating point and inlet geometry are presented. Finally, suggestions for continuing and extending the work presented in this thesis are put forward.

7.2 Conclusions

7.2.1 Methodology

Numerical setup

This subsection provides conclusions about the results yielded by the numerical setup used. The main features of this setup are the use of the DES turbulence model and a time discretization with 2° of impeller turn in each time step (TS). A value of 1°/TS is commonly used in the literature. The value of 2°/TS had been proposed as viable for acoustic predictions [24], [22]. This thesis provides actual information on the performance of this setup in a comprehensive study of flow field and compressor acoustics.

- The numerical model correctly predicts the operating variables (pressure ratio and isentropic efficiency) in compressor c1. In compressor c2, the irreversibility caused by the flow instabilities at the near surge point is underestimated. The backflow measurements at the inlet show that the calculated upstream extent of backflow is correct, but the temperature in the calculations is lower.

- The acoustic validation shows a good agreement between calculations and measurements except in the broadband between 5 and 10 kHz, corresponding to the tip clearance noise (TCN), whose amplitude is underestimated. This limitation is characteristic of DES models [24], and even some LES [22]. Otherwise, the numerical setup is appropriate for acoustic calculations, as the remainder frequencies are correctly represented by the model.

- The Ffowcs Williams and Hawkings (FW-H) analogy was used to complement the validation of the direct aeroacoustic calculation method in compressor c2. This model showed good agreement with the direct calculation and measurements. At the bep and hpr points of c2, the FW-H analogy showed a lower underestimation of the amplitude in the TCN

band. This suggests that some TCN sources are present on the blades' surface, and the amplitude defect at the duct probes is due to attenuated propagation through the domain.

Analysis methodology

The analysis methodology used is one of the original contributions of this thesis. To the author's knowledge, this is the first three-dimensional DMD study of the pressure field in the entire computational domain of a centrifugal compressor, including the impeller rotating region. The use of DMD has been exploited for dual functionality. The first is to highlight temporal and spatial patterns that subsequently allow the underlying flow mechanisms to be identified. The second is to link these flow mechanisms to a frequency in the spectrum, in an objective manner. This represents a new contribution to the methods used so far in the literature.

- The DMD method has succeeded in identifying spatial patterns at all the spectrum's relevant frequencies, including the BPF tone, the *whoosh* noise band, and even the TCN broadband. It is remarkable how the analysis method manages to identify oscillations at these frequencies at the place of their generation. In this way, noise sources can be found without paying the computational cost of their unattenuated propagation throughout the entire domain. This constitutes an improvement in the computational efficiency of the method.
- Through the application of the analysis methodology, the main noise-generating flow structures have been identified. These are the static pressure pattern in the leading edge (LE) for the BPF tone, the inducer vortices generating the *whoosh* noise, the interaction of the vortices with the impeller blade surface at the TCN frequencies, the jet-wake pattern in the trailing edge (TE) generating the 2×BPF tone, and the first two harmonics of the circumferential pressure profile in the diffuser, which excite the impeller TE at the BPF and 2×BPF.

7.2.2 Results

This subsection will show the results related to the thesis' objectives regarding identifying noise sources and the influence of operating conditions and inlet geometry. In addition, it clarifies certain gaps in the state of the art, such as the origin of *whoosh* and TCN noises. New contributions are also made to the mechanisms of tonal noise generation.

Noise-generating flow structures

- The backflow has been identified as one of the most influential flow structures in the acoustic response of compressors. Its presence affects both tonal noises, such as BPF, and broadbands at low frequencies, such as *whoosh*.

  - The presence of backflow in the inducer significantly reduces the flow velocity in the impeller LE tip, hindering the reaching of sonic conditions. This significantly reduces the amplitude of the BPF tone in the inlet duct.
  - A direct relationship has been observed between the presence of backflow and inducer vortices that cause *whoosh* noise and contribute to the TCN.
  - The correlation between the BPF tone amplitude and backflow's presence provides relevant information about the flow conditions inside the compressor, which can be readily accessed.

- One of the most important contributions of this thesis to the current knowledge has been the identification of DMD modes corresponding with inducer vortices. Two main vortices have been identified in the inducer at operating points where backflow is present, that cause pressure oscillations in the characteristic frequency range of the *whoosh* noise (1500 to 3500 Hz). In their movement around the impeller axis, these vortices shed numeruous smaller vortices that cause pressure oscillations around the same low-frequency range. The radial region of the inlet duct where these vortices appear had been identified by other researchers [49] as the inlet region of highest SPL, although they had attributed it to the backflow shear layer rather than the pressure oscillations caused by the vortices.

- In the diffuser, pressure oscillations at the same frequencies as the inducer vortices have been identified in the TE, diffuser, and volute tongue regions. These oscillations have been induced by the diffuser rotating stall, which is driven by the interaction of the inducer vortices with the LE through flow detachment at the suction side of the impeller blades. Thus, this work contributes further understand the phenomena giving rise to the *whoosh* noise in the inducer and diffuser.

- As for the TCN, its primary generation mechanism is likely to be absent from the flow field calculated by the numerical model, as discussed above. However, DMD modes have been identified at all operating conditions in the tip clearance (TC) zone oscillating at the TCN frequencies. At the operating points with inducer vortices, it has been shown that when the impeller blades cut the vortices, blade loading oscillations occur near the TC region and in the TCN frequency band. Although vortices contribute to this phenomenon, they are not the only flow mechanism that produces such noise. This is deduced from the fact that at the bep of compressor c1, the TCN band is measured, but there are no vortices in the flow field. Thus, the hypothesis that the *whoosh* noise and the TCN are different phenomena [27] is confirmed. The absence of part of the TCN-generating flow structures does not seem to affect the rest of the noise-generating flow structures identified. The TCN

is a local phenomenon spotted in the tip clearance, and the rest of the identified phenomena are consistent with other literature reports. Using scale-resolving turbulence models would enrich the number of phenomena identified using the presented methodology.

- It has been shown that the circumferential pressure distribution in the diffuser excites the BPF and 2×BPF modes at the impeller TE surface. Specifically, the harmonic with a circumferential wavenumber of 1 excites the BPF mode, while the harmonic with a wavenumber of 2 excites the 2×BPF. Also, a significant increase in the amplitude of these two harmonics was quantified when moving from the bep to the near surge point. The jet-wake pattern in the TE also reinforces the 2×BPF mode. This contribution highlights the fact that the generation mechanisms of BPF and 2×BPF tonal noises are different in the inducer and TE. For that reason, the inducer backflow may affect the generation of those tones at the inlet, while at the outlet, they are not affected.

Influence of the inlet geometry

- In compressor c1, noticeable differences in the measured spectra are observed among the different inlet geometries. However, the quantification of the noise-generating flow structures gives no relevant differences. This shows that the elements of the inlet geometry located between the inducer and the duct pressure probes cause the differences observed by their scattering (reflecting, transmitting, and damping) properties. That is to say, in compressor c1, there is no influence of the inlet geometry on the noise-generating flow structures, but there is an influence on the propagation of the acoustic oscillations.

  - The reservoir (rsv) shows low amplitude at its natural frequency and its harmonics at the nsg point. At bep and nsg, it also has the lowest amplitude of the four geometries in the tonal noises (BPF and RO).
  - The tapered duct (tap) shows uniform amplitude reduction over the entire frequency range.

- In compressor c2, the influence of the inlet duct on the noise-generating flow structures is patent. A correlation is observed between the amplitude of the *whoosh* noise broadband and the degree of distortion imposed by the inlet geometry on the inducer vortices. In the smaller radii elbows, which exhibit the greatest amplitude in that band, the upstream extension of the vortices is impeded by the proximity of the outer elbow wall. This distorts the vortices that are forced to change direction and thus interact with other vortices and the elbow walls. In the largest radius elbow and straight duct, the duct wall does not interfere with the upstream extension of the vortices, so they do not interact with each

other or with the walls. In those cases, lower *whoosh* amplitudes are produced.

- The elbow analyzed in compressor c1 has a curvature radius of 1.36 D, intermediate between the two larger radii of c2 elbows: 1 D and 1.5 D. However, the reason why there is no interaction between vortices and the inlet geometry in c1 is that the upstream extent of the vortices is less than in c2 and because the elbow is separated from the inducer by a 1.6 D duct span. In compressor c2, the separation between the elbow outlet and the inducer is only 0.43 D.
- Certain geometric parameters have been identified at the compressor inlet that are of particular relevance to acoustic emissions:
  - The presence of inducer backflow is correlated with increased noise at low frequencies as it gives rise to inducer vortices. Compressor c1 has higher axial velocity in the inducer for similar mass flow rates because its diameter is smaller than in c2 (36.1 vs. 41.4 mm). Compressor c1 does not present backflow in the bep, while compressor c2 shows backflow in all the operating conditions. Thus, a smaller inducer section is shown to delay the onset of backflow. However, the inducer section affects other aspects besides noise, such as compressor performance under high mass flow conditions, so the improvement obtained at low mass flow would have a downside at higher mass flow rates.
  - Regarding the inlet duct itself, it has been shown that it is important to have sufficient clear space upstream of the inducer to avoid distortion of the inducer vortices. If a change of duct direction upstream of the inducer is needed, large duct radii or a straight span between the elbow and the inducer should be used. Both options promote flow uniformity at the inducer, which is correlated with improved compressor performance.

7.3 Future works

The following are suggestions for the continuation and extension of the work presented in this thesis.

- The application of the presented analysis methodology to a flow field calculated using a more precise scale-resolving turbulence model (such as the LES) could provide additional information on the flow structures generating the TCN.
- The analysis methodology could be extended in several ways:
  - Other flow field decomposition techniques such as POD or volume FFT could be tested to show flow structures with broadband spectral content.

  - The DMD of the velocity field in the domain would provide interesting information about the flow structures at different frequencies, which could complement the pressure field information presented in this thesis.
  - The selection criteria of the most relevant modes could be modified to manually include interesting frequencies, even if they do not present one of the ten most prominent modes.
  - Programming an algorithm to recognize spatially coherent modes at different frequencies automatically would allow taking advantage of the information contained in the thousands of modes offered by the DMD. In the current methodology, visual inspection of the modes and searching for common patterns is the most laborious and subjective task.

- Concerning inlet elbows, some modifications to the analyzed configurations could enrich the results presented in this work:

  - The study of the noise-generating flow structures in elbows close to the inducer (such as those of compressor c2) at high mass flow conditions would complete the flow field characterization with these geometries. In particular, the small separation of the elbow outlet from the inducer could increase the influence of the Dean vortices in the noise.
  - The analysis of the dipole sources on the elbow walls would allow quantifying the contribution to noise from the interaction of the vortices with the walls.
  - A parametric study on the angular orientation of the elbow to the volute tongue could shed light on the interaction of the asymmetric pressure distribution in the diffuser with the inlet flow field.

- Calculating the flow field under other operating conditions could extend the understanding of noise-generating flow structures. In particular, other mass flow rates and compressor regimes would give rise to different combinations of backflow thickness and sonic conditions. It would also be interesting to provide further information on the actual mechanism of inducer vortex generation from swirling backflow and under which operating conditions both phenomena appear.

- Finally, it could be worth analyzing alternative inlet geometries such as the inlet step proposed by Karim et al. [60] consisting of a steep increase of the inlet duct section upstream of the LE, that could decrease noise by reducing the influence of the backflow on the incoming flow.

Bibliography

[1] Carl Sagan. *Greenhouse Effect conference before the U.S. Congress*. 1985. URL: https://www.c-span.org/video/?125856-1/greenhouse-effect.

[2] Secretariat of the World Meteorological Organization. *Annual report of the World Meteorological Organization 1985*. World Meteorological Organization, 1985.

[3] Joseph Fourier. "Remarques Generales sur les Temperatures Du Globe Terrestre et des Espaces Planetaires". In: *Annales de Chimie et de Physique* 27 (1824), pp. 136–167.

[4] Francis Molena. "The remarkable weather of 1911. The Effect of the Combistion of Coal on the Climate - What scientists Predict for the Future". In: *Popular Mechanics Magazine* March (1912), pp. 339–342.

[5] The International Council on Clean Transportation. *A technical summary of Euro 6/VI vehicle emission standards*. 2022. URL: https://theicct.org/sites/default/files/publications/ICCT_Euro6-VI_briefing_jun2016.pdf.

[6] U.S. Department of Transportation. *Corporate Average Fuel Economy (CAFE) Standards*. 2022. URL: https://www.transportation.gov/mission/sustainability/corporate-average-fuel-economy-cafe-standards.

[7] Florian Schumann, Fatih Sarikoc, Stefan Buri, Heiko Kubach, and Ulrich Spicher. "Potential of spray-guided gasoline direct injection for reduction of fuel consumption and simultaneous compliance with stricter emissions regulations". In: *International Journal of Engine Research* 14.1 (2013), pp. 80–91. DOI: 10.1177/1468087412451695.

[8] F. Payri and J. M. Desantes, eds. *Motores de combustión interna alternativos*. Reverté, 2011.

[9] Antonio J Torregrosa, Alberto Broatch, Xandra Margot, and Jorge García-Tíscar. "Experimental methodology for turbocompressor induct noise evaluation based on beamforming wave decomposition". In: *Journal of Sound and Vibration* 376 (2016), pp. 60–71. DOI: 10.1016/j.jsv.2016.04.035.

[10] Harald Stoffels and Markus Schroeer. "NVH Aspects of a Downsized Turbocharged Gasoline Powertrain with Direct Injection". In: *SAE Technical Paper* 2003-01-1664 (2003). DOI: 10.4271/2003-01-1664.

[11] Marco Badami, F Mallamo, F Millo, and EE Rossi. "Influence of multiple injection strategies on emissions, combustion noise and BSFC of a DI common rail diesel engine". In: *SAE Transactions* (2002), pp. 1118–1129.

[12] Carla Julio da Silveira Brizon and Eduardo Bauzer Medeiros. "Combining subjective and objective assessments to improve acoustic comfort evaluation of motor cars". In: *Applied Acoustics* 73.9 (2012), pp. 913–920. DOI: 10.1016/j.apacoust.2012.03.013.

[13] M.J.M. Nor, M.H. Fouladi, H. Nahvi, and A.K. Ariffin. "Index for vehicle acoustical comfort inside a passenger car". In: *Applied Acoustics* 69.4 (2008), pp. 343–353. DOI: 10.1016/j.apacoust.2006.11.001.

[14] Eurostat. *What is the source of the electricity we consume?* 2020. URL: https://ec.europa.eu/eurostat/cache/infographs/energy/bloc-3b.html.

[15] Eurostat. *Energy statistics - an overview.* 2020. URL: https://ec.europa.eu/eurostat/statistics-explained/index.php?title=Energy_statistics_-_an_overview.

[16] Council of the EU. *Fit for 55 package: Council reaches general approaches relating to emissions reductions and their social impacts.* 2022. URL: https://www.consilium.europa.eu/en/press/press-releases/2022/06/29/fit-for-55-council-reaches-general-approaches-relating-to-emissions-reductions-and-removals-and-their-social-impacts/.

[17] García Antonio, Javier Monsalve-Serrano, Santiago Martínez-Boggio, and Karsten Wittek. "Potential of hybrid powertrains in a variable compression ratio downsized turbocharged VVA Spark Ignition engine". In: *Energy* 195 (2020), p. 117039.

[18] Andrzej Szalek and Ireneusz Pielecha. "The Influence of engine downsizing in hybrid powertrains on the energy flow indicators under actual traffic conditions". In: *Energies* 14.10 (2021), p. 2872.

[19] John M Tyler and Thomas G Sofrin. *Axial flow compressor noise studies.* Tech. rep. SAE Technical Paper, 1962. DOI: 10.4271/620532.

[20] Paolo Candeloro, Daniele Ragni, and Tiziano Pagliaroli. "Small-Scale Rotor Aeroacoustics for Drone Propulsion: A Review of Noise Sources and Control Strategies". In: *Fluids* 7.8 (2022), p. 279.

[21] Nadine Aubry. "On the hidden beauty of the proper orthogonal decomposition". In: *Theoretical and Computational Fluid Dynamics* 2.5-6 (1991), pp. 339–352. DOI: 10.1007/BF00271473.

[22] S. Sharma, A. Broatch, J. García-Tíscar, A. K. Nickson, and J. M. Allport. "Acoustic and pressure characteristics of a ported shroud turbocompressor operating at near surge conditions". In: *Applied Acoustics* 148 (2019), pp. 434–447. DOI: https://doi.org/10.1016/j.apacoust.2019.01.005.

[23] Emma Alenius. "Flow Duct Acoustics: An LES Approach". PhD thesis. KTH, MWL Flow acoustics, 2012.

[24] Roberto Navarro García. "A numerical approach for predicting flow-induced acoustics at near-stall conditions in an automotive turbocharger compressor". PhD thesis. Universitat Politècnica de València (UPV), 2014. DOI: 10.4995/Thesis/10251/44114.

[25] Sharma S. "Numerical characterisation of flow-induced noise in a small high-speed centrifugal compressor with asing treatment". PhD thesis. University of Huddersfield, 2019.

[26] Till Raitor and Wolfgang Neise. "Sound generation in centrifugal compressors". In: *Journal of Sound and Vibration* 314 (2008), pp. 738–756. ISSN: 0022-460X. DOI: 10.1016/j.jsv.2008.01.034.

[27] J. García-Tíscar. "Experiments on Turbocharger Compressor Acoustics". PhD thesis. Universitat Politècnica de València (UPV), 2017.

[28] Sundström E. "Flow instabilities in centrifugal compressors at low mass flow rate". PhD thesis. Royal Institute of Technology (KTH), 2017.

[29] Eric P Trochon. "A new type of silencers for turbocharger noise control". In: *SAE Technical Paper* 110.6 (2001), pp. 1587–1592. DOI: 10.4271/2001-01-1436.

[30] K.Y. Soh, K.K. Euo, D.H. Bae, and K.T. Kang. "Noise reduction in turbocharger system of diesel engines". In: *INTER-NOISE and NOISE-CON Congress and Conference Proceedings*. Vol. 2003. Institute of Noise Control Engineering. 2003, pp. 155–162.

[31] D. Evans and A. Ward. "Minimizing Turbocharger Whoosh Noise for Diesel Powertrains". In: *SAE Technical Paper* 2005-01-2485 (2005). DOI: 10.4271/2005-01-2485.

[32] G. Gaudé, T. Lefèvre, R. Tanna, K. Jin, T. J. B. McKitterick, and S. Armenio. "Experimental and computational challenges in the quantification of turbocharger vibro-acoustic sources". In: *Proceedings of the 37th International Congress and Exposition on Noise Control Engineering (INTER-NOISE 2008)*. Vol. 2008. Institute of Noise Control Engineering. 2008, pp. 5754–5767. URL: http://www.ingentaconnect.com/content/ince/incecp/2008/00002008/00000003/art00009.

[33] C. Teng and S. Homco. "Investigation of Compressor Whoosh Noise in Automotive Turbochargers". In: *SAE Int. J. of Passeng. Cars-Mech. Syst.* 2.1 (2009), pp. 1345–1351. DOI: 10.4271/2009-01-2053.

[34] Ajith V. Pai, Stephen J. Walsh, Dan J. O'Boy, and Rui Chen. "Turbocharger surge noise measurement and solution using experimental techniques". In: *Proceedings of the 22nd International Congress on Sound and Vibration*. 2015, pp. 2433–2441. URL: http://iiav.org/archives_icsv_last/2015_icsv22/content/papers/papers/full_paper_255_20150313183259397.pdf.

[35] H. Rämmal and M. Åbom. "Acoustics of Turbochargers". In: *SAE Technical Paper* (2007). DOI: https://doi.org/10.4271/2007-01-2205.

[36] Michael James Lighthill. "On sound generated aerodynamically I. General theory". In: *Proceedings of the Royal Society of London. Series A. Mathematical and Physical Sciences* 211.1107 (1952), pp. 564–587.

[37] Michael James Lighthill. "On sound generated aerodynamically II. Turbulence as a source of sound". In: *Proceedings of the Royal Society of London. Series A. Mathematical and Physical Sciences* 222.1148 (1954), pp. 1–32.

[38] H. Tiikoja, H. Rämmal, M. Åbom, and H. Boden. "Investigations of Automotive Turbocharger Acoustics". In: *SAE International Journal of Engines* 4.2 (2011), pp. 2531–2542. DOI: 10.4271/2011-24-0221.

[39] Neil Figurella, Rick Dehner, Ahmet Selamet, Kevin Tallio, Keith Miazgowicz, and Robert Wade. "Noise at the mid to high flow range of a turbocharger compressor". In: *Noise Control Engineering Journal* 62.5 (2014), pp. 306–312. DOI: 10.3397/1/376229.

[40] Erwann Guillou, Russel DiMicco, Ephraim Gutmark, Ashraf Mohamed, and Matthieu Gancedo. *Characterization of a Ported Shroud Compressor using PIV Measurements*. Tech. rep. 2010-01-1225. SAE Technical Paper, 2010. DOI: 10.4271/2010-01-1225.

[41] AJ Torregrosa, A Broatch, X Margot, J García-Tíscar, Y Narvekar, and R Cheung. "Local flow measurements in a turbocharger compressor inlet". In: *Experimental Thermal and Fluid Science* 88 (2017), pp. 542–553. ISSN: 0894-1777. DOI: 10.1016/j.expthermflusci.2017.07.007.

[42] L. J. Eriksson. "Higher order mode effects in circular ducts and expansion chambers". In: *Journal of the Acoustical Society of America* 68 (1980), p. 545. DOI: 10.1121/1.384768.

[43] Y. Lee, D. Lee, Y. So, and D. Chung. "Control of Airflow Noise From Diesel Engine Turbocharger". In: *SAE Technical Paper* (2011). DOI: 10.4271/2011-01-0933.

[44] F. Mendonça, O. Baris, and G. Capon. "Simulation of Radial Compressor Aeroacoustics using CFD". In: *Proceedings of ASME Turbo Expo 2012*. ASME. 2012, pp. 1823–1832. DOI: 10.1115/GT2012-70028.

[45] A Broatch, J Galindo, R Navarro, J García-Tíscar, A Daglish, and RK Sharma. "Simulations and measurements of automotive turbocharger compressor whoosh noise". In: *Engineering Applications of Computational Fluid Mechanics* 9.1 (2015), pp. 12–20. DOI: 10.1080/19942060.2015.1004788.

[46] Elias Sundström, Bernhard Semlitsch, and Mihai Mihăescu. "Assessment of the 3D Flow in a Centrifugal compressor using Steady-State and Unsteady Flow Solvers". In: *SAE Technical Paper*. SAE International, 2014. DOI: 10.4271/2014-01-2856.

[47] Alberto Broatch, José Galindo, Roberto Navarro, and Jorge García-Tíscar. "Numerical and experimental analysis of automotive turbocharger compressor aeroacoustics at different operating conditions". In: *International Journal of Heat and Fluid Flow* (2016). DOI: 10.1016/j.ijheatfluidflow.2016.04.003.

[48] Bernhard Semlitsch and Mihai Mihăescu. "Flow phenomena leading to surge in a centrifugal compressor". In: *Energy* 103 (2016), pp. 572–587. ISSN: 0360-5442. DOI: https://doi.org/10.1016/j.energy.2016.03.032. URL: https://www.sciencedirect.com/science/article/pii/S0360544216302766.

[49] R. Dehner and A. Selamet. "Prediction of Broadband Noise in an Automotive Centrifugal Compressor with Three-Dimensional Computational Fluid Dynamics Detached Eddy Simulations". In: *SAE Technical Paper* (2019). DOI: https://doi.org/10.4271/2019-01-1487.

[50] JE Ffowcs Williams and David L Hawkings. "Sound generation by turbulence and surfaces in arbitrary motion". In: *Philosophical Transactions of the Royal Society of London A: Mathematical, Physical and Engineering Sciences* 264.1151 (1969), pp. 321–342. DOI: 10.1098/rsta.1969.0031.

[51] E. Sundström, B. Semlitsch, and M. Mihăescu. "Acoustic signature of flow instabilities in radial compressors". In: *Journal of Sound and Vibration* 434 (2018), pp. 221–236. DOI: https://doi.org/10.1016/j.jsv.2018.07.040.

[52] Chao Zhong, Liaoping Hu, Jinke Gong, Chenxi Wu, Shaoli Wang, and Xianlei Zhu. "Effects analysis on aerodynamic noise reduction of centrifugal compressor used for gasoline engine". In: *Applied Acoustics* 180 (2021), p. 108104. ISSN: 0003-682X. DOI: https://doi.org/10.1016/j.apacoust.2021.108104. URL: https://www.sciencedirect.com/science/article/pii/S0003682X21001973.

[53] Yunbae Kim, Abraham Engeda, Ron Aungier, and Greg Direnzi. "The influence of inlet flow distortion on the performance of a centrifugal compressor and the development of an improved inlet using numerical simulations". In: *Proceedings of the Institution of Mechanical Engineers, Part A: Journal of Power and Energy* 215.3 (2001), pp. 323–338. DOI: 10.1243/0957650011538550.

[54] Leilei Wang, Ce Yang, Ben Zhao, Dazhong Lao, Chaochen Ma, and Du Li. "The change of the inlet geometry of a centrifugal compressor stage and its influence on the compressor performance". English. In: *Journal of Thermal Science* 22.3 (2013), pp. 197–208. ISSN: 1003-2169. DOI: 10.1007/s11630-013-0613-2. URL: 10.1007/s11630-013-0613-2.

[55] Ben Zhao, Harold Sun, Leilei Wang, and Manxiang Song. "Impact of inlet distortion on turbocharger compressor stage performance". In: *Applied Thermal Engineering* 124 (2017), pp. 393–402. ISSN: 1359-4311. DOI: https://doi.org/10.1016/j.applthermaleng.2017.05.181. URL: https://www.sciencedirect.com/science/article/pii/S1359431117318574.

[56] Hongjuan Hou, Leilei Wang, Rui Wang, and Yanzhao Yang. "Effects of bending-torsional duct-induced swirl distortion on aerodynamic performance of a centrifugal compressor". In: *Journal of Thermal Science* 26.2 (2017), pp. 97–106.

[57] Hanzhi Zhang, Ce Yang, Changmao Yang, Hang Zhang, Leilei Wang, and Jiang Chen. "Inlet bent torsional pipe effect on the performance and stability of a centrifugal compressor with volute". In: *Aerospace Science and Technology* 93 (2019), p. 105322.

[58] José Ramón Serrano, Xandra Margot, Andrés Tiseira, and Luis Miguel García-Cuevas. "Optimization of the inlet air line of an automotive turbocharger". In: *International Journal of Engine Research* 14.1 (2013), pp. 92–104. DOI: 10.1177/1468087412449085.

[59] J. Galindo, J. R. Serrano, X. Margot, A. Tiseira, N. Schorn, and H. Kindl. "Potential of flow pre-whirl at the compressor inlet of automotive engine turbochargers to enlarge surge margin and overcome packaging limitations". In: *International journal of heat and fluid flow* 28.3 (2007), pp. 374–387. DOI: 10.1016/j.ijheatfluidflow.2006.06.002.

[60] Ahsanul Karim, Keith Miazgowicz, Brian Lizotte, and Abdelkrim Zouani. "Computational Aero-Acoustics Simulation of Compressor Whoosh Noise in AUtomotive Turbochargers". In: *SAE Technical Paper* (2013). DOI: 10.4271/2013-01-1880.

[61] Neil Figurella, Rick Dehmer, Ahmet Selamet, Kevin Tallio, Keith Miazgowicz, Robert Wade, Ahsanul Karim, Philip Keller, and John Shutty. "Effect of inlet vanes on centrifugal compressor acoustics and performance". In: *Noise Control Engineering Journal* 62.4 (2014), pp. 232–237. DOI: 10.3397/1/376223.

[62] José Galindo, A Tiseira, Roberto Navarro, Daniel Tarí, and Cesare Maria Meano. "Effect of the inlet geometry on performance, surge margin and noise emission of an automotive turbocharger compressor". In: *Applied Thermal Engineering* 110 (2017), pp. 875–882.

[63] A Broatch, X Margot, J García-Tíscar, and F Roig. "Impact of simple surge-enhancing inlet geometries on the acoustic behavior of a turbocompressor". In: *Internationa Journal of Engine Research* (2018). DOI: 10.1177/1468087418784125.

[64] A Broatch, S Ruiz, Jorge García-Tíscar, and F Roig. "On the influence of inlet elbow radius on recirculating backflow, whoosh noise and efficiency in turbocharger compressors". In: *Experimental Thermal and Fluid Science* 96 (2018), pp. 224–233.

[65] Johannes Moritz and Stefan Becker. "Sound radiation of the exhaust gas turbocharger as a function of the compressor inflow". In: *Journal of Sound and Vibration* 498 (2021), p. 115969.

[66] AJ Torregrosa, A Broatch, José Pastor, Jorge García-Tíscar, Raj K Sharma, and R Cheung. "Measuring turbocharger compressor inlet backflow through particle image velocimetry". In: *Experimental Thermal and Fluid Science* 99 (2018), pp. 420–432.

[67] H. K. Versteeg and W. Malalasekera. *An introduction to computational fluid dynamics: the finite volume method*. Prentice Hall, 2007.

[68] Elias Sundström, Bernhard Semlitsch, and Mihai Mihăescu. "Centrifugal compressor: The sound of surge". In: *21st AIAA/CEAS Aeroacoustics Conference*. 2015. DOI: 10.2514/6.2015-2674.

[69] Elias Sundström, Bernhard Semlitsch, and Mihai Mihăescu. "Generation mechanisms of rotating stall and surge in centrifugal compressors". In: *Flow, turbulence and combustion* 100.3 (2018), pp. 705–719.

[70] Siemens Digital Industries Software. *Simcenter STAR-CCM+ User Guide v. 2021.1*. Version 2021.1. 2021.

[71] M. Kaltenbacher, C. Freidhager, and S. Schoder. "Modelling and Numerical Simulation of the Noise Generated by an Automotive Turbocharger Compressor". In: *SAE Technical Paper* (2020). DOI: doi: 10.4271/2020-01-1512.

[72] Alberto Broatch, Jorge García-Tíscar, Ferran Roig, and Sidharath Sharma. "Dynamic mode decomposition of the acoustic field in radial compressors". In: *Aerospace Science and Technology* 90 (2019), pp. 388–400.

[73] P. Spalart and C. Streett. *Young-Person's Guide to Detached-Eddy Simulation Grids*. NASA. 2001. URL: https://ntrs.nasa.gov/citations/20010080473.

[74] Piñero G. and Vergara, L. and Desantes, J. M. and Broatch, A. "Estimation of velocity fluctuation in internal combustion engine exhaust systems through beamforming techniques". In: *Measurement Science & Technology* 11.11 (2000), pp. 1585–1595. DOI: 10.1088/0957-0233/11/11/307.

[75] A Broatch, J Galindo, R Navarro, and J García-Tíscar. "Methodology for experimental validation of a CFD model for predicting noise generation in centrifugal compressors". In: *International Journal of Heat and Fluid Flow* 50 (2014), pp. 134–144. ISSN: 0142-727X. DOI: 10.1016/j.ijheatfluidflow.2014.06.006.

[76] Peter Welch. "The use of fast Fourier transform for the estimation of power spectra: a method based on time averaging over short, modified periodograms". In: *Audio and Electroacoustics, IEEE Transactions on* 15.2 (1967), pp. 70–73.

[77] Stewart Glegg and William Devenport. *Aeroacoustics of low Mach number flows: fundamentals, analysis, and measurement.* Academic Press, 2017.

[78] Bernhard Semlitsch, Bhupatindra Malla, Ephraim J Gutmark, and Mihai Mihăescu. "The generation mechanism of higher screech tone harmonics in supersonic jets". In: *Journal of Fluid Mechanics* 893 (2020).

[79] F. Farassat, S.L. Padula, and M.H. Dunn. "Advanced turboprop noise prediction based on recent theoretical results". In: *Journal of Sound and Vibration* 119.1 (1987), pp. 53–79. ISSN: 0022-460X. DOI: https://doi.org/10.1016/0022-460X(87)90189-1.

[80] CL Morfey. "Rotating pressure patterns in ducts: their generation and transmission". In: *Journal of Sound and Vibration* 1.1 (1964), pp. 60–87. DOI: 10.1016/0022-460X(64)90007-0.

[81] Wolfgang Neise and Lars Enghardt. "Technology approach to aero engine noise reduction". In: *Aerospace Science and Technology* 7.5 (2003), pp. 352–363.

[82] D Casalino, F Diozzi, R Sannino, and A Paonessa. "Aircraft noise reduction technologies: a bibliographic review". In: *Aerospace Science and Technology* 12.1 (2008), pp. 1–17.

[83] DA Fink, NA Cumpsty, and EM Greitzer. "Surge Dynamics in a Free-Spool Centrifugal Compressor System". In: *Journal of Turbomachinery* 114.2 (1992), pp. 321–332. DOI: 10.1115/1.2929146.

[84] Hartmut Krain. "Review of centrifugal compressor's application and development". In: *J. Turbomach.* 127.1 (2005), pp. 25–34.

[85] IJ Day. "Stall, surge, and 75 years of research". In: *Journal of Turbomachinery* 138.1 (2016).

[86] JA Lorett and S Gopalakrishnan. "Interaction between impeller and volute of pumps at off-design conditions". In: *Journal of Fluids Engineering* (1986).

[87] Ce Yang, Wenli Wang, Hanzhi Zhang, Changmao Yang, and Yanzhao Li. "Investigation of stall process flow field in transonic centrifugal compressor with volute". In: *Aerospace Science and Technology* 81 (2018), pp. 53–64.

[88] Zhenzhong Sun, Wangzhi Zou, and Xinqian Zheng. "Instability detection of centrifugal compressors by means of acoustic measurements". In: *Aerospace Science and Technology* 82 (2018), pp. 628–635.

[89] Ibrahim Shahin, Mohamed Alqaradawi, Mohamed Gadala, and Osama Badr. "On the aero acoustic and internal flows structure in a centrifugal compressor with hub side cavity operating at off design condition". In: *Aerospace Science and Technology* 60 (2017), pp. 68–83.

[90] Sang-Bum Ma and Kwang-Yong Kim. "Optimization of discrete cavities in a centrifugal compressor to enhance operating stability". In: *Aerospace Science and Technology* 68 (2017), pp. 308–319.

[91] Xiao He and Xinqian Zheng. "Roles and mechanisms of casing treatment on different scales of flow instability in high pressure ratio centrifugal compressors". In: *Aerospace Science and Technology* 84 (2019), pp. 734–746.

[92] A Michalke. "On the propagation of sound generated in a pipe of circular cross-section with uniform mean flow". In: *Journal of Sound and Vibration* 134.2 (1989), pp. 203–234. DOI: 10.1016/0022-460X(89)90649-4.

[93] Walter Eversman. "Theoretical models for duct acoustic propagation and radiation". In: *Aeroacoustics of Flight Vehicles: Theory and Practice. (NASA Reference Publication 1258)*. Ed. by Harvey H. Hubbard. Vol. 2. NASA, 1991, pp. 101–163.

[94] A McAlpine and MCM Wright. "Acoustic scattering by a spliced turbofan inlet duct liner at supersonic fan speeds". In: *Journal of Sound and Vibration* 292.3 (2006), pp. 911–934. DOI: 10.1016/j.jsv.2005.09.010.

[95] CJ Moore. "Measurement of radial and circumferential modes in annular and circular fan ducts". In: *Journal of Sound and Vibration* 62.2 (1979), pp. 235–256. DOI: 10.1016/0022-460X(79)90024-5.

[96] Peter Limacher, Carsten Spinder, Marius C Banica, and Heinz-Jürgen Feld. "A Robust Industrial Procedure for Measuring Modal Sound Fields in the Development of Radial Compressor Stages". In: *Journal of Engineering for Gas Turbines and Power* 139.6 (2017), p. 062604. DOI: 10.1115/1.4035287.

[97] Marius C Banica, Peter Limacher, Heinz-Jürgen Feld, and Carsten Spinder. "Numerical Prediction of the Sources and the Modal Content of the Acoustic Field in a Radial Compressor Outflow". In: *Journal of Engineering for Gas Turbines and Power* 139.9 (2017), p. 092605. DOI: 10.1115/1.4036284.

[98] John Leask Lumley. "The structure of inhomogeneous turbulent flows". In: *Atmospheric Turbulence and Radio Wave Propagation – Proceedings of the International Colloquium*. Nauka, Moscow, 1967, pp. 166–178.

[99] D Rajpal, E Gillebaart, and R De Breuker. "Preliminary aeroelastic design of composite wings subjected to critical gust loads". In: *Aerospace Science and Technology* 85 (2019), pp. 96–112.

[100] Jiaqi Luo. "Design optimization of the last stage of a 4.5-stage compressor using a POD-based hybrid model". In: *Aerospace Science and Technology* 76 (2018), pp. 303–314. ISSN: 1270-9638. DOI: https://doi.org/10.1016/j.ast.2018.01.043. URL: https://www.sciencedirect.com/science/article/pii/S1270963817312129.

[101] D Lengani, D Simoni, R Pichler, RD Sandberg, V Michelassi, and F Bertini. "Identification and quantification of losses in a LPT cascade by POD applied to LES data". In: *International Journal of Heat and Fluid Flow* 70 (2018), pp. 28–40.

[102] Hüseyin Güner, David Thomas, Grigorios Dimitriadis, and VE Terrapon. "Unsteady aerodynamic modeling methodology based on dynamic mode interpolation for transonic flutter calculations". In: *Journal of Fluids and Structures* 84 (2019), pp. 218–232.

[103] Daniel Gil-Prieto, Pavlos K Zachos, David G MacManus, and Grant McLelland. "Unsteady characteristics of S-duct intake flow distortion". In: *Aerospace Science and Technology* 84 (2019), pp. 938–952.

[104] Peter J Schmid. "Dynamic mode decomposition of numerical and experimental data". In: *Journal of Fluid Mechanics* 656 (2010), pp. 5–28. DOI: 10.1017/S0022112010001217.

[105] Clarence W Rowley, Igor Mezic, Shervin Bagheri, Philipp Schlatter, and Dan S Henningson. "Spectral analysis of nonlinear flows". In: *Journal of fluid mechanics* 641 (2009), pp. 115–127. DOI: 10.1017/S0022112009992059.

[106] Kevin K Chen, Jonathan H Tu, and Clarence W Rowley. "Variants of dynamic mode decomposition: boundary condition, Koopman, and Fourier analyses". In: *Journal of nonlinear science* 22.6 (2012), pp. 887–915. DOI: 10.1007/s00332-012-9130-9.

[107] N Vinha, F Meseguer-Garrido, J De Vicente, and E Valero. "A dynamic mode decomposition of the saturation process in the open cavity flow". In: *Aerospace Science and Technology* 52 (2016), pp. 198–206.

[108] Jiaqing Kou, Soledad Le Clainche, and Weiwei Zhang. "A reduced-order model for compressible flows with buffeting condition using higher order dynamic mode decomposition with a mode selection criterion". In: *Physics of Fluids* 30.1 (2018), p. 016103.

[109] Majd Daroukh, Stéphane Moreau, Nicolas Gourdain, Jean-François Boussuge, and Claude Sensiau. "Tonal noise prediction of a modern turbofan engine with large upstream and downstream distortion". In: *Journal of Turbomachinery* 141.2 (2019).

[110] Antoine Renaud, Shigeru Tachibana, Shuta Arase, and Takeshi Yokomori. "Experimental study of thermo-acoustic instability triggering in a staged liquid fuel combustor using high-speed OH-PLIF". In: *Journal of Engineering for Gas Turbines and Power* 140.8 (2018).

[111] Dimitrios Papadogiannis, Gaofeng Wang, Stéphane Moreau, Florent Duchaine, Laurent Gicquel, and Franck Nicoud. "Assessment of the indirect combustion noise generated in a transonic high-pressure turbine stage". In: *Journal of Engineering for Gas Turbines and Power* 138.4 (2016).

[112] Jeremy Dahan, Romain Futrzynski, Ciarán O'Reilly, and Gunilla Efraimsson. "Aero-acoustic source analysis of landing gear noise via dynamic mode decomposition". In: *21st International Congress on Sound and Vibration*. 2014. URL: http://www.iiav.org/icsv21/content/papers/papers/full_paper_221_20140402145649114.pdf.

[113] Bernard O Koopman. "Hamiltonian systems and transformation in Hilbert space". In: *Proceedings of the National Academy of Sciences* 17.5 (1931), pp. 315–318. URL: http://www.pnas.org/content/17/5/315.full.pdf.

[114] T Sayadi, JW Nichols, PJ Schmid, and MR Jovanovic. "Dynamic mode decomposition of H-type transition to turbulence". In: *Proceedings of the Summer Program 2012*. 2012, pp. 5–14.

[115] Peter J Schmid, L Li, Matthew P Juniper, and O Pust. "Applications of the dynamic mode decomposition". In: *Theoretical and Computational Fluid Dynamics* 25.1-4 (2011), pp. 249–259. DOI: 10.1007/s00162-010-0203-9.

[116] Shervin Bagheri. "Koopman-mode decomposition of the cylinder wake". In: *Journal of Fluid Mechanics* 726 (2013), pp. 596–623. DOI: 10.1017/jfm.2013.249.

[117] Mihailo R Jovanovic, Peter J Schmid, and Joseph W Nichols. "Sparsity-promoting dynamic mode decomposition". In: *Physics of Fluids (1994-present)* 26.2 (2014), p. 024103. DOI: 10.1063/1.4863670.

[118] Alexander Sakowitz, Mihai Mihăescu, and Laszlo Fuchs. "Flow decomposition methods applied to the flow in an IC engine manifold". In: *Applied Thermal Engineering* 65.1 (2014), pp. 57–65. DOI: 10.1016/j.applthermaleng.2013.12.082.

[119] Romain Futrzynski and Gunilla Efraimsson. *Dymode: A parallel dynamic mode decomposition software*. KTH Royal Institute of Technology. 2015. ISBN: 978-91-7595-386-1. URL: http://kth.diva-portal.org/smash/record.jsf?pid=diva2%3A786623.

[120] Jiaqing Kou and Weiwei Zhang. "An improved criterion to select dominant modes from dynamic mode decomposition". In: *European Journal of Mechanics-B/Fluids* 62 (2017), pp. 109–129. DOI: 10.1016/j.euromechflu.2016.11.015.